Deposition of Metal Oxide Based Film for Gas Sensor Applications

by

Wangi Pandan Sari

A thesis submitted in partial fulfilment of the requirements for the degree of

Doctor of Philosophy in Engineering

School of Engineering

University of Warwick

May 2019

Abstract

As one of the most used gas sensor technology, MOX sensors has been studied with growing interest to improve sensor performance and explore further applications. This thesis presents investigations on a number of deposition techniques to fabricate metal oxide (MOX) based sensors for gas sensing applications. These techniques included three-dimensional printing (3DP) fused deposition modelling (FDM), aerosol assisted chemical vapour deposition (AACVD), spin coating, and screen-printing. They were employed to fabricate thin and thick film sensor devices with tungsten oxide and indium oxide as the base materials. Changes in material microstructures and composition through variations of sintering temperature, sensing layer thickness, operating temperature, and incorporation of additives, were investigated to understand the effects on sensor response. The fabricated sensors were characterised by various techniques including Scanning Electron Microscopy (SEM), Energy Dispersive X-ray Spectroscopy (EDS), X-ray Fluorescence (XRF), and X-Ray Photoelectron Spectroscopy (XPS) and the influence of the physical and chemical properties of the materials toward the targeted gas was also discussed. Here, the main application was found for detection of oxygen using tungsten oxide and indium oxide based sensor.

Declaration

This thesis is submitted to the University of Warwick in support of the application for the degree of Doctor of Philosophy in Engineering. It has not been submitted in part, or in whole, for a degree or other qualification at any other University. Parts of this work have been presented at international conferences and published in peer-reviewed research papers listed. The work described in this thesis is original and carried out by the author, except where otherwise indicated as in the cases below:

- The gas handling apparatus (section 2.5.1) was designed and built by Dr Siavash Esfahani and Samuel Agbroko.
- The gas handling software in LabVIEW and sensor chamber (section 2.5.2) were designed by Prof James Covington.
- Some of fabrication process was carried out in McGowan Sensor Labs with the support of Peter Smith.
- Sensor deposition by AACVD (Chapter 4) and XPS material characterisation were carried in collaboration with Prof Chris Blackman and Yiyun Zhu from University City College (UCL).

Dedication

untuk abah dan mamah

Thanks to your support, I can be where I am today

List of Published Work

Sari, Wangi, Simon Leigh, and James Covington. "Tungsten Oxide Based Sensor for Oxygen Detection." In *Multidisciplinary Digital Publishing Institute Proceedings*, vol. 2, no. 13, p. 952. 2018.

Sari, Wangi P., Chris Blackman, Yiyun Zhu, and James A. Covington. "AACVD Grown WO_3 Nanoneedles Decorated with Ag/Ag_2O Nanoparticles for Oxygen Measurement in a Humid Environment." *IEEE Sensors Journal* 19, no. 3 (2018): 826-832.

Sari, Wangi P., Chris Blackman, Yiyun Zhu, and James Covington. "Deposition of tungsten oxide and silver decorated tungsten oxide for use in oxygen gas sensing." In *2017 IEEE SENSORS*, pp. 1-3. IEEE, 2017.

Sari, Wangi, Peter Smith, Simon Leigh, and James Covington. "Oxygen Sensors Based on Screen Printed Platinum and Palladium Doped Indium Oxides." In *Multidisciplinary Digital Publishing Institute Proceedings*, vol. 1, no. 4, p. 401. 2017.

Acknowledgments

الحمد لله ربّ العالمين

All praises and thanks to Allah S.W.T for giving me the blessing and strength to complete this thesis.

I would like to thank Indonesia Endowment Fund/ Lembaga Pengelola Dana Pendidikan (LPDP) for the financial support during my PhD.

Special thanks go to my supervisors Prof. James Covington and Dr Simon Leigh for their guidance throughout my PhD. I would also like to thank Frank Courtney for his technical support. Thanks to my friends, Sam Agbroko and Dr Siavash Esfahani for their help in and beyond the lab. I would also like to express my thanks to Dr Chris Purssell and Dr Richard Watson for their support especially in early years of my PhD.

I'd also like to thank Peter Smith of McGowan Sensor Labs and Prof. Chris Blackman and Yiyun Zhu from UCL for their collaboration and support.

Last but not least, I'd like to thank my parents for their unconditional love and support throughout my PhD. Same goes for my brothers ka Fajar and ka Daus, and my sister Suci. For all your support, I have made it to the end of this journey.

Table of Contents

Abstract iv
Declaration v
Dedication vi
List of Published Work vii
Acknowledgments viii
Table of Contents ix
List of Figures xiii
List of Tables xix
List of Abbreviations xx
Chapter 1. Introduction 1
1.1 Background 1
1.2 Gas Sensor Technology 2
1.2.1 Electrochemical Gas Sensor 3
1.2.2 Pellistor (Catalytic Bead) Sensor 5
1.2.3 Nondispersive Infrared (NDIR) Sensor 6
1.2.4 Photoionisation Detector (PID) 7
1.2.5 Metal Oxide Sensor 9
1.3 Research Aims 10
1.4 Thesis Outline 12
1.5 References 14
Chapter 2. Metal Oxide Sensors: Technology and Characterisation 15
2.1 Introduction 15
2.2 Metal Oxide Sensors Review 15
2.2.1 Features and Characteristics 16
2.2.2 Semiconductor of n-type and p-type material 18
2.2.3 Thick-film vs Thin-film Metal Oxide 18
2.2.4 Sensing Mechanism 20
2.2.5 Application 22
2.3 Influencing Factors in Gas Response 23
2.3.1 Morphology 23
2.3.2 Temperature 25
2.3.3 Humidity 26
2.3.4 Incorporation of Additives 27
2.4 Material Characterisation 28
2.4.1 Thermogravimetric Analysis (TGA) 28
2.4.2 White Light Interferometry (WLI) 29
2.4.3 Scanning Electron Microscopy (SEM) 30

2.4.4 Transmission Electron Microscopy (TEM) 31
2.4.5 Energy-dispersive X-ray spectroscopy (EDX/EDS) 32
2.4.6 X-ray Powder Diffraction (XRD) 33
2.4.7 X-ray Fluorescence (XRF) 35
2.4.8 X-ray photoelectron spectroscopy (XPS) 36
2.5 Gas Sensing Characterisation 36
2.5.1 Gas Handling Apparatus 37
2.5.2 Gas Sensing Chamber 39
2.5.3 Experimental Setup and Data Acquisition 41
2.6 References 43
Chapter 3. Three-Dimensional Printed Tungsten Oxide Based Sensor 54
3.1 Introduction 54
3.2 Three-Dimensional Printing (3DP) Technology 55
3.2.1 Stereolithography (SLA) 55
3.2.2 Selective Laser Sintering (SLS) 56
3.2.3 Fused Deposition Modelling (FDM) 56
3.3 FDM Technology for Sensor Fabrication 57
3.4 Material Characterisation 62
3.5 Gas Testing 65
3.5.1 Gas Testing Using Permeation 66
3.6 Results and Analysis 69
3.6.1 Isobutylene 69
3.6.2 Low Concentration VOC 74
3.6.3 Sensor Performance 80
3.7 Conclusion 81
3.8 References 82
Chapter 4. AACVD Grown Tungsten Oxide Based Thin Film Sensors 85
4.1 Introduction 85
4.2 Chemical Vapour Deposition (CVD) 86
4.2.1 Thermally Activated Chemical Vapour Deposition (TACVD) 88
4.2.2 Aerosol Assisted Chemical Vapour Deposition (AACVD) 88
4.3 Synthesis of Metal Oxide Films 89
4.4 Material Characterisation 91
4.5 Gas Testing 96
4.5.1 WO_3 Thin Film 96
4.5.2 Ag/Ag_2O-WO_3 Thin Film (31% Ag Content) 97
4.5.3 Ag/Ag_2O -WO_3 Thin Film (38% Ag Content) 98
4.6 Analysis and Discussion 100
4.7 Conclusion 105
4.8 References 106

Chapter 5. Spin Coated Tungsten Oxide Based Thin Film Sensor 109
5.1 Introduction 109
5.2 Spin Coating Technology 109
5.3 Work Development 110
5.3.1 Ink Formulation 110
5.3.2 Deposition Process 111
5.3.3 Ultraviolet Curing and Developing 114
5.3.4 Sintering Process 118
5.4 Sensor Fabrication 121
5.5 Material Characterisation 128
5.6 Gas Testing 130
5.6.1 WO_3 850°C Film 130
5.6.2 WO_3 900°C Film 132
5.7 Analysis and Discussion 133
5.8 Conclusion 136
5.9 References 137
Chapter 6. Spin Coated Indium Oxide Based Thin Film Sensor 139
6.1 Introduction 139
6.2 Indium Oxide for Gas Sensing Application 139
6.2.1 Sensor Fabrication 140
6.2.2 Ink Formulation 140
6.2.3 Deposition Process 141
6.2.4 Ultraviolet Curing and Developing 142
6.2.5 Sintering Process 143
6.3 Material Characterisation 144
6.4 Gas Testing 149
6.4.1 Indium Oxide Films (In_2O_3) 150
6.4.2 Palladium Oxide Decorated Indium Oxide Film ($PdO\text{-}In_2O_3$) 152
6.4.3 Platinum Oxide Decorated Indium Oxide Film ($PtO_2\text{-}\ In_2O_3$) 154
6.5 Analysis and Discussion 157
6.5.1 Effect of Operating Temperature 157
6.5.2 Effect of Sintering Temperature 158
6.5.3 Effect of Humidity 159
6.5.4 Effect of Catalyst 161
6.6 Conclusion 163
6.7 References 164
Chapter 7. Screen Printed Indium Oxide Based Thick Film Sensor 167
7.1 Introduction 167
7.2 Screen Printing Technology for Thick-Film Deposition 167
7.2.1 Screen Printing Components 168

7.2.2 Screen Printing Setup 169
7.3 Sensor Fabrication 170
7.3.1 Ink Formulation 171
7.3.2 Deposition Process 172
7.4 Material Characterisation 174
7.5 Gas Testing 177
7.5.1 Palladium Oxide Decorated Indium Oxide Films ($PdO-In_2O_3$) 178
7.5.2 Platinum Oxide Decorated Indium Oxide Films ($PtO_2- In_2O_3$) 182
7.6 Analysis and Discussion 188
7.6.1 Influencing Factors on Sensor Performance 188
7.6.2 Sensor Repeatability and Reproducibility 193
7.7 Conclusion 196
7.8 References 197
Chapter 8. Development of Metal Oxide Based Sensor for Oxygen Detection 198
8.1 Introduction 198
8.2 Metal Oxide Sensor for Oxygen Detection 199
8.3 Sensor Fabrication Technique 200
8.4 Gas Testing 202
8.4.1 Experimental Set-up 202
8.4.2 Humidity Test 203
8.4.3 Selectivity Test 206
8.4.4 Interference Test 208
8.5 Analysis and Discussion 210
8.6 Conclusion 217
8.7 Reference 218
Chapter 9. Conclusions and Further Work 220
9.1 Conclusions 221
9.1.1 Sensor Comparison and Evaluation 224
9.1.2 Source of Error and Limitations 226
9.2 Further Work 227
9.2.1 Fabrication 227
9.2.2 Tests and Evaluation 228
9.2.3 Design and Packaging 229
Appendices I

List of Figures

Figure 1 - 1 Electrochemical gas sensors [2]. 3
Figure 1 - 2 Typical construction of an electrochemical sensor. 4
Figure 1 - 3 Construction of pellistor (catalytic beads) sensor. 5
Figure 1 - 4 Components of an NDIR sensor. 7
Figure 1 - 5 Basic principle of PID on VOC detection. Adapted and redrawn from [4]. 8
Figure 1 - 6 Metal oxide sensor. 9

Figure 2 - 1 Schematic of a typical sensor substrate. 16
Figure 2 - 2 Gas sensing mechanism of n-type semiconducting oxide upon interaction with (a) air and (b) target analyte CO. 21
Figure 2 - 3 Schematic model for the particle effects. Adapted and redrawn from [93]. 24
Figure 2 - 4 Sensing mechanisms of additives incorporated into metal oxide sensor: (a) chemical sensitisation and (b) electronic sensitisation. Redrawn and adapted from [92]. 27
Figure 2 - 5 Schematic of white light interferometer. 29
Figure 2 - 6 Schematic of a SEM instrument. 31
Figure 2 - 7 Schematic of a TEM instrument. 32
Figure 2 - 8 Schematic of electron beam interaction. 33
Figure 2 - 9 Construction of XRD instrument (left) and constructive interference based on Bragg's Law (right). 34
Figure 2 - 10 XRF irradiation. 35
Figure 2 - 11 Process involved in XPS surface analysis. 36
Figure 2 - 12 Gas handling apparatus from left to right: gas mixture, OVG-4, and humidity generator. 37
Figure 2 - 13 Schematic of a gas sensing procedure. 38
Figure 2 - 14 Software interface for the gas handling apparatus designed in LabVIEW. 38
Figure 2 - 15 Metal oxide sensor chamber when closed (left) and open (right). 40
Figure 2 - 16 AS330 SMS hardware and software interface. 41

Figure 3 - 1 Filament extruder (left) and extruded filament (right). 58
Figure 3 - 2 Thermogravimetric analysis of PCL. 59
Figure 3 - 3 Sintered WO_3 filament samples (left to right): 20%, 50%, 70%, 80%, and 85% content. 60
Figure 3 - 4 Printed WO3 with 70% (left) and 80% (right) content. 60
Figure 3 - 5 Sintering profile of WO_3 based sensor. 61
Figure 3 - 6 Sensor array on Al_2O_3 substrate: electrodes (left) and heater (right). 62
Figure 3 - 7 WO_3 based 3D printed sensor (left) and sensor packaging (right). 62
Figure 3 - 8 SEM of WO_3 samples sintered at 800°C (a);850°C (b);900°C (c);950°C (d);1000°C (e). 65
Figure 3 - 9 Standalone OVG-4 for (left) and permeation tube (right) [29]. 67
Figure 3 - 10 Sensor response at 20 ppm isobutylene operated at 250°C and 350°C. 70

Figure 3 - 11 Sensor response at 100 ppm isobutylene in 50% rh (device 1). 72
Figure 3 - 12 Sensor response at 100 ppm isobutylene in 50% rh (device 2). 72
Figure 3 - 13 Response and recovery time for isobutylene response (100 ppm). . 73
Figure 3 - 14 Sensor response to 100 ppm isobutylene at 350°C. 74
Figure 3 - 15 WO_3 sensor response at 350°C to 20ppb ethanol. 76
Figure 3 - 16 WO_3 sensor response at 350°C to 10ppb ethanol. 76
Figure 3 - 17 WO_3 device 1 response at 350°C to 5 and 10ppb ethanol. 77
Figure 3 - 18 WO_3 sensor responses at 350°C to 20ppb acetone. 78
Figure 3 - 19 WO_3 sensor response at 350°C to 2.5 ppth ethanol. 79
Figure 3 - 20 WO_3 sensor response at 350°C to 2.5-10 ppth ethanol. 79
Figure 3 - 21 WO_3 sensor response at 350°C to 2.5 & 5 ppth ethanol. 80

Figure 4 - 1 Schematic of CVD process. Adapted and redrawn from [1]. 87
Figure 4 - 2 Sensor array (from top to down: sensing material, electrodes, alumina substrate, heater). 91
Figure 4 - 3 XRD pattern of Ag thin films grown under different substrates temperature compared to standard pattern of metal Ag (JCPDS, 87-0718). 92
Figure 4 - 4 XRD patterns of WO_3 and Ag/Ag_2O-WO_3 deposited films on Al_2O_3 substrate. 93
Figure 4 - 5 XPS scans of W 4f core-level spectra of $AgWO_3$ on Al_2O_3 (left) and 3d Ag core-level spectra of $AgWO_3$ on Al_2O_3 (right). 94
Figure 4 - 6 SEM images of Ag-WO_3 thin film on Al_2O_3 substrate grown at 250°C. 95
Figure 4 - 7 The HR-TEM images of Ag/Ag_2O-WO_3 samples. 95
Figure 4 - 8 WO_3 dynamic response at different O_2 concentration at 150°C. 97
Figure 4 - 9 WO_3 dynamic response at different O_2 concentration at 350°C. 97
Figure 4 - 10 Baseline resistance and response comparison between WO_3 and $AgWO_3$ sensor. Information on the data is in Appendix B. 98
Figure 4 - 11 WO_3 based sensor responses at different temperature. 99
Figure 4 - 12 Dynamic response of WO_3 based sensors with different Ag/Ag_2O loading. 99
Figure 4 - 13 Response time of sensors with different silver/silver oxide loading. 103
Figure 4 - 14 Recovery time of sensors with different silver/silver oxide loading. 104
Figure 4 - 15 Gas response relationship as a function of oxygen concentration. 105

Figure 5 - 1 WO_3 (10:2 ratio) spin coated at 3000 rpm for 30 s from left to right: ink dropped by static dispense; after spinning; ink dropped by dynamic dispense. 112
Figure 5 - 2 WO_3 (10:9 ratio) spin coated at 3000 rpm for 30 s, from left to right: ink dropped by static dispense; after spinning; ink dropped by dynamic dispense. 113
Figure 5 - 3 WO_3 (10:2 ratio) spin coated for 30 s at 3000 rpm (a); 5000 rpm (b); 7000 rpm (c). 114
Figure 5 - 4 Mask pattern 50x50 mm. 114
Figure 5 - 5 Holder for smaller alumina substrate. 115
Figure 5 - 6 WO_3 ink (10:2 ratio) spin coated at 3000 rpm for 30 seconds at different UV exposure time 116

Figure 5 - 7 WO_3 ink (10:2 ratio) spin coated at 5000 rpm for 30 seconds at different UV exposure time. 117
Figure 5 - 8 WO_3 ink (10:2 ratio) spin coated at 7000 rpm for 30 seconds at different UV exposure time. 117
Figure 5 - 9 WO_3 ink (10:2 ratio) spin coated at 3000 rpm for 30 seconds and exposed at 5 minutes UV light. 118
Figure 5 - 10 Thermogravimetric of WO_3 sample. 119
Figure 5 - 11 Sintering profile of WO_3. 119
Figure 5 - 12 WO_3 samples (10:2 ratio) sintered at 850°C with spinning rate at: 3000 rpm (a); 5000 rpm (b); 7000 rpm (c). 120
Figure 5 - 13 WO_3 samples (10:1 ratio) sintered at 850°C with spinning rate 3000 rpm. 121
Figure 5 - 14 Scribed Al_2O_3 tiles with gold interdigitated electrodes. 121
Figure 5 - 15 WO_3 ink (10:1 ratio) on patterned tile spin coated at 3000 rpm and 5 minutes exposure: (a) before and (b) after sintering. 123
Figure 5 - 16 WO_3 ink (10:2 ratio) on patterned tile spin coated at 3000 rpm and 5 minutes exposure: (a) before and (b) after sintering. 124
Figure 5 - 17 WO_3 ink (10:1 ratio) on patterned tile spin coated at 2000 rpm and 8 minutes exposure: (a) before and (b) after sintering. 125
Figure 5 - 18 WO_3 ink (10:1 ratio) on patterned tile spin coated at 3000 rpm and 5 minutes exposure in 2 layers before and after sintering. 126
Figure 5 - 19 Sensing material 20% loading on individual tile after sintering process at 900°C. 127
Figure 5 - 20 Sensing material 33% loading on individual tile after sintering process at 900°C. 128
Figure 5 - 21 SEM images of WO_3 sensing material at different sintering temperature 129
Figure 5 - 22 Dynamic response of WO_3 sensor (annealed at 850°C) in dry and humid air at 350°C. 131
Figure 5 - 23 Response of WO_3 sensor (annealed at 850°C) in dry and humid air as a function of operating temperature. 131
Figure 5 - 24 Sensitivity of WO_3 sensor (annealed at 900°C) in dry and humid air as a function of operating temperature. 132
Figure 5 - 25 Dynamic response of WO_3 sensor (annealed at 900°C) in dry and humid air at 350°C. 133
Figure 5 - 26 Gas sensing mechanism of WO_3 sensor in dry air and wet air. 135
Figure 5 - 27 Sensitivity of WO_3 sensor in dry and humid air as a function of oxygen concentration. 136

Figure 6 - 1 Example of spin coated In_2O_3 based in deposited at 3000 rpm for 30 s. 142
Figure 6 - 2 Spin coated indium oxide on patterned alumina substrates after 6 minutes UV exposure and developing. 143
Figure 6 - 3 Sintering profile of spin coated In_2O_3. 144
Figure 6 - 4 Spin coated In_2O_3 based samples sintered at 850°C. 144
Figure 6 - 5 SEM images of pure In_2O_3 sensor annealed at 850°C (left) and 900°C (right). 145
Figure 6 - 6 SEM images of PdO-In_2O_3 sensor annealed at 850°C (left) and 900°C (right). 145
Figure 6 - 7 SEM images of PtO_2 - In_2O_3 sensor annealed at 850°C (left) and 900°C (right). 146

Figure 6 - 8 SEM images of In_2O_3 based sensor annealed at 850°C at a higher magnification. 146
Figure 6 - 9 EDS spectrum of indium oxide-based sensors deposited by spin coating. 147
Figure 6 - 10 XRD patterns of indium oxide-based sensors deposited by spin coating. 148
Figure 6 - 11 **(a)** Survey, **(b)** In 3d high resolution XPS spectra of In_2O_3, Pd-In_2O_3, and Pt-In_2O_3, **(c)** Pd 3d high resolution XPS spectrum of Pd-In_2O_3, **(d)** Pt 4f high resolution XPS spectrum of Pt-In_2O_3. 149
Figure 6 - 12 In_2O_3 (annealed at 850°C) responses to 20% O_2 in dry and humid environment. 150
Figure 6 - 13 Resistance of In_2O_3 (annealed at 850°C) exposed to oxygen in dry and humid air at 350°C. 151
Figure 6 - 14 In_2O_3 (annealed at 900°C) responses to 20% O_2 in dry and humid environment. 152
Figure 6 - 15 PdO-In_2O_3 (annealed at 850°C) responses to 20% O_2 in dry and humid environment. 152
Figure 6 - 16 PdO-In_2O_3 (annealed at 900°C) responses to 20% O_2 in dry and humid environment. 153
Figure 6 - 18 PtO_2- In_2O_3 (annealed at 850°C) resistance to 20% O_2 in dry and humid environment. 155
Figure 6 - 19 Pt O_2-In_2O_3 (annealed at 850°C) responses to 20% O_2 in dry and humid environment. 155
Figure 6 - 20 PtO_2- In_2O_3 film (annealed at 900°C) resistance to 20% O_2 in dry and humid environment. 156
Figure 6 - 21 PtO_2-In_2O_3 film (annealed at 900°C) responses to 20% O_2 in dry and humid environment. 156
Figure 6 - 22 Example of In_2O_3 sensor responses to 20% dry O_2 at various operating temperatures. 158
Figure 6 - 23 Resistance of indium oxide-based sensors in dry and humid environment at 350°C. 160
Figure 6 - 24 Resistance of the indium oxide-based sensors in dry (top)and humid environment (bottom). 162

Figure 7 - 1 Screen printing masks made of: (a) stencil metal [1] and (b) mesh [2]. 168
Figure 7 - 2 Basic of screen-printing instrument: (a) screen printer body, (b) mesh to print the pattern, and (c) the workholer to hold the substrate. 173
Figure 7 - 3 SEM images of PdO-In_2O_3 and PtO_2-In_2O_3 at lower magnification (top) and higher magnification (down). 174
Figure 7 - 4 EDS spectra of indium based thick-film sensors deposited by screen printing. 175
Figure 7 - 5 WDXRF spectra of PdO and PtO_2 decorated In_2O_3 thick-film sensors. 176
Figure 7 - 6 (a) Survey, (b) In 3d high resolution XPS spectra of In_2O_3, Pd-In_2O_3, and Pt-In_2O_3, (c) Pd 3d high resolution XPS spectrum of Pd-In_2O_3, (d) Pt 4f high resolution XPS spectrum of Pt-In_2O_3. 177
Figure 7 - 7 Resistance value across PdO-In_2O_3 thick films upon exposure to 20% O_2 (85% RH). 178
Figure 7 - 8 Example of PdO-In_2O_3 sensor responses to 20% O_2 in dry and humid (85% RH) air. 179

Figure 7 - 9 $PdO-In_2O_3$ thick film responses to 20% O_2 in dry and humid air (85% RH). 180
Figure 7 - 10 Film resistance changes of $PdO-In_2O_3$ toward 20% O_2 in humid air (top) and dry air (bottom). 181
Figure 7 - 11 $PdO-In_2O_3$ sensor response in humid air (85% RH): resistance changes toward various O_2 concentration (left) and the gas response relationship as a function of O_2 concentration (right). 182
Figure 7 - 12 $PdO-In_2O_3$ sensor response in dry air: resistance changes toward various O_2 concentration (left) and the gas response relationship as a function of O_2 concentration (right). 182
Figure 7 - 13 Resistance value across $PtO_2-In_2O_3$ thick films upon exposure to 20% O_2 (85% RH). 183
Figure 7 - 14 Example of $PtO_2-In_2O_3$ sensor responses to 20% O_2 in dry and humid (85% RH) air. 184
Figure 7 - 15 $PtO_2-In_2O_3$ thick film responses to 20% O_2 in dry and humid air (85% RH). 185
Figure 7 - 16 Film resistance changes of $PtO_2-In_2O_3$ toward 20% O2 in humid air (top) and dry air (bottom). 186
Figure 7 - 17 $PtO_2-In_2O_3$ sensor response in humid air (85% RH): resistance changes toward various O_2 concentration (left) and the gas response relationship as a function of O_2 concentration (right). 187
Figure 7 - 18 $PtO_2-In_2O_3$ sensor response in dry air: resistance changes toward various O_2 concentration (left) and the gas response relationship as a function of O_2 concentration (right). 187
Figure 7 - 19 PdO and PtO_2 based In_2O_3 sensor responses toward 20% O_2 in humid environment at various operating temperatures. 190
Figure 7 - 20 Resistance toward 20% O_2 at 200°C for $PdO-In_2O_3$ sensor (left) and 250°C for $PtO_2-In_2O_3$ (right). 191
Figure 7 - 21 Example of resistance changes of PdO and PtO_2 decorated In_2O_3 toward 20% O_2 (85% RH) at various operating temperatures. 192
Figure 7 - 22 PdO and PtO_2 decorated In_2O_3 thick film responses to 20% O_2 in humid air (top) and dry air (bottom). 193
Figure 7 - 23 Repeated measurements of $PdO-In_2O_3$ sensor under humid air at 200°C toward: 20% O_2 (left) and various O_2 concentration (right). . 194
Figure 7 - 24 Repeated measurements of $PtO_2-In_2O_3$ sensor under humid air toward: 20% O_2 (left) and various O_2 concentration (right). 194
Figure 7 - 25 Repeated measurements across $PdO-In_2O_3$ sensors under humid air toward: 20% O_2 (left) and various O_2 concentration (right). 195
Figure 7 - 26 Repeated measurements across $PtO_2-In_2O_3$ sensors under humid air toward: 20% O_2 (left) and various O_2 concentration (right). 196

Figure 8 - 1 Example of sensor responses toward 20% O_2 at 300°C for $PdO-In_2O_3$ sensor (top) and 250°C for PtO - In_2O_3 (bottom). 205
Figure 8 - 2 Example of sensor responses at various relative humidity level toward 20% O2 at 300°C for $PdO-In_2O_3$ sensor (top) and 250°C for $PtO-In_2O_3$ (bottom). 206
Figure 8 - 3 Selectivity toward different gases tested under humid air (85% RH) of $PdO-In_2O_3$ at 200°C (top) and $PtO_2-In_2O_3$ at 250°C (bottom). 207
Figure 8 - 4 Responses of $PdO-In_2O_3$ (top) and $PtO_2-In_2O_3$ (bottom) toward 1 ppm isobutylene as interference gas during oxygen measurement (20%). 209

Figure 8 - 5 Responses of $PdO-In_2O_3$ (top) and $PtO_2-In_2O_3$ (bottom) toward 1 ppm ethylene as interference gas during oxygen measurement (20%). 210
Figure 8 - 6 ACC tube connector set-up: (a) side view of the tube containing ACC filter, (b) front view of the tube connector, (c) 1/4 tube connectors adapted to 1/8 fittings. 212
Figure 8 - 7 Responses of $PdO-In_2O_3$ (top) and $PtO_2-In_2O_3$ (bottom) toward 1 ppm isobutylene as interference gas during oxygen measurement (20%) with and without ACC filter. 213
Figure 8 - 8 Responses of $PdO-In_2O_3$ (top) and $PtO_2-In_2O_3$ (bottom) toward 1 ppm ethylene as interference gas during oxygen measurement (20%) with and without ACC filter. 215
Figure 8 - 9 Responses of $PdO-In_2O_3$ (top) and $PtO_2-In_2O_3$ (bottom) toward 2.5 ppm ethylene as interference gas during oxygen measurement (20%) with and without ACC filter. 216
Figure 8 - 10 Responses of $PdO-In_2O_3$ (top) and $PtO_2-In_2O_3$ (bottom) toward 10 ppm ethylene as interference gas during oxygen measurement (20%) with and without ACC filter. 217

Figure A - 1 Cracks on 3D-printed WO_3 sensor. I
Figure A - 2 XRD patterns of Ag decorated WO_3 film on glass substrate as compared to standard data of monoclinic WO_3 (JCPDS, 72-0677) and metal Ag (JCPDS, 87-0718). II
Figure A - 3 SEM images of $Ag-WO_3$ on glass substrate at 200 °C (a and b) 0.06g $AgNO_3$ precursor used under different magnifications and (c and d) 0.09g $AgNO_3$ precursor used under different magnifications. III
Figure A - 4 High resolution scans XPS of Ag 3d core-level spectra of Ag on glass substrate by using AgNO3 in a 2:1 mixed solvent of acetone and methanol, at 250 °C and a flow of nitrogen. III
Figure A - 5 Baseline resistance and response comparison between WO_3 and Ag/Ag_2OWO_3 sensor with data label. IV
Figure A - 6 More example responses of $PdO-In_2O_3$ sensor to 20% O_2 in dry and humid (85% RH) air. Here, both sensors showed higher resistance observed in humid air than in dry air. V
Figure A - 7 More example responses of $PtO_2-In_2O_3$ sensor to 20% O_2 in dry and humid (85% RH) air. Here, both sensors showed overall higher resistance observed in humid air than in dry air. VI

List of Tables

Table 2 - 1 Change of resistance in semiconducting metal oxide materials..... 22

Table 3 - 1 Percentage of WO_3 in WO_3-PCL mixture..... 58
Table 3 - 2 Diameter of extruded filaments. 59
Table 3 - 3 Material density at different sintering temperatures. 61
Table 3 - 4 Flowrate and concentration of acetone and ethanol permeation devices..... 67
Table 3 - 5 Constants for Antoine's vapour pressure equations [30]..... 68
Table 3 - 6 Calculated concentration of sample vapours. 69

Table 5 - 1 Rate of response and recovery for spin coated WO_3 sensor. 133

Table 6 - 1 Components to create Pt- In_2O_3 and Pd-In_2O_3 powders. 141
Table 6 - 2 Response and recovery time of Pd-In_2O_3 films. 154
Table 6 - 3 Response and recovery time of PtO_2-In_2O_3 films. 157

Table 9 - 1 Response comparison of sensors fabricated by different deposition methods. 225

List of Abbreviations

2D	-	two-dimensional
3DP	-	three-dimensional printing
AACVD	-	aerosol assisted chemical vapour deposition
ACC	-	activated carbon cloth
$AgNO_3$	-	silver nitrate
APCVD	-	atmospheric pressure chemical vapour deposition
atm	-	atmosphere
BSE	-	backscattered secondary electron
BE	-	binding energy
CAD	-	Computer-aided design
CCVD	-	combustion chemical vapour deposition
CNC	-	Computer Numerical Control
CTO	-	Chromium Titanium Oxide
CuO	-	copper oxide
CVD	-	chemical vapour deposition
EDL	-	electron depleted layer
EDM	-	electrical discharge machine
EDS/EDX	-	energy-dispersive x-ray spectroscopy
FDM	-	fused deposition modeling
HAL	-	hole accumulation layer
HRTEM	-	high-resolution transmission electron microscopy
In_2O_3	-	indium oxide
ISB	-	isobutylene
KE	-	kinetics energy
LPCVD	-	lower pressure chemical vapour deposition
LSM	-	lanthanum strontium manganate
MEMS	-	Micro-ElectroMechanical Systems
MFC	-	mass flow controller
MOCVD	-	metalorganic chemical vapour deposition
MOX	-	metal oxide
MWCNT	-	multi-walled carbon nanotube
NP	-	nanoparticles
PCL	-	polycaprolactone
PdO	-	palladium oxide
PtO_2	-	platinum oxide
PID	-	photoionisation detector
ppm	-	part per million
ppth	-	part per thousand
ppb	-	part per billion
PTFE	-	polytetrafluoroethylene

RFID	-	radio-frequency identification
RH	-	relative humidity
SE	-	secondary electron
SEM	-	scanning electron microscopy
SLA	-	stereolithography
SLM	-	selective laser melting
SLS	-	selective laser sintering
SnO_2	-	tin oxide
STL	-	stereolithography
TACVD	-	thermally-activated chemical vapour deposition
TEM	-	transmission electron microscopy
UHVCVD	-	ultra-high vacuum chemical vapour deposition
UV	-	ultraviolet
VOC	-	volatile organic compound
VSI	-	vertical scanning interferometry
$W(CO)_6$	-	tungsten hexacarbonyl
WDXRF	-	wavelength dispersive x-ray fluorescence
WLI	-	white light interferometry
WO_3	-	tungsten oxide
XRD	-	x-ray powder diffraction
XRF	-	x-ray fluorescence
XPS	-	x-ray photoemission spectrometry
YSZ	-	yttria stabilised zirconia
ZnO	-	zinc oxide

Chapter 1. Introduction

1.1 Background

Advances in manufacturing have created negative effects on the environment. This started with the Industrial Revolution, which marked a major turning point in ecology of the earth and interaction between humans and environment. As fossil fuels replaced wind, water and wood as the source of energy used primarily for manufacturing processes, pollution and environmental damage became the consequence. While it is vital for economic growth and development of a society, industrialization is often accompanied by harmful environment problems. It produces pollutants in air, water, soil, and habitat, resulting in global environmental issues, health problems, and the green house effects amongst other things.

The biggest impact of industrialization is air pollution, caused by operations of factories from many diverse fields such as oil and gas operations, transportation industry, power plants, and agriculture. This does not only affect the air quality outdoor but also indoor and in confined spaces. Air within buildings and homes can even be more polluted than outdoor. The source of household pollutants may come from various appliances such as heating system, cooking, ventilation, chemicals in cleaning products, and building materials. In 2016, WHO reported 3.8 million deaths due to household air pollution and 4.2 million deaths due to ambient air pollution [1]. The harmful effects of pollutions clearly indicate the need to monitor and control the air quality we breathe in.

The air quality outdoors is monitored by various air quality monitoring stations established by government in various cities following on the EU standard methods for

air quality monitoring. These monitoring stations can provide data of outdoor air and the pollutants detected in the area, but they do not monitor the indoor air quality.

As people spend majority of their time inside buildings, indoor air quality (IAQ) system becomes clearly imperative. The system needs to monitor the level of oxygen and carbon dioxide in air to ensure of healthy values. Off balance O_2 and/or CO_2 levels may cause difficulty to concentrate, dizziness, and passing out. High level of CO_2 and low level of O_2 can be life threatening. If oxygen level drops too low for example, it may cause brain damage or even death. Therefore, the levels of O_2 as well of CO_2 should always be monitored especially in closed environments.

1.2 Gas Sensor Technology

Gas sensor is a device that detects the presence of gases. In general, a sensor is a device which senses physical quantity and convert it into signal that could be read by a user whereas a transducer is a device that converts one form of energy into another form. Some people use sensors interchangeably with transducers as transducers are sometimes found in sensors.

Gas sensor field can be segmented on the basis of the target gas/products, application, and technology. Based on the product, gas sensor can be classified into, for example, ammonia (NH_3) sensor, NO_x sensor, CO_2 sensor, CO sensor, O_2 sensor, Volatile Organic Compound (VOC) sensor, and so on. On the basis of the end-use applications, it can also be divided in to application, such as environmental, medical, automotive, industrial, petrochemical, appliances, ambient air monitoring, and others. The based on the core sensing technology, for example electrochemical, pellistors, infrared, photoisonisation detector, and metal oxide.

The classification of gas sensor technology is further discussed in the following.

1.2.1 Electrochemical Gas Sensor

Electrochemical gas sensors (Figure 1 - 1) measure the concentration of a target gas by a chemical reaction (oxidising or reducing the target gas) which produces an electrical signal related to the concentration of the target gas. They are commonly used to detect oxygen and toxic gases such as CO, H_2S, NO, NO_2, and SO_2.

Most electrochemical sensors are amperometric sensors that generate current proportional to the gas concentration, although other types are also available. These are potentiometric (change of membrane potential), conductometric (change of conductance), and impedimetric (change of impedance).

Figure 1 - 1 Electrochemical gas sensors [2].

An electrochemical sensor contains at least 2 electrodes (sensing electrode/ anode which serves as the transducer and counter electrode/ anode) in contact with an electrolyte and a diffusion barrier. The target gas first passes through the diffusion barrier to reach the working electrode. Upon contact, oxidation (accepting oxygen and/or giving up electrons) or reduction (giving up oxygen and/or accepting electrons) will occur on the sensing electrode through chemical reaction. For example, carbon monoxide (a reducing gas) is oxidised upon contact with the sensing electrode, causing a potential shift to a negative direction. The chemical reaction is as follow [3]:

Sensing-electrode

$$2CO + 2H_2O \rightarrow 2CO_2 + 4H^+ + 4e^- \quad (1.1)$$

Counter-electrode

$$O_2 + 4H^+ + 4e \rightarrow 2H_2O \quad (1.2)$$

Cell-reaction

$$2CO + O_2 \rightarrow 2CO_2 \quad (1.3)$$

An electrochemical sensor consisting of 3 electrodes utilises a reference electrode to eliminate interference. It has a stable potential and allows the sensing electrode potential to be biased. The typical construction of an electrochemical sensor is illustrated in Figure 1 - 2.

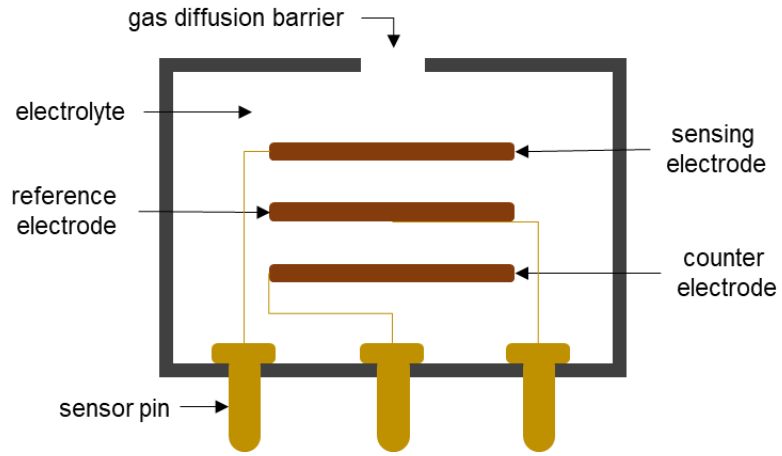

Figure 1 - 2 Typical construction of an electrochemical sensor.

Electrochemical sensors dominate the market for oxygen detections. They exhibit good selectivity with high level of accuracy and repeatability. The response of the sensors is linear to changes in gas concentration and generally not affected by humidity. However, their operation is affected by temperature and exposure to temperature >30°C may reduce their signal output and at >40°C the electrolyte will

dry out render the sensors useless [3]. The sensor life is limited to 1 – 3 years even when not in use. This is because the cells are still active despite in storage.

1.2.2 Pellistor (Catalytic Bead) Sensor

Pellistor sensors are designed to monitor combustible gases up to an upper explosion limit. The sensors, working based on the catalytic oxidation, are typically used to provide a hazardous condition threshold where an alarm will be triggered when combustible gases are present beyond the threshold level.

A pellistor sensor consists of two ceramic beads with fine coils of platinum embedded inside. The coils serve as an electrical heater (transducer), where the resistance (and thus temperature) of the heating element is measured. One of the beads is treated with a catalyst material, making it sensitive to flammable gases. The other bead has no catalytic material and acts as reference. If a combustible gas is present when the bead is heated, the gas will oxidise and so increase the temperature of the bead. The temperature increase produces an increase in the resistance of the coil. Since the reference bead is not affected by the combustible gas, its resistance differs from the resistance of the catalytic bead. This difference in resistance is measured to be proportional to the concentration of the combustible gas.

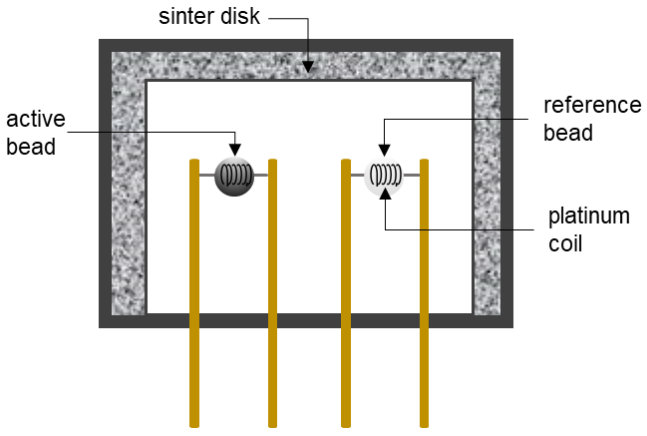

Figure 1 - 3 Construction of pellistor (catalytic beads) sensor.

Pellistor sensors are normally equipped in instruments used in areas where combustible gases can be found. An example of this is the detection of methane, which is usually found in coalmines and sewers. The sensors are widely used in a variety of applications ranging from monitoring methane and hydrogen to hydrocarbon and kerosene spillage. In addition to that, they are versatile, simple, and relatively inexpensive. Despite these advantages, pellistor sensors has a number of drawbacks including the need of oxygen to be present in system and susceptibility to chemical poisoning (e.g. organic silicones, derivatives of hydrocarbons, H_2S), which gradually decreases sensor performance or worse, it could cause total loss of sensitivity.

1.2.3 Nondispersive Infrared (NDIR) Sensor

Nondispersive infrared (NDIR) sensor is a spectroscopic based sensor that measures the spectrum of light radiated from an IR emitter adsorbed by the surrounding air to quantify the concentration of a specific gas. The sensors can detect air pollutants such as CO_2, CO, hydrocarbons, SO_2, CH_4, HF, HCl and NO_x. They are best known for CO_2 detection due to the high absorbance toward the gas (wavelength at 4.3 μm) and minimum interference from other elements.

The main components of NDIR sensors, shown in Figure 1 - 4, are an IR light source, a sample chamber or light tube, an optical filter, and an infrared detector. The presence of gases in the chamber results in absorption of specific wavelength measured by the detector. The optical filter which is located just before the detector serves to eliminate interference lights. Therefore, only the wavelength of the selected gas molecules are adsorbed by the detector which enables more accurate measurement.

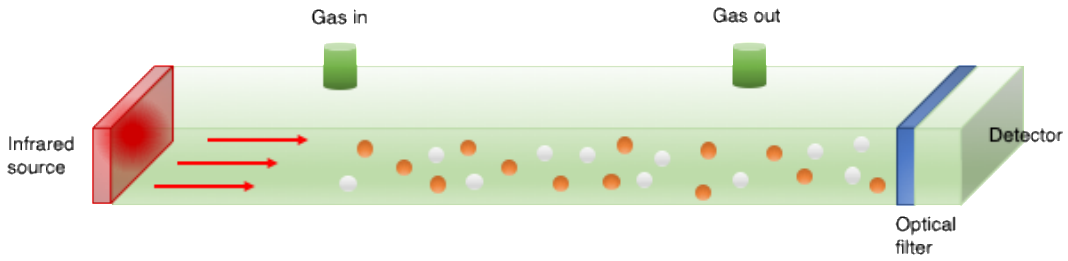

Figure 1 - 4 Components of an NDIR sensor.

NDIR sensors offer advantages such as low energy consumption, long life expectancy (exceeding 5 years), and fast response. They use physical sensing technique which make these sensors less affected by the chemical environment. Thus, NDIR sensors do not suffer from poisoning effects like pellistor sensors. However, not every gas concentration can be measured with NDIR sensors. Symmetrical molecules such as H_2, N_2, and O_2 are not excited by IR, hence can't be detected. Furthermore, the sensors suffer from a certain degree of cross-sensitivity toward other gases and humidity interference if the wavelength of absorption window overlaps.

1.2.4 Photoionisation Detector (PID)

PID is a gas detector that uses an ultraviolet light source to ionise gas to positive and negative ions that can be counted with a detector. It is typically designed for the detection of VOCs. The schematic of PID working principle is presented in Figure 1 - 5.

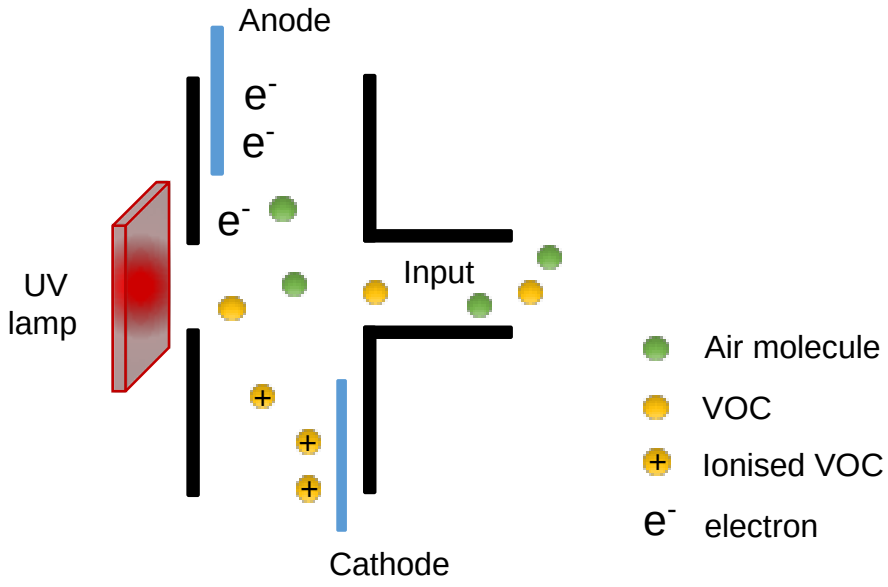

Figure 1 - 5 Basic principle of PID on VOC detection. Adapted and redrawn from [4].

A PID sensor is equipped with a UV lamp which emits photons of high energy UV light. As the VOC molecules drawn into the sensor chamber, the molecules will break into electrons and positively charged ions. This ionization process generates an electric current which is proportional to the concentration of the VOC. The ionization can only occur if the ionization potential of the molecules is lower than the UV lamp. The krypton lamp (10.6 eV) is usually used due to its high sensitivity, but other lamp such as Xenon (9.6 eV) can be used as well.

PID offers high sensitivity (down to part per billion (ppb) level) with high precision and quick response (less than 3 s). It can detect a broad range of gases and generally not affected by temperature and humidity changes. In comparison with the aforementioned technologies, PID comes at a much higher price and despite its rapid response and high accuracy, it cannot identify the compounds detected.

1.2.5 Metal Oxide Sensor

Metal oxide (MOX) semiconducting sensor is a chemiresistive based sensor that detects gases through a surface reaction at the surface of the metal oxide. Upon contact with gas, resistance of the sensing material changes and this can be measured to correspond to the gas concentration.

Figure 1 - 6 illustrates MOX sensor, which mainly comprises of sensor substrate, sensing material, electrodes to measure the resistance change of the sensor and a heater (if heating is required).

Figure 1 - 6 Metal oxide sensor.

The family of MOX sensors has been very successful, having more than 25% market share of the global gas sensor market [5]. These sensors are inexpensive, easy to use and to integrate with other electronic devices, stable and very sensitive with extensively long-life span and ability to survive in a harsh environment. Additionally, they also operate at a low power consumption. For example, metal oxide based sensors from Alphasense has a typical heater resistance value of 24 ± 4 Ohm, voltage of 2.7 ± 0.2 V, and power consumption of 350 ± 40 mW when sensors with resistance in air at 50% RH is around 250 ± 100 kOhm is operated at 400°C [6].

TGS2600 metal oxide based air quality sensor from Figaro has a typical heater resistance value of 83 Ohm, voltage of 5.0±0.2V, and power consumption of 210mW with the sensor resistance at 10kΩ ~ 90kΩ operated at room temperature [7]. A lower operating temperature as well as higher sensing film conductivity contribute to a lower power consumption which is a desired criteria for remote applications. Therefore, in order to develop metal oxide based sensors with high response and lower power consumption, it is important to aim for lower optimum operating temperature.

Metal oxide sensors have been used in a range of different applications to detect different type of air pollutants, namely, greenhouses gases (CH_4, CO_2), particulate matter ($PM_{2.5}$, PM_{10}) using a combined a commercial dust sensor and a complementary metal-oxide-semiconductor transducer [8] and toxic gases (CO, H_2S, SO_x, NO_X, VOCs). However, these sensors are known to suffer from selectivity issue and humidity intolerance.

1.3 Research Aims

The advances in manufacturing has brought negative effects on the environment and health, costing huge financial lost and millions of deaths. Therefore, it is imperative to monitor and control air quality which is mainly evaluated by the means of gas detectors. Different gas sensing technologies as highlighted in the previous section has its own pro and cons. Depending on the application, one technology could be suited better than the others. For example, for the detection of VOCs which require a high level of accuracy and precision, using a PID would be better, especially when cost is not an issue. However, if the cost is something to consider and such high

precision is not required (such as for air cabin quality for automobiles), then other technologies such as electrochemical and MOX sensors would be better suited.

Amongst the gas sensing technologies, metal oxide-based sensor has been comprehensively studied but the interest on developing these sensors is still growing over the years. It is because there are still factors that influence gas sensor performance that could be explored, such as utilising different materials and/or material combinations tested for a particular gas. For example, using a heterojunction of n-type and p-type materials to detect various compounds. Parameters such as range of fabrication techniques, materials and gas sensing characteristics, contribute to gas sensor performance and these could still be improved. Moreover, MOX based sensor can be further explored and extensively investigated for a wider range of applications such as to measure ozone or oxygen.

The aim of this thesis is to explore various manufacturing techniques through the integration of inorganic materials into a range of binder systems to fabricate metal oxide (MOX) based films for gas sensing applications. The novelty of the research lies in the combination of the fabrication techniques and the investigation of MOX sensor application for oxygen detection. For instance, the fabrication method by a three-dimensional (3D) printing technique for gas sensing application has been presented here and this has not been reported before. MOX sensors have been investigated for oxygen detection previously, but not to the extensive level presented here.

The objectives of the research are as follows:

- To determine if sensor responses are improved with a particular manufacturing technique

- To determine if sensor responses are improved when applying different materials and combination of materials as the sensing materials
- To investigate the influencing factors in metal oxide sensors and optimise them to give the best responses
- To understand any interactions between the sensor and compound of interest
- To investigate the interference of humidity and other gases in sensor responses
- Finally, to understand the effects of overall factors including microstructures, material composition and thickness, porosity, and temperature on the behaviour of the fabricated sensors.

1.4 Thesis Outline

A summary of the chapters presented in this thesis is listed below.

Chapter 2 covers in greater details review of the technology for metal oxide sensor, including the applications, features, and different type of materials available in MOX sensor. A number of influencing factors in gas responses are discussed. This chapter also presents review on materials and gas sensing characterisation.

Chapter 3 primarily describes the fabrication process of MOX sensor using a 3D printing technique. Tungsten oxide (WO_3) was incorporated into polycaprolactone (PCL) matrix and printed by a fused deposition modelling technique (FDM). The sensors were printed as thick-films and tested for the detection of VOCs.

Chapter 4 discusses the fabrication process of WO_3 based sensor using aerosol assisted chemical vapour deposition (AACVD) method. Pure and decorated thin-film

sensors were fabricated and the tested for oxygen detection. The response from both type of sensors was compared and analysed.

Chapter 5 details the deposition technique to fabricate WO_3 based sensor by spin coating technique. The tungsten oxide has been incorporated into a negative photoresist before developed to create a well-defined pattern. The sensors were tested for oxygen and the obtained results were analysed and compared with the WO_3 sensors deposited by AACVD.

Chapter 6 utilises the same spin coating technique to fabricate thin-film sensor based on indium oxide. Pure and decorated indium oxide sensors were produced and tested for oxygen in humid and dry air. The response of the sensors was analysed and compared to understand the effect of humidity and catalyst in gas sensor performance.

Chapter 7 presents the fabrication technique to create a thick-film based indium oxide sensors using a screen-printing technique. The sensors were tested for oxygen under humid and dry environment. The response of the fabricated thick-film sensors was analysed and compared to the thin-film sensors to examine the effects of film thickness in the sensor performance.

Chapter 8 discusses the development of the fabricated MOX sensor for oxygen detection. This chapter, building on the previous chapters, compare response from all the fabricated sensors to obtain the sensors with the highest response. The sensors are further tested for selectivity and interference to other gases.

Chapter 9 provides the concluding remarks about the thesis and gives an account of further works that could be undertaken to improve the sensor performance.

1.5 References

[1] J. Puigcorbé et al., "Thermo-mechanical analysis of micro-drop coated gas sensors," Sensors and Actuators A: Physical, vol. 97-98, pp. 379-385, 2002/04/01/ 2002.

[2] Hazardex. (2016, 29 October). Understanding gas sensor lifespan [Online]. Available: http://www.hazardexonthenet.net/article/128977/Understanding-gas-sensor-lifespan.aspx

[3] G. L. Anderson and D. M. Hadden, The gas monitoring handbook. Avocet Press Inc, 1999.

[4] Sysmatec. (31 December). VOCs measurement with PID sensors [Online]. Available: http://www.sysmatec.ch/eJ6_Example12.html.

[5] Technavio, "Global Industrial Gas Sensors Market - Forecasts and Opportunity Assessment by Technavio," Accessed on: November 24th, 2018. [Online]. Available: https://www.businesswire.com/news/home/20170721005608/en/Global-Industrial-Gas-Sensors-Market---Forecasts

[6] Alphasense, "p-type Metal Oxide Sensor Overview and Interface Circuit," in "Alphasense Application Note " Alphasense.

[7] Figaro, "TGS 2600 - for the detection of Air Contaminants."

[8] C. Chiang, "Design of a High-Sensitivity Ambient Particulate Matter 2.5 Particle Detector for Personal Exposure Monitoring Devices," IEEE Sensors Journal, vol. 18, no. 1, pp. 165-169, 2018.

Chapter 2. Metal Oxide Sensors: Technology and Characterisation

2.1 Introduction

This chapter details the underlying principles of semiconducting metal-oxide gas sensors and the characterisations of these sensing materials. The first section describes the sensor characteristics and classification of metal oxide sensor, based on the type of material and its thickness. The applications and how MOX sensors detect gases are presented. This is followed by a discussion on factors that influence the gas sensor performance.

The next section of this chapter expands on the sensor characterisation, which is separated into two parts, i.e. material and gas sensing characterisation. The former describes several techniques employed to characterise the sensing materials and the latter details the apparatus and experimental methods used to evaluate the sensors performance.

2.2 Metal Oxide Sensors Review

This section presents an overview of metal oxide gas sensors in terms of characteristics, sensing mechanism, influencing factors, and the applications of the sensors.

2.2.1 Features and Characteristics

Metal oxide (MOX) sensors have found favour as a gas sensitive material because of their high sensitivity and ability to operate in harsh environments (such as high temperatures). Moreover, they have long life span and come in compact size, which can ease integration with other electronic devices. The sensors are manufactured at a very low cost, in comparison with other sensor technologies, such as electrochemical sensors and PID (Photo Ionisation Detectors).

MOX sensors, shown in Figure 2 - 1, generally consist of a substrate such as alumina (Al_2O_3), heater(s), interdigitated electrodes, sensitive material, and a housing/packaging. Gold interdigitated electrodes are printed on the top of the substrate and platinum heater is printed on the other side. The sensing material that is a semiconducting metal oxide is deposited on top of the interdigitated electrodes as thick or thin-film, which can be achieved through a range of deposition techniques, such as screen printing, sputtering, sol-gel, and chemical vapour deposition (CVD) which will be discussed in a later section.

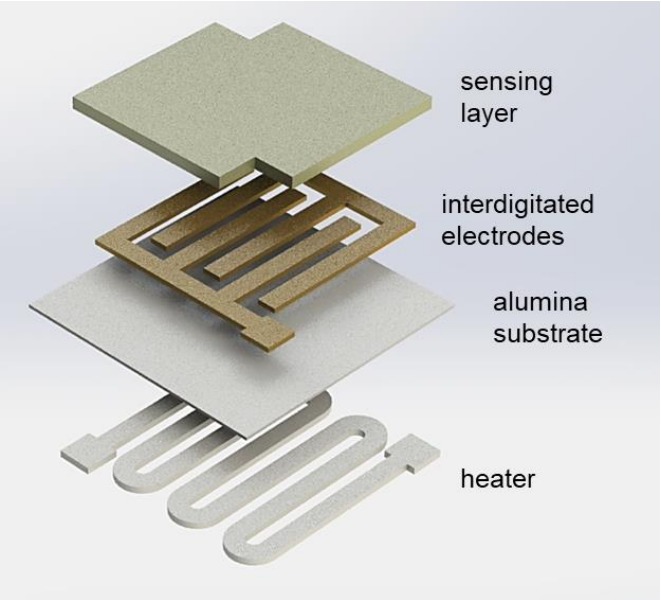

Figure 2 - 1 Schematic of a typical sensor substrate.

Despite their advantages, MOX sensors are known for their broad sensing ability, which means they are not able to selectively respond to a single compound of interest [1, 2]. For example, H_2 sensor based on Pd-SnO_2/MoS_2 materials showed a high response toward NH_3 with a response ratio of 3:4 to that of response toward H_2 [3]. Similarly, study on SnO_2 multi-walled carbon nanotube (MWCNT) nanocomposites showed a high response toward acetone, but the sensor also showed significant response towards alcohol, butane, and methane [1]. Commercial MOX sensors such as MICS-5524 (SGXSensortech, Switzerland) can detect CO, NO_2, ethanol, H_2, ammonia, and methane. Likewise, AS-MLV-P2 sensor (AMS, Austria) based on MOX technology is also used for broad detection of reducing gas such as CO and VOCs (volatile organic compounds). Although other sensor technologies like electrochemical sensors also reported cross-sensitivity to other compounds [4], MOX sensors appear to suffer worse. Studies have been conducted to address this issue, such as modulating operating temperature and adding decorations or dopants to metal oxide materials to improve selectivity of the sensors to certain compounds [5, 6] and introducing another nano-structured material to create nonhomogeneous complex materials for the sensing layer [7-9]. Another method to reduce cross-sensitivity is to add an active and/or passive layer to act as a barrier to these interference gases. These gases will be absorbed by the filter layer so that only the compounds of interest pass through and get adsorbed on the sensing material [10-13].

The response of metal oxide gas sensors is also known to be affected by changes in humidity level [14-16]. Study on ZnO based sensor reported a significant decreased in sensor response as the relative humidity increased, i.e. response (see section 2.5.3 for response definition) dropped by more than 40% (from R_a/R_g=170 at 30% RH to less than R_a/R_g=100 at 90% RH [17]. Similar findings were also reported

for SnO_2 based sensors for ethanol detection where the response dropped by ~60% when relative humidity increased from 0% to around 70% R.H. [15]. This is discussed further Section 2.3.2.

2.2.2 Semiconductor of n-type and p-type material

Materials for metal oxide sensors can be classified into n-type and p-type materials. In n-type materials, the majority charge carriers are electrons whereas in p-type materials, the majority charge carriers are holes. Upon exposure to gases, the resistance of metal oxide sensors may decrease or increase depending upon the type of the carriers and the nature of the gas molecules (reducing or oxidising gases). This response will be discussed further in Section 2.2.4.

Several well-known n-type based gas sensors include WO_3 [18-20], SnO_2 [21-23], TiO_2 [24-26], Ga_2O_3 [27, 28], ZnO [29-31], and In_2O_3 [32-34]. Whereas p-type based sensors include Cr_2O_3 [35-37], CuO [38, 39], Chromium Titanium Oxide (CTO) [19], and NiO [40, 41]. These sensors behave differently upon contact with targeted gas and are further discussed in Section 2.3.4.

2.2.3 Thick-film vs Thin-film Metal Oxide

Sensing materials in MOX based gas sensors can be categorised as thick or thin film. The thickness range of thick and thin film sensors are varied in the literatures, but generally thick-film sensors are in broad µm, whereas thin-film sensors are in nm range up to a few µm thickness.

Thick-film sensors are often produced by screen printing technique. It is a conventional method that has been used for decades to fabricate commercial metal oxide devices [42, 43]. Screen printing is desirable for its ease of use and ability to

produce devices in mass production with good uniformity in a relatively short period of time. This fabrication technique is further explored in Chapter 7.

Another deposition method to produce thick-film sensors is by dropping the sensitive MOX material onto the sensor substrate, so called drop-coating method [44, 45]. The process involves preparing the MOX solution using a solvent and then depositing the material using a calibrated volumetric pipette. This method is straightforward and easy but may result in poor uniformity and reproducibility as sensor deposition is carried out on individual sensor substrate. However, studies on sensors fabricated by this method reported stable and repeatable responses [46, 47]. Tomchenko et al. for instance, fabricated SnO_2, ZnO, WO_3, In_2O_3 and CuO by drop coating method and found sensor responses to be reliable, stable, and reversible relative to the gases of interest [46]. The method was also applied to deposit commercial thick-film sensors at AppliedSensor GmbH [48] which was acquired by AMS in 2014.

Thin-film sensors can be produced by fabrication techniques such as CVD [49, 50] and sol-gel [51-53]. The former method utilises vapour formed from precursor solution, which is transported and deposited onto heated substrate, producing a thin-film sensor. Sol-gel process involves preparing precursor solution which forms a sol through hydrolysis. The solution is then deposited on the sensor substrate via methods such as spray coating and spin coating. A CVD technique and spin coating were applied in this work to fabricate thin-film sensors. Each technique is further discussed in Chapter 4 (AACVD) and Chapter 5 (Spin Coating).

2.2.4 Sensing Mechanism

Metal oxide sensors work by a modulation of the resistance in the sensing material as it reacts with the surrounding atmosphere. Two models of sensing mechanism are presented in the literatures, namely adsorption-desorption process of oxygen molecules [54-56] and the oxygen vacancy model [57]. Both models have raised contradictions due to lack of spectroscopic observations and inaccurate representation of real environment [58]. Nonetheless, the former is more widely accepted in the literature and will be discussed further in the following.

In atmospheric air, oxygen molecules are adsorbed on the surface of the sensing material in the form of molecular ($O_{2\ ads}^{-}$) or atomic (O_{ads}^{-} or O_{ads}^{2-}) depending on the operating temperatures [59-61]. The range of the operating temperatures varied in the literatures, but generally oxygen species are adsorbed in the molecular form at lower temperature (<200°C) and adsorbed in the forms of O_{ads}^{-} or O_{ads}^{2-} at higher temperatures. At lower temperature, oxygen species are adsorbed in the form In order to stabilise, the adsorbed oxygen species need to be reduced by electrons, which are drawn from the conduction band of metal oxide. These electrons are trapped at the surface and create a formation of an electron depleted layer (EDL) or space charge layer at the surface of metal oxide.

In the presence of a reducing gas, such as CO, oxidation reaction occurs between the analyte and the adsorbed anionic oxygen special to form CO_2 molecules, which desorb off the surface. The surface density decreases as the trapped electrons are released into EDL/ space charge layer. The release of electrons reduces the potential barrier (also known as Schottky barrier) and allows more current to pass freely through the sensors. Thus, less resistance is observed in the sensor. The sensing mechanism is illustrated in Figure 2 - 2.

In the case of contact with an oxidising gas such as O_3 and NO_2, the resistance of the sensors increases. This is because the presence of oxidising gas, just like O_2, draws electrons from the metal oxide, increasing the size of the EDL. As more electrons populate the surface of the metal oxide, current flow is more restricted and thus a higher resistance is observed.

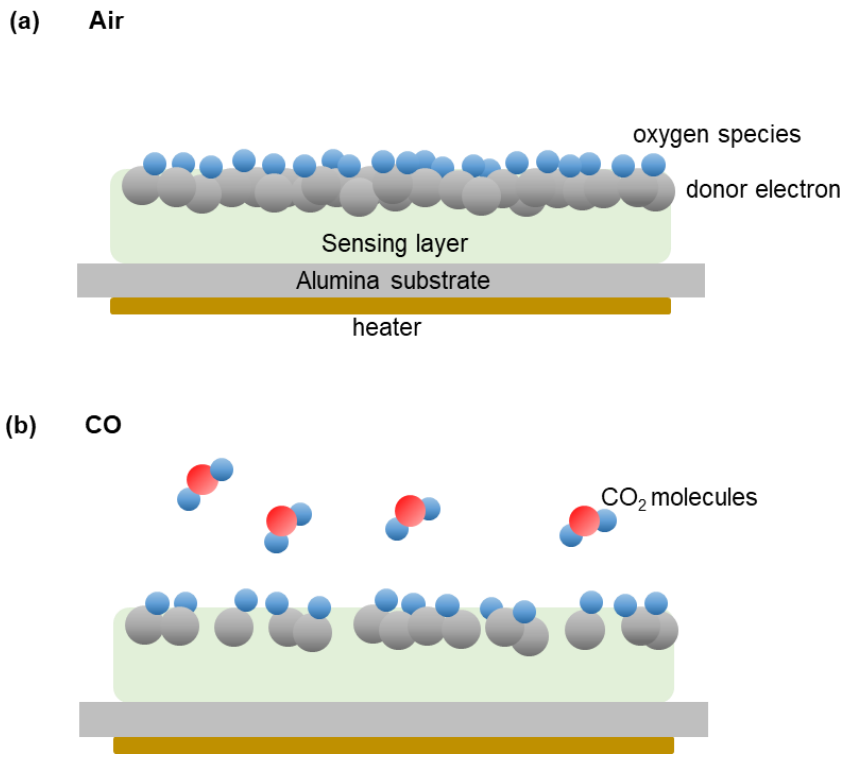

Figure 2 - 2 Gas sensing mechanism of n-type semiconducting oxide upon interaction with (a) air and (b) target analyte CO.

Sensor made of p-type materials, behaves in the opposite way. When in contact with atmospheric air, the oxygen molecules are adsorbed in the form of $O_{2\text{-}ads}^{-}$, O_{ads}^{-}, O_{ads}^{2-} on the surface of metal oxide. This leads to electrons abstraction to populate on the surface of the material. Since holes serve as the majority charge carrier in p-type sensors, a hole accumulation layer (HAL) is formed [62].

Upon contact, reducing gas such as CO interacts with the adsorbed oxygen species and thus releasing the electrons from the surface of the material. This enables electron interaction with positive holes in HAL (electron-hall recombination process) [63] which reduces the concentration of the holes in the HAL and thus increase the resistance of the sensor. On contrary, exposure to oxidising gas reduces the sensor resistance. This is because the oxidising gas reacts with the electrons on the surface of the material, increasing the concentration of holes and thus the conductivity of the sensors (less resistance). These resistance changes in n-type and p-type sensors are highlighted in Table 2 - 1.

Table 2 - 1 Change of resistance in semiconducting metal oxide materials.

Sensor type	Reducing gas	Oxidising gas
n-type	Decrease	Increase
p-type	Increase	Decrease

2.2.5 Application

Extensive range of MOX materials have been extensively studied in the literature and shown to detect a wide range of gases [64-67]. WO_3 based sensors for instance, have been investigated to detect acetone [63, 64, 68], NO [65], NO_2 [18, 69], H_2S [70], CO [66], and VOCs [71, 72]. Likewise, Sn_2O based films have been explored as sensors for NO_2 [73-75], CO [76, 77], H_2 [78, 79], and VOCs [80, 81] [80-82] to name a few. Using the same base material to detect many compounds raises a selectivity issue, as it won't be able to detect a particular compound in the presence of others. Indeed, this inability to selectively detect a targeted gas can hinder the sensor performance greatly. However, in many applications (such as process control), the target is only a single molecule in a background of clean air, making this use of these sensors achievable.

Despite the drawbacks, MOX based gas sensors have been widely used in various applications with a market share of more than 25% of the global gas sensor market in 2016 [83]. The number is expected to increase due to higher demands for air quality monitoring systems [84, 85]. On top of that, MOX sensors also find applications in areas such as leak detection [86-88], industrial safety [89], and process control [90]. Therefore, there has been a high interest to investigate metal oxide sensors for further improvement, especially in addressing the drawbacks highlighted earlier.

2.3 Influencing Factors in Gas Response

Several factors influencing the performance of MOX based sensors which include particle size, film thickness, temperature, humidity, and incorporation of additives to the sensor. Each of these will be discussed in the following.

2.3.1 Morphology

The morphology of the sensitive MOX layer affects the electrical properties of the sensors, producing different resistance values and thus changing the responsivity of the sensors. The morphology of MOX sensor here is associated to size and shape of the sensing material, which can vary due to differences in grain/particle size, sensor porosity, and thickness of the material.

The effects of particle size and boundary on sensor responses have been well studied in the literatures [91-93]. Smaller particles size has been reported to promote sensor response due to having a larger surface area for the targeted gas to interact with. The response also depends on the relationship between the particle size (D) and the width of the space charge layer (L) as reported in [93, 94]. This relationship

was proposed by three models (Figure 2 - 3), namely grain-boundary control (D>>EDL), neck control (D ≥ 2L), and grain control (D < 2L). In the first model, the conductivity depends on the inner mobile charge carriers and the barrier height hence less sensitive to the charges from the surface reactions. When D is comparable with 2L, the conductivity depends on the particles boundaries barriers and the cross-section area around the neck which make the particles sensitive to the ambient gas. Finally, when D is smaller than 2L, the conductivity of the particles is dominated by the EDL region. The sensitivity is essentially governed by the grain themselves and so the response was the most sensitive [93].

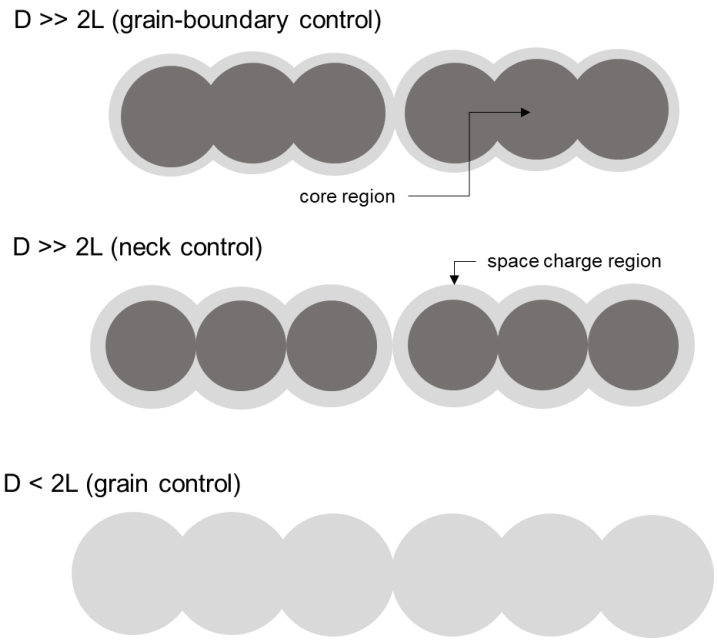

Figure 2 - 3 Schematic model for the particle effects. Adapted and redrawn from [93].

Annealing temperature alters the structure of the grain boundary and sensor porosity, hence affecting the sensor responses [95, 96]. Just like sintering temperature, fabrication method of MOX sensors also leads to variations in porosity which can greatly influence the responsivity of the sensors [97]. In gas sensing material, porous material is preferred as it can better facilitate adsorption/desorption

process and thus enhance sensor response. Cao *et. al*. fabricated a nickel oxide microfibers (NiO-MFs) calcined between 300 – 500°C and found sensors prepared at lower temperature, exhibit ultrasensitive response with lower detection limit [98]. Similar findings were also reported in the literatures [99, 100].

Film thickness has been shown to influence sensor performance [101, 102]. Increasing thickness in thin-film sensors inherently increased the grain size of the sensing material [103]. The thicker films were more porous and more densely packed and so the films became more responsive to targeted analyte. Likewise, increasing film thickness from 55 nm to 213 nm was found to increase SnO_2 sensor response toward CO [104]. However, the effect is contradictive in the literatures as some reported an increased in sensor response as the film thickness increased [105] while some others found increasing film thickness reduced the sensor responses [106, 107]. It is important to note that even in the controlled environment, other factors might affect sensor responses therefore a variation in findings is sometimes inevitable.

2.3.2 Temperature

As discussed in Section 2.3.4, changes in sensor resistance are due to adsorption and desorption process of oxygen species on the surface of metal oxide sensors. Gurlo detailed the different oxygen species that populate the sensor surface as a function of operating temperature [108]. They are assumed to be adsorbed in the molecular form ($O_{2\,ads}^{-}$) at lower temperature (150 - 200°C) and in atomic forms (O_{ads}^{2-} and O_{ads}^{-}) at higher temperature (200 – 400°C). It is important to note that other studies reported a different temperature ranges [18, 59, 109]. In addition to that, Gurlo also highlighted the issue arises from these assumptions, which contradict the chemical sense and spectroscopic findings [108]. Regardless the argument on this model, temperature is indeed affecting the sensor responses as extensively observed

in the literatures [54, 60, 110, 111]. CuO decorated WO_3 thin film sensors for example, were tested for H_2S at 270 – 390°C and the result demonstrated variance in sensor response with higher response observed at 390° [112]. Similarly, WO_3 based sensors for O_3 detection showed the highest response at around 320°C when tested between 150 – 420°C [113].

2.3.3 Humidity

Water vapour can be adsorbed on the surface of metal oxide sensors by physisorption or hydrogen bonding depending on the temperature (100 – 500°C) [114]. The adsorption of water vapour leads to molecular water at lower temperatures and formation hydroxyl group at higher temperatures. The chemisorbed water molecules occupy the available sites on the metal oxide surface and form 2 hydroxyl ions for each water molecules through a dissociative mechanism [115].

The presence of water vapour in ambient atmosphere have been reported to reduce the resistance of the sensor [116-118]. This is because the number of available sites for the oxygen molecules reduces as the hydroxyl groups populate the surface of the materials. As more water vapour introduced to the system, the resistance of the sensors decreased, which results in lower sensor response [17, 117, 119]. Hydroxyl groups begins to desorb off the surface of the metal oxide at 400°C [120] although other literature reported a lower starting temperature at 250°C but still present even after 500°C [121]. This means as the hydroxyls start to desorb, more active sites are available for the oxygen molecules and therefore lower interference are observed at high temperature [122].

2.3.4 Incorporation of Additives

It has been known that the addition of metal/metal oxide to the base material can promote sensor performance. The additives not only serve to enhance the response of the sensors to oxidising and reducing gases, but also improve the rate of the response as reported previously [123-125]. The common additives used include noble metals such as gold (Au), silver (Ag), palladium (Pd), and platinum (Pt). How the additives incorporated to the additives to the base sensors (Figure 2 - 4) has been proposed by 2 sensing mechanisms, namely chemical and electronic sensitisation [120].

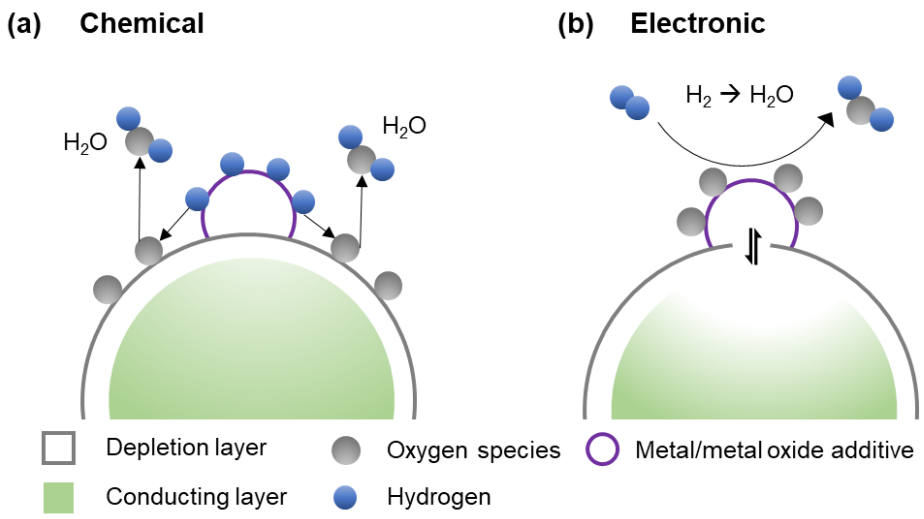

Figure 2 - 4 Sensing mechanisms of additives incorporated into metal oxide sensor: (a) chemical sensitisation and (b) electronic sensitisation. Redrawn and adapted from [92].

In chemical sensitisation, change of resistance of the sensor can be attributed to the contribution of metal/metal oxide decoration to accelerate the catalytic surface reaction between the analyte and the sensing material through a spill-over mechanism [92]. This alters the density of the oxygen species and therefore changes

the conductivity of the sensor. For example, the addition Pt catalyst in hydrogen sensor which was incorporated to TiO_2 [126] and In_2O_3 [127].

In the case of electronic sensitisation, addition of metal/metal oxide to the sensing material promotes changes in sensor electrical properties through a change in the oxidation state of the additives with the surrounding atmosphere. This affects the position of the surface energy level in which the additive serves as donor or acceptor of electrons of the host semiconductors. The example is addition of Ag nanoclusters on Sn_2O nanowire networks, significantly enhanced the selectivity and response to ethanol [125]. The electronic sensitization effect of PdO in PdO/ZnO catalysts loaded on to Sn_2O nanotubes for acetone detection was also reported to increase sensor sensitivity with high selectivity and stability [128].

2.4 Material Characterisation

This section describes the materials characterisation techniques that were used to investigate the chemical and physical properties of the metal oxide materials.

2.4.1 Thermogravimetric Analysis (TGA)

TGA is a characterisation method in which change of mass of a sample is monitored over time as the temperature changes in a controlled environment. The method can provide physical and chemical information about material such as phase transition, oxidation, quantifying loss of water/ plasticiser, and decomposition. For gas sensing application, it is particularly useful in determining the decomposition temperature of the vehicle/binder used in the sensor materials in order to set appropriate firing temperature.

2.4.2 White Light Interferometry (WLI)

WLI is a non-contact optical method that works on the basic principle of Michelson interferometer. It is also known as coherence scanning interferometry (CSI) and vertical scanning interferometry (VSI). WLI is used for optical measurement of surface structures for a variety of applications such as surface profiling for lens and optics [129], medical imaging [130, 131], thickness measurement [132, 133].

Just like a laser interferometry, WLI works by merging two or more light sources to create interference patterns. It utilises white light (a broadband light source) which allows multiple data points to be extracted from the sample. The schematic of the WLI is presented in Figure 2 - 5. The light from the white light source is collimated and split into 2 beams of reference beam and object beam. The latter is reflected from the sample and measured while the reference beam is reflected off the mirror, back to the beam splitter, and measured. Since the beams travel in different ways, they are out of phase. This creates a pattern of light and dark areas called interference fringes which are captured and analysed in the detector to extract information.

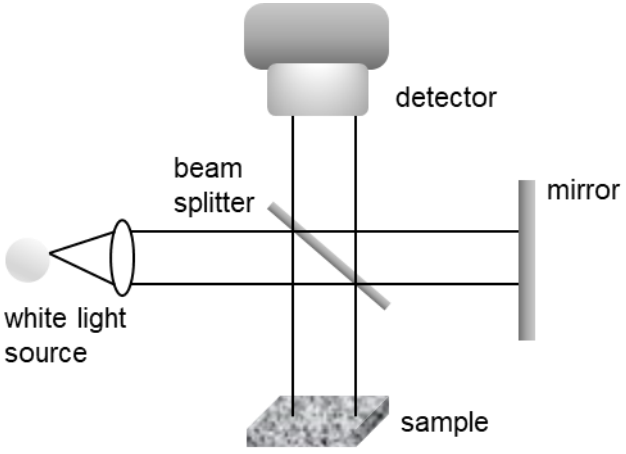

Figure 2 - 5 Schematic of white light interferometer.

2.4.3 Scanning Electron Microscopy (SEM)

SEM is a microscopy technique using a focused beam of electrons to scan over the surface of a sample to generate an image. It can provide information on topology, morphology, and composition of materials being analysed. SEM is one of the mostly used characterisation technique in materials science to investigate a wide range of materials of different thickness. The applications include detection of gunshot residue in forensic investigations [134, 135], identification of bacteria in biological sciences [136-138], analysis of blood and tissue samples in medical science [139, 140].

Electrons are generated at the top of the column and accelerated down at voltage up to 30 kV. They pass through electromagnetic field which controls the electrons path, producing a focused beam that hits the sample. The interaction of the sample and the electron beam produces signals including secondary electrons (SE), back-scattered electrons (BSE), and characteristics X-rays. These signals are collected by one or more detectors to generate an image. Secondary electrons are commonly used for SEM imaging and the detector is the basic of a SEM instrument. Additional detectors can be added to provide more information on the materials such EDS (see section 2.4.5) to acquire elemental analysis and BSE for discrimination of material phases. The schematic of a SEM instrument is illustrated Figure 2 - 6.

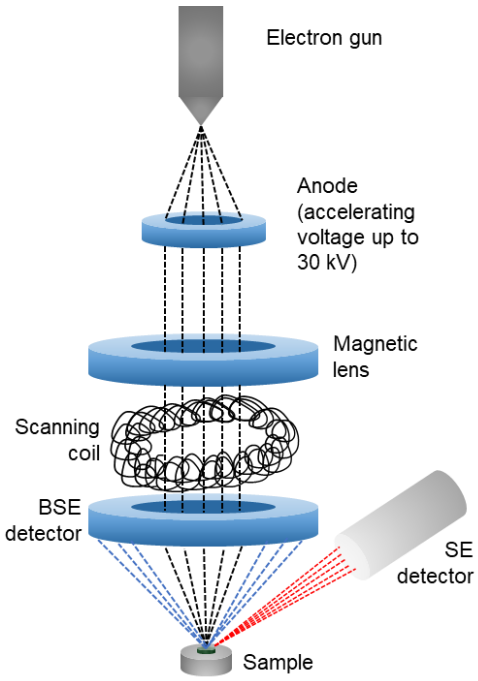

Figure 2 - 6 Schematic of a SEM instrument.

SEM produces 3D images at high resolution with magnification up to 2 million times [141]. It is considered easy to operate and the preparation of the samples are mostly simple. Sample coating using either gold or carbon is sometimes necessary for electrically insulating materials to prevent build-up charges.

2.4.4 Transmission Electron Microscopy (TEM)

TEM is another microscopy technique which applies a transmitted beam of electrons to generate an image. Unlike SEM, it is a 2D projection image of the inner structure of the sample and therefore suitable to observe very thin specimen in nanometre range. TEM provides information on topology, morphology, composition, and crystalline of materials. It has been widely used in various applications such as study viral and bacterial infections [142] and phase transformations in steels [143].

TEM instrument works in a similar way with a light microscope but using beam of electrons instead of light. Electrons are produced and accelerated down through

electromagnetic field at high voltage ranging from ~60 to 300 kV [141]. This creates a focused beam which is then transmitted through the sample and into another electromagnetic field to focus the electrons before projected onto the fluorescent screen to create the image. This is shown in Figure 2 - 7.

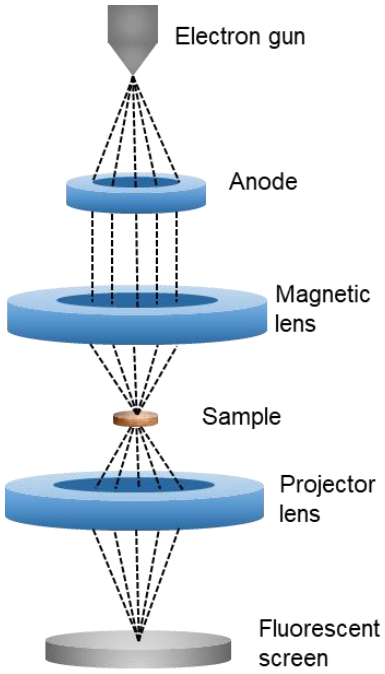

Figure 2 - 7 Schematic of a TEM instrument.

Specimens for TEM must be very thin (~150 nm) so that electrons can pass through. In addition, the samples need to be mounted on a mesh grid usually made of copper. These can make sample preparation quite laborious. However, it can provide much higher magnification than SEM, up to 50 million times which enable study on nano range materials.

2.4.5 Energy-dispersive X-ray spectroscopy (EDX/EDS)

EDS is a chemical microanalysis technique used in conjunction with an electron microscope. It utilises the x-ray spectrum emitted from samples to obtain elemental composition characteristics of the samples. In combination with SEM and/or TEM,

EDS can provide information on failure analysis [144, 145], identification of contaminant [146], and evaluation of materials [147, 148].

As previously explained, interaction between a sample and electrons produces signal including x-rays (Figure 2 - 8). Electrons of an atom within the sample are in the ground state/ unexcited while at rest. When the beam of electrons hit the sample, electrons receive transfer of energy from the beam and cause some electrons to get ejected off the shell, creating electron vacancies. This attracts negatively-charged electrons from higher state to fill the hole. When this occurs, the energy difference between the two shells is released in the form of an X-ray. The released X-ray becomes a characteristic unique to each element and so can be used to identify what elements exist in a sample.

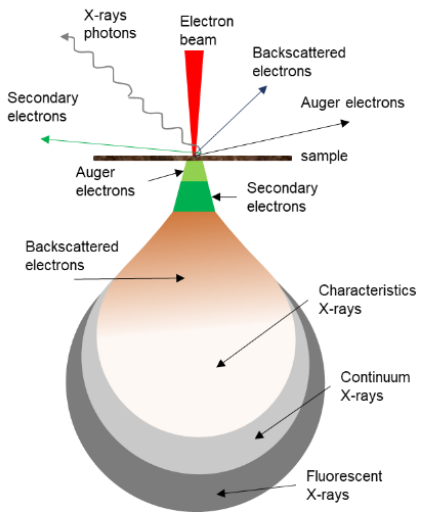

Figure 2 - 8 Schematic of electron beam interaction.

2.4.6 X-ray Powder Diffraction (XRD)

XRD is a non-destructive characterisation technique for crystalline materials that works based on constructive interference of monochromatic x-ray and crystalline specimen. It can provide information such as crystalline phases and orientation as

well as structural properties such as grain size strain and phase composition. The applications for XRD include solid-state drug analysis in pharmaceutical field [149, 150], trace analysis for forensic investigation [151, 152], mineral exploration [153], microelectronics [154], and glass industry [155].

XRD instrument consists of three basic elements (Figure 2 - 9): X-ray tube, sample holder, and X-ray detector. X-rays are generated in the X-ray tube by generating and accelerating electrons toward the target material (usually Cu, Fe, Mo, or Cr). When the electrons hit the material, the electrons in the inner shell of the material are dislodged off their shell, producing characteristic X-ray spectra. The generated X-rays are filtered foils or crystal monochrometers to produce monochromatic X-rays. These X-rays are collimated and directed toward the sample. When the incident X-rays satisfy the Bragg's Law [156] (**n λ = 2d sin θ**, where n = positive integer; λ = the wavelength of the incident wave), constructive interference and a peak in intensity occur. The intensity of the reflected X-rays is recorded as the sample and the detector are rotated. This is what becomes the fingerprint of the materials.

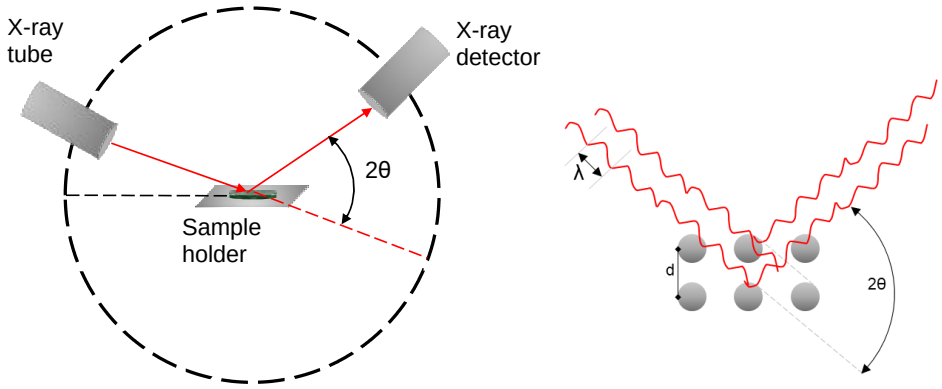

Figure 2 - 9 Construction of XRD instrument (left) and constructive interference based on Bragg's Law (right).

2.4.7 X-ray Fluorescence (XRF)

XRF is another non-destructive characterisation technique that is used to determine the elemental composition of materials. It works by measuring the fluorescent X-ray emitted from a sample when it is excited due to the bombardment of the x-ray beam. Each element in the sample produces a characteristic that is unique to that element hence the elemental composition of the sample can be identified. The application of XRF includes for geological field [157, 158], dental and medical specimens [159], forensic investigations [160], and pharmaceutical industry [161].

The XRF process (Figure 2 - 10) involves irradiation of the sample with x-ray beam with enough energy to dislodge electrons in the inner shell of the atoms of the materials. This energy should be greater than atoms' K or L shell binding energy. When the irradiation occurs, electrons from the inner shell thrown out of their orbit, creating electrons vacancies. For the atoms to stabilise, electrons from higher state (outer shell) fill the vacancy which produces a drop in energy state (electrons in outer shell have higher energy level). X-ray fluorescence is released and measurement of this energy loss is the basis of XRF analysis.

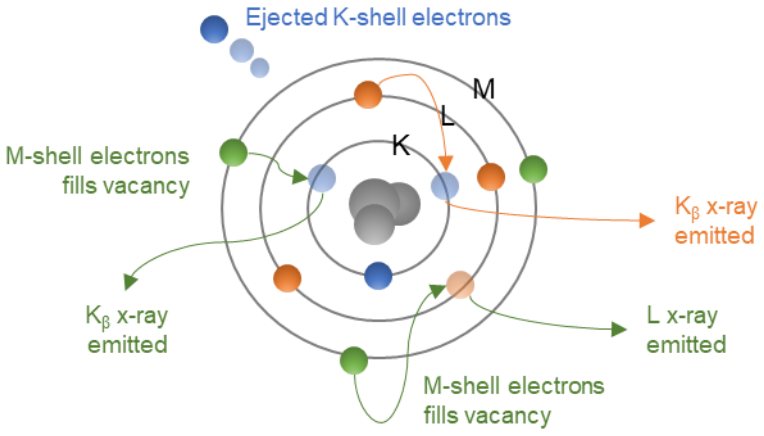

Figure 2 - 10 XRF irradiation.

2.4.8 X-ray photoelectron spectroscopy (XPS)

XPS is a characterisation technique to measure the surface chemistry of a material. It provides information on elemental composition, empirical formula, chemical and electronic state of the elements of the samples being analysed. XPS has been widely applied in many areas such as in semiconductor industry [162], orthopaedic [163], and gas sensor industry [164].

XPS works based on irradiation of sample with X-rays of sufficient energy to excite the electrons in the atoms of the sample (Figure 2 - 11). When this occurs, the electrons in the inner shell of the materials are ejected off the shell. This produces kinetic energy (KE) that depends on photon energy (hv) and binding energy of the electrons (BE). Elements present in the sample can be identifying by measuring the kinetic energy of the dislodged electrons chemical state of an atom changes the binding energy, which alters the kinetic energy. By measuring this, chemical shifts in the sample can be identified.

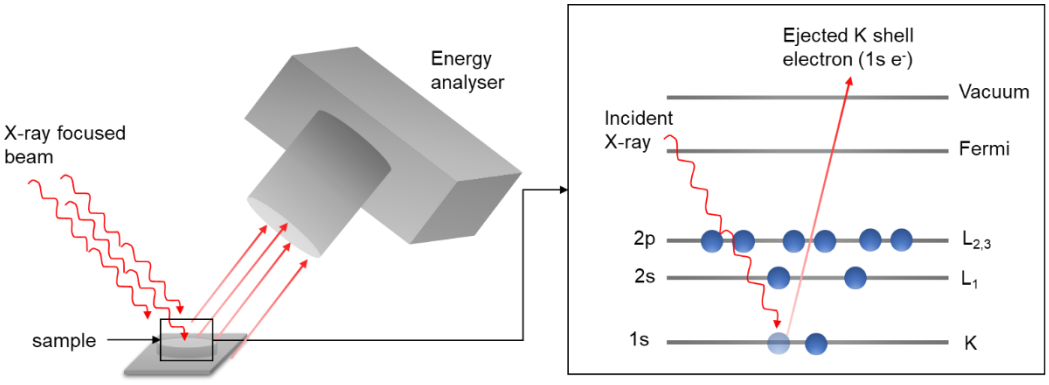

Figure 2 - 11 Process involved in XPS surface analysis.

2.5 Gas Sensing Characterisation

This section presents the process involved in gas sensing characterisation which starts from the equipment used to defining the responsivity of the fabricated sensors.

2.5.1 Gas Handling Apparatus

A gas handling apparatus had been previously designed and built by Dr Siavash Esfahani in collaboration with Samuel Agbroko in in the School of Engineering, University of Warwick [165]. The instrument (Figure 2 - 12) consists of a gas mixture (gas rig), a fitted commercial VOC generator OVG 4/GEN-SYS (Owlstone Inc.), and a humidity generator. The schematic of a gas sensing procedure is laid out in Figure 2 - 13.

Figure 2 - 12 Gas handling apparatus from left to right: gas mixture, OVG-4, and humidity generator.

The gas mixture can supply up to 2 gas lines, which are combined in a mixing chamber. Each gas line is controlled with a mass flow controller MFC UFC-1100 of 500 sccm (Brooks, USA). The user controls the gas rig through a computer programme written in LabVIEW 2017 (National Instruments) by Prof James Covington. Through the interface shown in Figure 2 - 14, the user is able to vary flow rate of each gas, the test sequence, and the period of each test.

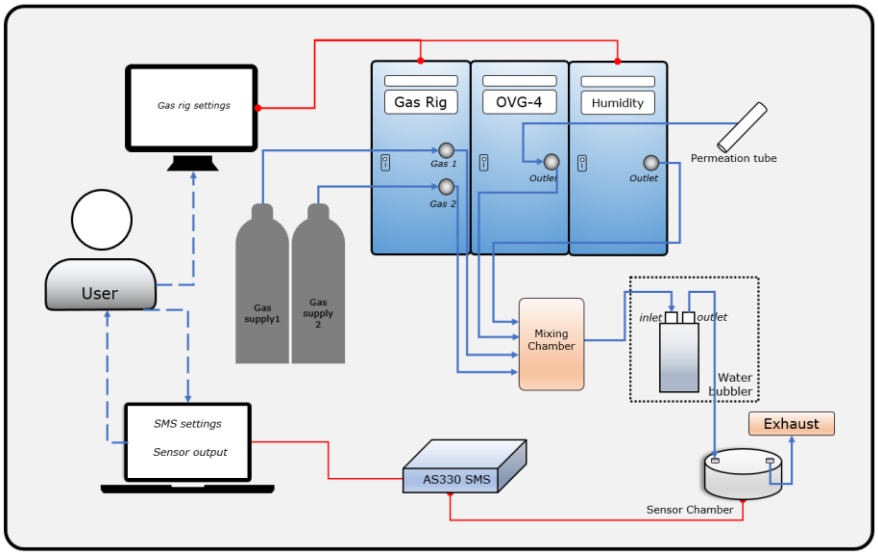

Figure 2 - 13 Schematic of a gas sensing procedure.

The OVG-4 calibration gas generator (Owlstone, UK) can generate a range of concentrations of chemicals using a permeation tube. The setting for this unit is controlled by a Eurotherm PID controller mounted on the front of the instrument. A more detail explanation on tests using OVG-4 is discussed in Chapter 3.

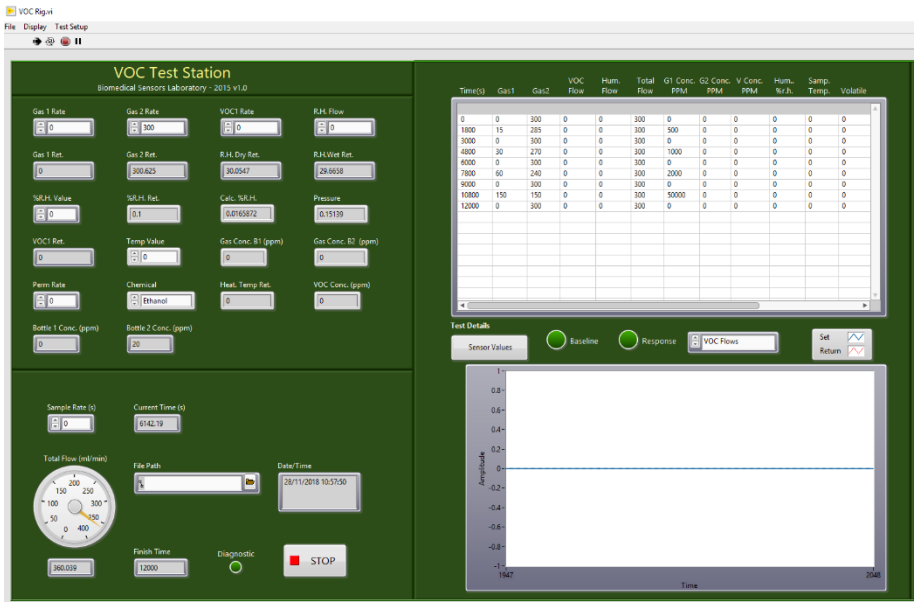

Figure 2 - 14 Software interface for the gas handling apparatus designed in LabVIEW.

The humidity generator can supply air at various humidity levels by mixing a humidified air (pass through water bubbler) and dry air to achieve desired humidity level. It is used in conjunction with the gas mixture and/or OVG-4 to dilute and humidify the compound of interest. The humidity generator is controlled through the same software used in the gas mixture.

There are two different settings for obtain humid gas. First, the humidity is generated in the humidity generator. In this case, the gas from either the gas mixture of the OVG-4 is diluted with air from the humidity generator to get the desired gas concentration at a desired humidity level. After passing through the mixing chamber as, the gas is directly channelled to the sensor chamber for measurement. When humidity generator is used, humidity level can vary between dry up to 80%. Second, the humidity is generated by passing the mixture gas through the water bubbler. In this case, the humidity generator is not used. The gas from either the gas mixture or OVG-4 is diluted with air connected to the second MFC of the gas mixture. The combined gas is passed through the water bubbler and then to the sensing chamber for measurement.

2.5.2 Gas Sensing Chamber

Gas at a certain concentration and relative humidity is connected to an airtight chamber, which was designed and built in the School of Engineering by Prof James Covington [166]. The chamber is constructed of four components and designed to have low dead volume and to house 8 sensors. The components are the lower plate containing the inlet and outlet holes, the centre plate containing eight 1.0 mm holes to allow gas flow to the sensor, top plate in which the sensors are mounted in, and the last is an interface PCB which connects the sensors to the measurement instrument.

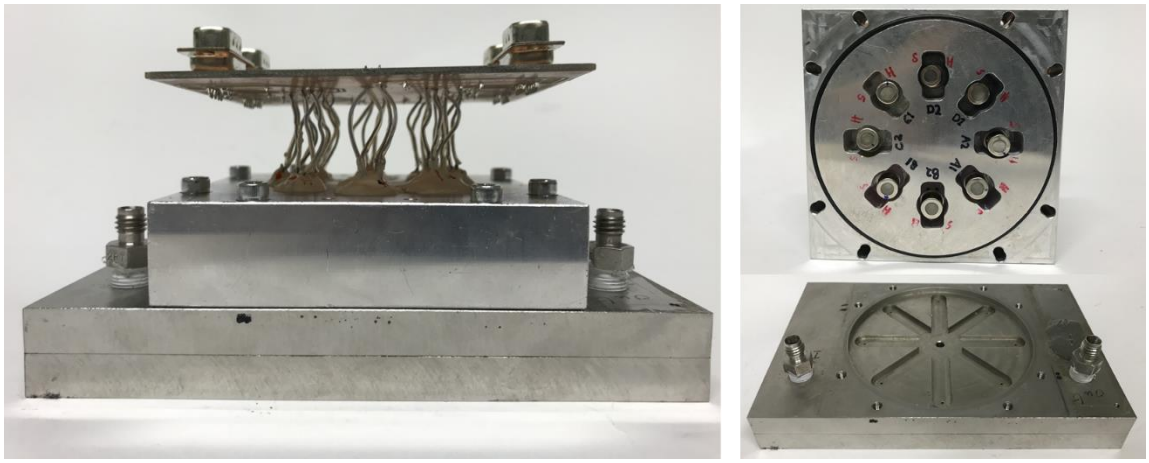

Figure 2 - 15 Metal oxide sensor chamber when closed (left) and open (right).

Flow injection analysis was carried out for the sensor chamber and the result showed that the chamber is only 11.1 ml being exhausted in less than 1.5 seconds with the flow rate set at 300 ml/min [166]. This demonstrates a fast response time for the gas to enter and exit the chamber. As the sensor chamber can house up to 8 sensors, delivery period at which the gas arrives at gas inlet for each individual sensor may vary. However, as the whole process takes <1.5 seconds, the gas distribution for each channel is not significant and can be neglected.

The chamber is connected via D-sub connectors to the measurement instrument AS330 Sensor Management System (AS330 SMS). AS330 SMS is a sensor management system unit manufactured by Atmospheric Sensor, UK. The unit is designed to measure up to 8 metal oxide sensor with a circuit designed to control sensor heater temperature. It is supplied with a main to 12V power supply plug hence the measurement is based on AC power instead of DC. The unit also comes with the PC monitor software which enables controlling of several parameters such as sensor heater resistance, temperature ramps, timed temperature schedules, and external control using RS485 interface. All the data measured by AS330 SMS are logged and

saved in the PC where the software is installed. AS330 SMS hardware and software interface is shown in Figure 2 - 16.

Figure 2 - 16 AS330 SMS hardware and software interface.

2.5.3 Experimental Setup and Data Acquisition

The fabricated sensors would typically be heated to a range of temperatures to determine the optimal operating temperature at which they become the most responsive to the targeted gas. The temperature ranges from 150 – 400ºC although some sensors were tested at slightly lower temperature ranges due to sensors' high conductivity.

Experiments consisted of a 30-minute cycle of gas of certain concentration. The tests in this work were mostly for oxygen detection and were carried out in nitrogen gas. The baseline resistance of the sensors was that of 99.999% N_2. Some sensors in the early work were tested for VOC in which the baseline resistance was of air.

For oxygen sensing measurement, line 1 of the gas mixture is connected to zero air (20% O_2) and line 2 is connected to nitrogen generator capable of producing 99.999% N_2 (Lehman Instrument, France). Changes in oxygen concentration are obtained by varying the flow rate of each gas using the MFC controlled by the LabVIEW software while keeping the total flow rate constant. Humid air is achieved

by passing the gas mixture to a water bubbler before entering the sensor chamber. The humidity level is obtained at around 85% RH which is monitored and logged with a humidity data logger (Lascar Electronics). When dry gas is desired, the water bubbler is not used and the mixture gas is channelled directly to the sensor chamber.

Sensor response (S_r) is the comparison of the sensor response in the baseline resistance (R_a) to that in the presence of the targeted gas (R_g). For an n-type semiconducting material, exposure to a reducing gas leads to a decreased resistance (conductive response) and the response is defined by $\mathbf{S_r = R_a/R_g}$ whereas exposure to an oxidizing gas leads to an increased resistance (resistive response) and is calculated as $\mathbf{S_r = R_g/R_a}$**.** It is the opposite for a p-type material where the response to a reducing gas is defined by $\mathbf{S_r = R_g/R_a}$ and the response to an oxidizing gas is defined by $\mathbf{S_r = R_a/R_g}$.

The gas response relationship is fitted by a power law, which is commonly observed in metal oxide sensors. It conveys the concentration dependency of the compound of interest within the concentration ranges tested and is expressed by $\mathbf{S_r - 1 = k * conc^{\alpha}}$ where k is constant for gas and α is alpha value. The alpha value is critical in determining whether the resistance output from the sensors can be used to effectively calculate the gas concentration, in this case for oxygen. Generally, the value is between 0.5 and 1.0 produces a good measurement but higher number is preferred. When the alpha value is very close to 1, the sensors respond linearly to changes in concentration.

Sensor response time (T_{res}) is defined as the corresponding time required by the sensor to reach 90% of its saturation value when exposed to the targeted gas.

Similarly, sensor recovery time (T_{rec}) is defined as the time required to return to within 10% of its initial baseline when the targeted gas is switched off.

2.6 References

[1] M. Narjinary, P. Rana, A. Sen, and M. Pal, "Enhanced and selective acetone sensing properties of SnO2-MWCNT nanocomposites: Promising materials for diabetes sensor," *Materials & Design,* vol. 115, pp. 158-164, 2017/02/05/ 2017.

[2] V. Krivetskiy *et al.*, "Selective detection of individual gases and CO/H2 mixture at low concentrations in air by single semiconductor metal oxide sensors working in dynamic temperature mode," *Sensors and Actuators B: Chemical,* vol. 254, pp. 502-513, 2018/01/01/ 2018.

[3] D. Zhang, Y. e. Sun, C. Jiang, and Y. Zhang, "Room temperature hydrogen gas sensor based on palladium decorated tin oxide/molybdenum disulfide ternary hybrid via hydrothermal route," *Sensors and Actuators B: Chemical,* vol. 242, pp. 15-24, 2017/04/01/ 2017.

[4] G. L. Anderson and D. M. Hadden, *The gas monitoring handbook*. Avocet Press Inc, 1999.

[5] F. E. Annanouch *et al.*, "Aerosol-Assisted CVD-Grown PdO Nanoparticle-Decorated Tungsten Oxide Nanoneedles Extremely Sensitive and Selective to Hydrogen," *ACS Applied Materials & Interfaces,* vol. 8, no. 16, pp. 10413-10421, 2016/04/27 2016.

[6] M. S. Barbosa, P. H. Suman, J. J. Kim, H. L. Tuller, J. A. Varela, and M. O. Orlandi, "Gas sensor properties of Ag- and Pd-decorated SnO micro-disks to NO2, H2 and CO: Catalyst enhanced sensor response and selectivity," *Sensors and Actuators B: Chemical,* vol. 239, pp. 253-261, 2017/02/01/ 2017.

[7] G. Korotcenkov and B. K. Cho, "Metal oxide composites in conductometric gas sensors: Achievements and challenges," *Sensors and Actuators B: Chemical,* vol. 244, pp. 182-210, 2017/06/01/ 2017.

[8] A. Gaskov and M. Rumyantseva, "Metal Oxide Nanocomposites: Synthesis and Characterization in Relation with Gas Sensing Phenomena," in *Sensors for Environment, Health and Security*, Dordrecht, 2009: Springer Netherlands, pp. 3-30.

[9] A. M. Gas'kov and M. N. Rumyantseva, "Nature of Gas Sensitivity in Nanocrystalline Metal Oxides," *Russian Journal of Applied Chemistry,* vol. 74, no. 3, pp. 440-444, 2001/03/01 2001.

[10] M. Frietsch, F. Zudock, J. Goschnick, and M. Bruns, "CuO catalytic membrane as selectivity trimmer for metal oxide gas sensors," *Sensors and Actuators B: Chemical,* vol. 65, no. 1, pp. 379-381, 2000/06/30/ 2000.

[11] V. Srivastava and K. Jain, "Highly sensitive NH3 sensor using Pt catalyzed silica coating over WO3 thick films," *Sensors and Actuators B: Chemical,* vol. 133, no. 1, pp. 46-52, 2008/07/28/ 2008.

[12] A. Cabot, J. Arbiol, A. Cornet, J. R. Morante, F. Chen, and M. Liu, "Mesoporous catalytic filters for semiconductor gas sensors," *Thin Solid Films,* vol. 436, no. 1, pp. 64-69, 2003/07/22/ 2003.

[13] M. Fleischer, S. Kornely, T. Weh, J. Frank, and H. Meixner, "Selective gas detection with high-temperature operated metal oxides using catalytic filters," *Sensors and Actuators B: Chemical,* vol. 69, no. 1, pp. 205-210, 2000/09/10/ 2000.

[14] B. Zhang *et al.*, "Enhanced gas sensing properties to acetone vapor achieved by α-Fe2O3 particles ameliorated with reduced graphene oxide sheets," *Sensors and Actuators B: Chemical,* vol. 241, pp. 904-914, 2017/03/31/ 2017.

[15] C. A. Zito, T. M. Perfecto, and D. P. Volanti, "Impact of reduced graphene oxide on the ethanol sensing performance of hollow SnO2 nanoparticles under humid atmosphere," *Sensors and Actuators B: Chemical,* vol. 244, pp. 466-474, 2017/06/01/ 2017.

[16] L. Zhu and W. Zeng, "Room-temperature gas sensing of ZnO-based gas sensor: A review," *Sensors and Actuators A: Physical,* vol. 267, pp. 242-261, 2017/11/01/ 2017.

[17] R. K. Sonker, B. C. Yadav, A. Sharma, M. Tomar, and V. Gupta, "Experimental investigations on NO2 sensing of pure ZnO and PANI–ZnO composite thin films," *RSC Advances,* 10.1039/C6RA07103A vol. 6, no. 61, pp. 56149-56158, 2016.

[18] B. Urasinska-Wojcik, T. A. Vincent, M. F. Chowdhury, and J. W. Gardner, "Ultrasensitive WO3 gas sensors for NO2 detection in air and low oxygen environment," *Sensors and Actuators B: Chemical,* vol. 239, pp. 1051-1059, 2017/02/01/ 2017.

[19] L. A. Horsfall, D. C. Pugh, C. S. Blackman, and I. P. Parkin, "An array of WO3 and CTO heterojunction semiconducting metal oxide gas sensors used as a tool for explosive detection," *Journal of Materials Chemistry A,* 10.1039/C6TA08253J vol. 5, no. 5, pp. 2172-2179, 2017.

[20] S. S. Shendage *et al.*, "Sensitive and selective NO2 gas sensor based on WO3 nanoplates," *Sensors and Actuators B: Chemical,* vol. 240, pp. 426-433, 2017/03/01/ 2017.

[21] R. Peng *et al.*, "Reduced graphene oxide decorated Pt activated SnO2 nanoparticles for enhancing methanol sensing performance," *Journal of Alloys and Compounds,* vol. 762, pp. 8-15, 2018/09/25/ 2018.

[22] G. Korotcenkov, V. Brinzari, and B. K. Cho, "Interference effects between hydrogen and ozone in the response of SnO2-based gas sensors," *Sensors and Actuators B: Chemical,* vol. 243, pp. 507-515, 2017/05/01/ 2017.

[23] Y. Li, N. Chen, D. Deng, X. Xing, X. Xiao, and Y. Wang, "Formaldehyde detection: SnO2 microspheres for formaldehyde gas sensor with high sensitivity, fast response/recovery and good selectivity," *Sensors and Actuators B: Chemical,* vol. 238, pp. 264-273, 2017/01/01/ 2017.

[24] D. S. Dhawale, T. P. Gujar, and C. D. Lokhande, "TiO2 Nanorods Decorated with Pd Nanoparticles for Enhanced Liquefied Petroleum Gas Sensing Performance," *Analytical Chemistry,* vol. 89, no. 16, pp. 8531-8537, 2017/08/15 2017.

[25] O. Krško *et al.*, "Flexible highly sensitive hydrogen gas sensor based on a TiO2 thin film on polyimide foil," *Sensors and Actuators B: Chemical,* vol. 240, pp. 1058-1065, 2017/03/01/ 2017.

[26] X. Tong, W. Shen, X. Chen, and J.-P. Corriou, "A fast response and recovery H2S gas sensor based on free-standing TiO2 nanotube array films prepared by one-step anodization method," *Ceramics International,* vol. 43, no. 16, pp. 14200-14209, 2017/11/01/ 2017.

[27] S. Oh, C.-K. Kim, and J. Kim, "High Responsivity β-Ga2O3 Metal–Semiconductor–Metal Solar-Blind Photodetectors with Ultraviolet Transparent Graphene Electrodes," *ACS Photonics,* vol. 5, no. 3, pp. 1123-1128, 2018/03/21 2018.
[28] X. Gao, T. Liu, J. Yu, and L. Li, "Limiting current oxygen sensor based on La0.8Sr0.2Ga0.8Mg0.2O3−δ as both dense diffusion barrier and solid electrolyte," *Ceramics International,* vol. 43, no. 8, pp. 6329-6332, 6/1/ 2017.
[29] Y. H. Navale *et al.*, "Zinc oxide hierarchical nanostructures as potential NO2 sensors," *Sensors and Actuators B: Chemical,* vol. 251, pp. 551-563, 2017/11/01/ 2017.
[30] V. Postica *et al.*, "Multifunctional Materials: A Case Study of the Effects of Metal Doping on ZnO Tetrapods with Bismuth and Tin Oxides," *Advanced Functional Materials,* vol. 27, no. 6, p. 1604676, 2017/02/01 2016.
[31] Q. Deng, S. Gao, T. Lei, Y. Ling, S. Zhang, and C. Xie, "Temperature & light modulation to enhance the selectivity of Pt-modified zinc oxide gas sensor," *Sensors and Actuators B: Chemical,* vol. 247, pp. 903-915, 2017/08/01/ 2017.
[32] D. Han, L. Zhai, F. Gu, and Z. Wang, "Highly sensitive NO2 gas sensor of ppb-level detection based on In2O3 nanobricks at low temperature," *Sensors and Actuators B: Chemical,* vol. 262, pp. 655-663, 2018/06/01/ 2018.
[33] S. D. Han *et al.*, "Versatile approaches to tune a nanocolumnar structure for optimized electrical properties of In2O3 based gas sensor," *Sensors and Actuators B: Chemical,* vol. 248, pp. 894-901, 2017/09/01/ 2017.
[34] Z. Li *et al.*, "Hydrogen gas sensor based on mesoporous In2O3 with fast response/recovery and ppb level detection limit," *International Journal of Hydrogen Energy,* vol. 43, no. 50, pp. 22746-22755, 2018/12/13/ 2018.
[35] T.-H. Kim, J.-W. Yoon, Y. C. Kang, F. Abdel-Hady, A. A. Wazzan, and J.-H. Lee, "A strategy for ultrasensitive and selective detection of methylamine using p-type Cr2O3: Morphological design of sensing materials, control of charge carrier concentrations, and configurational tuning of Au catalysts," *Sensors and Actuators B: Chemical,* vol. 240, pp. 1049-1057, 2017/03/01/ 2017.
[36] C. Ding *et al.*, "Ordered Large-Pore Mesoporous Cr2O3 with Ultrathin Framework for Formaldehyde Sensing," *ACS Applied Materials & Interfaces,* vol. 9, no. 21, pp. 18170-18177, 2017/05/31 2017.
[37] P. Jayamurugan *et al.*, "Investigation of Annealing Temperature on Structural and Morphological Properties of Cr2O3 Nanoparticles for Humidity Sensor Application," *Sensing and Imaging,* vol. 18, no. 1, p. 22, 2017/06/20 2017.
[38] X. Hu, Z. Zhu, C. Chen, T. Wen, X. Zhao, and L. Xie, "Highly sensitive H2S gas sensors based on Pd-doped CuO nanoflowers with low operating temperature," *Sensors and Actuators B: Chemical,* vol. 253, pp. 809-817, 2017/12/01/ 2017.
[39] A. Umar, A. A. Alshahrani, H. Algarni, and R. Kumar, "CuO nanosheets as potential scaffolds for gas sensing applications," *Sensors and Actuators B: Chemical,* vol. 250, pp. 24-31, 2017/10/01/ 2017.
[40] H. Gao *et al.*, "The design of excellent xylene gas sensor using Sn-doped NiO hierarchical nanostructure," *Sensors and Actuators B: Chemical,* vol. 253, pp. 1152-1162, 2017/12/01/ 2017.
[41] B. Urasinska-Wojcik and J. W. Gardner, "H₂S Sensing in Dry and Humid H₂ Environment With p-Type CuO Thick-Film Gas Sensors," *IEEE Sensors Journal,* vol. 18, no. 9, pp. 3502-3508, 2018.

[42] J. Spannhake, A. Helwig, O. Schulz, and G. Müller, "Micro-fabrication of gas sensors," in *Solid State Gas Sensing*: Springer, 2009, pp. 1-46.
[43] R. H. Clark, "Screen Printing," in *Handbook of Printed Circuit Manufacturing*, R. H. Clark, Ed. Dordrecht: Springer Netherlands, 1985, pp. 216-244.
[44] R. S. o. Chemistry, "Drop Coating," Accessed on: November 25th, 2018[Online]. Available: http://www.rsc.org/publishing/journals/prospect/ontology.asp?id=CMO:0002163&MSID=b909734a
[45] M. Graf, A. Gurlo, N. Bârsan, U. Weimar, and A. Hierlemann, "Microfabricated gas sensor systems with sensitive nanocrystalline metal-oxide films," *Journal of Nanoparticle Research,* vol. 8, no. 6, pp. 823-839, 2006/12/01 2006.
[46] A. A. Tomchenko, G. P. Harmer, B. T. Marquis, and J. W. Allen, "Semiconducting metal oxide sensor array for the selective detection of combustion gases," *Sensors and Actuators B: Chemical,* vol. 93, no. 1, pp. 126-134, 2003/08/01/ 2003.
[47] D. Briand *et al.*, "Design and fabrication of high-temperature micro-hotplates for drop-coated gas sensors," *Sensors and Actuators B: Chemical,* vol. 68, no. 1, pp. 223-233, 2000/08/25/ 2000.
[48] J. Courbat, D. Briand, L. Yue, S. Raible, and N. F. de Rooij, "Drop-coated metal-oxide gas sensor on polyimide foil with reduced power consumption for wireless applications," *Sensors and Actuators B: Chemical,* vol. 161, no. 1, pp. 862-868, 2012/01/03/ 2012.
[49] K. L. Choy, "Chemical vapour deposition of coatings," *Progress in Materials Science,* vol. 48, no. 2, pp. 57-170, 2003/01/01/ 2003.
[50] W. A. Bryant, "The fundamentals of chemical vapour deposition," *Journal of Materials Science,* vol. 12, no. 7, pp. 1285-1306, 1977/07/01 1977.
[51] T. K. Tseng, Y. S. Lin, Y. J. Chen, and H. J. I. j. o. m. s. Chu, "A review of photocatalysts prepared by sol-gel method for VOCs removal," vol. 11, no. 6, pp. 2336-2361, 2010.
[52] A. Kumar, Gaurav, A. K. Malik, D. K. Tewary, and B. Singh, "A review on development of solid phase microextraction fibers by sol–gel methods and their applications," *Analytica Chimica Acta,* vol. 610, no. 1, pp. 1-14, 2008/03/03/ 2008.
[53] L. L. Hench and J. K. J. C. r. West, "The sol-gel process," vol. 90, no. 1, pp. 33-72, 1990.
[54] E. Comini, "Metal oxide nano-crystals for gas sensing," *Analytica Chimica Acta,* vol. 568, no. 1, pp. 28-40, 2006/05/24/ 2006.
[55] A. Afzal, N. Cioffi, L. Sabbatini, and L. Torsi, "NOx sensors based on semiconducting metal oxide nanostructures: Progress and perspectives," *Sensors and Actuators B: Chemical,* vol. 171-172, pp. 25-42, 2012/08/01/ 2012.
[56] M. E. Franke, T. J. Koplin, and U. Simon, "Metal and Metal Oxide Nanoparticles in Chemiresistors: Does the Nanoscale Matter?," *Small,* vol. 2, no. 1, pp. 36-50, 2006/01/01 2005.
[57] B. Kamp, R. Merkle, R. Lauck, and J. Maier, "Chemical diffusion of oxygen in tin dioxide: Effects of dopants and oxygen partial pressure," *Journal of Solid State Chemistry,* vol. 178, no. 10, pp. 3027-3039, 2005/10/01/ 2005.
[58] A. Gurlo and R. Riedel, "In Situ and Operando Spectroscopy for Assessing Mechanisms of Gas Sensing," *Angewandte Chemie International Edition,* vol. 46, no. 21, pp. 3826-3848, 2007/05/18 2007.

[59] R. K. Sharma, M. C. Bhatnagar, and G. L. Sharma, "Mechanism of highly sensitive and fast response Cr doped TiO2 oxygen gas sensor," *Sensors and Actuators B: Chemical,* vol. 45, no. 3, pp. 209-215, 1997/12/15/ 1997.
[60] N. Barsan, D. Koziej, and U. Weimar, "Metal oxide-based gas sensor research: How to?," *Sensors and Actuators B: Chemical,* vol. 121, no. 1, pp. 18-35, 2007/01/30/ 2007.
[61] G. Lu, N. Miura, and N. Yamazoe, "High-temperature hydrogen sensor based on stabilized zirconia and a metal oxide electrode," *Sensors and Actuators B: Chemical,* vol. 35, no. 1, pp. 130-135, 1996/09/01/ 1996.
[62] H.-J. Kim and J.-H. Lee, "Highly sensitive and selective gas sensors using p-type oxide semiconductors: Overview," *Sensors and Actuators B: Chemical,* vol. 192, pp. 607-627, 2014/03/01/ 2014.
[63] S.-J. Choi *et al.*, "Selective Diagnosis of Diabetes Using Pt-Functionalized WO3 Hemitube Networks As a Sensing Layer of Acetone in Exhaled Breath," *Analytical Chemistry,* vol. 85, no. 3, pp. 1792-1796, 2013/02/05 2013.
[64] S. Kim, S. Park, S. Park, and C. Lee, "Acetone sensing of Au and Pd-decorated WO3 nanorod sensors," *Sensors and Actuators B: Chemical,* vol. 209, pp. 180-185, 2015/03/31/ 2015.
[65] L. Chen and S. C. Tsang, "Ag doped WO3-based powder sensor for the detection of NO gas in air," *Sensors and Actuators B: Chemical,* vol. 89, no. 1, pp. 68-75, 2003/03/01/ 2003.
[66] M. Hübner, C. E. Simion, A. Haensch, N. Barsan, and U. Weimar, "CO sensing mechanism with WO3 based gas sensors," *Sensors and Actuators B: Chemical,* vol. 151, no. 1, pp. 103-106, 2010/11/26/ 2010.
[67] I. Lee *et al.*, *The stability, sensitivity and response transients of ZnO, SnO2 and WO3 sensors under acetone, toluene and H2S environments*. 2014, pp. 300–307.
[68] L. Wang, A. Teleki, S. E. Pratsinis, and P. I. Gouma, "Ferroelectric WO3 Nanoparticles for Acetone Selective Detection," *Chemistry of Materials,* vol. 20, no. 15, pp. 4794-4796, 2008/08/01 2008.
[69] Y. Wang *et al.*, "Preparation of Ag-loaded mesoporous WO3 and its enhanced NO2 sensing performance," *Sensors and Actuators B: Chemical,* vol. 225, pp. 544-552, 2016/03/31/ 2016.
[70] W.-H. Tao and C.-H. Tsai, "H2S sensing properties of noble metal doped WO3 thin film sensor fabricated by micromachining," *Sensors and Actuators B: Chemical,* vol. 81, no. 2, pp. 237-247, 2002/01/05/ 2002.
[71] K. Kanda and T. Maekawa, "Development of a WO3 thick-film-based sensor for the detection of VOC," *Sensors and Actuators B: Chemical,* vol. 108, no. 1, pp. 97-101, 2005/07/22/ 2005.
[72] S. Luo, G. Fu, H. Chen, and Y. Zhang, "Gas sensing properties and complex impedance analysis of La2O3-added WO3 nanoparticles to VOC gases," *Materials Chemistry and Physics,* vol. 109, no. 2, pp. 541-546, 2008/06/15/ 2008.
[73] A. Sharma, M. Tomar, and V. Gupta, "Enhanced response characteristics of SnO2 thin film based NO2 gas sensor integrated with nanoscaled metal oxide clusters," *Sensors and Actuators B: Chemical,* vol. 181, pp. 735-742, 2013/05/01/ 2013.
[74] A. Karthigeyan *et al.*, "Low temperature NO2 sensitivity of nano-particulate SnO2 film for work function sensors," *Sensors and Actuators B: Chemical,* vol. 78, no. 1, pp. 69-72, 2001/08/30/ 2001.

[75] M. Law, H. Kind, B. Messer, F. Kim, and P. Yang, "Photochemical Sensing of NO2 with SnO2 Nanoribbon Nanosensors at Room Temperature," *Angewandte Chemie,* vol. 114, no. 13, pp. 2511-2514, 2002/07/03 2002.
[76] M. Schweizer-Berberich *et al.*, "The effect of Pt and Pd surface doping on the response of nanocrystalline tin dioxide gas sensors to CO," *Sensors and Actuators B: Chemical,* vol. 31, no. 1, pp. 71-75, 1996/02/01/ 1996.
[77] N. Bârsan and U. Weimar, "Understanding the fundamental principles of metal oxide based gas sensors; the example of CO sensing with SnO 2 sensors in the presence of humidity," *Journal of Physics: Condensed Matter,* vol. 15, no. 20, p. R813, 2003.
[78] A. Katsuki, K. J. S. Fukui, and A. B. Chemical, "H2 selective gas sensor based on SnO2," vol. 52, no. 1-2, pp. 30-37, 1998.
[79] L. Liu *et al.*, "Improved H2 sensing properties of Co-doped SnO2 nanofibers," vol. 150, no. 2, pp. 806-810, 2010.
[80] T. Kida, T. Doi, and K. J. C. o. M. Shimanoe, "Synthesis of monodispersed SnO2 nanocrystals and their remarkably high sensitivity to volatile organic compounds," vol. 22, no. 8, pp. 2662-2667, 2010.
[81] D.-S. Lee, J.-K. Jung, J.-W. Lim, J.-S. Huh, D.-D. J. S. Lee, and A. B. Chemical, "Recognition of volatile organic compounds using SnO2 sensor array and pattern recognition analysis," vol. 77, no. 1-2, pp. 228-236, 2001.
[82] D.-S. Lee, Y. T. Kim, J.-S. Huh, and D.-D. J. T. S. F. Lee, "Fabrication and characteristics of SnO2 gas sensor array for volatile organic compounds recognition," vol. 416, no. 1-2, pp. 271-278, 2002.
[83] Technavio, "Global Industrial Gas Sensors Market - Forecasts and Opportunity Assessment by Technavio," Accessed on: November 24th, 2018. [Online]. Available: https://www.businesswire.com/news/home/20170721005608/en/Global-Industrial-Gas-Sensors-Market---Forecasts
[84] N. Masson, R. Piedrahita, M. J. S. Hannigan, and A. B. Chemical, "Approach for quantification of metal oxide type semiconductor gas sensors used for ambient air quality monitoring," vol. 208, pp. 339-345, 2015.
[85] S. Zampolli *et al.*, "An electronic nose based on solid state sensor arrays for low-cost indoor air quality monitoring applications," vol. 101, no. 1-2, pp. 39-46, 2004.
[86] S. Okazaki *et al.*, "Sensing characteristics of an optical fiber sensor for hydrogen leak," vol. 93, no. 1-3, pp. 142-147, 2003.
[87] A. Somov *et al.*, "Deployment and evaluation of a wireless sensor network for methane leak detection," vol. 202, pp. 217-225, 2013.
[88] K. Wetchakun *et al.*, "Semiconducting metal oxides as sensors for environmentally hazardous gases," *Sensors and Actuators B: Chemical,* vol. 160, no. 1, pp. 580-591, 12/15/ 2011.
[89] L. Boon-Brett *et al.*, "Identifying performance gaps in hydrogen safety sensor technology for automotive and stationary applications," vol. 35, no. 1, pp. 373-384, 2010.
[90] A. J. S. Berna, "Metal oxide sensors for electronic noses and their application to food analysis," vol. 10, no. 4, pp. 3882-3910, 2010.
[91] N. Yamazoe, G. Sakai, and K. J. C. S. f. A. Shimanoe, "Oxide semiconductor gas sensors," vol. 7, no. 1, pp. 63-75, 2003.
[92] N. Yamazoe, "New approaches for improving semiconductor gas sensors," *Sensors and Actuators B: Chemical,* vol. 5, no. 1, pp. 7-19, 1991/08/01/ 1991.

[93] Y. Shimizu and M. Egashira, "Basic Aspects and Challenges of Semiconductor Gas Sensors," *MRS Bulletin,* vol. 24, no. 6, pp. 18-24, 1999.
[94] Y.-F. Sun *et al.*, "Metal oxide nanostructures and their gas sensing properties: a review," vol. 12, no. 3, pp. 2610-2631, 2012.
[95] Q. Ma, F. Peng, R. Li, S. Yin, and C. Dai, "Effect of calcination temperature on microstructure and electrochemical performance of lithium-rich layered oxide cathode materials," *Materials Science and Engineering: B,* vol. 213, pp. 123-130, 2016/11/01/ 2016.
[96] J. Yu, L. Qi, B. Cheng, and X. Zhao, "Effect of calcination temperatures on microstructures and photocatalytic activity of tungsten trioxide hollow microspheres," *Journal of Hazardous Materials,* vol. 160, no. 2, pp. 621-628, 2008/12/30/ 2008.
[97] H. Liu, S. P. Gong, Y. X. Hu, J. Q. Liu, and D. X. Zhou, "Properties and mechanism study of SnO2 nanocrystals for H2S thick-film sensors," *Sensors and Actuators B: Chemical,* vol. 140, no. 1, pp. 190-195, 2009/06/18/ 2009.
[98] F. Cao, S. Guo, H. Ma, D. Shan, S. Yang, and J. Gong, "Nickel oxide microfibers immobilized onto electrode by electrospinning and calcination for nonenzymatic glucose sensor and effect of calcination temperature on the performance," *Biosensors and Bioelectronics,* vol. 26, no. 5, pp. 2756-2760, 2011/01/15/ 2011.
[99] S. Tsubota, T. Nakamura, K. Tanaka, and M. Haruta, "Effect of calcination temperature on the catalytic activity of Au colloids mechanically mixed with TiO2 powder for CO oxidation," *Catalysis Letters,* vol. 56, no. 2, pp. 131-135, 1998/12/01 1998.
[100] S. C. Naisbitt, K. F. E. Pratt, D. E. Williams, and I. P. Parkin, "A microstructural model of semiconducting gas sensor response: The effects of sintering temperature on the response of chromium titanate (CTO) to carbon monoxide," *Sensors and Actuators B: Chemical,* vol. 114, no. 2, pp. 969-977, 2006/04/26/ 2006.
[101] J. F. Chang, H. H. Kuo, I. C. Leu, and M. H. Hon, "The effects of thickness and operation temperature on ZnO:Al thin film CO gas sensor," *Sensors and Actuators B: Chemical,* vol. 84, no. 2, pp. 258-264, 2002/05/15/ 2002.
[102] R. Salunkhe, C. J. S. Lokhande, and A. B. Chemical, "Effect of film thickness on liquefied petroleum gas (LPG) sensing properties of SILAR deposited CdO thin films," vol. 129, no. 1, pp. 345-351, 2008.
[103] G. Korotcenkov and B. K. Cho, "Thin film SnO2-based gas sensors: Film thickness influence," *Sensors and Actuators B: Chemical,* vol. 142, no. 1, pp. 321-330, 2009/10/12/ 2009.
[104] E. M. Preiß, T. Rogge, A. Krauß, and H. Seidel, "Tin oxide-based thin films prepared by pulsed laser deposition for gas sensing," *Sensors and Actuators B: Chemical,* vol. 236, pp. 865-873, 2016/11/29/ 2016.
[105] G. Martinelli and M. C. Carotta, "Sensitivity to reducing gas as a function of energy barrier in SnO2 thick-film gas sensor," *Sensors and Actuators B: Chemical,* vol. 7, no. 1, pp. 717-720, 1992/03/01/ 1992.
[106] C. Liewhiran and S. Phanichphant, "Influence of Thickness on Ethanol Sensing Characteristics of Doctor-bladed Thick Film from Flame-made ZnO Nanoparticles," *Sensors (Basel, Switzerland),* vol. 7, no. 2, pp. 185-201, 2007.
[107] K. Sahner, R. Moos, M. Matam, J. J. Tunney, and M. Post, "Hydrocarbon sensing with thick and thin film p-type conducting perovskite materials," *Sensors and Actuators B: Chemical,* vol. 108, no. 1, pp. 102-112, 2005/07/22/ 2005.

[108] A. Gurlo, "Interplay between O2 and SnO2: oxygen ionosorption and spectroscopic evidence for adsorbed oxygen," *Chemphyschem,* vol. 7, no. 10, pp. 2041-52, Oct 13 2006.
[109] G. Neri, A. Bonavita, G. Micali, G. Rizzo, N. Pinna, and M. Niederberger, "In2O3 and Pt-In2O3 nanopowders for low temperature oxygen sensors," *Sensors and Actuators B: Chemical,* vol. 127, no. 2, pp. 455-462, 2007.
[110] C. Wang, L. Z. Yin, L., D. Xiang, and R. Gao, "Metal Oxide Gas Sensors: Sensitivity and Influencing Factors. Sensors," *Sensors,* vol. 10, no. 3, pp. 2088-2106, 2010.
[111] K. Wetchakun *et al.*, "Semiconducting metal oxides as sensors for environmentally hazardous gases," vol. 160, no. 1, pp. 580-591, 2011.
[112] F. E. Annanouch *et al.*, "Aerosol-Assisted CVD-Grown WO3 Nanoneedles Decorated with Copper Oxide Nanoparticles for the Selective and Humidity-Resilient Detection of H2S," *ACS Applied Materials & Interfaces,* vol. 7, no. 12, pp. 6842-6851, 2015/04/01 2015.
[113] L. A. Obvintseva, "Metal oxide semiconductor sensors for determination of reactive gas impurities in air," *Russian Journal of General Chemistry,* vol. 78, no. 12, pp. 2545-2555, 2008// 2008.
[114] N. Barsan and U. Weimar, "Conduction Model of Metal Oxide Gas Sensors," *Journal of Electroceramics,* journal article vol. 7, no. 3, pp. 143-167, December 01 2001.
[115] E. Traversa, "Ceramic sensors for humidity detection: the state-of-the-art and future developments," *Sensors and Actuators B: Chemical,* vol. 23, no. 2, pp. 135-156, 1995/02/01/ 1995.
[116] J. Gong, Q. Chen, M.-R. Lian, N.-C. Liu, R. G. Stevenson, and F. Adami, "Micromachined nanocrystalline silver doped SnO2 H2S sensor," *Sensors and Actuators B: Chemical,* vol. 114, no. 1, pp. 32-39, 2006.
[117] Q. Qi *et al.*, "Electrical response of Sm2O3-doped SnO2 to C2H2 and effect of humidity interference," *Sensors and Actuators B: Chemical,* vol. 134, no. 1, pp. 36-42, 2008/08/28/ 2008.
[118] M. Egashira, M. Nakashima, S. Kawasumi, and T. Selyama, "Temperature programmed desorption study of water adsorbed on metal oxides. 2. Tin oxide surfaces," *The Journal of Physical Chemistry,* vol. 85, no. 26, pp. 4125-4130, 1981/12/01 1981.
[119] P. Van Tong, N. D. Hoa, N. Van Duy, D. T. T. Le, and N. Van Hieu, "Enhancement of gas-sensing characteristics of hydrothermally synthesized WO3 nanorods by surface decoration with Pd nanoparticles," *Sensors and Actuators B: Chemical,* vol. 223, pp. 453-460, 2016/02/01/ 2016.
[120] N. Yamazoe, J. Fuchigami, M. Kishikawa, and T. Seiyama, "Interactions of tin oxide surface with O2, H2O AND H2," *Surface Science,* vol. 86, pp. 335-344, 1979/07/02/ 1979.
[121] E. W. Thornton and P. G. Harrison, "Tin oxide surfaces. Part 1.—Surface hydroxyl groups and the chemisorption of carbon dioxide and carbon monoxide on tin(IV) oxide," *Journal of the Chemical Society, Faraday Transactions 1: Physical Chemistry in Condensed Phases,* 10.1039/F19757100461 vol. 71, no. 0, pp. 461-472, 1975.
[122] G. Korotcenkov, "Metal oxides for solid-state gas sensors: What determines our choice?," *Materials Science and Engineering: B,* vol. 139, no. 1, pp. 1-23, 2007/04/25/ 2007.
[123] S. Cui *et al.*, "Ag nanocrystal as a promoter for carbon nanotube-based room-temperature gas sensors," vol. 4, no. 19, pp. 5887-5894, 2012.

[124] C.-M. Chang, M.-H. Hon, and C. J. R. A. Leu, "Improvement in CO sensing characteristics by decorating ZnO nanorod arrays with Pd nanoparticles and the related mechanisms," vol. 2, no. 6, pp. 2469-2475, 2012.
[125] S. Mubeen, T. Zhang, B. Yoo, M. A. Deshusses, and N. V. Myung, "Palladium Nanoparticles Decorated Single-Walled Carbon Nanotube Hydrogen Sensor," *The Journal of Physical Chemistry C,* vol. 111, no. 17, pp. 6321-6327, 2007/05/01 2007.
[126] A. Esfandiar, S. Ghasemi, A. Irajizad, O. Akhavan, and M. R. Gholami, "The decoration of TiO2/reduced graphene oxide by Pd and Pt nanoparticles for hydrogen gas sensing," *International Journal of Hydrogen Energy,* vol. 37, no. 20, pp. 15423-15432, 2012/10/01/ 2012.
[127] Y. Wang *et al.*, "Room-temperature hydrogen sensor based on grain-boundary controlled Pt decorated In2O3 nanocubes," *Sensors and Actuators B: Chemical,* vol. 201, pp. 351-359, 2014/10/01/ 2014.
[128] W.-T. Koo, J.-S. Jang, S.-J. Choi, H.-J. Cho, and I.-D. Kim, "Metal–Organic Framework Templated Catalysts: Dual Sensitization of PdO–ZnO Composite on Hollow SnO2 Nanotubes for Selective Acetone Sensors," *ACS Applied Materials & Interfaces,* vol. 9, no. 21, pp. 18069-18077, 2017/05/31 2017.
[129] J. H. Bruning, D. R. Herriott, J. E. Gallagher, D. P. Rosenfeld, A. D. White, and D. J. Brangaccio, "Digital Wavefront Measuring Interferometer for Testing Optical Surfaces and Lenses," *Appl. Opt.,* vol. 13, no. 11, pp. 2693-2703, 1974/11/01 1974.
[130] P. F. Escobar *et al.*, "Diagnostic efficacy of optical coherence tomography in the management of preinvasive and invasive cancer of uterine cervix and vulva," vol. 14, no. 3, pp. 470-474, 2004.
[131] J. G. Fujimoto, "Optical coherence tomography for ultrahigh resolution in vivo imaging," *Nature Biotechnology,* vol. 21, p. 1361, 10/31/online 2003.
[132] S.-W. Kim and G.-H. Kim, "Thickness-profile measurement of transparent thin-film layers by white-light scanning interferometry," *Appl. Opt.,* vol. 38, no. 28, pp. 5968-5973, 1999/10/01 1999.
[133] Y.-S. Ghim and S.-W. Kim, "Thin-film thickness profile and its refractive index measurements by dispersive white-light interferometry," *Opt. Express,* vol. 14, no. 24, pp. 11885-11891, 2006/11/27 2006.
[134] A. Martiny, A. P. C. Campos, M. S. Sader, and M. A. L. Pinto, "SEM/EDS analysis and characterization of gunshot residues from Brazilian lead-free ammunition," *Forensic Science International,* vol. 177, no. 1, pp. e9-e17, 2008/05/02/ 2008.
[135] F. Saverio Romolo and P. Margot, "Identification of gunshot residue: a critical review," *Forensic Science International,* vol. 119, no. 2, pp. 195-211, 2001/06/15/ 2001.
[136] M. Hashimoto *et al.*, "SEM and TEM analysis of water degradation of human dentinal collagen," vol. 66B, no. 1, pp. 287-298, 2003.
[137] J. C. Araujo *et al.*, "Comparison of hexamethyldisilazane and critical point drying treatments for SEM analysis of anaerobic biofilms and granular sludge," *Journal of Electron Microscopy,* vol. 52, no. 4, pp. 429-433, 2003.
[138] I. Sondi and B. Salopek-Sondi, "Silver nanoparticles as antimicrobial agent: a case study on E. coli as a model for Gram-negative bacteria," *Journal of Colloid and Interface Science,* vol. 275, no. 1, pp. 177-182, 2004/07/01/ 2004.
[139] V. Sokolova *et al.*, "Characterisation of exosomes derived from human cells by nanoparticle tracking analysis and scanning electron microscopy," *Colloids and Surfaces B: Biointerfaces,* vol. 87, no. 1, pp. 146-150, 2011/10/01/ 2011.

[140] G. Knott, H. Marchman, D. Wall, and B. Lich, "Serial Section Scanning Electron Microscopy of Adult Brain Tissue Using Focused Ion Beam Milling," *The Journal of Neuroscience,* 10.1523/JNEUROSCI.3189-07.2008 vol. 28, no. 12, p. 2959, 2008.
[141] A. Nanakoudis, "SEM and TEM: what's the difference?," Accessed on: Nov 1, 2018[Online]. Available: http://blog.phenom-world.com/sem-tem-difference
[142] A. Curry, H. Appleton, and B. Dowsett, "Application of transmission electron microscopy to the clinical study of viral and bacterial infections: Present and future," *Micron,* vol. 37, no. 2, pp. 91-106, 2006/02/01/ 2006.
[143] D. Boyd and Z. Yao, "16 - Application of modern transmission electron microscopy (TEM) techniques to the study of phase transformations in steels," in *Phase Transformations in Steels*, vol. 2, E. Pereloma and D. V. Edmonds, Eds.: Woodhead Publishing, 2012, pp. 507-531.
[144] P. Kuisma-Kursula, "Accuracy, precision and detection limits of SEM–WDS, SEM–EDS and PIXE in the multi-elemental analysis of medieval glass," vol. 29, no. 1, pp. 111-118, 2000.
[145] P. Braun, M. Moeder, S. Schrader, P. Popp, P. Kuschk, and W. Engewald, "Trace analysis of technical nonylphenol, bisphenol A and 17α-ethinylestradiol in wastewater using solid-phase microextraction and gas chromatography–mass spectrometry," *Journal of Chromatography A,* vol. 988, no. 1, pp. 41-51, 2003/02/21/ 2003.
[146] P. R. Shukla, S. Wang, H. Sun, H. M. Ang, and M. Tadé, "Activated carbon supported cobalt catalysts for advanced oxidation of organic contaminants in aqueous solution," *Applied Catalysis B: Environmental,* vol. 100, no. 3, pp. 529-534, 2010/10/20/ 2010.
[147] K. M. Lee, Z. Cai, J. A. Griggs, L. Guiatas, D. J. Lee, and T. Okabe, "SEM/EDS evaluation of porcelain adherence to gold-coated cast titanium," vol. 68B, no. 2, pp. 165-173, 2004.
[148] Y. Yuan, Y. Shimada, S. Ichinose, and J. Tagami, "Qualitative analysis of adhesive interface nanoleakage using FE-SEM/EDS," *Dental Materials,* vol. 23, no. 5, pp. 561-569, 2007/05/01/ 2007.
[149] M. Wei, Q. Yuan, D. G. Evans, Z. Wang, and X. Duan, "Layered solids as a “molecular container” for pharmaceutical agents: l-tyrosine-intercalated layered double hydroxides," *Journal of Materials Chemistry,* 10.1039/B416068A vol. 15, no. 11, pp. 1197-1203, 2005.
[150] N. V. Phadnis, R. K. Cavatur, and R. Suryanarayanan, "Identification of drugs in pharmaceutical dosage forms by X-ray powder diffractometry," *Journal of Pharmaceutical and Biomedical Analysis,* vol. 15, no. 7, pp. 929-943, 1997/04/01/ 1997.
[151] E. T. Bergslien, M. Bush, and P. J. Bush, "Identification of cremains using X-ray diffraction spectroscopy and a comparison to trace element analysis," *Forensic Science International,* vol. 175, no. 2, pp. 218-226, 2008/03/05/ 2008.
[152] A. Ruffell and P. Wiltshire, "Conjunctive use of quantitative and qualitative X-ray diffraction analysis of soils and rocks for forensic analysis," *Forensic Science International,* vol. 145, no. 1, pp. 13-23, 2004/10/04/ 2004.
[153] A. B. Pour and M. Hashim, "Identification of hydrothermal alteration minerals for exploring of porphyry copper deposit using ASTER data, SE Iran," *Journal of Asian Earth Sciences,* vol. 42, no. 6, pp. 1309-1323, 2011/11/11/ 2011.
[154] H. Wang, R. Liu, F. Cheng, Y. Cao, G. Ding, and X. Zhao, "Electrodepositing amorphous Ni-W alloys for MEMS," *Microelectronic Engineering,* vol. 87, no. 10, pp. 1901-1906, 2010/10/01/ 2010.

[155] D. U. Tulyaganov, M. J. Ribeiro, and J. A. Labrincha, "Development of glass-ceramics by sintering and crystallization of fine powders of calcium-magnesium-aluminosilicate glass," *Ceramics International,* vol. 28, no. 5, pp. 515-520, 2002/01/01/ 2002.
[156] D. M. Moore and R. C. Reynolds, *X-ray Diffraction and the Identification and Analysis of Clay Minerals*. Oxford university press Oxford, 1989.
[157] E. Marguí, I. Queralt, and M. Hidalgo, "Application of X-ray fluorescence spectrometry to determination and quantitation of metals in vegetal material," *TrAC Trends in Analytical Chemistry,* vol. 28, no. 3, pp. 362-372, 2009/03/01/ 2009.
[158] T. Kemper and S. Sommer, "Estimate of Heavy Metal Contamination in Soils after a Mining Accident Using Reflectance Spectroscopy," *Environmental Science & Technology,* vol. 36, no. 12, pp. 2742-2747, 2002/06/01 2002.
[159] M. Uo, T. Wada, and T. Sugiyama, "Applications of X-ray fluorescence analysis (XRF) to dental and medical specimens," *Japanese Dental Science Review,* vol. 51, no. 1, pp. 2-9, 2015/02/01/ 2015.
[160] J. Zięba-Palus and R. Borusiewicz, "Examination of multilayer paint coats by the use of infrared, Raman and XRF spectroscopy for forensic purposes," *Journal of Molecular Structure,* vol. 792-793, pp. 286-292, 2006/07/03/ 2006.
[161] H. Wu and M. Khan, "THz spectroscopy: An emerging technology for pharmaceutical development and pharmaceutical Process Analytical Technology (PAT) applications," *Journal of Molecular Structure,* vol. 1020, pp. 112-120, 2012/08/08/ 2012.
[162] S. Jeon and H. Hwang, "Electrical and physical characteristics of PrTixOy for metal-oxide-semiconductor gate dielectric applications," *Applied Physics Letters,* vol. 81, no. 25, pp. 4856-4858, 2002/12/16 2002.
[163] A. Kocijan, I. Milošev, and B. Pihlar, "Cobalt-based alloys for orthopaedic applications studied by electrochemical and XPS analysis," *Journal of Materials Science: Materials in Medicine,* vol. 15, no. 6, pp. 643-650, 2004/06/01 2004.
[164] R. Arsat *et al.*, "Graphene-like nano-sheets for surface acoustic wave gas sensor applications," *Chemical Physics Letters,* vol. 467, no. 4, pp. 344-347, 2009/01/05/ 2009.
[165] S. Esfahani, "Electronic nose implementation for biomedical applications," PhD, School of Engineering, University of Warwick, University of Warwick Publications service & WRAP, 2018.
[166] J. Covington, "CMOS and SOI CMOS FET-based gas sensors," PhD, School of Engineering, University of Warwick, University of Warwick Publications service & WRAP, 2001.

Chapter 3. Three-Dimensional Printed Tungsten Oxide Based Sensor

3.1 Introduction

Since its development in the 1980s, additive manufacturing (also known as three-dimensional (3D) printing) has brought benefits in many areas. This technology offers advantages in fabrication of one of a kind and low volume productions, without the expense of tooling, while being able to create complex 3D structures that would be difficult to produce using more conventional manufacturing techniques [1]. It has been used since its early development for rapid prototyping of products before production, being deployed in areas including industrial design [2], medical [3-7], military and biotechnology [8, 9], and even food [10-13] and fashion [14-16]. The recent development in additive manufacturing specifically reduction in cost for both machines and raw materials, improved resolution, and an increase in available materials has enabled this technology to make end-use products beyond fit and form prototypes. For example, designers use 3D printing to create shoes and clothing that are ready to wear [14, 17]. In the medical area, recent advances in 3D printing have enabled the formation of biocompatible material into 3D functional living tissues, although this is still limited by the properties of the chosen material [7, 18, 19]. One area of increased interest is the use of 3D printing technology to create precisely structured functional devices, with gas sensing being one such application [20-22].

This chapter discusses the fabrication of metal oxide-based sensor using 3D printing technology. The first section describes variants of 3D printing manufacturing techniques followed by the sensor fabrication process. The section continues on

characterising the material and testing the sensors to detect several compounds. The last section describes the gas testing results and analysis.

3.2 Three-Dimensional Printing (3DP) Technology

Three-dimensional printing (3DP) is an additive manufacturing technique that creates an object by successively printing a layer of material at a time until the object is created. These layers considered as a thinly stacked horizontal cross-section of the object. The technology allows creation of a complex and/or functional device that otherwise would be difficult to produce using traditional manufacturing techniques, such as injection moulding or Computer Numerical Control (CNC) machining.

The printing process starts with designing the object in a digital format, using a computer-aided design (CAD) software such as SolidWorks, Autodesk Inventor, and Fusion 360. The file is then converted into an STL format and then transferred to the instrument that controls the 3D printer. There are various 3D fabrication techniques available, such as stereolithography (SLA), selective laser sintering (SLS), selective laser melting (SLM), fused deposition modelling (FDM), and electronic beam melting (EDM). Some variants of these techniques are discussed in the following.

3.2.1 Stereolithography (SLA)

SLA forms objects by curing or solidifying liquid photosensitive polymer by using irradiation [23]. After the first layer of liquid/ resin is cured, the platform with the cured structured is then lowered and a new layer of liquid/resin is applied on top. The process of curing and lowering platform is repeated until the object is formed.

SLA typically use materials including epoxies and acrylics [20, 24]. It offers fabrication of high feature resolution object (~1.2μm) [25], smooth surface finish, and

complex shapes. However, the disadvantages include limited variants of materials, the need to print support for complex structures, and entrapment of unreacted monomer and residual photo initiator [24].

3.2.2 Selective Laser Sintering (SLS)

SLS creates objects by fusing powders using a binding agent or heat [26]. The process starts with an empty build platform, which will be coated with a layer of powders when the printing starts. The technology employs a laser aimed at points defined by the 3D model, which fuse the powders, creating a solidified object. After the first layer is fused, the powder bed is lowered as a new layer of powder is deposited on top. This process continues until the part is completed.

The technique uses materials including polymers, wax, ceramics, metals, metal/polymer, alloys or steels, and nylon [27, 28]. It allows the creation of strong and complex parts and unlike SLA, it does not require supports as the powder itself acts as the necessary support. It can also print a relatively larger build volume than SLA. The disadvantages include grainy surface finish and thermal distortion that may cause object shrinkage and warping.

3.2.3 Fused Deposition Modelling (FDM)

FDM creates objects by melting a filament of thermoplastic material through a temperature-controlled extruder and depositing the semi-molten polymer onto a platform [25]. As a layer of material is deposited, the platform descends for the deposition of the next layer and this process is repeated until the object finished. The materials commonly used include various polymers such as Acrylonitrile butadiene styrene (ABS), polylactic acid (PLA), nylon, and polycaprolactone (PCL). The advantages of FDM include cheaper price, easier to operate, and availability of

various materials. The disadvantages are lower resolution and existence of a seam line between deposited layers.

3.3 FDM Technology for Sensor Fabrication

In this work, FDM was used to print gas sensitive layers. This was chosen as it is the most suitable technique for the intended application. The FDM printer, BFB-3000 was used to a thick-film sensing material. The printer resolution is 0.125 mm (0.125 µm) with tolerance of ± 1%. The thickness of the commercial thick-films are generally between 60 – 70 µm and therefore printing using BFB-3000 might result in a thicker film than desired. However, this would not be a problem as the sensing material will be incorporated into a vehicle which will be burnt out after the deposition process completed. Therefore, the desired thickness should be achievable. Furthermore, FDM technology is the cheapest option compared to with SLA and SLS which would enable low fabrication cost. Additionally, it is safer and easier to operate.

Filament was prepared from a mixture of thermoplastic material and metal oxide powders. Tungsten trioxide (WO_3) was chosen as it is one of the most commonly used material in metal oxide gas sensors. The polymer chosen was polycaprolactone (PCL) due to its low melting point at around 60°C, which can speed up the extrusion process. It also has good adhesion, which can help the material stick better to the substrate.

Tungsten trioxide (New Metals & Chemical Ltd, UK) was incorporated into a polycaprolactone (PCL) matrix by solution method. PCL pellets were previously dissolved in dichloromethane before adding WO_3 powders into the mixture and stirred using Magnetic Hotplate Stirrer until blended. The mixture was left at room temperature for a while until it slightly hardened and then shaped into pellets. These

pellets were dried overnight for solvent to completely evaporate. Various ratios of WO_3 were calculated in mass percentage of the total mass of WO_3 and PCL, as shown in Table 3 - 1, to determine the best mixture ratio.

Table 3 - 1 Percentage of WO_3 in WO_3-PCL mixture.

Percentage of WO_3	WO_3 weight (g)	PCL weight (g)
20%	10	40
50%	26	26
70%	42	18
80%	40	10
85%	51	9

A filament extruder with a 3-mm nozzle, as shown in Figure 3 - 1, was used to extrude the pellets at the optimised temperature of 65°C. It was found that lower temperatures created bulges along the filament while higher temperatures melted the filament and reduced the diameter quite significantly than the desired dimension at 3.00 mm. The extruding process was repeated three times to increase uniformity of the mixture. The diameter was measured for each ratio at random points along the extrusion length (see Table 3 - 2).

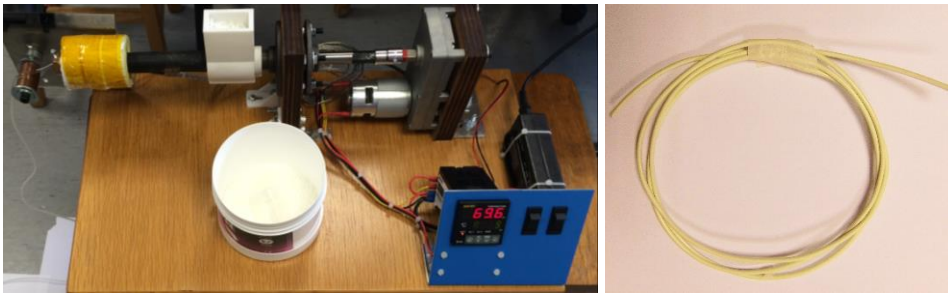

Figure 3 - 1 Filament extruder (left) and extruded filament (right).

Table 3 - 2 Diameter of extruded filaments.

Percentage of WO_3	Average Ø (mm)
20%	2.86
50%	2.79
70%	2.71
80%	2.72
85%	2.70

Thermogravimetric Analyzer (Mettler Toledo, USA) was used to examine PCL mass loss characteristics. As illustrated in Figure 3 - 2, mass loss occurred around 400°C and PCL was completely burned out at 600°C. This was used as a reference for the first sintering temperature to burn out PCL. The second point was to form a solid mass of WO_3 while providing enough porosity along the body. This was initially set at 900°C.

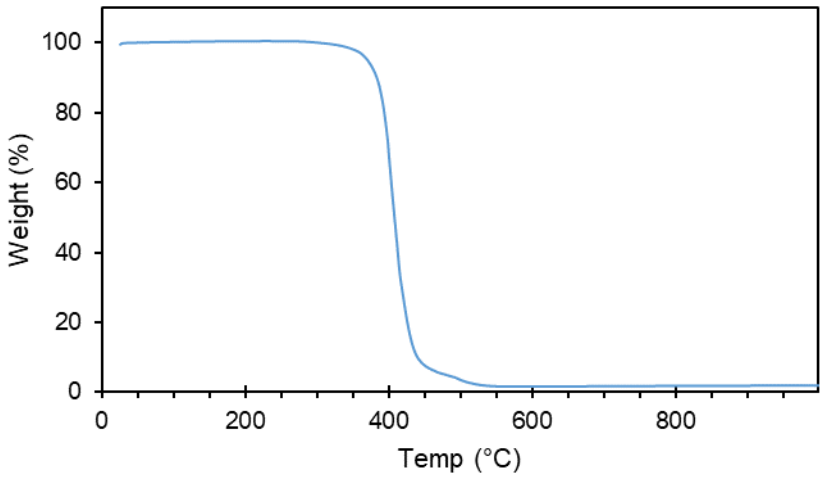

Figure 3 - 2 Thermogravimetric analysis of PCL.

After the sintering process, shown in Figure 3 - 3, the 20% and 50% WO_3 filament samples turned into loose powders as there wasn't enough powder present for binding. The rest of the samples remained intact. The filaments of these samples were used for 3D printing.

Figure 3 - 3 Sintered WO_3 filament samples (left to right): 20%, 50%, 70%, 80%, and 85% content.

Using a modified BFB-300 FDM printer (3D Systems, USA), filaments were printed into straight lines on to some blank ceramic tiles. Filaments of 70% and 80% were successfully printed on the tile at 200°C and 240°C respectively. The 85% loading could not be printed as it got stuck in the nozzle, indicating the loading content was too high for the printer. Once completed, the printed lines were sintered in a furnace. The results (Figure 3 - 4) showed lines of 70% WO_3 were broken indicating insufficient WO_3 in the mixture whilst the 80% ones stayed the same. Henceforth, this ratio was used for further experiments.

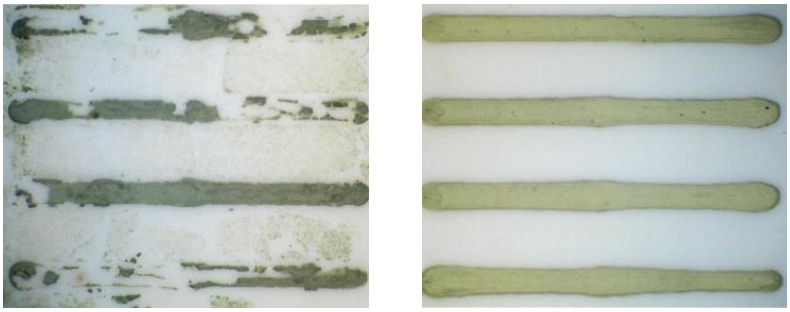

Figure 3 - 4 Printed WO_3 with 70% (left) and 80% (right) content.

Filaments samples of 80% tungsten trioxide, cut at 10 mm long, were sintered at 900°C to examine material density by direct measurement of mass and volume. Other temperatures were also tried at 800, 850, 950, and 1000°C to see the effect of sintering on the density and microstructures. The various sintering profiles can be seen in Figure 3 - 5. The results of density calculations are shown in

Table 3 - 3.

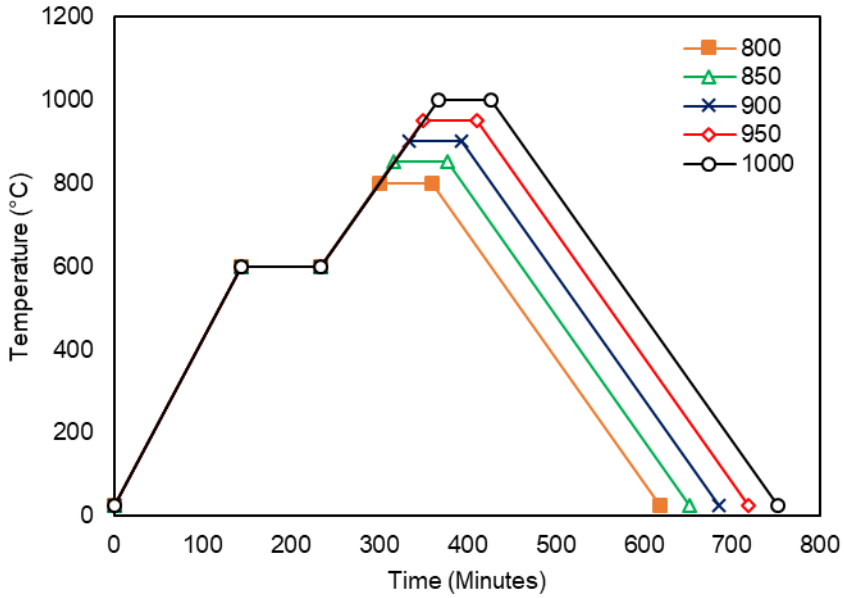

Figure 3 - 5 Sintering profile of WO_3 based sensor.

Sintered samples formed a denser body as the temperature increased. A less dense material will likely have less mechanical strength but more porosity. Vice versa, denser material will have higher mechanical strength but less porosity. For gas sensing application, porosity is desired but the same time, the material needs to be strong enough thus it won't easily crumble. Scanning electron microscopy (SEM) analysis was later carried out to examine the microstructure of the material.

Table 3 - 3 Material density at different sintering temperatures.

Temperature (°C)	Density (g/cm^3)
800	2.800
850	3.086
900	3.343
950	3.382
1000	3.967

Alumina tile of 2 x 2 mm (sourced from Alphasense Ltd, UK), shown in Figure 3 - 6, patterned with gold interdigitated electrodes on one side and platinum heater on the reverse was used as the sensor substrates. The electrodes consist of 7 interdigitated pair with a track and spacing of 75 µm and 65 µm respectively. The platinum heater provides a resistance of 20 ± 2.5 Ohm at room temperature.

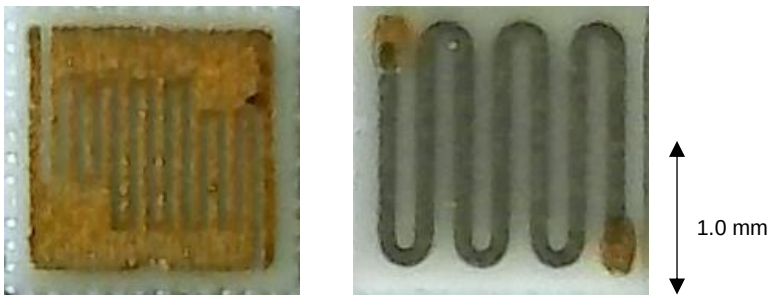

Figure 3 - 6 Sensor array on Al_2O_3 substrate: electrodes (left) and heater (right).

A single line of 80% WO_3 filament was printed on top of interdigitated electrodes and further sintered. These sensors were then welded and packed into a TO5 housing. The sensors and TO5 housing are shown in Figure 3 - 7.

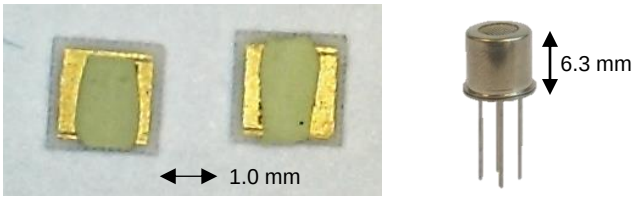

Figure 3 - 7 WO_3 based 3D printed sensor (left) and sensor packaging (right).

3.4 Material Characterisation

The morphology of the sensing material was investigated by Phillip XL30 SEM at accelerating voltage 25 kV. The samples were gold-coated prior to testing and the imaging results are shown in Figure 3 - 8.

The thickness of the sensing material for thick-films was aimed at 60-70 µm which is based on the thickness of the commercial thick-film sensors. This was measured using a Contour GT 3D Optical Microscope (Bruker, UK) before and after sintering. The thickness was found to be 110 µm before sintering and shrunk to 65 ± 5 µm afterwards.

It can be observed that the structure of the material became denser and less porous as the sintering temperature increased. Samples sintered at 800°C and 850°C exhibit porous body. Samples sintered at 900°C are still quite porous with the particles bonded closer with each other. Samples sintered at 950°C and 1000°C were more compact with very little porosity on the body. This indicates that firing temperature of 900°C and below are likely more suitable for the gas sensing application. The experiments were repeated several times and showed that samples sintered at 800°C were quite fragile and easily broken. Therefore, the best sintering temperature for the samples was set at 850°C for sensing material printed on the patterned electrodes.

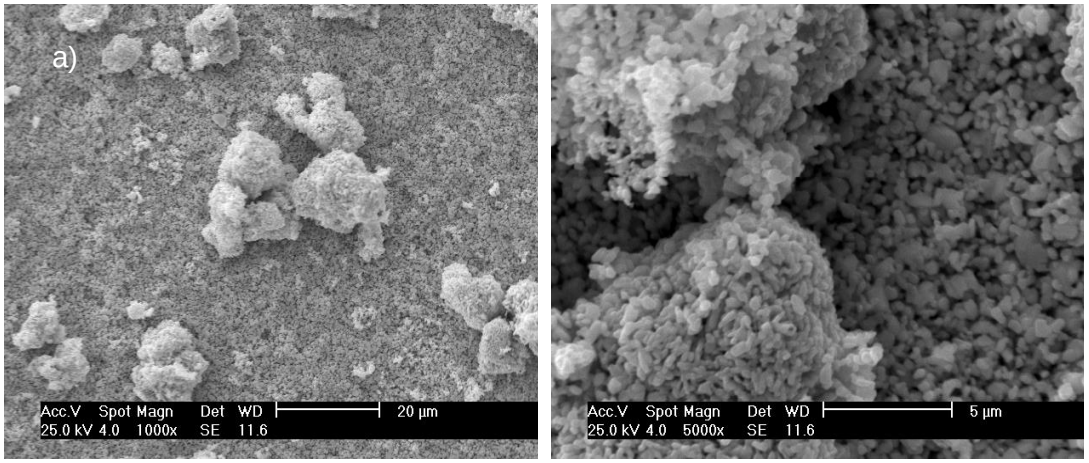

(a) 800°C

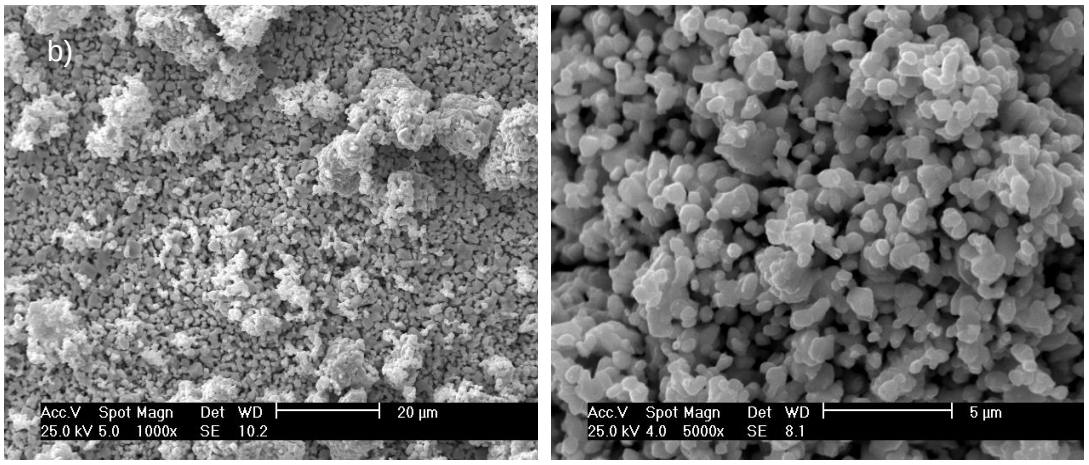

(b) 850°C

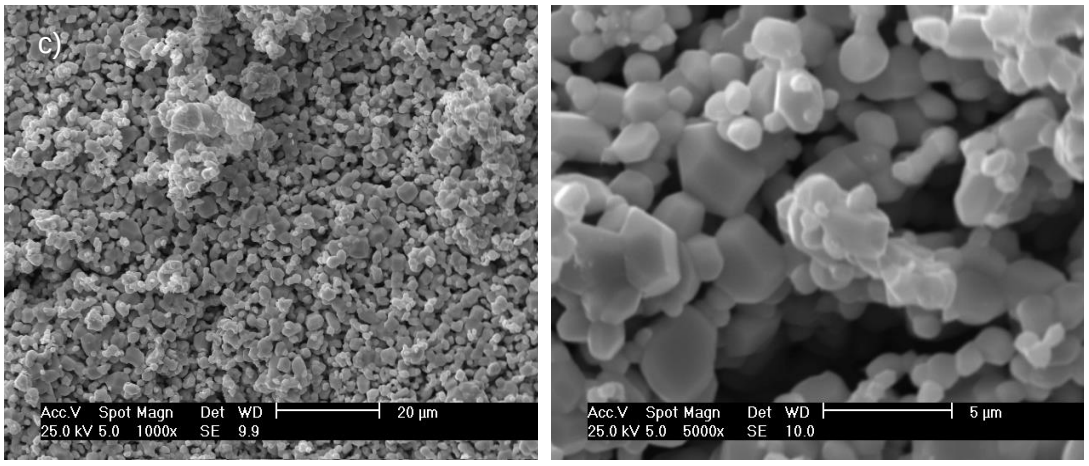

(c) 900°C

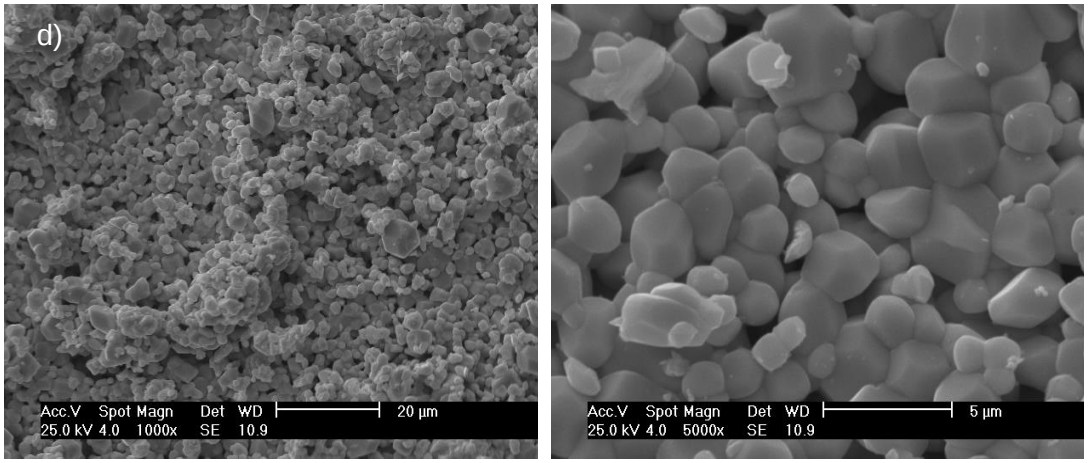

(d) 950°C

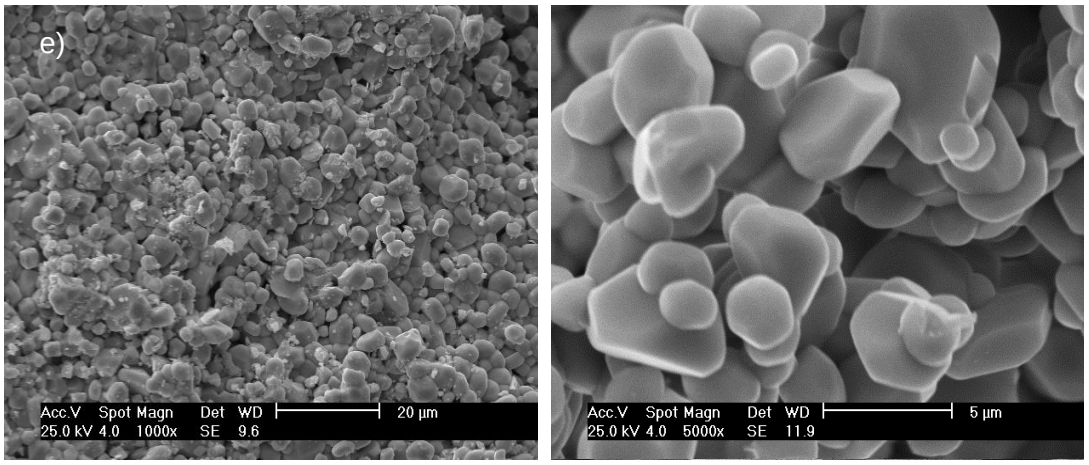

(e) 1000°C

Figure 3 - 8 SEM of WO_3 samples sintered at 800°C (a);850°C (b);900°C (c);950°C (d);1000°C (e).

3.5 Gas Testing

The 3D printed WO_3 gas sensors were tested to isobutylene which is a common type of volatile organic compound (VOC) used in gas sensors. The isobutylene was available in gas cylinder at 100 ppm (BOC, UK). Other VOCs used were ethanol and acetone, available in the forms of liquid and/or permeation tubes.

Experiments using isobutylene were carried out by connecting the gas cylinder directly to gas handling apparatus previously discussed in Chapter 2. For experiments with VOCs in liquid form, air was bubbled through the compounds and the outcome

gas line was then connected to the gas mixture. VOCs source from permeation tube were tested using The Owlstone Calibration Gas Generator (OVG-4) by Owlstone. The test procedure for each type is discussed in more detail in the following.

3.5.1 Gas Testing Using Permeation

The permeation tubes for the OVG-4 is constructed from 1/4" PTFE tubing and rod as illustrated in Figure 3 - 9. It contains chemical compound in a two phase-phase system between its liquid and its gas phase. Operated at a constant temperature as suggested by the manufacturer specification, the compound's gas phase permeates through the tube walls at a constant rate. The concentration of the compound can be calculated by:

$$[i] = \frac{PR}{F_{SA}} \tag{3.3}$$

Where $[i] =$ concentration (ng/ml)

$PR =$ permeation rate (ng/min)

$F_{SA} =$ sample flow (ml/min)

Permeation device is loaded into Owlstone Vapour Generator (OVG-4), which is designed to house and incubate permeation devices. After loading the permeation source into the oven inlet and setting the temperature using Eurotherm controller, 1/8" tubing is connected from the sample outlet fitting into the gas inlet of the chamber.

Figure 3 - 9 Standalone OVG-4 for (left) and permeation tube (right) [29].

Each compound was tested at different flow rate to obtain different concentrations as shown in Table 3 - 4. The flow rate was limited to min 50 ml/min up to 500 ml/min. Tests were carried out by alternating the analyte and air keeping the total flow rate constant.

Table 3 - 4 Flowrate and concentration of acetone and ethanol permeation devices.

Concentration (ng/ml)		20	10	5
Analyte	**Permeation rate (ng/min)**	**Sample flow (ml/min)**		
Acetone	3590	180	359	-
Ethanol	1039	50	100	200

3.1.1 Gas Testing Using Chilled Liquid

Acetone and ethanol compounds were kept in a glass container and chilled at certain temperature using an RTE-300 Refrigerated Chiller (Neslab, USA). Air was bubbled through each compound and its vapour pressure was calculated using the Antoine vapour pressure equation (Equation 3.1). This equation describes the relation between vapour pressure p (mmHg) and temperature t (°C) for pure components. A, B, and C are component-specific constants for a given temperature range and can be

obtained from Lange's Handbook of Chemistry [30]. The data are shown in Table 3 - 5.

$$\log p = A - \frac{B}{t + C} \tag{3.1}$$

The concentration of the compound can be quantified by calculating the theoretical saturation concentration in the headspace above the liquid as expressed in Equation 3.2.

$$ppm = \frac{p}{760\ mmHg} 10^6 \tag{3.2}$$

Table 3 - 5 Constants for Antoine's vapour pressure equations [30].

Analytes	Temp Range (°C)	A	B	C
Acetone	Liquid	7.11714	1210.595	229.664
Ethanol	-2 – 100	8.32109	1718.1	237.52

Solving for Equation 3.1 and 3.2, concentration of the compound can be modified by changing the chilling temperature and can be reduced further by diluting it with air. Table 3 - 6 shows example calculations for set temperature of each compound at different flow rate to achieve different concentrations.

Table 3 - 6 Calculated concentration of sample vapours.

Sample flow rate (ml/min)			50	100
Total flow rate (ml/min)			300	300
Analytes	**Temp (°C)**	**Conc. (ppth)**	**Conc. of diluted compound (ppth)**	
Acetone	-25.7	19.998	3.333	6.666
Ethanol	-1	15.003	2.500	5.001

3.6 Results and Analysis

Sensors were tested to isobutylene and VOC using both the permeation device and the chilled liquid. The concentration range was obtained in part per billion (ppb) for the permeation device and part per thousand (ppth) for the chilled VOC liquid. The concentration of isobutylene range was obtained in part per million (ppm).

3.6.1 Isobutylene

Sensors were initially tested for isobutylene at 50% relative humidity and to a maximum concentration of 20 ppm. The test was set up at 30 minutes cycle with the flow rate kept at 300 ml/min, alternating between air and isobutylene. The operating temperatures was varied from 200 - 400°C but no response was observed at the tested range as illustrated in Figure 3 - 10. The results from device 1 and device 2 showed sensors operate at similar resistance ranges. However, these sensors were not responsive to ISB at 20 ppm. Here, the resistance of the sensors at 250°C (8 – 11 kOhm) is higher than sensor resistance at 350°C (3 – 5 kOhm). As previously discussed in Chapter 2, this behaviour can be explained based on the adsorption/desorption characteristics of oxygen species formed on the surface of the tungsten oxide. The oxygen species attract electrons from the conducting band and

this creates an electron depleted region (EDL). As a result, a Schottky barrier is formed preventing electric current flow as observed in the increased resistance. That is why at 250°C, the resistance of the sensor is high. Increasing the resistance to 350°C resulted in decreased resistance because at a higher temperature, the adsorbed oxygen species start to desorb and this decreases the surface density of the metal oxide as the electrons are released back into the tungsten oxide. This allows current to flow more freely through the sensor and thus decreased the sensor resistance.

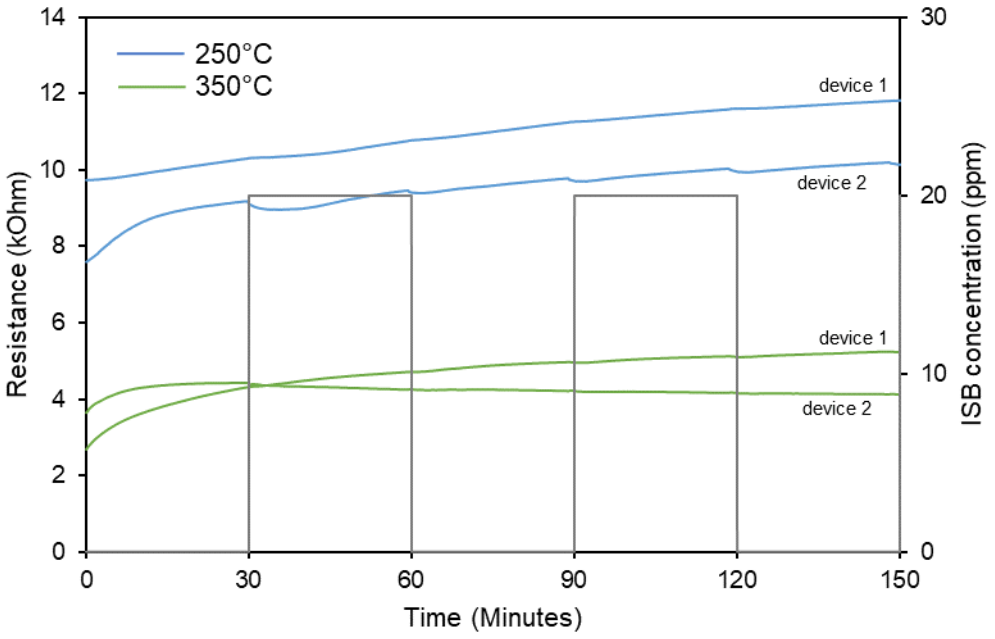

Figure 3 - 10 Sensor response at 20 ppm isobutylene operated at 250°C and 350°C.

The test was repeated with isobutylene at 100 ppm and at 50% relative humidity. Figure 3 - 11 and Figure 3 - 12 shows the response obtained from 2 sensor devices tested at 200- 350°C. Both devices exhibited similar resistance value with a sensor baseline <20 kOhm. As the operating temperature increased, the sensors drifted less and the baseline resistance decreased.

At low temperature, there is not enough energy present to facilitate the adsorption/desorption process. During O_2 exposure, the abstractions of electrons occurs at a slow rate hence the increase is very gradual. When the ISB is introduced to the system, the adsorbed oxygen species desorb off the surface of metal oxide, releasing the electrons back to the conduction band. As this also occurs at a slow rate, the decreased resistance is observed gradually. At this temperature range, sensor drift may be observed due to different rates at which the oxygen species adsorbed and desorbed off the surface. As the operating temperature increases, dissociation of oxygen species is favoured and the adsorption/desorption happens at a higher rate. During O_2 exposure, adsorbed oxygen species withdraw electrons from the conduction band at a higher rate (faster response time) and reach steady state (sensor resistance no longer increases). Likewise, the oxygen species desorb off the surface at a higher rate when ISB is introduced, reaching steady state at which the resistance no longer decreases. Therefore, the shape of the response at lower temperature is more like a triangle which changes to be more like a square by increasing the temperature. This is consistent with the sensor responses as seen in Figure 3 - 11 and Figure 3 - 12. At 200° and 250°C, the responses follows a triangle shape whereas at 300°C and 350°C, the responses are more like a square.

From visual observation, device 1 drifted at temperature 250°C and lower. Whereas device 2 showed less drift for the same temperature. The responses from both sensors are also quite different especially at higher temperatures. At 300°C, the baseline resistance of device 1 is around 14 kOhm whereas device 2 is around 7 kOhm. Similarly, the baseline resistance for device 1 is 9 kOhm and for device 2 is 3 kOhm at 350°C. As the flow rate is kept constant at 300 ml/min, this is unlikely the cause of the variation. The variation in gas distribution of the sensor may occurs, the effect is not significant (as discussed in Section 2.5.2). The difference in response is

more likely contributed to the variation in the microstructure of the sensors. This is further discussed in Section 3.6.3.

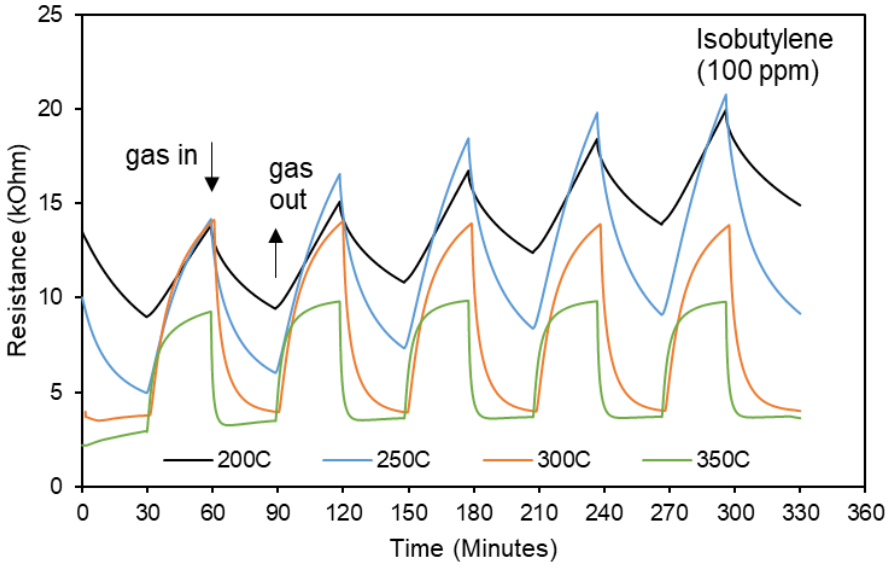

Figure 3 - 11 Sensor response at 100 ppm isobutylene in 50% rh (device 1).

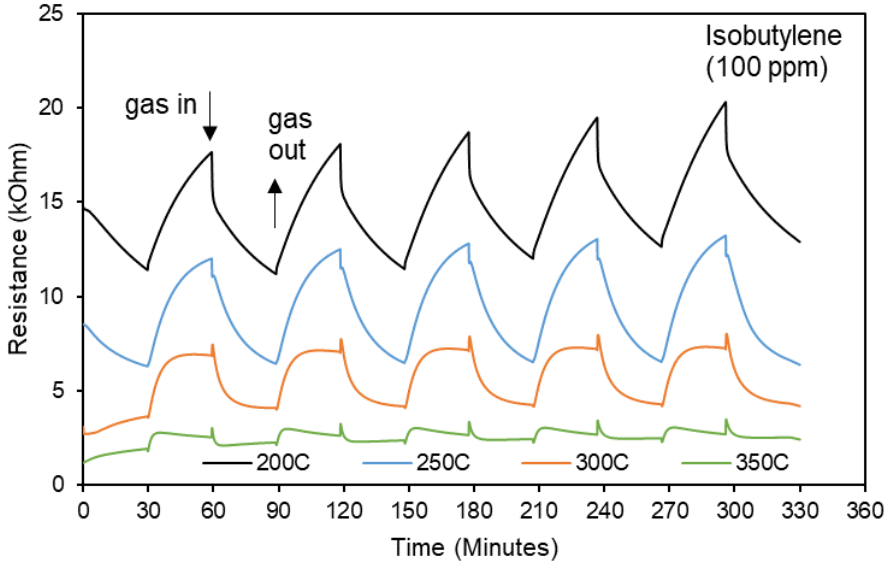

Figure 3 - 12 Sensor response at 100 ppm isobutylene in 50% rh (device 2).

The response and recovery times are important properties for gas sensor performance. In this case exposure toward reducing gas, the response time is defined

as the time required to reach 10% of its steady-state resistance value. Whereas the recovery time is defined outlined as the time needed to obtain 90% of its saturation value when subjected to clean air.

Figure 3 - 13 illustrates sensor recovery and response times for isobutylene response at 100 ppm. Higher operating temperature generally reduced the response time and recovery time. However, the calculation was not done for device 2 at 350°C as the response was not good. The fastest response was obtained at 350°C for device 1 where the response time is 3 minutes and the recovery time 11.9 minutes. These values are not definite. The rate of response can be effected by the flow rate of the gas flowing to the sensors, but these effects should not be significant. These values are particularly useful for guidance on what the response/recovery time to expect when operating the sensors. Furthermore, the flow rate was kept constant at 300 ml/min throughout the tests. Hence, the results obtained is accurate for determining the temperature at which the sensors respond the fastest.

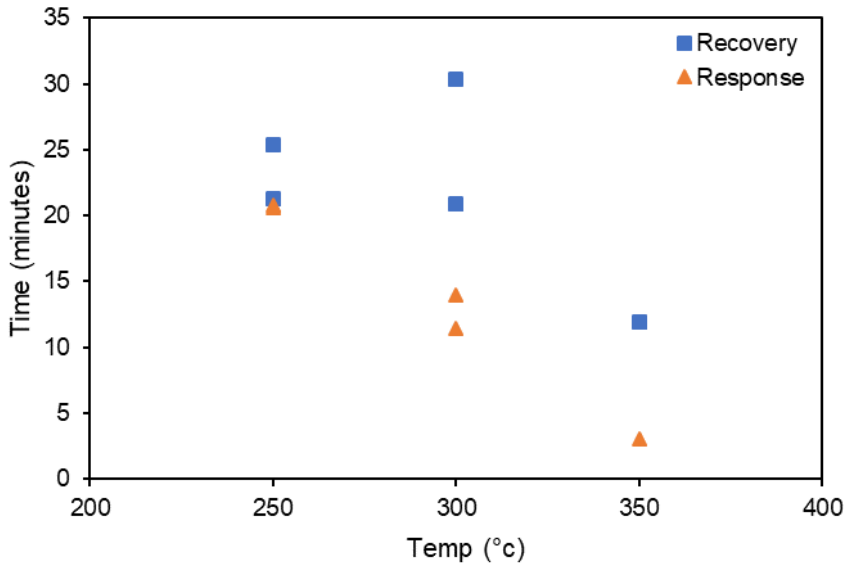

Figure 3 - 13 Response and recovery time for isobutylene response (100 ppm).

The sensor response for reducing gases, defined as $\mathbf{S_r = R_a/R_g}$ where R_a is sensor resistance in reference gas (baseline resistance) and R_g is sensor resistance of the targeted gas in the reference gas, was obtained at $\mathbf{R_a/R_g}$ =**2.8** and shown in Figure 3 - 14.

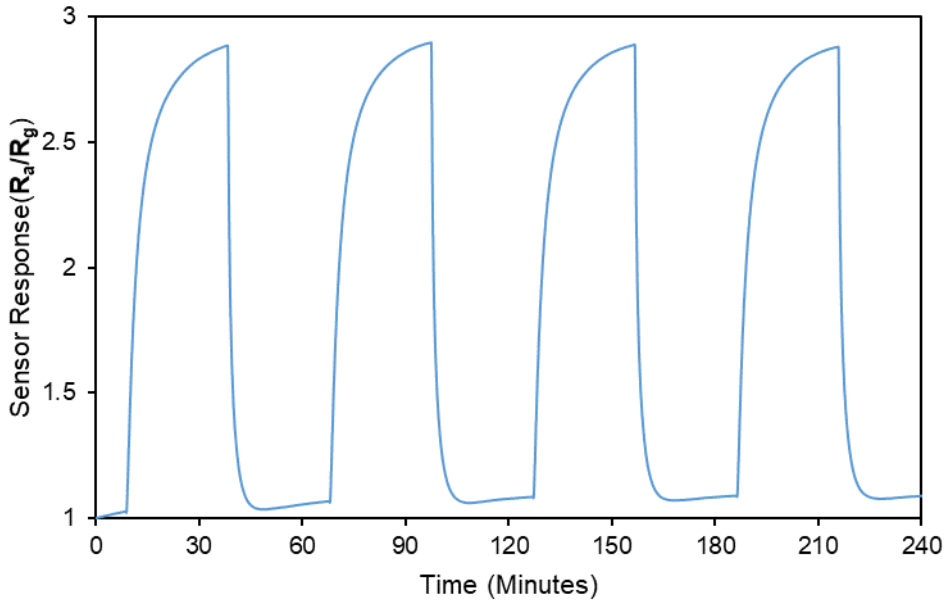

Figure 3 - 14 Sensor response to 100 ppm isobutylene at 350°C.

3.6.2 Low Concentration VOC

Low concentration VOC in ppb level was obtained using a permeation tube. Tests was set at 20-minute cycle periods, alternating between zero air and 20 ppb of ethanol, and operating temperature at 350°C in dry air.

Both sensors showed an almost identical response, as illustrated in Figure 3 - 15 with sensors drifting upwards with more cycles. The response was noted at around 10 kOhm and the baseline resistance was around 12 kOhm which further drifted to 16 kOhm. There may be an imbalance during the adsorption/desorption process causing drifts to occur. The oxygen species adsorbed on the metal oxide when exposed to air may not fully desorb off the surface when air is purged from the surface

as ethanol is introduced to the sensors. Therefore, when the cycle is repeated, more oxygen species are adsorbed, producing an increase in the EDL. As a result, higher resistance (upward drifts) is observed with more cycles.

Drift is not an uncommon issue encountered in metal oxide-based devices. Sensors may experience drifts due to changes of the properties caused by bias induced drift or gradual poisoning of the sensor material, ageing and sensor degradation. Environmental disturbances can also produce changes in sensor responses that further reduce their accuracy in longer period. Considering the importance of chemical sensor stability, sensor drifts have been considerably studied in the past decades to investigate ways to deal with the issue including modelling the systematic changes in sensor responses and applying a correction factor or calibration to mitigate the drift effects [31-36].

Another test was set in dry air at 15 minutes cycle time to detect 10 ppb of ethanol at 350°C. The response illustrated in Figure 3 - 16 shows baseline resistance at around 9.5 kOhm for device 1 and around 4.3 kOhm for device 2. The response of device 2 was similar to the response toward isobutylene, where a shift of peak was observed at the end of each cycle. The test for 20 ppb ethanol was conducted first and then followed by isobutylene test after 4 months. It is possible that during the period, sensors had change properties, particularly for device 2 where sensor response deteriorated.

When sensors are exposed to continuous humid environment, gradual formation of stable chemisorbed OH^- on the surface, resulting in a progressive deterioration of the sensor responsivity. Furthermore, presence of cracks in film morphology (Appendix A) is likely to contribute to sensor deterioration as has been previously reported [37]. Additionally, exposure to high range of VOC concentrations could also

result in sensor deterioration. In this case, the sensor might be accidentally exposed when VOCs were tested in the lab.

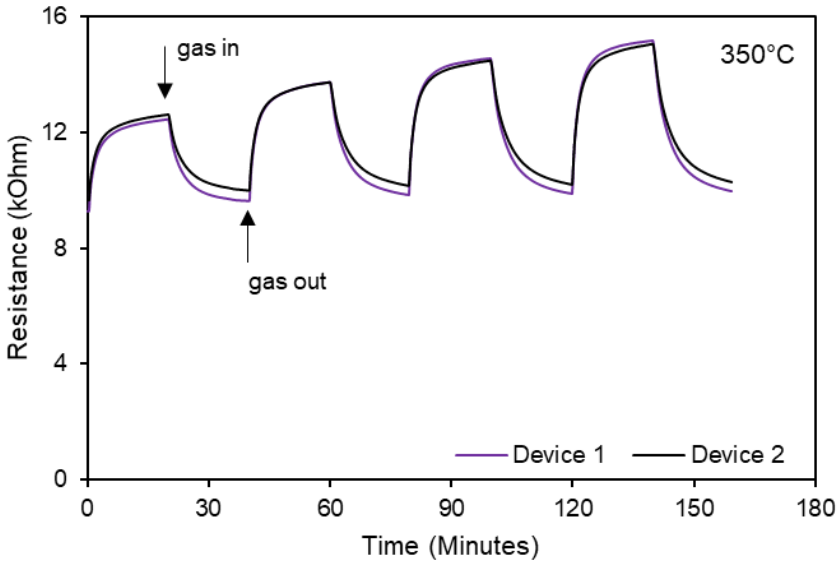

Figure 3 - 15 WO_3 sensor response at 350°C to 20ppb ethanol.

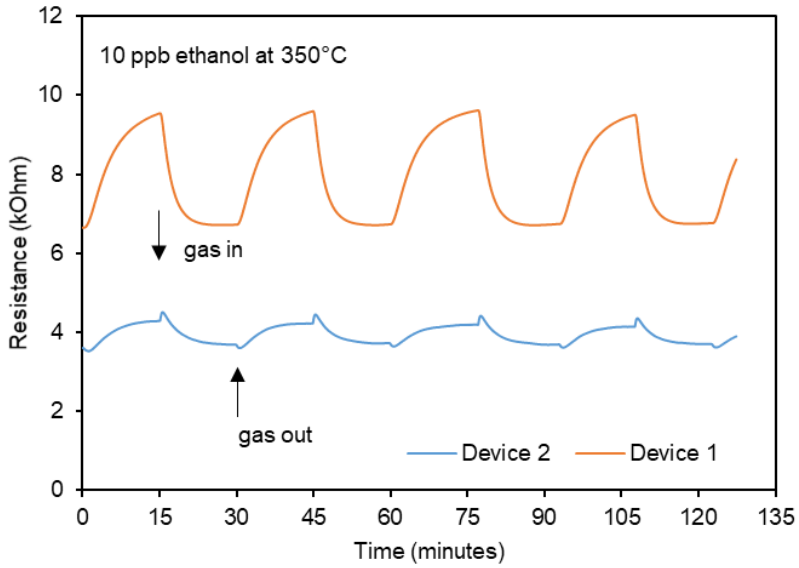

Figure 3 - 16 WO_3 sensor response at 350°C to 10ppb ethanol.

The test was repeated for 5 ppb ethanol with the same setting for device 1 (in dry air at 15 minutes cycle period and at 350°C). The sensor showed similar response

to 5 and 10 ppb ethanol with the baseline resistance reduced to 8.7 kOhm for test with 5 ppb ethanol (Figure 3 - 17).

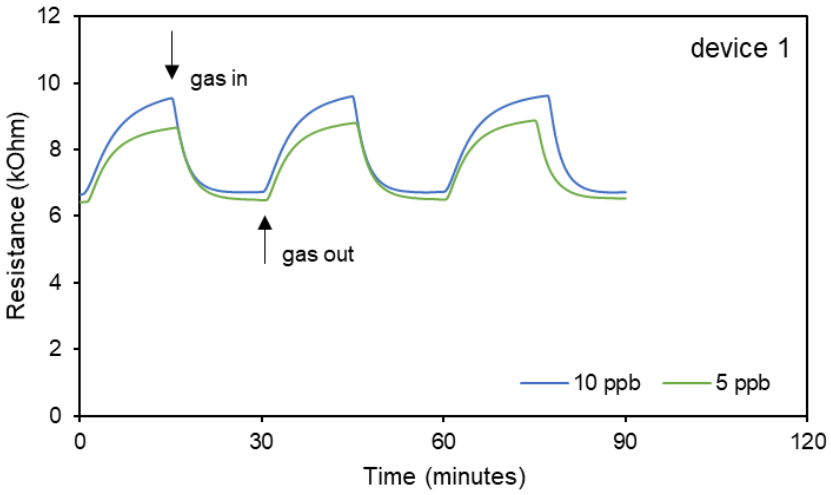

Figure 3 - 17 WO_3 device 1 response at 350°C to 5 and 10ppb ethanol.

Test was also conducted for 20 ppb acetone at 350°C in dry air, keeping the cycle period at 15 minutes. The response as illustrated in Figure 3 - 18 indicated poor selectivity to acetone. In the first run, the baseline resistance was found around 11 kOhm for device 1 and around 4.3 kOhm for device 2. In the second run, the baseline resistance for device 1 plummeted from 11 kOhm to less than 0.5 kOhm (decreased by 95%) whereas for device 2, the resistance dropped to 2.7 kOhm (decreased by 35%). In comparison with sensor performance against ethanol, it can be observed that the sensors reacted poorly to acetone, showing significant inconsistency in sensor response from both device 1 and device 2.

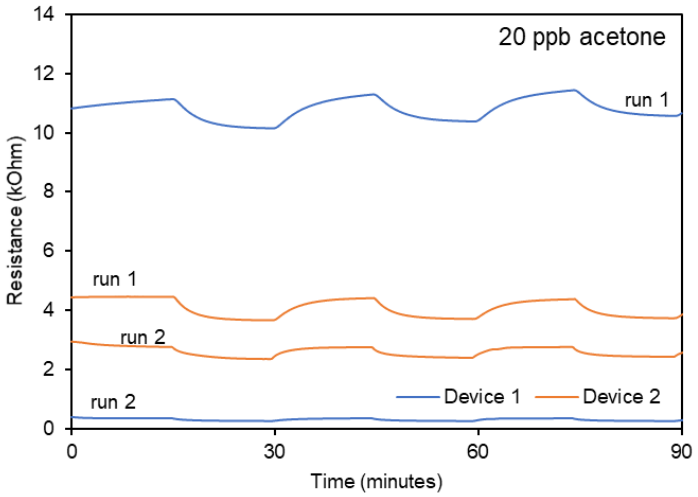

Figure 3 - 18 WO_3 sensor responses at 350°C to 20ppb acetone.

3.6.1. High Concentration VOC

Ethanol was diluted with air using the gas rig apparatus detailed in Chapter 2. The test was set at 30 minutes cycle period, 50% relative humidity, and alternating zero air and 2.5 ppth ethanol. The sensors were operated at 350°C and the response in Figure 3 - 19 showed sensor baseline resistance between 6-7 kOhm for device 1 and at around 4 kOhm for device 2. Whereas the sensor response was noted at 4-5 kOhm (device 1) and between 2-3 kOhm (device 2). No significant drift was observed and second run test showed consistent results.

Adding the concentration steps from 2.5 ppth to 10 ppth using the same setting, Figure 3 - 20 showed similar response from 2 runs. Both sensors showed a slight drift over the cycle and a decrease in resistance as the concentration increased. It can be seen from the graph that the rate of sensor response was faster than the rate of recovery.

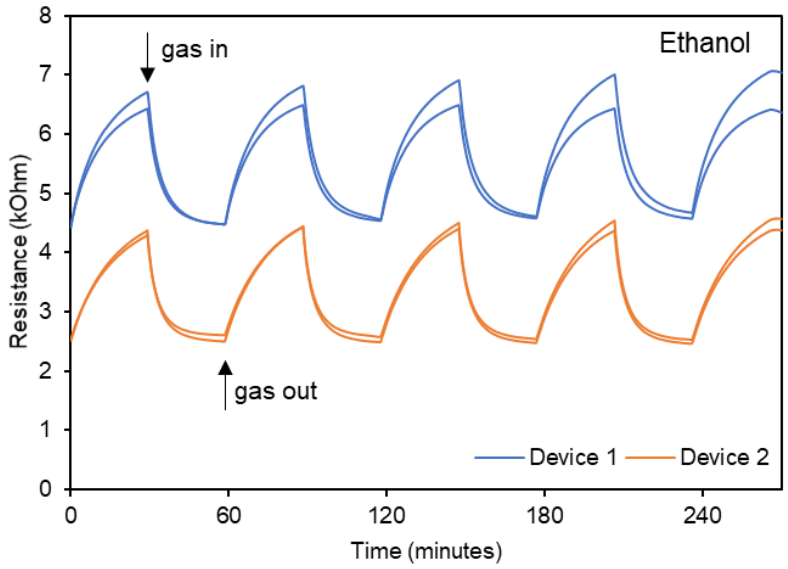

Figure 3 - 19 WO_3 sensor response at 350°C to 2.5 ppth ethanol.

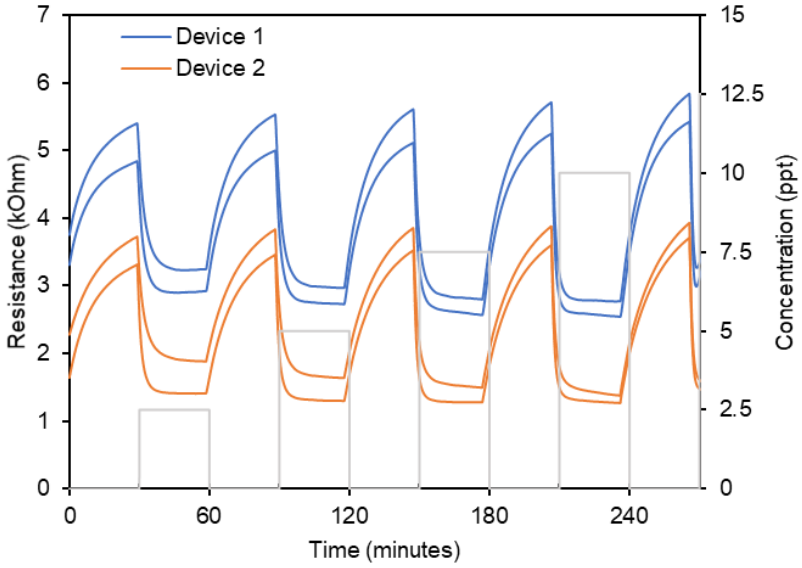

Figure 3 - 20 WO_3 sensor response at 350°C to 2.5-10 ppth ethanol.

Another test was carried out for 5 ppth of ethanol. The response was compared to 2.5 ppth and shown in Figure 3 - 21. Sensors showed consistent baseline resistance at 6-7 kOhm (device 1) and 4-5 kOhm (device 2). As ethanol concentration

changed to 5 ppth, the sensor resistance decreased to around 3.6 kOhm for device 1 and 2 kOhm for device 2.

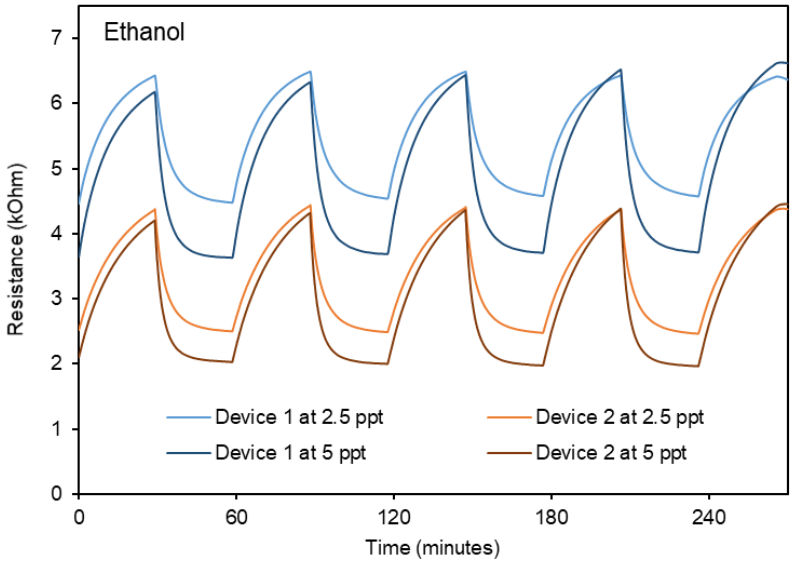

Figure 3 - 21 WO_3 sensor response at 350°C to 2.5 & 5 ppth ethanol.

3.6.3 Sensor Performance

The sensors can detect 100 ppb isobutylene and showed better selectivity to ethanol than acetone. They can detect up to 5 ppb ethanol, which is a much lower concentration than the detection limit of a similar commercial sensor MiCS-5524 (SGXSensortech, Switzerland) at 10 ppm.

Since metal oxide-based gas sensors rely on chemical interaction and influenced by external factors such as humidity, variation in sensor response is inevitable. Commercial MOX VOC sensor (Alphasense, UK) noted a variation up to 20% for its baseline resistance. The baseline resistance was calculated at 6.0 ± 1.2 kOhm for device 1 and 4.5 ± 1.2 kOhm for device 2, which are 20% and 27% variations respectively. The variations of the fabricated sensors are still comparable with a commercial device. However, comparing performance between devices shows a

much higher variation. This is likely due to the 3D printing itself, i.e. the 3D printer cannot produce identical sensing material in term of shape and thickness. Hence, some sensors may work better than the other.

The rate of sensor response improved as the temperature increased. In general, sensors showed faster rate of response than rate of recovery. At 350°C, the sensors recorded 5.1 minutes response time and 5.4 minutes recovery time to 5 ppb ethanol. The rate is considered quite fast compared to previously reported 6 minutes response for 100 ppb acetone and 6 minutes recovery time for 600 ppb acetone using Si-doped WO_3 operated at 400°C [38].

Understanding gas sensing mechanism during gas exposure and recovery can provide a better insight sensor behaviour toward targeted gases. Other factors such as humidity and different fabrication process can also contribute to changes in sensor behaviour. These will be discussed in later sections. Further research is needed to improve sensor performance, but this work has shown a feasibility to fabricate working sensors using FDM, a 3DP technology.

3.7 Conclusion

In this work, tungsten oxide-based sensor has been successfully manufactured by Fused Deposition Modelling (FDM) technique. The sensors can detect 100 ppm isobutylene and up to 5 ppb ethanol. This shows as a proof of principle, it is feasible to 3D print gas sensing materials.

3.8 References

[1] A. M. M. S. Ullah et al., "Comparison between Wooden and Conventional Prototyping:An Eco-Manufacturing Perspective," Dordrecht, 2012, pp. 877-881: Springer Netherlands.

[2] M.-S. Kim, W.-S. Chu, Y.-M. Kim, A. P. G. Avila, and S.-H. Ahn, "Direct metal printing of 3D electrical circuit using rapid prototyping," *International Journal of Precision Engineering and Manufacturing,* journal article vol. 10, no. 5, pp. 147-150, December 01 2009.

[3] S. C. Cox, J. A. Thornby, G. J. Gibbons, M. A. Williams, and K. K. Mallick, "3D printing of porous hydroxyapatite scaffolds intended for use in bone tissue engineering applications," *Materials Science and Engineering: C,* vol. 47, pp. 237-247, 2015/02/01/ 2015.

[4] B. Leukers *et al.*, "Hydroxyapatite scaffolds for bone tissue," *Journal of Materials Science:Materials in Medicine,* vol. 16, pp. 1121-1124, 2005.

[5] Q. Lv, L. Nair, and C. T. Laurencin, "Fabrication, characterization, and in vitro evaluation of poly(lactic acid glycolic acid)/nano-hydroxyapatite composite microsphere-based scaffolds for bone tissue engineering in rotating bioreactors," *J Biomed Mater Res A,* vol. 91, no. 3, pp. 679-91, Dec 2009.

[6] Z. Zhou, F. Buchanan, C. Mitchell, and N. Dunne, "Printability of calcium phosphate: Calcium sulfate powders for the application of tissue engineered bone scaffolds using the 3D printing technique," *Materials Science and Engineering: C,* vol. 38, pp. 1-10, 2014/05/01/ 2014.

[7] S. Murphy and A. Atala, "3D bioprinting of tissues and organs," *Nature Biotechnology,* vol. 32, pp. 773–785, 2014.

[8] S. K. Moon, Y. E. Tan, J. Hwang, and Y.-J. Yoon, "Application of 3D printing technology for designing light-weight unmanned aerial vehicle wing structures," *International Journal of Precision Engineering and Manufacturing-Green Technology,* journal article vol. 1, no. 3, pp. 223-228, July 01 2014.

[9] B. C. Gross, J. L. Erkal, S. Y. Lockwood, C. Chen, and D. M. Spence, "Evaluation of 3D Printing and Its Potential Impact on Biotechnology and the Chemical Sciences," *Analytical Chemistry,* vol. 86, no. 7, pp. 3240-3253, 2014/04/01 2014.

[10] F. C. Godoi, S. Prakash, and B. R. Bhandari, "3d printing technologies applied for food design: Status and prospects," *Journal of Food Engineering,* vol. 179, pp. 44-54, 2016/06/01/ 2016.

[11] M. Lille, A. Nurmela, E. Nordlund, S. Metsä-Kortelainen, and N. Sozer, "Applicability of protein and fiber-rich food materials in extrusion-based 3D printing," *Journal of Food Engineering,* vol. 220, pp. 20-27, 2018/03/01/ 2018.

[12] J. Sun, Z. Peng, W. Zhou, J. Y. H. Fuh, G. S. Hong, and A. Chiu, "A Review on 3D Printing for Customized Food Fabrication," *Procedia Manufacturing,* vol. 1, pp. 308-319, 2015/01/01/ 2015.

[13] J. Sun, W. Zhou, L. Yan, D. Huang, and L.-y. Lin, "Extrusion-based food printing for digitalized food design and nutrition control," *Journal of Food Engineering,* vol. 220, pp. 1-11, 2018/03/01/ 2018.

[14] R. Melnikova, A. Ehrmann, and K. Finsterbusch, "3D printing of textile-based structures by Fused Deposition Modelling (FDM) with different polymer materials," *IOP Conference Series: Materials Science and Engineering,* vol. 62, no. 1, p. 012018, 2014.

[15] Y. L. Yap and W. Y. Yeong, "Additive manufacture of fashion and jewellery products: a mini review," *Virtual and Physical Prototyping,* vol. 9, no. 3, pp. 195-201, 2014/07/03 2014.
[16] M. Korger, J. Bergschneider, M. Lutz, B. Mahltig, K. Finsterbusch, and M. Rabe, "Possible Applications of 3D Printing Technology on Textile Substrates," *IOP Conference Series: Materials Science and Engineering,* vol. 141, no. 1, p. 012011, 2016.
[17] C. E. Dombroski, M. E. R. Balsdon, and A. Froats, "The use of a low cost 3D scanning and printing tool in the manufacture of custom-made foot orthoses: a preliminary study," *BMC Research Notes,* vol. 7, no. 1, p. 443, 2014/07/10 2014.
[18] J. Karoly, N. Cyrille, M. Francoise, M. Keith, V.-N. Gordana, and F. Gabor, "Tissue engineering by self-assembly and bio-printing of living cells," *Biofabrication,* vol. 2, no. 2, p. 022001, 2010.
[19] V. Liu Tsang and S. N. Bhatia, "Three-dimensional tissue fabrication," *Advanced Drug Delivery Reviews,* vol. 56, no. 11, pp. 1635-1647, 2004/09/22/ 2004.
[20] C. P. Purssell, "Materials and Methods for Microstereolithography," PhD Thesis or Dissertation (PhD), School of Engineering, University of Warwick University of Warwick Publications service & WRAP, 2012.
[21] L. Rui, D. Haiyan, L. Jian, S. Fangping, C. Zheng, and Z. Ting, "Fabrication of platinum-decorated single-walled carbon nanotube based hydrogen sensors by aerosol jet printing," *Nanotechnology,* vol. 23, no. 50, p. 505301, 2012.
[22] R. Vyas *et al.*, "Inkjet Printed, Self Powered, Wireless Sensors for Environmental, Gas, and Authentication-Based Sensing," *IEEE Sensors Journal,* vol. 11, no. 12, pp. 3139-3152, 2011.
[23] P. J. Bártolo, *Stereolithography*. Springer New York Dordrecht Heidelberg London, 2011.
[24] H. Chia and B. Wu, "Recent advances in 3D printing of biomaterials," (in English), *Journal of Biological Engineering,* vol. 9, no. 1, pp. 1-14, 2015/03/01 2015, Art. no. 4.
[25] X. Zhang, X. N. Jiang, and C. Sun, "Micro-stereolithography of polymeric and ceramic microstructures," *Sensors and Actuators A: Physical,* vol. 77, no. 2, pp. 149-156, 10/12/ 1999.
[26] S. Bose, S. Vahabzadeh, and A. Bandyopadhyay, "Bone tissue engineering using 3D printing," *Materials Today,* vol. 16, no. 12, pp. 496-504, 2013/12/01/ 2013.
[27] N. Guo and M. Leu, "Additive manufacturing: technology, applications and research needs," (in English), *Frontiers of Mechanical Engineering,* vol. 8, no. 3, pp. 215-243, 2013/09/01 2013.
[28] S. Kumar, "Selective laser sintering: A qualitative and objective approach," (in English), *JOM,* vol. 55, no. 10, pp. 43-47, 2003/10/01 2003.
[29] Owlstone. (2017, 15 September). Available: https://www.owlstoneinc.com/products/v-ovg/
[30] N. A. Lange and J. A. Dean, *Lange's Handbook of chemistry* (no. v. 12). McGraw-Hill, 1979.
[31] A. C. Romain and J. Nicolas, "Long term stability of metal oxide-based gas sensors for e-nose environmental applications: An overview," *Sensors and Actuators B: Chemical,* vol. 146, no. 2, pp. 502-506, 2010/04/29/ 2010.
[32] G. Korotcenkov and B. K. Cho, "Instability of metal oxide-based conductometric gas sensors and approaches to stability improvement (short

survey)," *Sensors and Actuators B: Chemical,* vol. 156, no. 2, pp. 527-538, 2011/08/01/ 2011.
[33] G. Korotcenkov, "Metal oxides for solid-state gas sensors: What determines our choice?," *Materials Science and Engineering: B,* vol. 139, no. 1, pp. 1-23, 2007/04/25/ 2007.
[34] G. Korotcenkov and B. K. Cho, "Metal oxide composites in conductometric gas sensors: Achievements and challenges," *Sensors and Actuators B: Chemical,* vol. 244, pp. 182-210, 2017/06/01/ 2017.
[35] J. Fonollosa, L. Fernández, A. Gutiérrez-Gálvez, R. Huerta, and S. Marco, "Calibration transfer and drift counteraction in chemical sensor arrays using Direct Standardization," *Sensors and Actuators B: Chemical,* vol. 236, pp. 1044-1053, 2016/11/29/ 2016.
[36] A. C. Romain, P. André, and J. Nicolas, "Three years experiment with the same tin oxide sensor arrays for the identification of malodorous sources in the environment," *Sensors and Actuators B: Chemical,* vol. 84, no. 2, pp. 271-277, 2002/05/15/ 2002.
[37] G. Korotcenkov, B. J. S. Cho, and A. B. Chemical, "Instability of metal oxide-based conductometric gas sensors and approaches to stability improvement (short survey)," vol. 156, no. 2, pp. 527-538, 2011.
[38] M. Righettoni, A. Tricoli, and S. E. Pratsinis, "Si:WO3 Sensors for Highly Selective Detection of Acetone for Easy Diagnosis of Diabetes by Breath Analysis," *Analytical Chemistry,* vol. 82, no. 9, pp. 3581-3587, 2010/05/01 2010.

Chapter 4. AACVD Grown Tungsten Oxide Based Thin Film Sensors

4.1 Introduction

Chemical vapour deposition (CVD) has been in development since 1960s and is now a mature and reliable manufacturing process. In its early development era, this method was used to make carbon black pigment from the soot in a furnace. It was later used to produce cheaper and reliable light bulbs from tungsten filaments, which lasted longer and gave brighter light than carbon filaments. CVD technology has been used in several industrial sectors including semiconductor and ceramic industry. The advantages of chemical vapour deposition include good conformality in thickness uniformity, wide range of chemical precursors, and relatively low deposition temperature. It also allows adjustable deposition rates and the process can be used to control the crystal structure, stoichiometry, surface morphology, and orientation of the CVD manufactured products. However, the method can be quite complex and chemical precursors may present health and safety hazard if not handle appropriately.

This chapter describes the fabrication process of metal oxide sensors using a specific type of chemical vapour deposition technique. The first section explains about chemical vapour deposition and some of its variants. The next section covers the sensor fabrication process followed by material characterisation of the sensing material. The last section presents gas testing results and analysis of sensor performance.

4.2 Chemical Vapour Deposition (CVD)

Chemical vapour deposition is a process used to deposit thin films onto substrates through chemical reactions in the vapour phase. In CVD, reactant/precursor gases are delivered into a reaction chamber, at a certain temperature, where they come in contact with a heated substrate and react to form a thin layer on the surface of the substrate.

The steps involved in a CVD process, shown in Figure 4 - 1, are summarised in the following [1]:

1. Reactant gaseous are transported into the reaction chamber.
2. Reactant species diffuse through the boundary layer and/or undergo reactions forming intermediate species.
3. Adsorption of reactants or intermediates on the substrate surface.
4. Surface diffusion, heterogenous reactions take place which produces the deposit and by-product species.
5. The deposits diffuse and form crystallisation centre leading to film growth.
6. Desorption and diffusion of by-product species.
7. Mass transport of by-product species away from the substrate.

The film growth rate and composition are determined by parameters such as pressure, temperature, and reactant concentration. When CVD processes are carried at atmospheric pressure, parameters such as substrate temperature, gas flow rate and viscosity affect the growth rate and film microstructure. CVD carried out in low pressure (<1 atm) can reduce the hydrodynamics dependence in the CVD reactor and chemical reactions become a more crucial factor for the film characteristics [2].

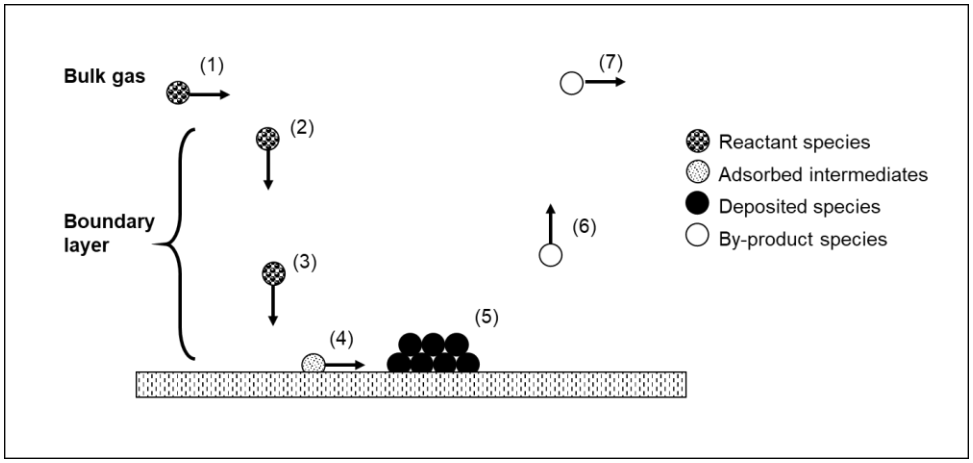

Figure 4 - 1 Schematic of CVD process. Adapted and redrawn from [1].

Operating temperature determines the deposition mechanism. At lower temperatures, the deposition mechanism is governed by the kinetics of the chemical reactions. Increasing the temperature leads to an increase in the deposition rate. At higher temperatures, surface kinetics becomes so rapid that it is limited by reactants diffusion (mass transport limited). In this range, the deposition rate almost becomes independent of temperature. Increasing the temperature even higher may decrease the deposition rate as the reactants deplete and/or desorption rate increases. At increasingly high temperatures, homogeneous gas phase reactions will take place in addition to the heterogeneous reactions. This will interrupt the growth of coating and often lead to poorly adherent films with a non-uniform or porous microstructure [2].

A wide range of CVD deposition techniques are available which can be classified by certain parameter such as:

- Pressure: CVD can be carried out at atmospheric pressure (APCVD) [3-5] at lower pressure (LPCVD) [6-10] or at ultrahigh vacuum (UHVCVD) [11, 12].
- Vapour physical characteristics: the precursors are transported in form of liquid (MLICVD) or through aerosol (AACVD) [13-16].

- Substrate heating: the reaction chamber can be either a hot wall or a cold wall CVD.

Other variants of CVD include thermally activated CVD (TACVD) and plasma enhance CVD (PECVD) which uses light and plasma, respectively, to activate the chemical reactions. Metalorganic CVD (MOCVD) [10, 17-19] uses metalorganic as the precursor and combustion chemical vapour deposition (CCVD) is another variant that uses a flame-based technique to deposit thin films. Some of the variants are discussed in the following sub-sections.

4.2.1 Thermally Activated Chemical Vapour Deposition (TACVD)

Thermally activated CVD (TACVD) is a conventional CVD process that uses thermal energy to initiate the chemical reactions in a cold or hot wall reactor using inorganic chemical precursors. The reactants can be activated in the form of infrared radiation, r.f. heating, or resistive heating in the vicinity of the heated substrate and undergo chemical reactions to form a film on the substrate. It can operate at atmospheric temperature (APCVD), at low pressure in range of 0.01 – 1.33 kPa (LPCVD), and at ultrahigh vacuum less than 10^{-4} kPa (UHVCVD).

4.2.2 Aerosol Assisted Chemical Vapour Deposition (AACVD)

Aerosol assisted chemical vapour deposition is another variant of CVD process that delivers the precursors in form of liquid droplets/ aerosol. The precursors come in liquid form and can be prepared by dissolving solid or liquid chemical in solvent. The droplets are generated using an ultrasonic atomiser, electrostatic generator, or electrospraying method and then transported into a reactor where the reactants undergo chemical reaction.

Droplets size can vary depending on the method used to generate the aerosol. Ultrasonic aerosol generator uses piezoelectric transducer to create a high frequency vibration to produce tiny droplets. Electrostatic generator method applies electrical charge after using the ultrasonic to create fine droplets. Whereas the electrospraying method involves applying electrical potential to a nozzle which leads to the formation of fine droplets.

AACVD offer several advantages in comparison with conventional CVD methods. It omits the need to use bubbler/vaporiser, hence it is an easier delivery method. It can also be carried out at atmospheric pressure rather than in vacuum and so the cost is relatively low. The deposition times is relatively short as it allows rapid formation of the deposited phases [15]. Furthermore, it uses single-source precursors to overcome nonstoichiometric films due to multisource precursors [20].

The CVD technique employed to fabricate thin films was AACVD carried out at atmospheric temperature, in collaboration with Prof. Chris Blackman and Yiyun Zhu from University College London (UCL).

4.3 Synthesis of Metal Oxide Films

AACVD was used to deposit tungsten oxide-based films onto glass and ceramic substrates. Two type of sensors were fabricated, i.e. pure tungsten-oxide and silver decorated tungsten-oxide films. The precursors were silver nitrate [$AgNO_3$] (≥99.0%) and tungsten hexacarbonyl [$(W(CO)_6)$] (≥97.0%), purchased from Scientific Laboratory Supplies and Sigma-Aldrich respectively. They were used without any purification process and initially grew on glass substrates to investigate how reaction condition parameters affect the material morphologies.

Tungsten oxide films were deposited on a glass substrate of 25 x 50 mm using settings previously described [13, 21]. The substrate was cleaned with isopropanol and acetone before placed inside the reactor preheated at 375°C. Tungsten hexacarbonyl of 0.06 g, 0.17 mmol was dissolved in a 15-ml mixed solution of 2:1 acetone and methanol (Sigma-Aldrich, ≥ 99.6 %). The tungsten solution was sonicated for 5 minutes and then transferred to a glass flask. Using an ultrasonic atomizer/ humidifier Liquifog 2 (Johnson Matthey, UK), the precursor solution was generated to aerosol droplets, which then transported to the heated glass substrate by a nitrogen gas flow at 300 ml/min. Under these conditions, the time needed to transport the entire volume of the droplets, i.e. the deposition time, was between 30 and 40 minutes. The reactor was then allowed to cool down to room temperature once the precursor solution has been used up. Annealing of the samples was carried out in air at 500°C for 2 hours, heated from room temperature at 10 °C/min before cooled down to room temperature subsequently.

Silver decorated tungsten oxide thin films were fabricated by an additional deposition of silver on top of the tungsten oxide layer. First, tungsten oxide was deposited onto the glass substrate using the same method and setting as previously described. Second, the silver precursor solution consisted of $AgNO_3$ [0.06 g, 0.35 mmol], 10 ml acetone (Sigma-Aldrich, ≥ 99.6 %) and 5 ml methanol (Sigma-Aldrich, ≥ 99.6 %) was aerosolised before deposited at 350°C on via a nitrogen carrier (300 ml/min flow rate). Deposition was also carried out at other temperatures, i.e. 200, 250, and 300°C to investigate how it may influence the morphology of silver decorations.

Once the optimised operating temperature had been obtained, the process was repeated to deposit the thin films on alumina substrate with gold electrodes on the surface and a platinum heater on the reverse (sourced from Alphasense, UK). The

electrodes consist of 4 interdigitated pair with a track and spacing of 140 µm and 80 µm respectively. The platinum heater provides a resistance of 10 ±1.5 Ohm at room temperature. The sensor array is illustrated in Figure 4 - 2.

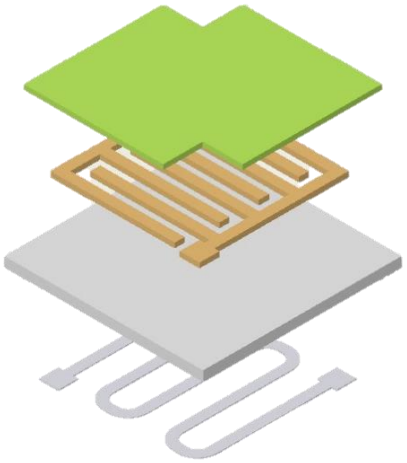

Figure 4 - 2 Sensor array (from top to down: sensing material, electrodes, alumina substrate, heater).

The fabricated sensors were classified into 3 types, plain WO_3 sensor, Ag/Ag_2O -WO_3 sensor with 0.06g $AgNO_3$ precursor (31% Ag content), and Ag/Ag_2O-WO_3 sensor with 0.09g $AgNO_3$ precursor Ag/Ag_2O-WO_3 (38% Ag content). After the deposition process had been completed, the sensors were then welded to TO5 housing and ready for testing.

4.4 Material Characterisation

Silver layer of Ag WO_3 thin films were deposited at various temperatures to examine its effect on the morphology of the sensing material. Deposition temperature is known to influence the nucleation and growth kinetics of the material, which in turn may affect the material microstructure as previously demonstrated [14, 16]. The thin films were characterised by X-ray diffraction (XRD), scanning electron microscopy

(SEM), and X-ray photoelectron spectroscopy (XPS). Supporting information on material characterisation of the sensing layer deposited on glass substrate is available in Appendix B.

Figure 4 - 3 shows the XRD pattern of Ag-WO_3 thin films grown at different temperatures. No distinct peak was observed at temperature 350°. A single peak of Ag was observed in the remaining XRD patterns corresponding to (111) plane. With an increase in growth temperature from 200 to 350°C, the intensity of (111) diffraction peak decreased. This means lower temperature is favoured for growing the Ag layer. The most intense XPD peak was observed on thin films grown at 200°C and 250°C. However, it was found that the precursor $AgNO_3$ deposited at 200°C was too thin. Therefore, the optimum growth temperature was determined at 250°C and used as the temperature for depositing the silver layer onto the alumina substrate.

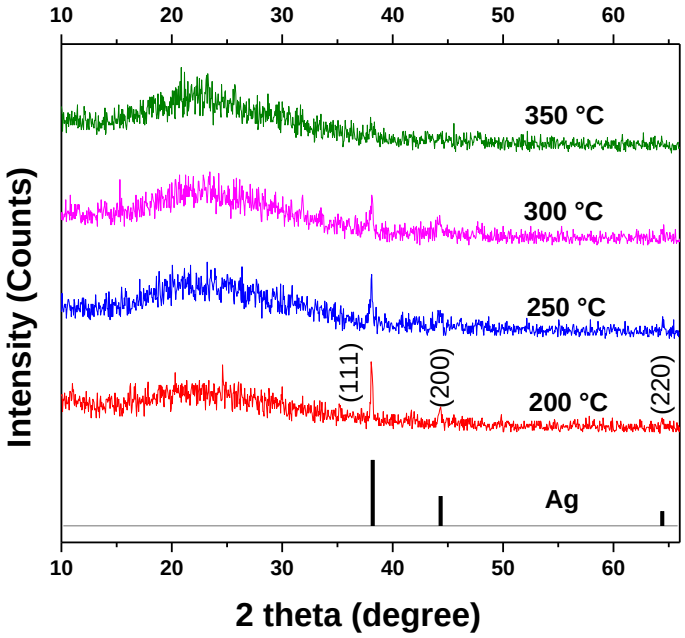

Figure 4 - 3 XRD pattern of Ag thin films grown under different substrates temperature compared to standard pattern of metal Ag (JCPDS, 87-0718).

As the optimised growth temperature was determined at 250°C, this temperature was used to deposit the Ag/Ag_2O layer on top of WO_3 layer to produce Ag/Ag_2O-WO_3 thin film. After deposition, XRD analysis of Ag/Ag_2O-WO_3 grown on alumina substrate in Figure 4 - 4 showed the presence of peaks associated with tungsten oxide, suggested the formation of the monoclinic phase (γ-WO_3 structure, $P2_{1/n}$, a = 7.30084(7), b = 7.53889(7), c = 7.68962(7) Å, β = 90.892(1)°) with strong preferred orientation in the (002) plane and peaks associated with the alumina substrate. The peaks present in WO_3 film (red line) and Ag/Ag_2O-WO_3 film are almost identical. No peaks associated with silver or silver oxide were observed in the silver decorated samples. This means silver might not be deposited in the Ag/Ag_2O-WO_3 film. However, it is more likely that that the decoration was present in the sample, but the peaks were not detected by the XRD instrument due to the small size and/or relatively low amount of decoration present. Another materials characterisation, i.e. XPS, was also carried out. Using XPS analysis, the silver/silver oxide decoration was detected in the sample.

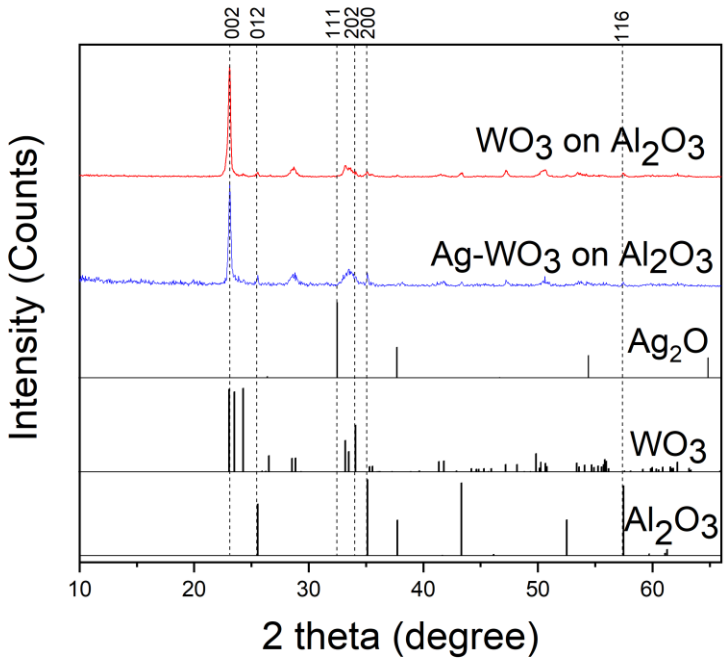

Figure 4 - 4 XRD patterns of WO_3 and Ag/Ag_2O-WO_3 deposited films on Al_2O_3 substrate.

XPS analysis as shown Figure 4 - 5 was used to study the oxidation states and impurity levels of the annealed WO_3 samples. Analysis of W 4f core-level spectrum from pure WO_3 sample showed identical result with Ag/Ag_2O-WO_3 sample. The W 4f spectrum showed the presence of two intense peaks centred at 35.5 and 37.6 eV associated with the W $4f_{7/2}$ and W $4f_{5/2}$ doublets respectively. These binding energies are similar with reference values for stoichiometric WO_3 with the oxidation state W^{6+} [22]. Figure 4 - 5 (right) displays the XPS of Ag 3d core level spectrum where two intense peaks can be observed at 367.7 and 373.6 eV associated with the Ag $3d_{5/2}$ and Ag $3d_{3/2}$ respectively. The highest intensity peak (Ag $3d_{5/2}$) corresponds to Ag_2O and the absence of a loss peak confirms the assignment [23].

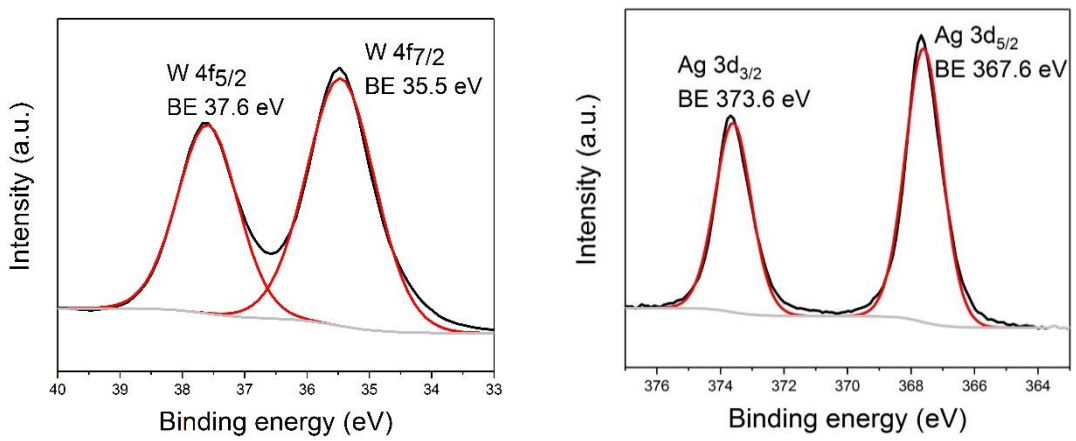

Figure 4 - 5 XPS scans of W 4f core-level spectra of $AgWO_3$ on Al_2O_3 (left) and 3d Ag core-level spectra of $AgWO_3$ on Al_2O_3 (right).

SEM images in Figure 4 - 6 illustrate the morphology of Ag/Ag_2O decorated WO_3 thin film. The films exhibited nanoneedles structure previously observed for tungsten oxide deposited [24, 25] under these conditions. The nanoneedles were about ~1300 nm long with diameters varied between 100 and 200 nm. The film displayed a quite porous body structure, which is desirable in gas sensing application as it can facilitate gas adsorption.

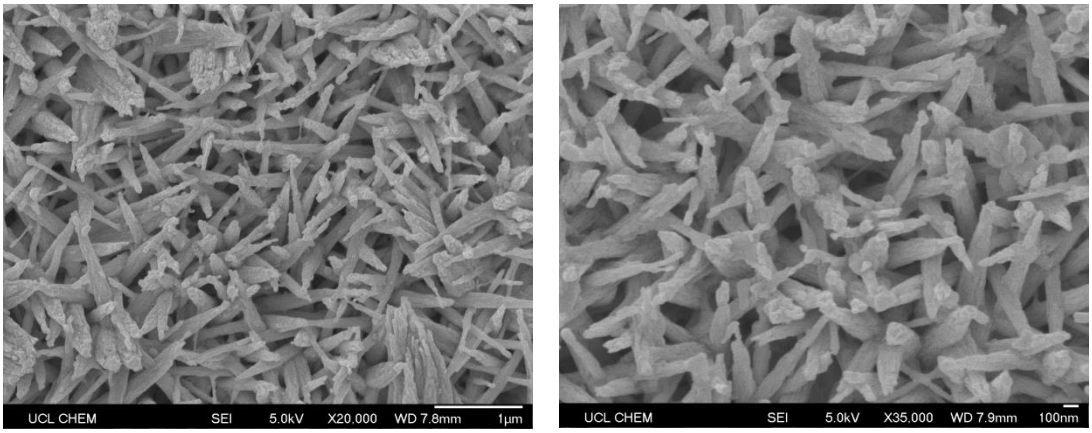

Figure 4 - 6 SEM images of Ag-WO_3 thin film on Al_2O_3 substrate grown at 250°C.

Details on the morphological features of Ag/Ag_2O-WO_3 were further examined by HR-TEM. The images in Figure 4 - 7 (a) display the presence of well-dispersed nanoparticles along the surface of WO_3 nanoneedles, similar with the ones seen for gold and palladium functionalized WO_3 NNs [16, 26]. Cubic Ag_2O can also be confirmed from the fringe image (Figure 4 - 7 (b)) alongside Ag metal. The combined XPS and TEM analysis suggest the particles observed are an Ag/Ag_2O 'core-shell', e.g. an Ag core where the air-exposed faces are oxidised to Ag_2O, although the absence of satellite peaks for Ag metal in the XPS analysis suggests the shell must be thicker than ~ 2 nm.

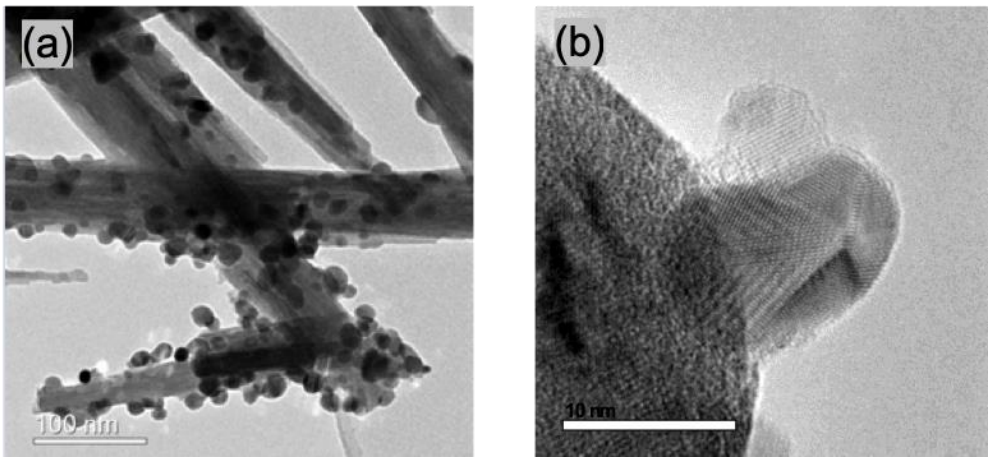

Figure 4 - 7 The HR-TEM images of Ag/Ag_2O-WO_3 samples.

4.5 Gas Testing

Fabricated sensors were investigated for use in oxygen sensing applications. The tests were carried out using a gas handling apparatus previously explained in Chapter 2. Measurements were carried out in humid environment (~85% relative humidity) with a 30-minute cycle period to detect oxygen ranging from 0 to 20% concentration. Sensor temperatures were varied from 150°C to 400°C to determine the optimum operating temperature where sensors exhibit the highest response for each type. This is expressed as R_g/R_a where R_a is the sensor baseline resistance in reference gas N_2 and R_g is the sensor resistance of targeted gas O_2 in reference gas.

4.5.1 WO_3 Thin Film

WO_3 thin films responded to oxygen changes at temperature ≥200°C but no response was observed at 150°C as illustrated in Figure 4 - 8 and Figure 4 - 9. Increasing operating temperature reduced the sensor baseline resistance (in 0% O_2) from ≥200 kOhm at 150°C to ≤60 kOhm at 400°C. The highest sensitivity was found to be **R_g/R_a= ~6** at 400°C as indicated in Figure 4 - 11. The response and recovery time were 10 and 12 minutes respectively.

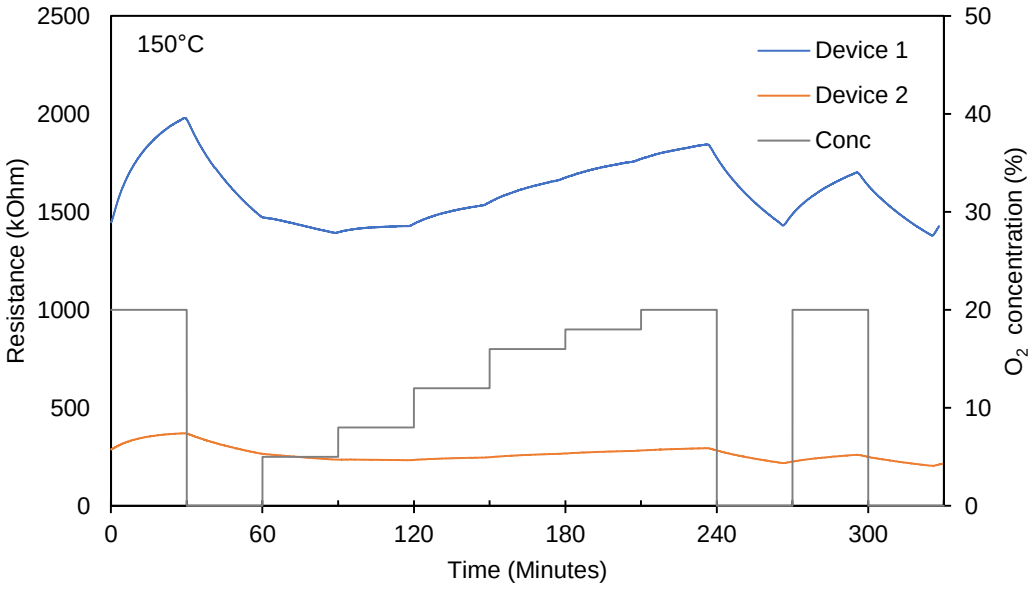

Figure 4 - 8 WO_3 dynamic response at different O_2 concentration at 150°C.

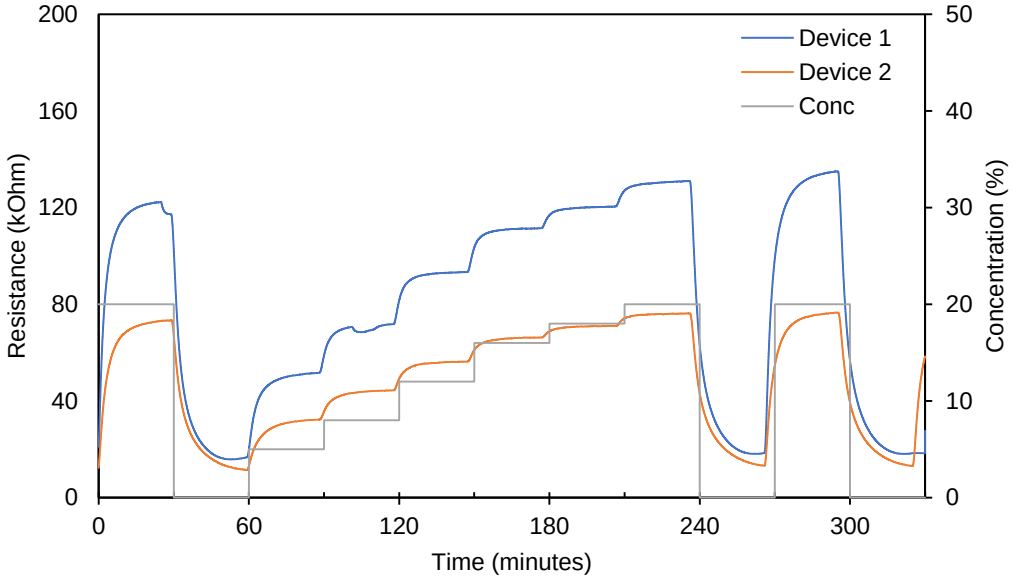

Figure 4 - 9 WO_3 dynamic response at different O_2 concentration at 350°C.

4.5.2 Ag/Ag_2O-WO_3 Thin Film (31% Ag Content)

For Ag-WO_3 thin film tested under the same condition, the sensor also showed no response at temperatures ≤200°C. Sensor baseline resistance was around

150kOhm at 150°C which decreased to about 10kOhm at 400°C. Figure 4 - 10 compares baseline resistance (0% O_2) and sensor response (20% O_2), indicating sensor with silver loading exhibited higher conductivity. Ag/Ag_2O-WO_3 sensor also had a higher response at about $\mathbf{R_g/R_a=8}$ at 400°C than WO_3 films at $\mathbf{R_g/R_a= 6}$. The response time and recovery time for the sensor were at 9 minutes.

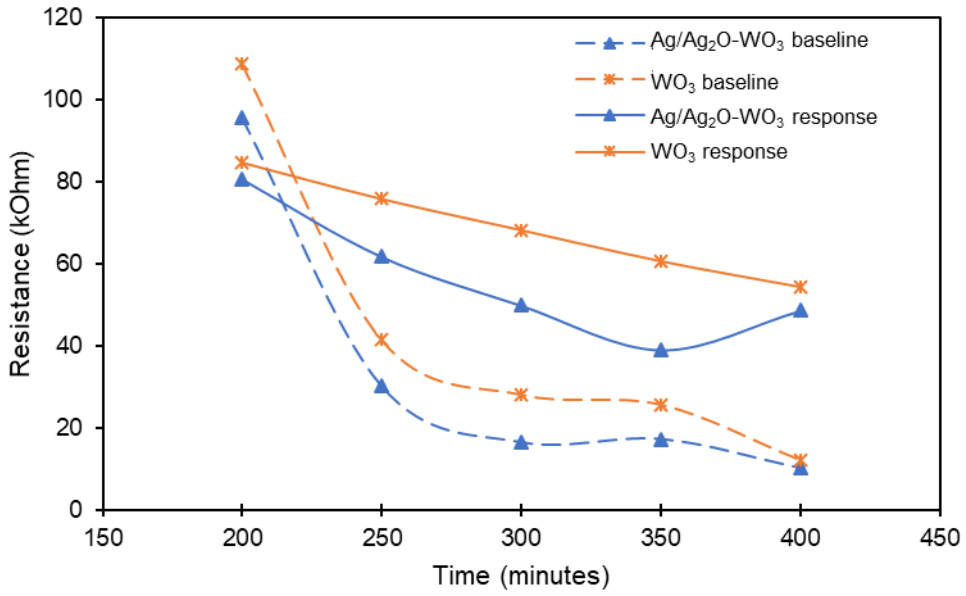

Figure 4 - 10 Baseline resistance and response comparison between WO_3 and $AgWO_3$ sensor. Information on the data is in Appendix B.

4.5.3 Ag/Ag_2O -WO_3 Thin Film (38% Ag Content)

All sensors showed a good response to oxygen at temperatures ≥200°C with the optimum operating temperature obtained at 350°C and the best response calculated at $\mathbf{R_g/R_a=23.}$ This number is 4x higher compared to the sensors with no silver loading where the best response was calculated at R_g/R_a=~6 at 400°C**.** This number showed that the presence of silver decoration can be effective in increasing sensor response.

The response and recovery rate were both found at 9 minutes. Comparing sensor dynamic performance as seen in Figure 4 - 12, sensors with no Ag loading

showed the highest resistance, both in baseline value and response value. Addition of silver increased conductivity and lowered optimum operating temperature, which would contribute to lower power consumption.

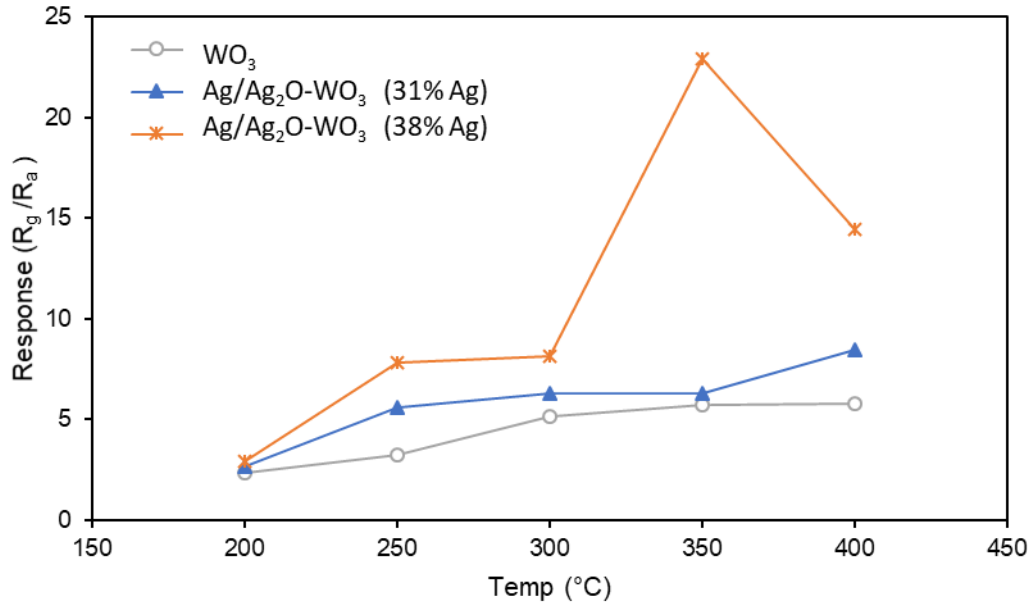

Figure 4 - 11 WO_3 based sensor responses at different temperature.

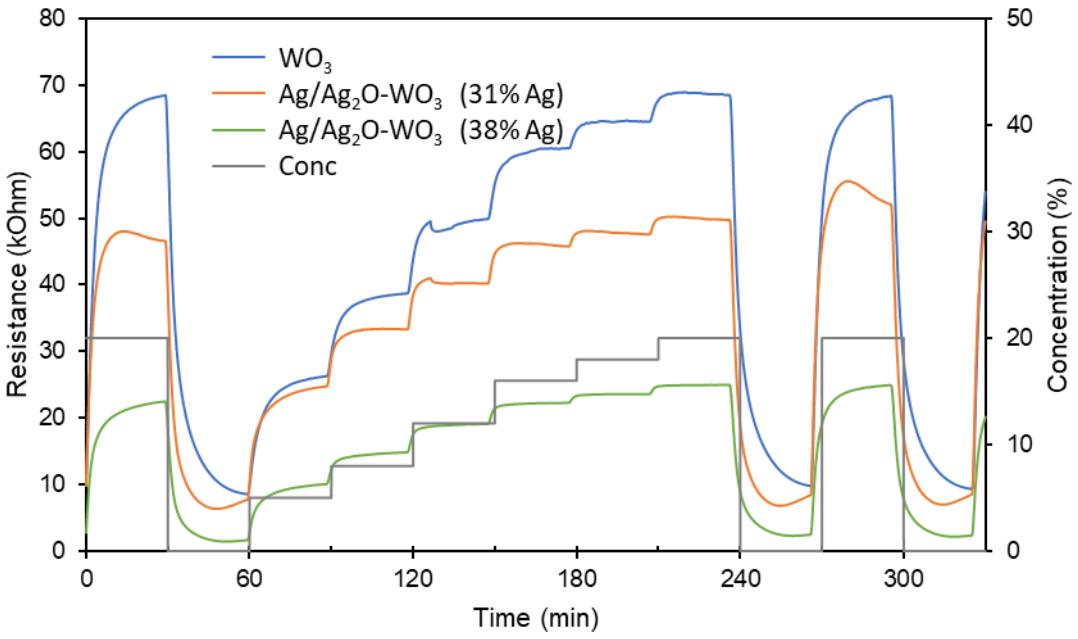

Figure 4 - 12 Dynamic response of WO_3 based sensors with different Ag/Ag_2O loading.

4.6 Analysis and Discussion

The dynamic response of the sensors showed a stable and reversible behaviour. No drift was observed and sensors resistance returned to the same value before and after oxygen exposure.

The fabricated sensor showed no response at temperature ≤150°C. Although sensors started responding at 200°C, the best response was noted at 400°C for WO_3 sensors and 350°C for sensors decorated with highest silver content. At lower temperatures, it is likely that not enough energy is present to facilitate adsorption/desorption process of oxygen species during gas exposure. Depending on the operating temperature, oxygen molecules can form chemisorbed species such as O_2^-, O^-, O^{2-} [27]. Previously reported study on WO_3 showed oxygen ions predominantly exist in the form of O^{2-} at temperature ≥ 300°C [28]. In this form, oxygen adsorbates trap more electrons from the conduction band, leading to formation of electron-depletion layer, which increases resistance of the sensing material. Higher operating temperature provides more energy for the oxygen molecules to dissociate that can contribute to higher response and faster response rate. This is consistent with our result where optimum operating temperature was obtained at 400°C.

The addition of catalyst to the tungsten oxide has shown to improve sensor performance as previously reported [26, 29-32], though not for oxygen detection. Copper oxide was reported to increase WO_3 thin film response from 4 to 27.5 for detection of 500 ppm hydrogen sulphide (H_2S) at 390°C [29]. Addition of palladium amplified the sensors sensitivity by more than 5x higher for the detection of ammonia (NH_3) [31]. Gold/palladium decoration in WO_3 films was reported to increase sensor detection for acetone by 50% [32]. Similarly, platinum in WO_3 can also improve a

sensors performance from $R_a/R_g<1$ to about $R_a/R_g=5$ for acetone detection in exhaled breath [30].

In this work, the response of the undecorated sensors was calculated at $R_g/R_a=6$ (400°C) in comparison to the decorated sensors at $R_g/R_a=23$ for 31% Ag content films (400°C) and $R_g/R_a=23$ for 38% Ag content films (350°C). Here, it can be observed that addition of silver/silver decoration to the films have improved the sensor performance as supported by the literatures. Furthermore, it also reduced the optimum operating temperature from 400°C to 350°C. This effect of Ag/Ag_2O decorations can be described by 2 proposed sensitisation mechanisms a discussed in Chapter 2, i.e. chemical and electronic sensitisation [33].

In chemical sensitisation, silver nanoparticles can facilitate the chemical reactions and increase chemical rate between oxygen molecules and tungsten oxide surface via spill-over mechanism [33, 34]. On the other hand, electronic sensitisation occurs through a direct electron interaction between the additives and metal oxide surface. This case is more likely to occur for silver catalyst [33]. Silver is known to form oxides in air and can reduced to metal with an inflammable gas. This is confirmed by the XPS analysis of the thin films in earlier section. Upon contact the Ag_2O shell will exchange electrons with WO_3, with the direction of exchange expected be toward WO_3 (data found in literature showing the conduction band of Ag_2O at -1.3 eV [35, 36] whilst WO_3 is at 0.4 eV [37]). The potential difference provides a considerable driving force for the electrons from Ag_2O to populate the conduction band of WO_3. For an n-type semiconductor, this would increase the carrier concentration and hence reduce the resistance of the sensors, which was observe experimentally. However, this electron exchange would not explain an enhanced response toward O_2. It is possible that changes in oxygen partial pressure would change electron density at the Ag_2O

shell and this is reflected by a measured change in resistance in the WO_3. On the other, spill-over taking place whereby Ag_2O could act to spill-over oxygen could not be ruled out either. This would increase the population of O_2 on the surface which could explain a higher response towards oxygen. However, this might be expected to increase the baseline resistance in ambient air, although it could be difficult to disentangle the electronic effect on the resistance from any attributable to spill-over. Therefore, in this case, Ag/Ag_2O in WO_3 films undergo both electronic sensitisation where the decorations exchange electrons with the host materials thus decreasing the resistance of the film and chemical sensitisation where the decorations act to spill-over oxygen, enriching the oxygen species on the films which lead to higher sensor response.

Increasing the operating temperature generally improved the rate of response and recovery, as illustrated in Figure 4 - 13 and Figure 4 - 14 respectively. The response time was noted at 9.6 minutes whereas the recovery time was recorded at 11.9 minutes. The addition of silver/silver oxide resulted in a faster response and recovery time as noted in decorated sensors with 31% Ag (T_{res}=8 .6 min and T_{rec}=9.4 min). However, this is not affected by the silver loading as higher concentration of silver (at 38%) did not reduce the response and recovery time Ag (T_{res}=9.2 min and T_{rec}=9.0 min). It can be seen from Figure 4 - 14 that recovery time for decorated films at 31% Ag and 38% Ag are quite similar especially at temperature ≥350°C. Whereas for recovery time, it can be observed that at higher temperature (≥350°C), the response time for all fabricated sensors are quite similar and thus addition of silver in the films does not contribute to a faster response time. Nonetheless, response and recovery times of the fabricated sensors are quite fast considering the relatively low operating temperature. These rates are faster than previously reported Pt-doped In_2O_3 sensor operated at room temperature with response and recovery time at 18

and 35 minutes respectively [38]. Faster response rate was reported for Ga_2O_3 based films at less than 1 minutes, but the sensors were operated at a high temperature 1000°C [39]. Similarly, response time was observed at less than 1 minute for TiO_2 based films but the film was operated at 800°C [27]. Increasing operating temperature of the fabricated AACVD based sensor will potentially reduce the response and recovery time quite significantly. However, this will also increase the power consumption of the sensors which is undesirable.

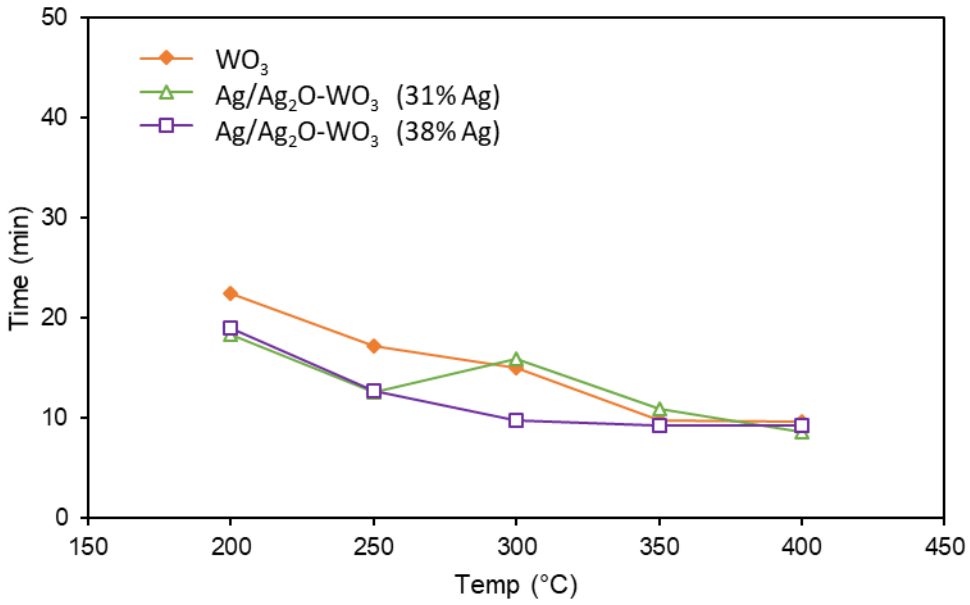

Figure 4 - 13 Response time of sensors with different silver/silver oxide loading.

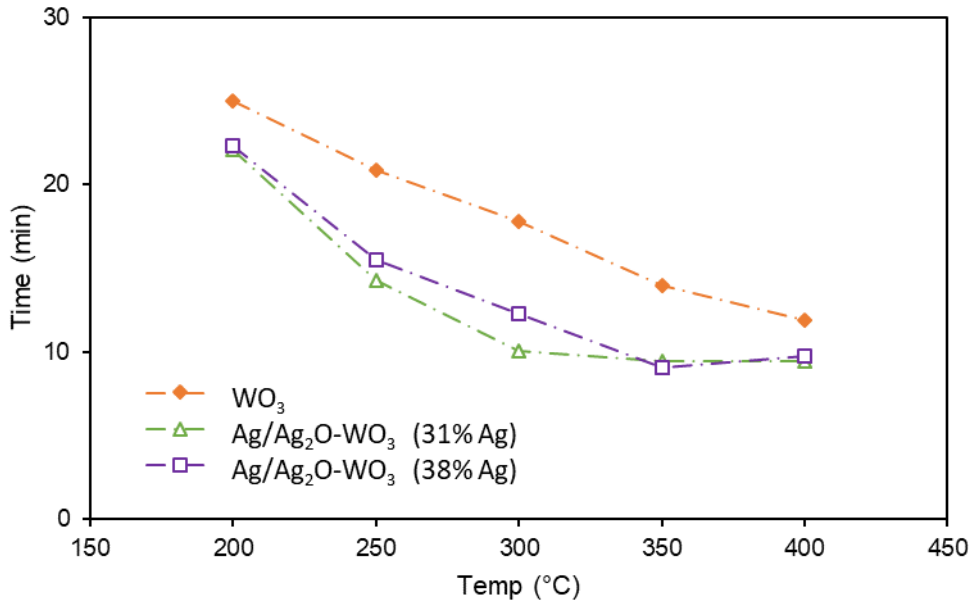

Figure 4 - 14 Recovery time of sensors with different silver/silver oxide loading.

The gas response relationship, illustrated in Figure 4 - 15, shows oxygen concentration changing linearly for bare WO_3 thin film, whereas silver decorated thin films follow a traditional power law with alpha value of 0.66 and 0.76 for Ag/Ag_2O-WO_3 (31% Ag content), and Ag/Ag_2O-WO_3 (38% Ag content) respectively. Power law relationship expresses concentration dependency at a certain range. In this case, Ag/Ag_2O-WO_3 thin films show $pO_2^{0.67}$ and $pO_2^{0.76}$ dependencies toward oxygen concentration 5 – 20%. The alpha value is critical to calculate the oxygen concentration. Generally, values between 0.5 and 1.0 are good with values closer to 1.0 produces higher measurement accuracy.

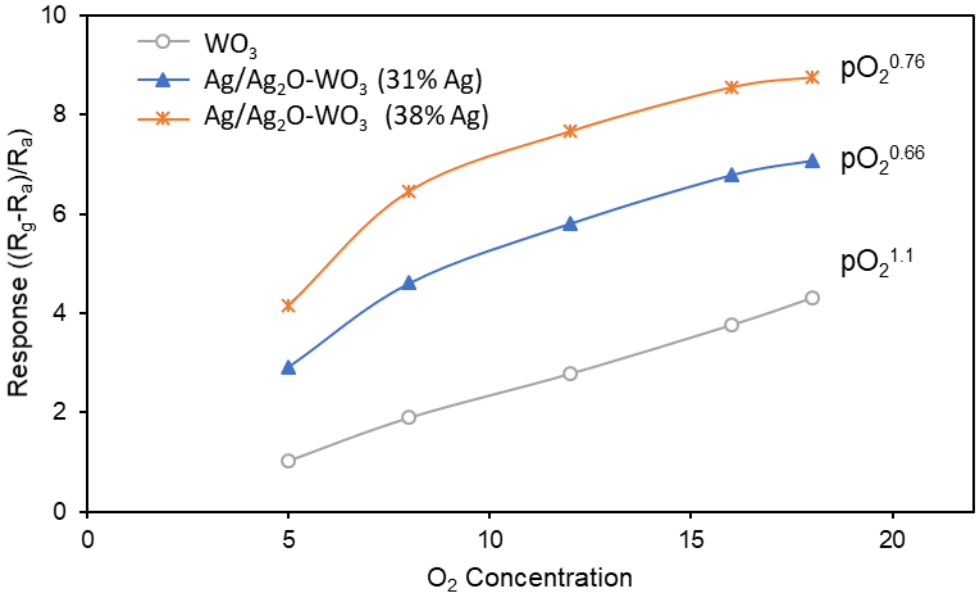

Figure 4 - 15 Gas response relationship as a function of oxygen concentration.

As mentioned earlier, tungsten oxide films fabricated with and without additives have been tested to detect various. Tungsten oxide just like any other metal oxide material has been known to suffer from cross sensitivity across gases, which may hinder its performance for a specified gas in presence of others. Therefore, it is important to do selectivity test which will be carried out in a later section.

4.7 Conclusion

Tungsten oxide-based sensors has been successfully deposited by aerosol assisted CVD method and tested for oxygen detection. Silver decoration on WO_3 thin films improved sensor response by more than 400% (from R_g/R_a= 6 to 23). Furthermore, the addition of silver enabled a lower optimum operating temperature dropping from 400°C to 350°C. Gas response relationship shows that bare WO_3 follows a more linear fashion, whereas Ag/Ag_2O decorated WO_3 follow a traditional power law trendline with alpha value ≥ 0.5, which produces effective measurement

for oxygen level calculation. Selectivity and cross-sensitivity test will be investigated in a later section.

4.8 References

[1] Y. Xu and X.-T. Yan, Chemical Vapour Deposition: An Integrated Engineering Design for Advanced Materials (no. Engineering Materials and Processes). Springer, London, 2010.

[2] K. L. Choy, "Chemical vapour deposition of coatings," Progress in Materials Science, vol. 48, no. 2, pp. 57-170, 2003/01/01/ 2003.

[3] C. W. H. Dunnill, Z. A. Aiken, J. Pratten, M. Wilson, D. J. Morgan, and I. P. Parkin, "Enhanced photocatalytic activity under visible light in N-doped TiO2 thin films produced by APCVD preparations using t-butylamine as a nitrogen source and their potential for antibacterial films," Journal of Photochemistry and Photobiology A: Chemistry, vol. 207, no. 2, pp. 244-253, 2009/09/25/ 2009.

[4] M. Kambe, M. Fukawa, N. Taneda, and K. Sato, "Improvement of a-Si solar cell properties by using SnO2:F TCO films coated with an ultra-thin TiO2 layer prepared by APCVD," Solar Energy Materials and Solar Cells, vol. 90, no. 18, pp. 3014-3020, 2006/11/23/ 2006.

[5] P. Zhang et al., "Oriented Ti doped hematite thin film as active photoanodes synthesized by facile APCVD," Energy & Environmental Science, 10.1039/C0EE00656D vol. 4, no. 3, pp. 1020-1028, 2011.

[6] S. Faÿ, J. Steinhauser, S. Nicolay, and C. Ballif, "Polycrystalline ZnO: B grown by LPCVD as TCO for thin film silicon solar cells," Thin Solid Films, vol. 518, no. 11, pp. 2961-2966, 2010/03/31/ 2010.

[7] T. I. Kamins, "Structure and Properties of LPCVD Silicon Films," Journal of The Electrochemical Society, vol. 127, no. 3, pp. 686-690, March 1, 1980 1980.

[8] S. D. S. Malhi et al., "Characteristics and Three-Dimensional Integration of MOSFET's in Small-Grain LPCVD Polycrystalline Silicon," IEEE Journal of Solid-State Circuits, vol. 20, no. 1, pp. 178-201, 1985.

[9] B. S. Meyerson and M. L. Yu, "Phosphorus-Doped Polycrystalline Silicon via LPCVD: II . Surface Interactions of the Silane/Phosphine/Silicon System," Journal of The Electrochemical Society, vol. 131, no. 10, pp. 2366-2368, October 1, 1984 1984.

[10] S. Nicolay, M. Despeisse, F. J. Haug, and C. Ballif, "Control of LPCVD ZnO growth modes for improved light trapping in thin film silicon solar cells," Solar Energy Materials and Solar Cells, vol. 95, no. 3, pp. 1031-1034, 2011/03/01/ 2011.

[11] B. S. Meyerson, "UHV/CVD growth of Si and Si:Ge alloys: chemistry, physics, and device applications," Proceedings of the IEEE, vol. 80, no. 10, pp. 1592-1608, 1992.

[12] B. S. Meyerson, K. E. Ismail, D. L. Harame, F. K. LeGoues, and J. M. C. Stork, "UHVCVD growth of Si/SiGe heterostructures and their applications," Semiconductor Science and Technology, vol. 9, no. 11S, p. 2005, 1994.

[13] M. Ling and C. Blackman, "Growth mechanism of planar or nanorod structured tungsten oxide thin films deposited via aerosol assisted chemical vapour

deposition (AACVD)," physica status solidi (c), vol. 12, no. 7, pp. 869-877, 2015.
[14] P. Marchand, I. A. Hassan, I. P. Parkin, and C. J. Carmalt, "Aerosol-assisted delivery of precursors for chemical vapour deposition: expanding the scope of CVD for materials fabrication," Dalton Transactions, 10.1039/C3DT50607J vol. 42, no. 26, pp. 9406-9422, 2013.
[15] S. J. A. Moniz et al., "A novel route to Pt–Bi2O3 composite thin films and their application in photo-reduction of water," Inorganica Chimica Acta, vol. 380, pp. 328-335, 2012/01/15/ 2012.
[16] S. Vallejos et al., "Au nanoparticle-functionalised WO3 nanoneedles and their application in high sensitivity gas sensor devices," Chemical Communications, 10.1039/C0CC02398A vol. 47, no. 1, pp. 565-567, 2011.
[17] S. P. DenBaars, B. Y. Maa, P. D. Dapkus, A. D. Danner, and H. C. Lee, "Homogeneous and heterogeneous thermal decomposition rates of trimethylgallium and arsine and their relevance to the growth of GaAs by MOCVD," Journal of Crystal Growth, vol. 77, no. 1, pp. 188-193, 1986/09/01/ 1986.
[18] Y. Liu et al., "Ultraviolet detectors based on epitaxial ZnO films grown by MOCVD," Journal of Electronic Materials, journal article vol. 29, no. 1, pp. 69-74, January 01 2000.
[19] R. Venkatasubramanian, T. Colpitts, E. Watko, M. Lamvik, and N. El-Masry, "MOCVD of Bi2Te3, Sb2Te3 and their superlattice structures for thin-film thermoelectric applications," Journal of Crystal Growth, vol. 170, no. 1, pp. 817-821, 1997/01/01/ 1997.
[20] G. Korotcenkov, Handbook of Gas Sensor Materials. Properties, Advantages and Shortcomings for Applications Volume 1: Conventional Approaches (no. Integrated Analytical Systems). Springer-Verlag New York, 2013, pp. XIX, 442.
[21] F. Di Maggio, M. Ling, A. Tsang, J. Covington, J. Saffell, and C. Blackman, "Aerosol-assisted CVD synthesis, characterisation and gas-sensing application of gold-functionalised tungsten oxide," Journal of Sensors and Sensor Systems, vol. 3, no. 2, pp. 325-330, 2014.
[22] F. Y. Xie et al., "XPS studies on surface reduction of tungsten oxide nanowire film by Ar+ bombardment," Journal of Electron Spectroscopy and Related Phenomena, vol. 185, no. 3, pp. 112-118, 2012/04/01/ 2012.
[23] J.-B. Lee, S.-Y. Jeong, W.-J. Moon, T.-Y. Seong, and H.-J. Ahn, "Preparation and characterization of electro-spun RuO2–Ag2O composite nanowires for electrochemical capacitors," Journal of Alloys and Compounds, vol. 509, no. 11, pp. 4336-4340, 2011/03/17/ 2011.
[24] A. Kafizas et al., "Optimizing the Activity of Nanoneedle Structured WO3 Photoanodes for Solar Water Splitting: Direct Synthesis via Chemical Vapor Deposition," The Journal of Physical Chemistry C, vol. 121, no. 11, pp. 5983-5993, 2017/03/23 2017.
[25] S. Vallejos et al., "Single-Step Deposition of Au- and Pt-Nanoparticle-Functionalized Tungsten Oxide Nanoneedles Synthesized Via Aerosol-Assisted CVD, and Used for Fabrication of Selective Gas Microsensor Arrays," Advanced Functional Materials, vol. 23, no. 10, pp. 1313-1322, 2013.
[26] F. E. Annanouch et al., "Aerosol-Assisted CVD-Grown PdO Nanoparticle-Decorated Tungsten Oxide Nanoneedles Extremely Sensitive and Selective to Hydrogen," ACS Applied Materials & Interfaces, vol. 8, no. 16, pp. 10413-10421, 2016/04/27 2016.

[27] R. K. Sharma, M. C. Bhatnagar, and G. L. Sharma, "Mechanism of highly sensitive and fast response Cr doped TiO2 oxygen gas sensor," Sensors and Actuators B: Chemical, vol. 45, no. 3, pp. 209-215, 1997/12/15/ 1997.
[28] S. Bai, K. Zhang, R. Luo, D. Li, A. Chen, and C. C. Liu, "Low-temperature hydrothermal synthesis of WO3 nanorods and their sensing properties for NO2," Journal of Materials Chemistry, 10.1039/C2JM30997A vol. 22, no. 25, pp. 12643-12650, 2012.
[29] F. E. Annanouch et al., "Aerosol-Assisted CVD-Grown WO3 Nanoneedles Decorated with Copper Oxide Nanoparticles for the Selective and Humidity-Resilient Detection of H2S," ACS Applied Materials & Interfaces, vol. 7, no. 12, pp. 6842-6851, 2015/04/01 2015.
[30] S.-J. Choi et al., "Selective Diagnosis of Diabetes Using Pt-Functionalized WO3 Hemitube Networks As a Sensing Layer of Acetone in Exhaled Breath," Analytical Chemistry, vol. 85, no. 3, pp. 1792-1796, 2013/02/05 2013.
[31] P. Van Tong, N. D. Hoa, N. Van Duy, D. T. T. Le, and N. Van Hieu, "Enhancement of gas-sensing characteristics of hydrothermally synthesized WO3 nanorods by surface decoration with Pd nanoparticles," Sensors and Actuators B: Chemical, vol. 223, pp. 453-460, 2016/02/01/ 2016.
[32] S. Kim, S. Park, S. Park, and C. Lee, "Acetone sensing of Au and Pd-decorated WO3 nanorod sensors," Sensors and Actuators B: Chemical, vol. 209, pp. 180-185, 2015/03/31/ 2015.
[33] N. Yamazoe, "New approaches for improving semiconductor gas sensors," Sensors and Actuators B: Chemical, vol. 5, no. 1, pp. 7-19, 1991/08/01/ 1991.
[34] C. Wang, L. Z. Yin, L., D. Xiang, and R. Gao, "Metal Oxide Gas Sensors: Sensitivity and Influencing Factors. Sensors " Sensors, vol. 10, no. 3, pp. 2088-2106, 2010.
[35] S. Rtimi, R. Sanjines, C. Pulgarin, A. Houas, J. C. Lavanchy, and J. Kiwi, "Coupling of narrow and wide band-gap semiconductors on uniform films active in bacterial disinfection under low intensity visible light: Implications of the interfacial charge transfer (IFCT)," Journal of Hazardous Materials, vol. 260, pp. 860-868, 2013/09/15/ 2013.
[36] D. P. Kumar, N. L. Reddy, M. Karthik, B. Neppolian, J. Madhavan, and M. V. Shankar, "Solar light sensitized p-Ag2O/n-TiO2 nanotubes heterojunction photocatalysts for enhanced hydrogen production in aqueous-glycerol solution," Solar Energy Materials and Solar Cells, vol. 154, pp. 78-87, 2016/09/01/ 2016.
[37] G. R. Bamwenda, K. Sayama, and H. Arakawa, "The effect of selected reaction parameters on the photoproduction of oxygen and hydrogen from a WO3–Fe2+–Fe3+ aqueous suspension," Journal of Photochemistry and Photobiology A: Chemistry, vol. 122, no. 3, pp. 175-183, 1999/03/31/ 1999.
[38] G. Neri et al., "A highly sensitive oxygen sensor operating at room temperature based on platinum-doped In2O3 nanocrystals," Chem Commun (Camb), no. 48, pp. 6032-4, Dec 28 2005.
[39] C. Baban, Y. Toyoda, and M. Ogita, "Oxygen sensing at high temperatures using Ga2O3 films," Thin Solid Films, vol. 484, no. 1–2, pp. 369-373, 7/22/ 2005.

Chapter 5. Spin Coated Tungsten Oxide Based Thin Film Sensor

5.1 Introduction

This chapter discusses a different approach to deposit metal oxide sensing materials, by means of spin coating. It is one of the most common methods to deposit a uniform and thin film onto substrates. It has been widely used for applications such as integrated circuit [1], television screen [2], and dielectric/ insulating layers [3-5]. As it is simple and easy to apply, this method can provide a good benchmark to other methods (discussed in previous chapters), especially AACVD where both techniques can produce thin films.

The first section starts by describing how spin technology works and the factors that influence film thickness and quality. Next, the work development is presented by optimising the process from ink formulation to ink deposition, curing and developing, and sintering process. The later sections discuss the experiments carried out with the manufactured sensors to detect targeted gas and finally the performance of the sensors is analysed.

5.2 Spin Coating Technology

Spin coating is a common technology for applying a thin film onto substrates. It works by depositing fluid/ ink at the centre, which will spread to the edge of the substrate due to centrifugal acceleration, leaving a thin film.

The fluid can be deposited either by dynamic dispense, i.e. dropping the fluid whilst the substrate is spinning, or static dispense where the fluid is dropped before

the spin starts. Dynamic dispense is usually preferred as it can get an even coverage using much lower volumes of fluid.

Factors that influence film thickness and quality are mainly spin speed [6] and solution concentration [7]. When the sample is spun at higher spin speeds, the amount of ink forced from the centre also increases and this results in thinner coating. Spin time can also influence the coating coverage for a short period of time. However, increasing the spin time diminishes the effect of the coverage and after a certain point, the influence is minimal. In general, the spin time is set so that the substrate is kept spinning until the ink becomes dry. The thickness also depends on the ink concentration or viscosity. Ink with higher viscosity will result in a thicker film as demonstrated in previous studies [7-9].

5.3 Work Development

Spin coating was used to deposit sensing layers for gas sensor applications to create a thin film layer about 6 – 9 µm thickness. Ink formulation, deposition process and developing, and sintering process were optimised to obtain a well-defined sensing structure. In this development work, blank ceramic tiles scribed to 2x2 mm were used as substrates. Once the optimal composition had been achieved, work was done on tiles patterned with interdigitated electrodes.

5.3.1 Ink Formulation

Ink was prepared from a mixture of photoresist and tungsten oxide (WO_3) powder as one of the most commonly used materials in metal oxide gas sensors. A photoresist is a light-sensitive material that can be classified into being a positive and negative photoresist. Upon exposure to UV light, exposed part of a positive

photoresist becomes soluble to its developer and the unexposed part remains as the structure. On the contrary, exposed part of a negative photoresist becomes insoluble and so the unexposed part is dissolved by the photoresist developer.

Dirasol 22 (Fujifilm Sericol, UK) is a diazo emulsion, which is formulated for use with solvent-based and UV curing inks. It served as a negative photoresist and was used as a vehicle as it has good solvent resistance and provides good definition as well as being soluble in water. Previous study with tin chromium oxide [10] showed high solid loading more difficult to spin coat and the optimum ratio was found for Dirasol 22 added to CTO in ratio of 5 : 1. With reference to this work, provisional experiment were conducted using the same ratio to assess the feasibility of this method when used with tungsten oxide. The ratio would be further optimised to find the best quality of sensing material.

Ink was prepared in a yellow light room by mixing 60 grams of Dirasol with 12 grams of tungsten oxide (New Metals and Chemicals Ltd, UK), to which 7.2 grams of deionised water was added to obtain ratio of 10:1. The mixture was placed into a bowl mill with alumina milling media (10 of 20 mm and 35 of 6mm). The ink components were milled using a high energy Laboratory Fast Mill Mod. Speedy (Nannetti slr, Italy) for 35 minutes to create smooth and consistent ink.

5.3.2 Deposition Process

Spin coating was carried out in a yellow light room to stop activation of the photoresist using the Spin Coater G3P-8 (Specialty Coating Systems, USA). Disposable pipette was initially used to drop the ink on a clean alumina substrate initially set to spin at 3000 rpm for 30 s. This method did not work because the ink was too viscous for the pipette. The tip of the pipette was cut to obtain larger aperture.

The ink could be dropped but this caused numerous bubbles. Adjustable volume pipettor was also tried but showed the same result. The ink was then altered such that the ratio of oxide added emulsion and water became 10:2 and 10:9. Ink deposition was done by static and dynamic dispense. Less viscous mixture was easier to drop and gave better result compared to 10:2 mixture.

Figure 5 - 1 and Figure 5 - 2 show the comparison of 2 different methods for depositing the ink. Using the same amount of ink, dynamics dispense showed better more coverage on the tiles. From these figures, it can be concluded that dynamic dispense is more suitable as it uses less ink cover the same area compared to static response. Figure 5 - 2 shows uniformly spread ink on the tile by dynamic dispense. However, bubbles were still present even though less viscosity mixture was used. This issue was solved by using 1mm syringe instead of pipette. With this, the mixture with higher viscosity could be deposited onto the substrate. Additionally, a mixture of 10:9 ratio resulted in very thin coverage, hence a more viscous mixture was used for further experiments.

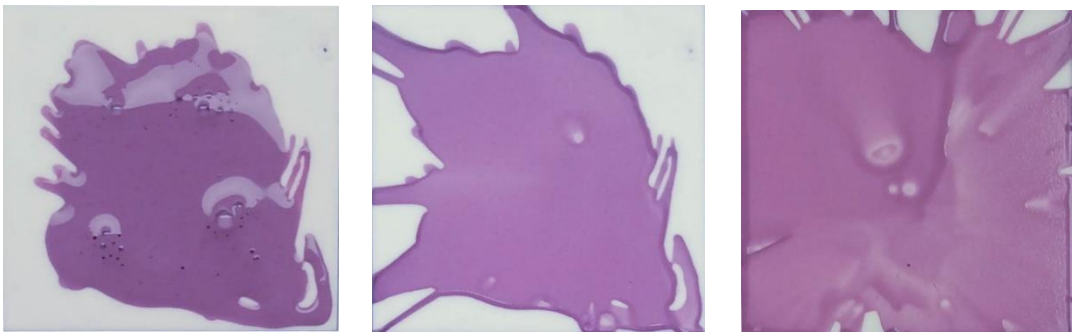

Figure 5 - 1 WO_3 (10:2 ratio) spin coated at 3000 rpm for 30 s from left to right: ink dropped by static dispense; after spinning; ink dropped by dynamic dispense.

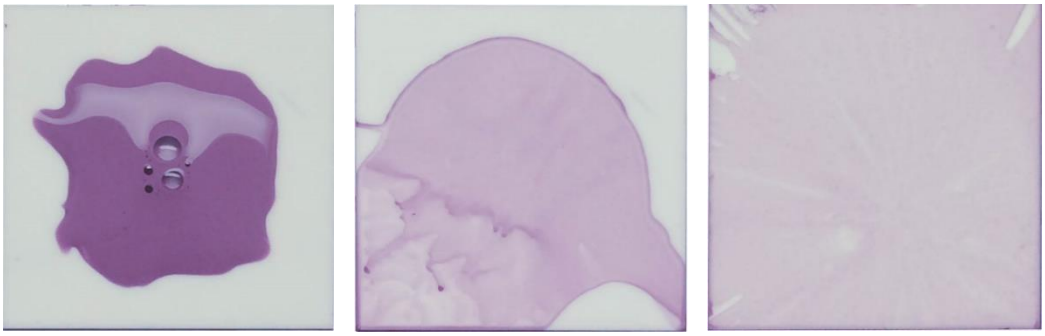

Figure 5 - 2 WO_3 (10:9 ratio) spin coated at 3000 rpm for 30 s, from left to right: ink dropped by static dispense; after spinning; ink dropped by dynamic dispense.

Figure 5 - 3 shows ink coverage spun at different speeds. At 3000 rpm, the ink produced a poor coverage on the tiles compared to the ones spun at 5000 and 7000 rpm. As the spinning speed increased, the coverage became thinner. At low speed, more ink was built up at the edge of substrate. The coating was repeated several times and variations occurred from tile to tile due the location from where the ink was dropped. As the syringe had a thicker body than the pipette, the aperture on the lid was not big enough for the syringe to get through and this distance from the lid to the substrate caused inaccuracy when aiming at the centre of the substrate. This was solved by allowing the spin coater to operate without the lid so the ink can be dropped closer to the substrate, making the process more repeatable. The tiles were dried at 55°C for 5 minutes on a hot plate prior to ultraviolet light exposure.

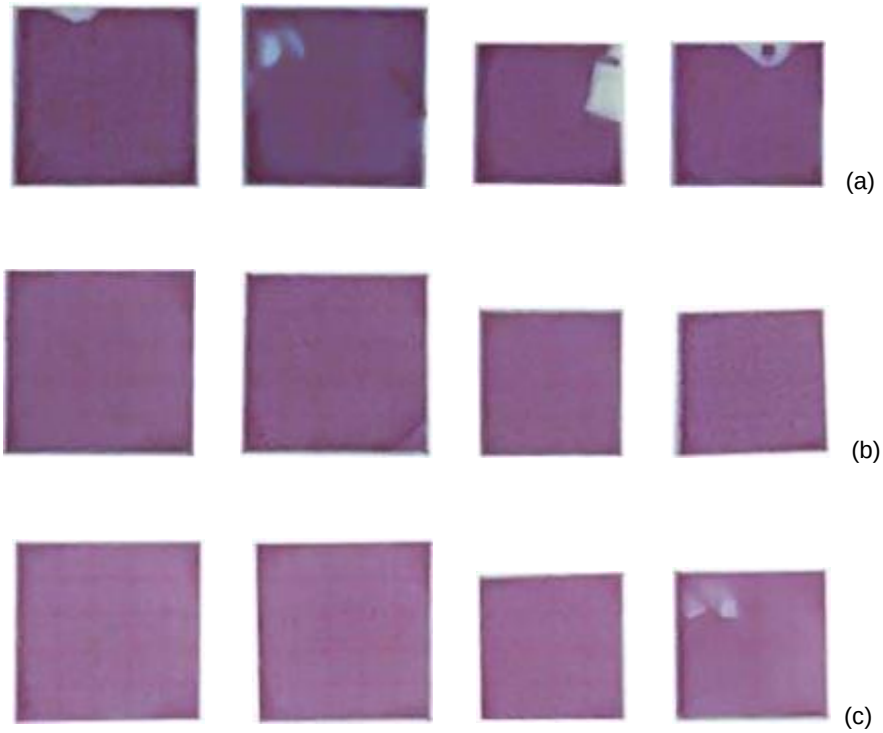

Figure 5 - 3 WO_3 (10:2 ratio) spin coated for 30 s at 3000 rpm (a); 5000 rpm (b); 7000 rpm (c).

5.3.3 Ultraviolet Curing and Developing

Spin coated tiles were exposed to UV light through a mask made to fit 50 x 50 mm ceramic tiles. The mask pattern, shown in Figure 5 - 4, was drawn in Altium Designer and manufactured as a metal stencil. UV lights were fitted into a box to allow exposure from top/bottom of the substrate. For development work, the alumina substrates previously scribed to 2 x 2 mm were snapped into smaller sizes.

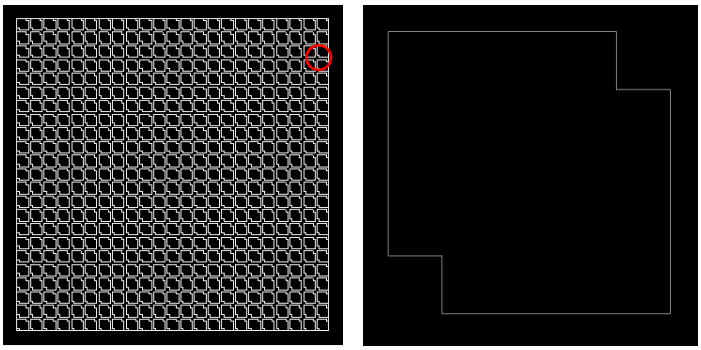

Figure 5 - 4 Mask pattern 50x50 mm.

As the snapped tiles are smaller than the original mask size, a holder was designed to aid with the alignment. Figure 5 - 5 shows holder design to hold the tiles of 6, 8, 10, and 12 mm in place and was made by laser cutting an poly(methyl methacrylate) (PMMA) also known as acrylic.

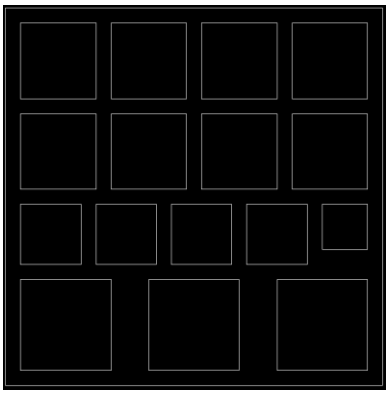

Figure 5 - 5 Holder for smaller alumina substrate.

Ink from mixture of 10:2 ratio was deposited on tiles at 3000 rpm for 30 s. The tiles were dried and aligned to the mask. Upon ultraviolet light exposure for 1, 3, and 5 minutes, the tiles were subsequently rinsed and lightly sprayed with deionised water. The exposed part of the ink remained while the unexposed part was washed away. The results are shown in Figure 5 - 6.

Tiles exposed for 1 minutes gave a good definition with individual patterns well separated. Some patterns were lifted while some unexposed parts were not properly washed away. Increasing the exposure time gave better adhesion to the substrate but less defined pattern with more rounded edges. The individual pattern was not well separated and image definition was even worse for tiles exposed for 5 minutes, which is due to prolonged UV exposure allowing UV light dispersion around the edges of the mask.

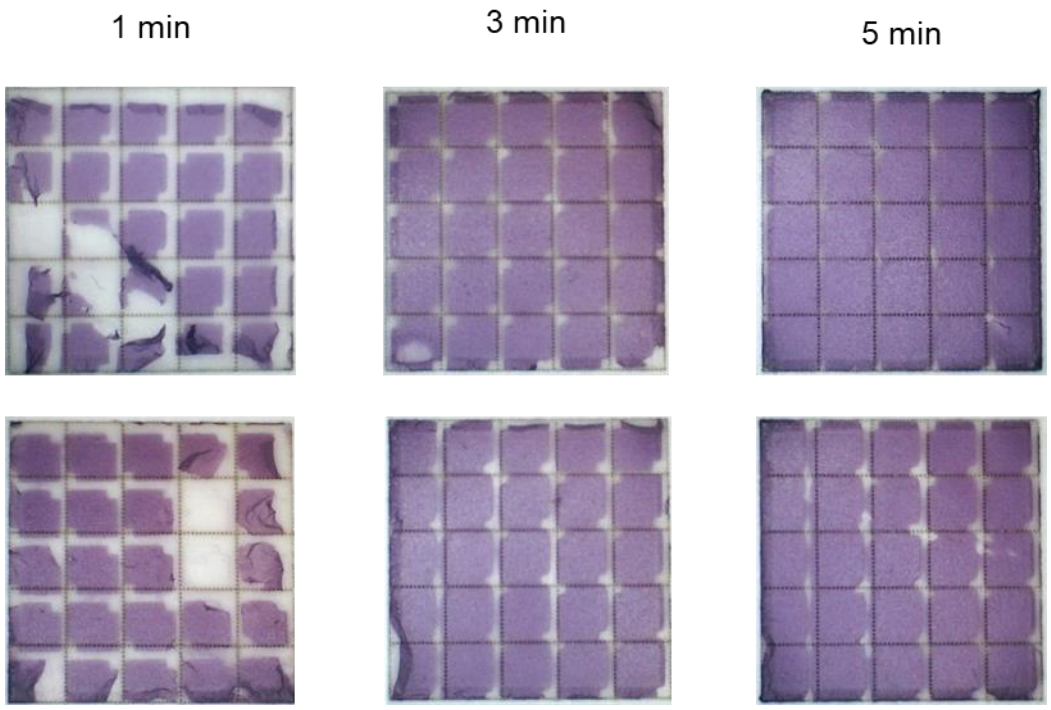

Figure 5 - 6 WO_3 ink (10:2 ratio) spin coated at 3000 rpm for 30 seconds at different UV exposure time

Ink was also spun at 5000 and 7000 rpm and exposed to UV light for the same period of time. The results are shown in Figure 5 - 7 and Figure 5 - 8. The tiles exposed for 1 minutes gave the best definition for both samples. Increasing the exposure times reduced image definition significantly and because of this, no samples spun at 7000 rpm were exposed to 5 minutes UV light.

Among the samples, tiles spun at 7000 rpm and exposed for 1 minute UV light showed the best result. The thickness of this sample was measured using ContourGT 3D Optical Microscope (Bruker, USA) and found to be 3 – 4 µm. The thickness of the samples spun at 3000 rpm and 5000 rpm and exposed at 1 minute UV were also measured and found to be 4.5 – 6 µm and 3 – 4.5 µm respectively.

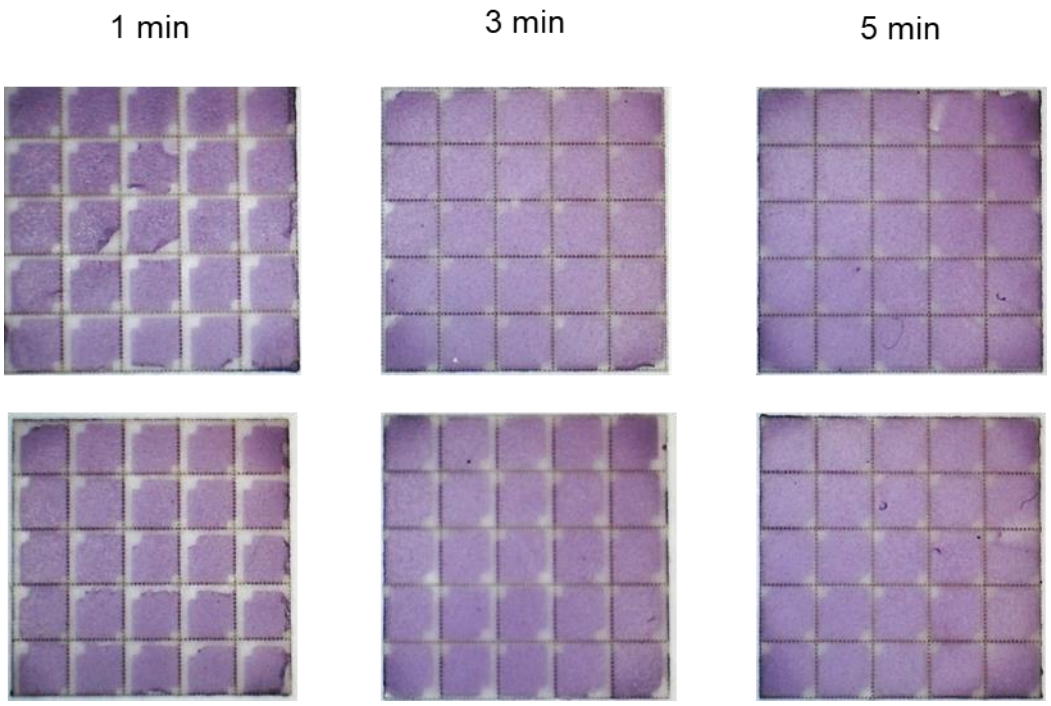

Figure 5 - 7 WO_3 ink (10:2 ratio) spin coated at 5000 rpm for 30 seconds at different UV exposure time.

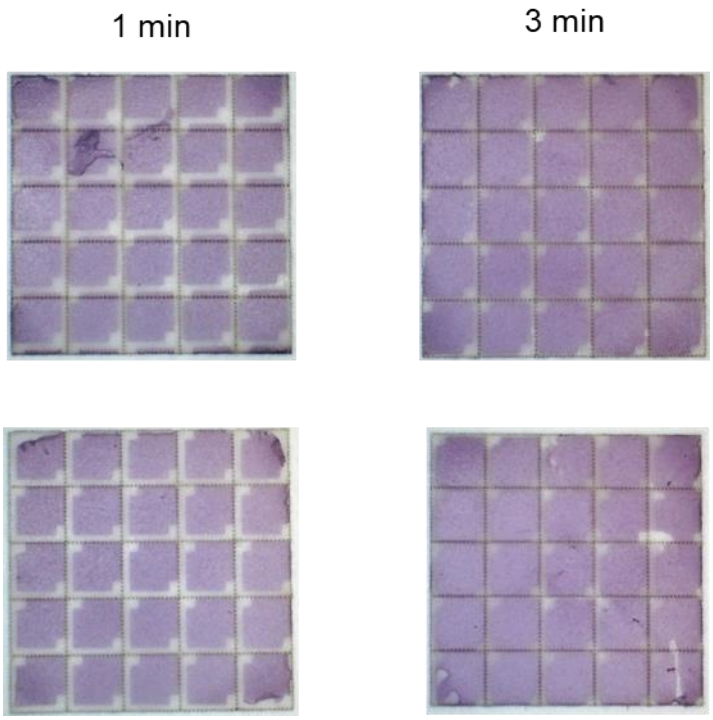

Figure 5 - 8 WO_3 ink (10:2 ratio) spin coated at 7000 rpm for 30 seconds at different UV exposure time.

Some samples showed misalignment even with the holder. Another batch of samples was aligned without the holder for comparison. Samples were aligned by visual inspection and held in place using masking tape. The samples aligned without the holder showed better results than the ones aligned with. Using masking tape also helped reducing any gap between samples and mask and this resulted in better pattern separation when exposed to longer UV light, which was required to develop more viscous or thicker films onto the substrate.

Ink from mixture of 10:1 was deposited onto the tile at 3000 rpm for 30 s and exposed to UV light for 5 minutes as shown in Figure 5 - 9. The pattern was separated and stuck well onto the tiles. The samples were later sintered to burn out the vehicle, leaving only the tungsten oxide on the surface of the tiles.

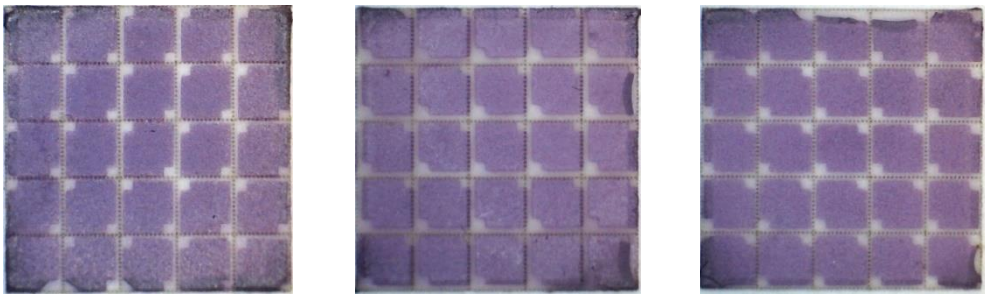

Figure 5 - 9 WO_3 ink (10:2 ratio) spin coated at 3000 rpm for 30 seconds and exposed at 5 minutes UV light.

5.3.4 Sintering Process

Thermogravimetric Analyzer (Mettler Toledo, USA) was used examine binder characteristic in mass loss. As illustrated in Figure 5 - 10 , mass reduced significantly at around 250°C and the binder completely burned out after 450°C, leaving only tungsten oxide in the mixture. This temperature is used as the first sintering point to burn out the binder. The second sintering point is to form a solid mass of WO_3 while providing enough porosity throughout the body. This point was set at 800, 850, and

900°C. The sintering profile, illustrated in Figure 5 - 11, was set to ramp temperature at 4°C/min to 450°C and dwell for 2 hours, then ramp to a maximum temperature at 3°C/min and dwell for 1.5 hours before cooling down to room temperature at 3°C/min.

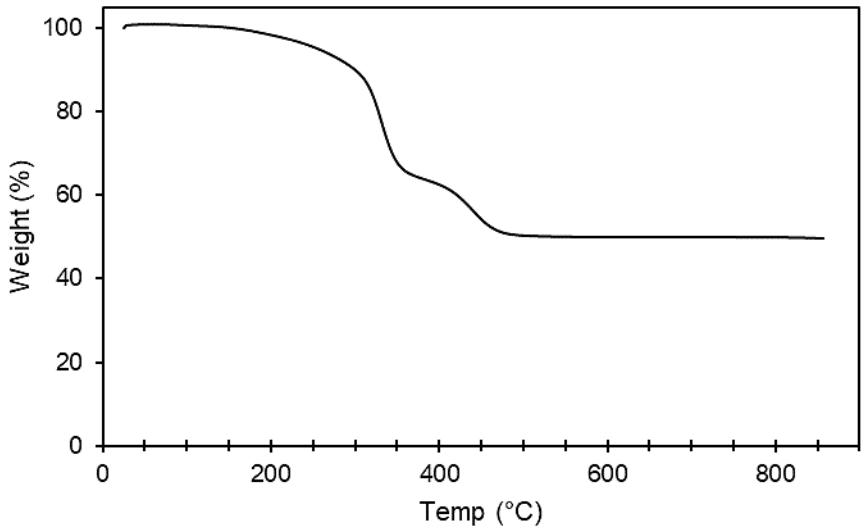

Figure 5 - 10 Thermogravimetric of WO_3 sample.

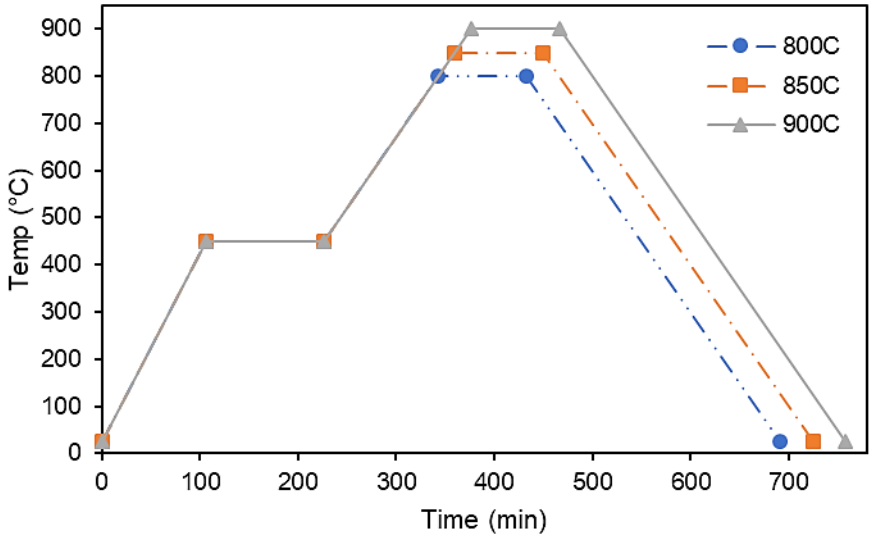

Figure 5 - 11 Sintering profile of WO_3.

Samples from 10:2 ink ratio were sintered in a furnace (Lenton Furnace UAF 16-5, UK) and the results are shown in Figure 5 - 12. Tiles spun at higher spinning rate had less WO_3 content and this caused failure in solidifying WO_3 as the pattern intended. The best result was obtained from sample spun at 3000 rpm and exposed to UV light at 5 minutes.

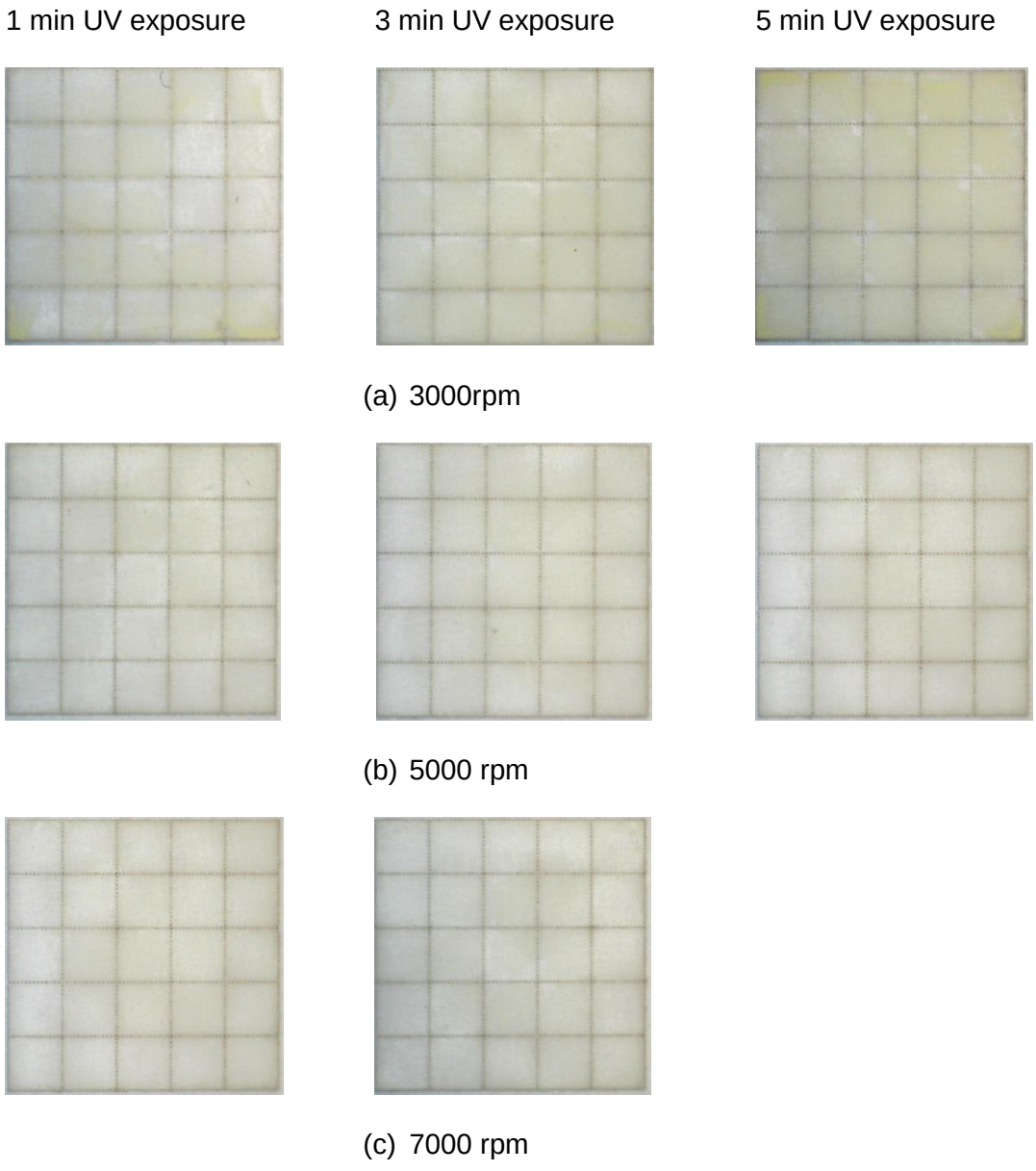

Figure 5 - 12 WO_3 samples (10:2 ratio) sintered at 850°C with spinning rate at: 3000 rpm (a); 5000 rpm (b); 7000 rpm (c).

More viscous samples from an ink ratio of 10:1, spun at 3000 rpm, were sintered and are shown in Figure 5 - 13. The results showed higher WO_3 loading and better uniformity. Pattern separation after exposure at 5 minutes UV light was also better than the less viscous samples, especially those spun at higher spinning rate. This formulation was used to pattern the sensing material on tiles with interdigitated electrodes.

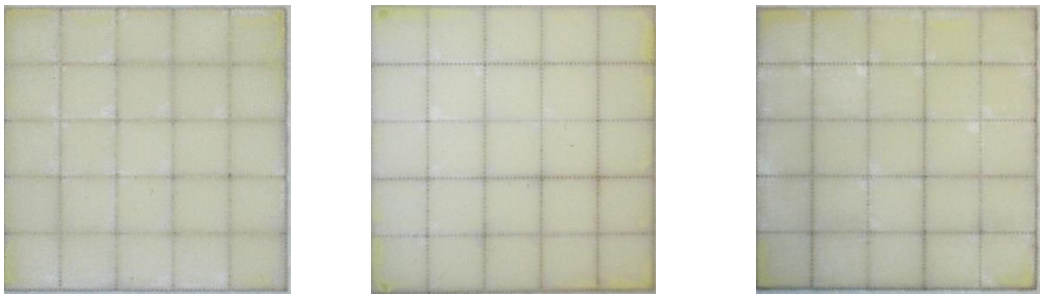

Figure 5 - 13 WO_3 samples (10:1 ratio) sintered at 850°C with spinning rate 3000 rpm.

5.4 Sensor Fabrication

Sensing material was deposited onto patterned tiles, as shown in Figure 5 - 14. The tile, previously discussed in Chapter 4, was patterned with gold interdigitated electrodes with a platinum heater. The tile was snapped into smaller sizes to evaluate material deposition before depositing onto a full tile.

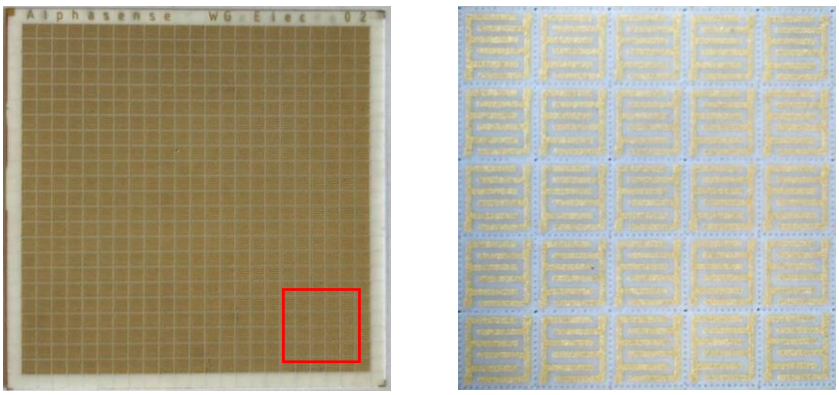

Figure 5 - 14 Scribed Al_2O_3 tiles with gold interdigitated electrodes.

Ink from ratio of 10:1 and 10:2 was deposited on the patterned tiles at 3000 rpm for 30 seconds. The tiles were dried at 55°C for 5 minutes on hot plate to dry the ink before exposure to UV light for 5 minutes. Samples were subsequently rinsed in deionised water and gently sprayed to remove any residual ink from the unexposed part. The samples were sintered following the sintering profile illustrated in Figure 5 - 11, initially up to 850°C.

Samples were well separated with good definition after exposure and developing process. There was ink built up at the edge of the tiles but this would not be an issue when deposited on the full tile as the outer tile is not patterned. After sintering, no sensing material can be observed on top of the patterned tiles but at the edge of some samples with no electrodes, a thin and faded yellow structures can be observed. This indicates that the thickness of the sensing material was too low to sit on top of the electrodes. Samples before and after sintering can be seen in Figure 5 - 15 and Figure 5 - 16.

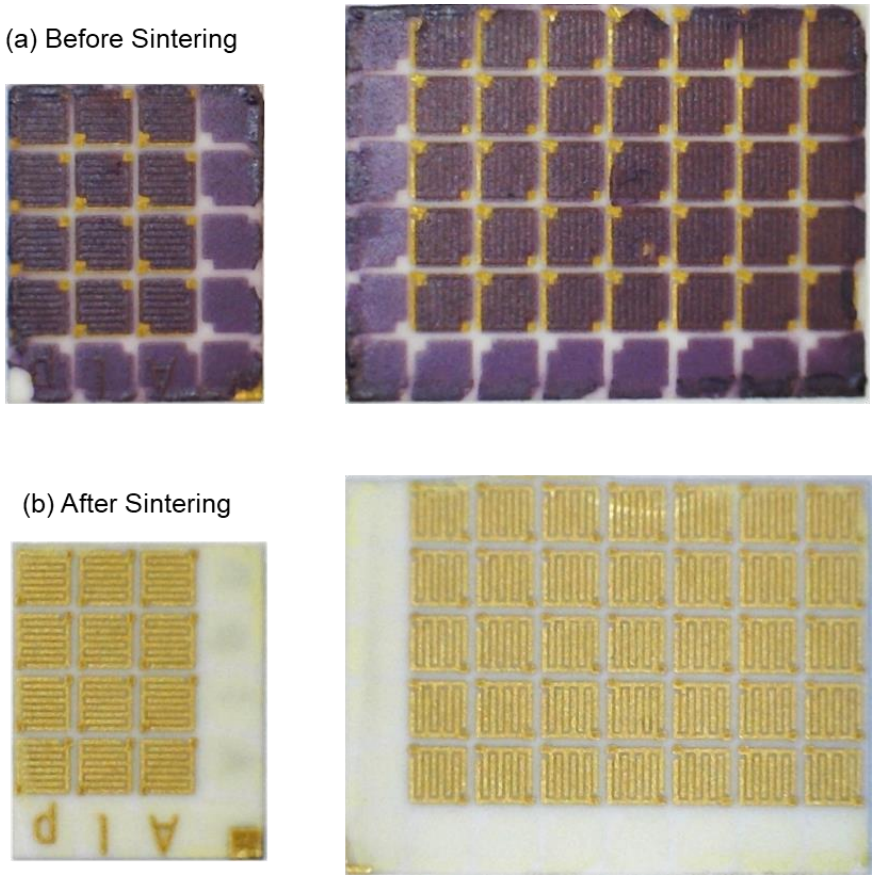

Figure 5 - 15 WO_3 ink (10:1 ratio) on patterned tile spin coated at 3000 rpm and 5 minutes exposure: (a) before and (b) after sintering.

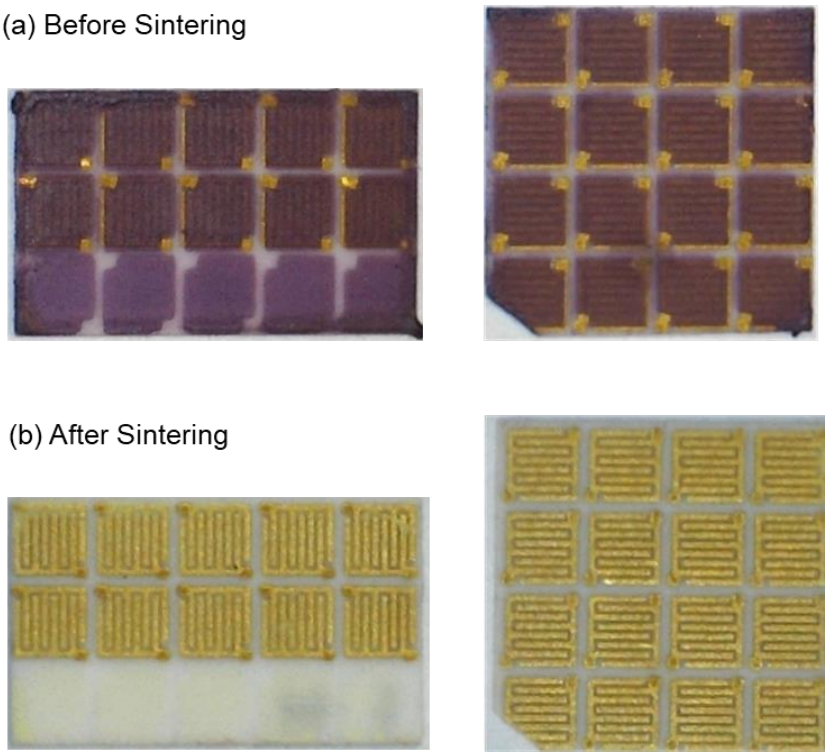

Figure 5 - 16 WO_3 ink (10:2 ratio) on patterned tile spin coated at 3000 rpm and 5 minutes exposure: (a) before and (b) after sintering.

Further experiments were carried out to obtain a thicker film. First, the rotational speed of the spin coater was reduced to 2000 rpm. Ink from ratio 10:1 was deposited on patterned tiles at this speed for 30 seconds. Upon drying on a hot plate at 55°C for 5 minutes, ink was exposed to UV light for 8 minutes to compensate for thicker film. The result showed more ink built up at the edge, but the pattern was separated and developed well around the centre of the tile. These samples were annealed at 850°C and the results can be seen in Figure 5 - 17.

.

(a) Before Sintering

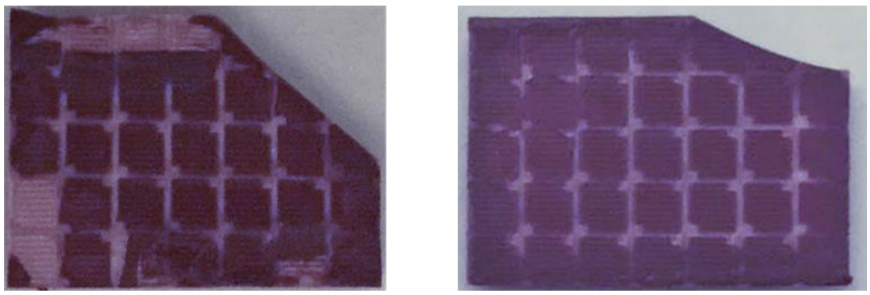

(b) After Sintering

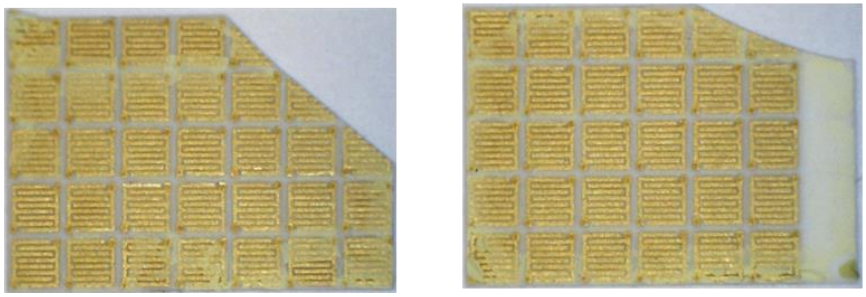

Figure 5 - 17 WO_3 ink (10:1 ratio) on patterned tile spin coated at 2000 rpm and 8 minutes exposure: (a) before and (b) after sintering.

Another method was to repeat coating process to increase the layer thickness of the film. Ink from 10:1 ratio was deposited at 3000 rpm for 30 seconds, dried on a hot plate at 55°C for 5 minutes, exposed to UV light for 5 minutes, and then developed by rinsing the tiles in deionised water. The tiles were dried on a hot plate at 55°C for about 10 minutes. The whole process was repeated from ink deposition until developing the pattern before the tiles were sintered in the furnace. The result of this method can be observed in Figure 5 - 18.

(a) Before Sintering

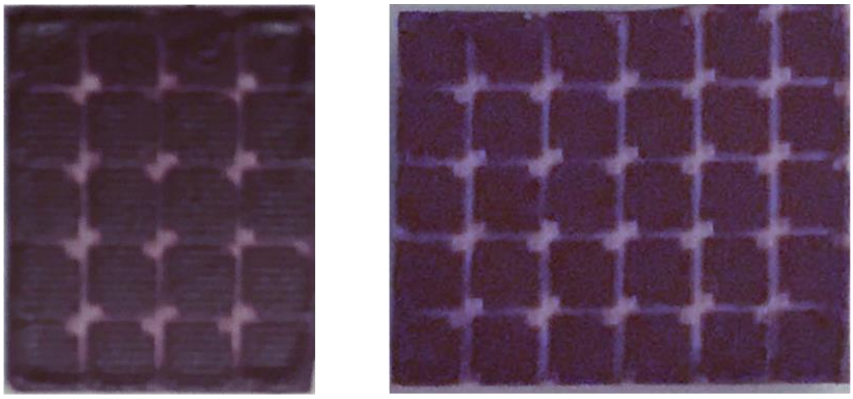

(b) After Sintering

Figure 5 - 18 WO_3 ink (10:1 ratio) on patterned tile spin coated at 3000 rpm and 5 minutes exposure in 2 layers before and after sintering.

Reducing the spinning rate to increase thickness of sensing material did not work out well. The layer was still too thin and the ink was not uniformly spread. Repeating the process to enable 2 layers deposition showed better coverage on patterned tiles. However, observation using a higher magnification microscope, as illustrated in Figure 5 - 19, showed the coverage was not uniform for some tiles and small sections on the tile were still uncovered by the material, indicating too little material content for the application.

A new batch of ink was made with 1/3 tungsten oxide loading. The ink was prepared in a yellow light room by mixing 60 gr Dirasol with 20 gr of tungsten oxide

powder added with 8.0 gr of deionised water. The mixture was milled with alumina milling media (10 of 20 mm and 35 of 6mm) using a high energy Laboratory Fast Mill Mod. Speedy for 35 minutes. The deposition process on the patterned tiles was carried out using this ink. Similar to the previous work, 1-layer deposition did not turn out well, but good results were obtained from 2-layer deposition as seen in Figure 5 - 20.

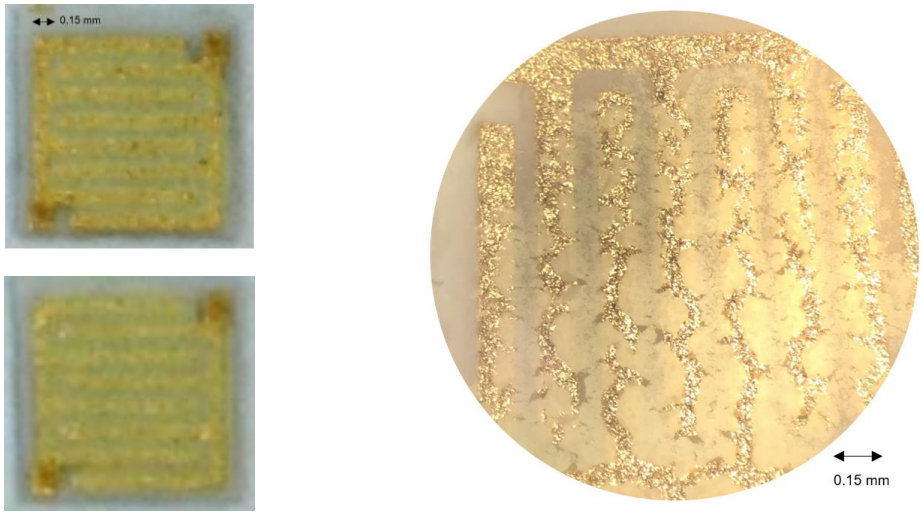

Figure 5 - 19 Sensing material 20% loading on individual tile after sintering process at 900°C.

The patterned tiles were initially snapped manually to individual tile of 2x2 mm after sintering process. However, a lot of tiles were damaged as the sensing material was scraped during snapping. The deposition process was repeated to obtain 2 layers of sensing material. The tiles were snapped before the sintering process instead of after. Whilst still mixed with the vehicle, the sensing material had strong structure and was not damaged during snapping process. After snapping, the individual tiles were then sintered at 800, 850, and 900°C. The results, as illustrated in Figure 5 - 19 and Figure 5 - 20, showed intact structure. The individual tiles of 33% WO_3 loading were later outsourced for welding and packaging in TO5 housing.

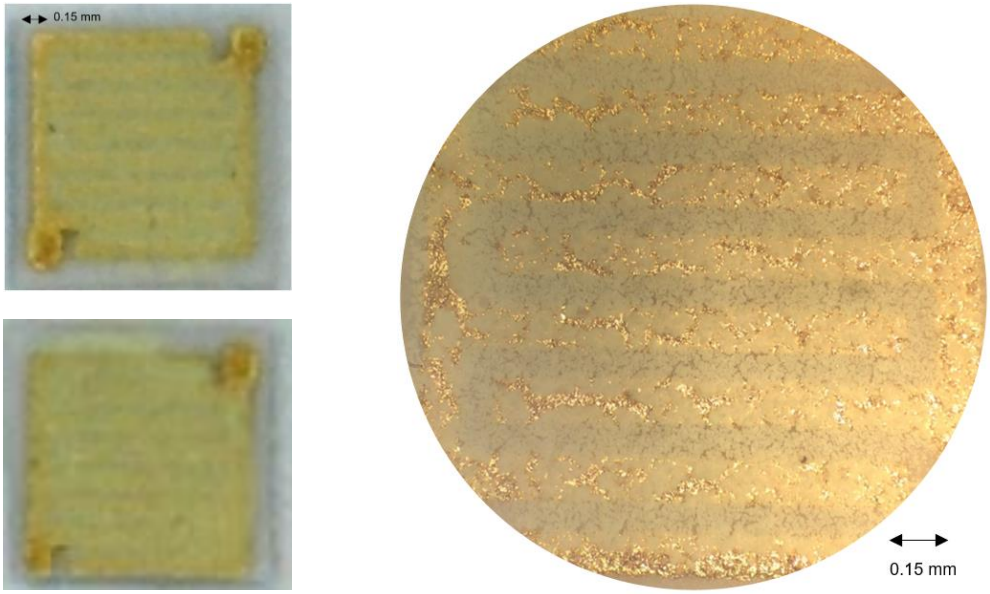

Figure 5 - 20 Sensing material 33% loading on individual tile after sintering process at 900°C.

5.5 Material Characterisation

The microstructure of the sensing material was investigated by SEM (Zeiss Supra 55) as shown in Figure 5 - 21. The images display a porous structure across different sintering temperatures with particles size measured up to 2 µm. However, it can be observed that WO_3 particles exhibited more agglomerations and fused together as the sintering temperature increased, creating a bulkier structure. The thickness of the sensing material on alumina sensor substrate was measured using Contour GT 3D Optical Microscope (Bruker, USA) and found to be at 9 ± 1.5 µm.

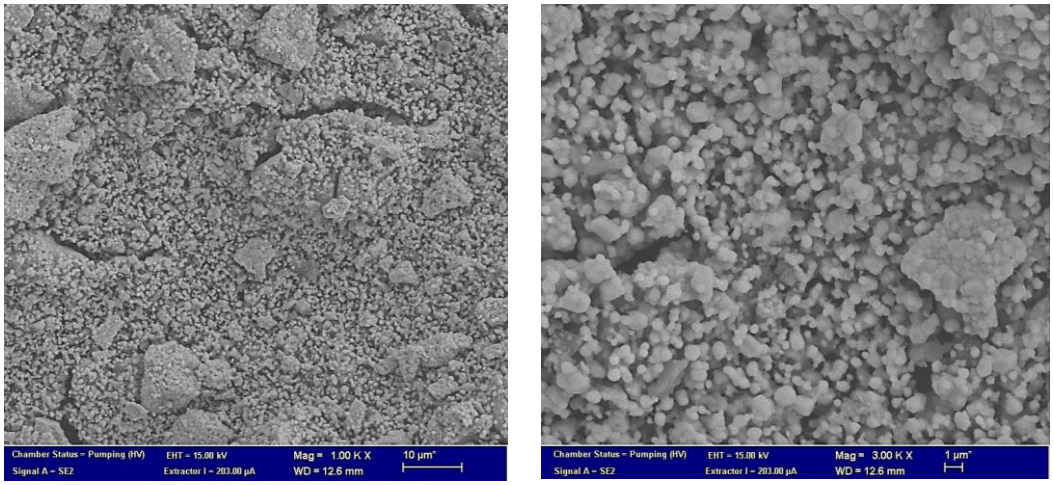

800°C

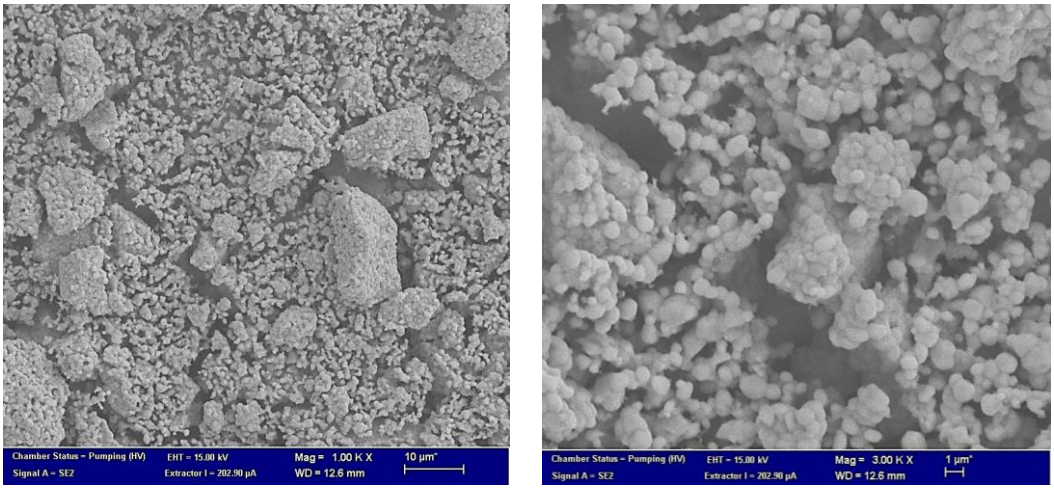

850°C

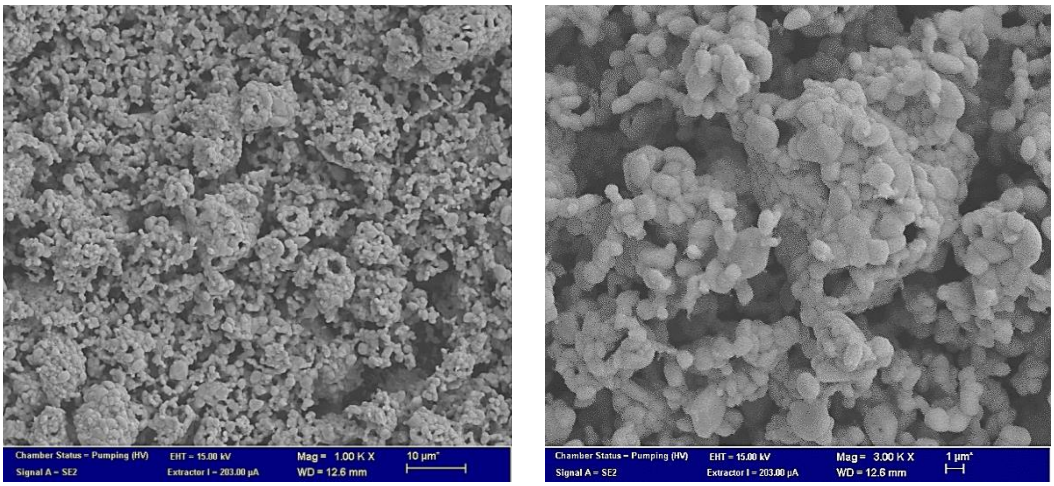

900°C

Figure 5 - 21 SEM images of WO_3 sensing material at different sintering temperature

5.6 Gas Testing

The fabricated tungsten oxide sensors were tested for oxygen concentration ranging from 0 to 20%. The test was set at 30 minutes cycle with sensors operated between 150 – 400°C in in both dry and humid air (~85% relative humidity (RH)). Sensors sintered at 800°C failed in the welding process, leaving sensors sintered at 850°C and 900°C for testing.

5.6.1 WO_3 850°C Film

Sensor did not respond to changes in oxygen concentration at 150°C. Although the sensor started to show a response from 200°C onwards, good response was not observed until sensor operated at 300°C. Sensor exhibited highest sensitivity at 350°C in both dry and humid air with baseline resistance at about 0.3 MOhm. The response was observed around 8 MOhm and 3 MOhm in dry and humid air respectively as seen in Figure 5 - 22. Figure 5 - 23 shows the response of the film was calculated at $\mathbf{R_g/R_a = 23.6}$ in dry air, which is more than 2x higher than the response in humid air at $\mathbf{R_g/R_a = 11.3}$. The response time and recovery time for the sensors tested in wet air were 5.1 and 8.3 minutes respectively. Whereas in dry air, the sensors took 8.4 minutes to respond and 6.4 minutes to recover.

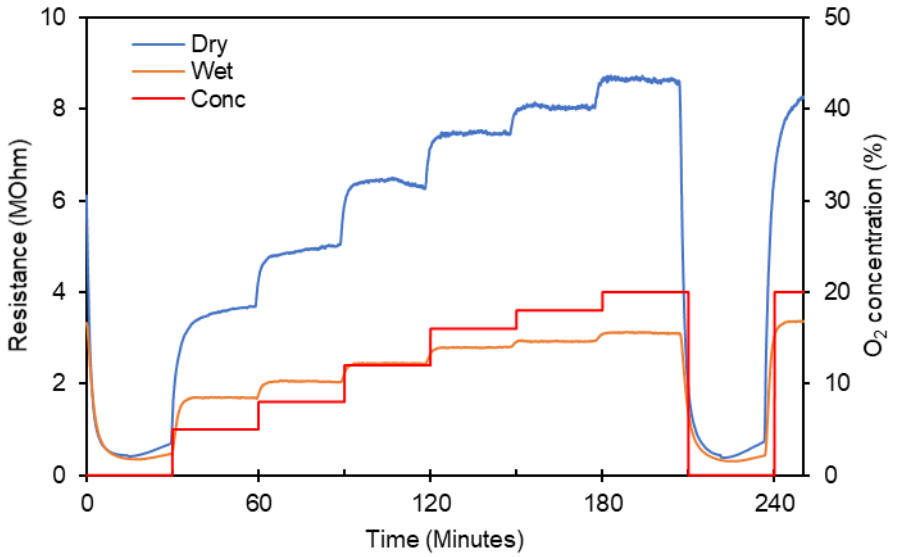

Figure 5 - 22 Dynamic response of WO_3 sensor (annealed at 850°C) in dry and humid air at 350°C.

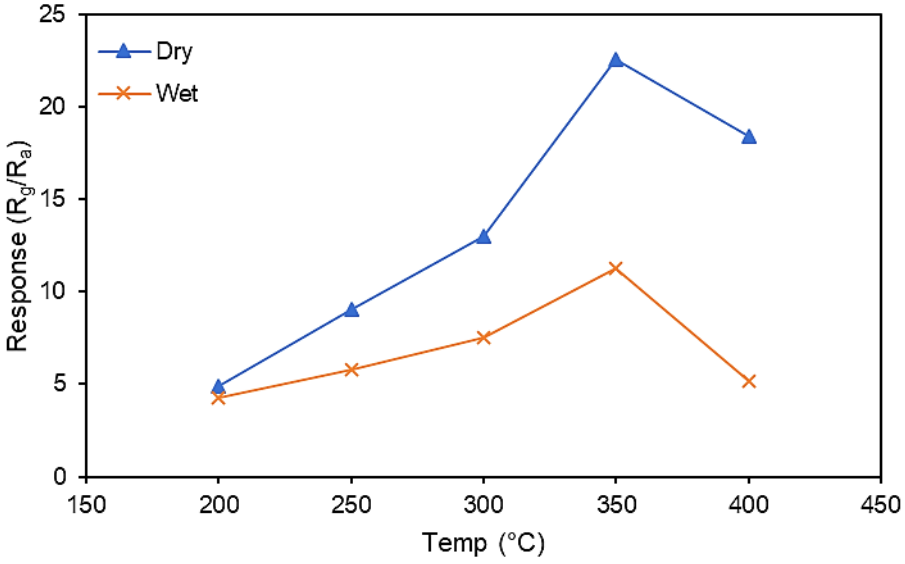

Figure 5 - 23 Response of WO_3 sensor (annealed at 850°C) in dry and humid air as a function of operating temperature.

5.6.2 WO_3 900°C Film

These sensors also started to show 'good' responses at operating temperatures ≥300°C with no response observed at 150°C. The best response, shown in Figure 5 - 24, was found at 350°C where the response was calculated at **R_g/R_a= 19** in wet air compared to **R_g/R_a= 12** in dry air. At this temperature, the baseline resistance was around 0.3 – 0.4 MOhm. The response was observed in 13.4 minutes at 0.9 MOhm with recovery rate at 5.8 minutes. In wet air, the response 0.3 MOhm in 4.7 minutes in dry air compared to 0.3 MOhm in wet air. The response and recovery time, summarised in Table 5 - 1, was calculated at 4.7 and 8.2 minutes respectively.

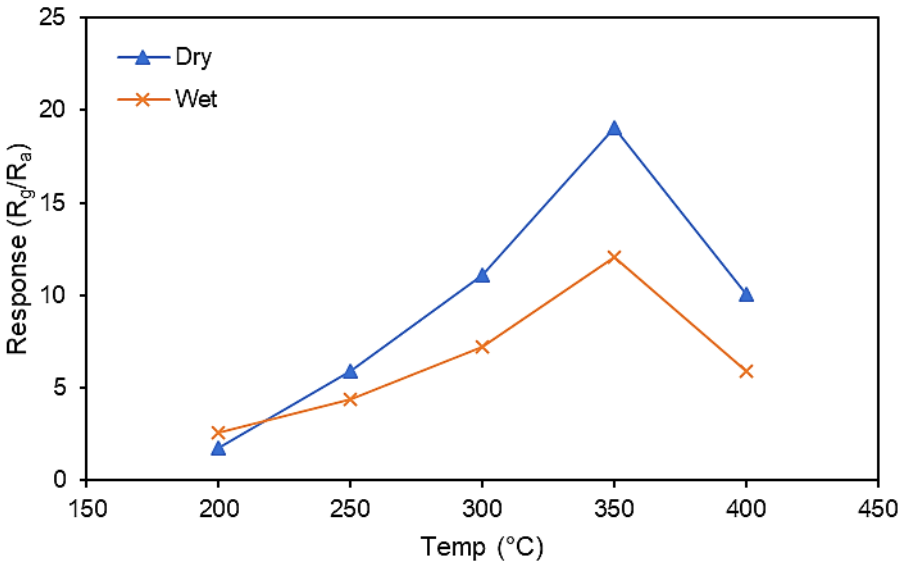

Figure 5 - 24 Sensitivity of WO_3 sensor (annealed at 900°C) in dry and humid air as a function of operating temperature.

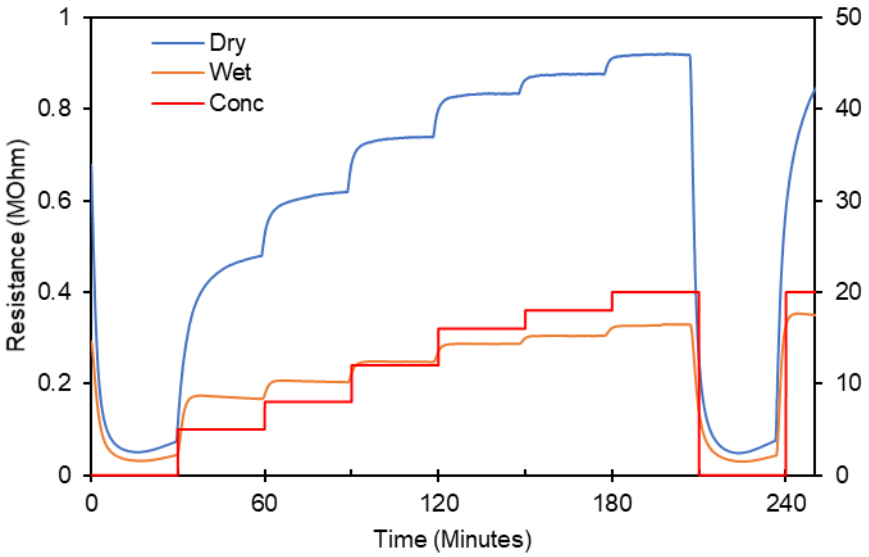

Figure 5 - 25 Dynamic response of WO_3 sensor (annealed at 900°C) in dry and humid air at 350°C.

Table 5 - 1 Rate of response and recovery for spin coated WO_3 sensor.

Temperature	Humidity	Response time (min)	Recovery time (min)
850°C	Wet (85% RH)	5.1	8.3
850°C	Dry	8.4	6.4
900°C	Wet (85% RH)	4.7	8.2
900°C	Dry	13.4	5.8

5.7 Analysis and Discussion

Sintering temperatures affect the morphologies of sensing material, which here resulted in different film conductivity. The resistance value of the sensors annealed at 850°C was 10x higher than the sensors annealed at 900°C. However, the normalised response of both types of sensors were quite similar in both dry and humid air.

Oxygen gas testing carried out in wet air (85% RH) revealed sensors fabricated by spin coating exhibited higher response than tungsten oxide grown by aerosol assisted CVD method. Spin coated WO_3 sensors had a response of R_g/R_a=11.3 and R_g/R_a=12 for films annealed at 850°C and 900°C respectively, twice higher than

AACVD grown WO_3 film response at R_g/R_a=6. As discussed in Chapter 2, using a smaller grain size for the sensing material can improve gas response [11-13]. However, AACVD grown nanoneedles at 1300 nm long with diameter varies between 100 and 200 nm was smaller than the spin coated WO_3 particles with dimension measured up to 2000 nm. This shows smaller grain size does not necessarily mean improvement in sensor performance. As thin films were fabricated by 2 different methods, the microstructure produced were also different. The enhancement in gas response can be attributed to a more porous crystalline microstructure produced by spin coated rather than the one produced by the AACVD method. Porous body can facilitate better oxygen adsorption, which leads to higher response. A similar finding was found in a study using tin oxide (SnO_2) where nanocrystals prepared by gel combustion method (~50 nm) showed a higher response than the one prepared by hydrothermal method (12-13 nm) [14].

Sensors exhibited less response in wet air than in dry air, although the response time was found to be faster in wet air. As observed in Figure 5 - 22 and Figure 5 - 25, resistance of thin films in N_2 ambience (baseline resistance) was unaffected by humidity. On the other hand, presence of humidity made the resistance of the sensor decrease in ambient air; hence the lower response. Similar findings (despite not for oxygen detection) have been reported in previous studies on metal oxide sensors [15-17].

The explanation of humidity influence on sensor performance is schematically proposed in Figure 5 - 26. The decrease in resistance can be attributed to the dissociation of water molecules with oxygen species forming hydroxyl ions, described in equation (5.1). This leads to oxygen vacancies on the surface of the sensing material thus creating less potential barrier on the grain boundary and less resistance.

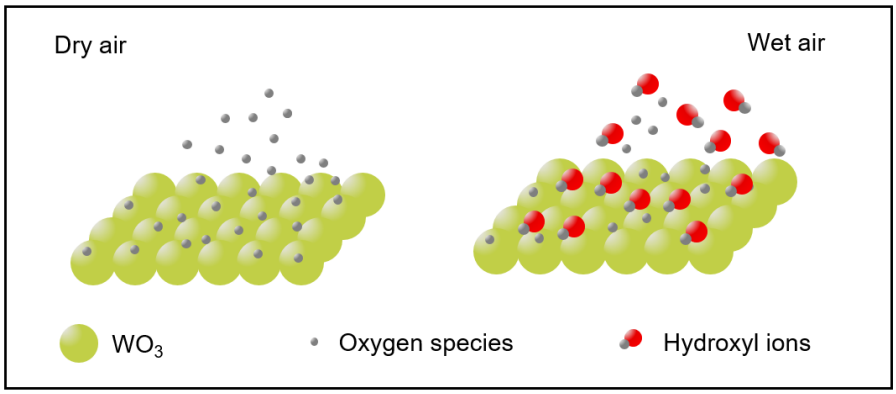

Figure 5 - 26 Gas sensing mechanism of WO_3 sensor in dry air and wet air.

$$O^{2-}{}_{(ad)} + H_2O \rightarrow 2OH^-{}_{(ad)} \qquad 5.1$$

It can be seen from Table 5 - 1 that humidity made the response faster and the recovery slower. This can be explained by less chemisorption of oxygen species on the surface of tungsten oxide film in wet air, hence faster response time. However, the recovery time was longer due to desorption of the surface hydroxyl ions and chemisorbed oxygen species on the surface of the film.

The gas response relationship, as illustrated in Figure 5 - 27, shows a traditional power law for oxygen tested in dry and humid air. In humid air, the alpha values were calculated at $pO_2^{0.69}$ and $pO_2^{0.56}$ for films annealed at 850°C and 900°C respectively. Although the alpha values decreased and sensors showed a lower response in wet air, a good oxygen discrimination over concentration range 5 – 20% was still obtained as the values ranging between 0.5 and 1.0.

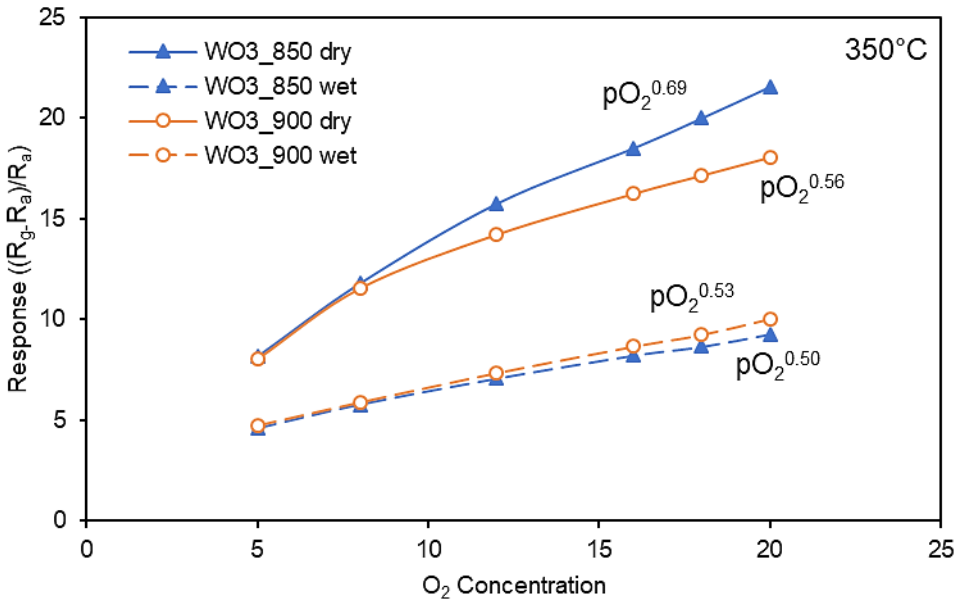

Figure 5 - 27 Sensitivity of WO_3 sensor in dry and humid air as a function of oxygen concentration.

5.8 Conclusion

Tungsten oxide-based sensor have been deposited by a combination of spin coating method and photolithographic process to define the sensing area. The highest response for sensors annealed at 850°C was obtained at R_g/R_a = 22.6 in dry and R_g/R_a = 11.3 in humid air. Whereas for sensors annealed at 900°C, the highest response was noted at R_g/R_a = 19 (dry) and R_g/R_a = 12 (humid). This showed lower sintering temperature lead to higher response as observed here and that humid air lead to lower sensor response. Nonetheless, this work is a significant improvement (enhanced response by 200%) over the previous work with tungsten oxide grown by AACVD method, most likely due to a more porous microstructure of spin coated sensing material. The gas response relationship showed that films follow power law trendline, with alpha value ≥ 0.5 which demonstrate good oxygen differentiation.

5.9 References

[1] G. H. Gelinck, T. C. T. Geuns, and D. M. de Leeuw, "High-performance all-polymer integrated circuits," *Applied Physics Letters,* vol. 77, no. 10, pp. 1487-1489, 2000.

[2] D. K. Flattery, C. R. Fincher, D. L. LeCloux, M. B. O'Regan, and J. S. Richard, "Clearing the Road to Mass Production of OLED television," *Journal of Society for Information Display,* vol. 27, no. 10, pp. 8-13, 2011.

[3] Y. Kato *et al.*, "High mobility of pentacene field-effect transistors with polyimide gate dielectric layers," *Applied Physics Letters,* vol. 84, no. 19, pp. 3789-3791, 2004.

[4] R. Parashkov, E. Becker, G. Ginev, T. Riedl, H. H. Johannes, and W. Kowalsky, "All-organic thin-film transistors made of poly(3-butylthiophene) semiconducting and various polymeric insulating layers," *Journal of Applied Physics,* vol. 95, no. 3, pp. 1594-1596, 2004.

[5] H. Klauk, M. Halik, U. Zschieschang, G. Schmid, W. Radlik, and W. Weber, "High-mobility polymer gate dielectric pentacene thin film transistors," *Journal of Applied Physics,* vol. 92, no. 9, pp. 5259-5263, 2002.

[6] J. F. Taylor, "Spin coating: An overview," *Metal Finishing,* vol. 99, no. 1, pp. 16-21, 2001/01/01/ 2001.

[7] J. H. Lai, "An investigation of spin coating of electron resists," *Polymer Engineering & Science,* vol. 19, no. 15, pp. 1117-1121, 1979.

[8] B. T. Chen, "Investigation of the solvent-evaporation effect on spin coating of thin films," *Polymer Engineering & Science,* vol. 23, no. 7, pp. 399-403, 1983.

[9] S. Middleman, "The effect of induced air-flow on the spin coating of viscous liquids," *Journal of Applied Physics,* vol. 62, no. 6, pp. 2530-2532, 1987.

[10] U. Capteur Sensors and Analysers Ltd, "Silicon/Glass Microstructures for Innovative Gas Sensing System Deliverable 5: First Report on Thick/Thin Film Materials, Models and Deposition Techniques," 2000.

[11] A. Rothschild and Y. Komem, "The effect of grain size on the sensitivity of nanocrystalline metal-oxide gas sensors," *Journal of Applied Physics,* vol. 95, no. 11, pp. 6374-6380, 2004.

[12] X. Wang, S. S. Yee, and W. P. Carey, "Transition between neck-controlled and grain-boundary-controlled sensitivity of metal-oxide gas sensors," *Sensors and Actuators B: Chemical,* vol. 25, no. 1, pp. 454-457, 1995/04/01/ 1995.

[13] G. Zhang and M. Liu, "Effect of particle size and dopant on properties of SnO2-based gas sensors," *Sensors and Actuators B: Chemical,* vol. 69, no. 1, pp. 144-152, 2000/09/10/ 2000.

[14] H. Liu, S. P. Gong, Y. X. Hu, J. Q. Liu, and D. X. Zhou, "Properties and mechanism study of SnO2 nanocrystals for H2S thick-film sensors," *Sensors and Actuators B: Chemical,* vol. 140, no. 1, pp. 190-195, 2009/06/18/ 2009.

[15] J. Gong, Q. Chen, M.-R. Lian, N.-C. Liu, R. G. Stevenson, and F. Adami, "Micromachined nanocrystalline silver doped SnO2 H2S sensor," *Sensors and Actuators B: Chemical,* vol. 114, no. 1, pp. 32-39, 2006.

[16] Q. Qi *et al.*, "Electrical response of Sm2O3-doped SnO2 to C2H2 and effect of humidity interference," *Sensors and Actuators B: Chemical,* vol. 134, no. 1, pp. 36-42, 2008/08/28/ 2008.

[17] M. Egashira, M. Nakashima, S. Kawasumi, and T. Selyama, "Temperature programmed desorption study of water adsorbed on metal oxides. 2. Tin oxide

surfaces," *The Journal of Physical Chemistry,* vol. 85, no. 26, pp. 4125-4130, 1981/12/01 1981.

Chapter 6. Spin Coated Indium Oxide Based Thin Film Sensor

6.1 Introduction

In the previous chapter, the development of metal oxide gas sensors using tungsten oxide materials was presented. This chapter builds on the previous by applying the same deposition technique to make thin film sensors using a different metal oxide material, i.e. indium oxide. This material has higher conductivity than tungsten oxide which could enable lower operating temperature. Furthermore, indium oxide has been previously proposed for oxygen detection and so further study on this material could potentially provide a better oxygen discrimination than the previously fabricated tungsten oxide-based sensors.

The first section of the chapter briefly discusses the application of indium oxide in gas sensing. The following section describes the fabrication process from the ink formulation to the sintering process. The last section discusses the gas sensing tests and analysis on sensor performance based on different materials deposited by the same technique.

6.2 Indium Oxide for Gas Sensing Application

Indium oxide is an n-type semiconductor material that has been used (with or without doping) in many applications including as a coating in optoelectronic device [1, 2], touch screens [3], liquid crystal displays (LCD) [4, 5], ultraviolet lasers [6], light emission diodes [7], and gas sensors [8-10]. Indium oxide can be prepared through

different synthesis methods such as sol-gel, spin coating, screen printing, sputtering, and solid-state reaction to create a thick or thin film.

In its cubic (bixbyite) phase, indium oxide film is known to have lots of oxygen vacancies that are responsible for the good electrical conductivity. The conductivity of the film depends on various parameter such as doping/ material decorations, annealing temperatures, operating temperatures and film thickness [11, 12].

Indium oxide is suited for use in gas sensing application as its high electrical conductivity can enable lower operating temperatures, which in turn can assist to reduce power consumption of the sensors. The use of indium oxide for gas sensing applications has been studied previously to detect gases such as CO and NO_2 [8, 13], NH_3 [9, 14], and volatile organic compounds (VOCs) [15-18]. In this chapter, indium oxide has been successfully deposited by a spin coating method and tested for oxygen detection.

6.2.1 Sensor Fabrication

The fabrication process started by formulating the ink and preparing the substrates. Formulated ink was deposited on the alumina substrate patterned with gold interdigitated electrodes printed on one side and platinum heater on the other. These are the same substrates used in the previous chapter.

6.2.2 Ink Formulation

Indium oxide-based ink was prepared in 3 different types, i.e. pure In_2O_3, In_2O_3 decorated with palladium powders, and In_2O_3 decorated with platinum powders. The indium oxide powders of 99.9% purity and 325 mesh grade were obtained from ABSCO Ltd, UK. Palladium and platinum powders were sourced from Pt-salt of

tetraammineplatinum(II) hydroxide hydrate ($Pt(NH_3)_4(OH)_2 \cdot xH_2O$) and Pd-salt of tetraammineplatinum(II) acetate ($Pd(NH_3)_4(CH_3CO_2)_2$) respectively, both obtained from Sigma-Aldrich, UK.

The vehicle used was Dirasol 22 (Fujifilm Sericol Ltd, UK), which served as a negative photoresist with water as its developer. Before mixing the powders with the vehicle, the platinum and palladium powders were incorporated into indium oxide by wet mixing the components described in Table 6 - 1. The components were mixed in a ceramic bowl and milled for 6 minutes. The mixtures were left overnight and the dry powders were subsequently sieved through 75 µm aperture sieve.

Table 6 - 1 Components to create Pt- In_2O_3 and Pd-In_2O_3 powders.

Components	**Pd-In_2O_3**	**Pt-In_2O_3**
6 mm media (gr)	50.097	50.007
3 mm media (gr)	100.063	100.025
In_2O_3 (gr)	20.01	20.06
Salt (gr)	0.306	0.304
DI water (gr)	30.72	30.69

Ink was prepared in a yellow light room by mixing 36 grams of Dirasol 22 with 12 grams of indium oxide-based powder, added with 4.8 grams deionised water. The mixture was placed into a ceramic pot with 10 large media (20 mm) and 35 medium media (6 mm) made of alumina. The ink components were milled using a high energy Laboratory Fast Mill Mod. Speedy (Nannetti slr, Italy) for 35 minutes to create smooth and consistent ink.

6.2.3 Deposition Process

The substrate was previously cleaned in acetone and isopropanol before placed inside a spin coater G3P-8 (Specialty Coating Systems, USA). Using a 1-ml syringe,

the indium oxide-based ink was deposited by dynamic dispense on the patterned alumina substrates. The deposition was carried out for 30 seconds at 3000 rpm speed and showed good coverage and distribution as demonstrated in Figure 6 - 1. The substrates were then placed on a hot plate heated at 55°C for 5 minutes to dry the ink prior to ultraviolet exposure.

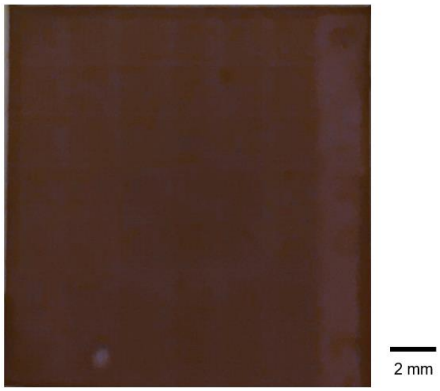

Figure 6 - 1 Example of spin coated In_2O_3 based in deposited at 3000 rpm for 30 s.

6.2.4 Ultraviolet Curing and Developing

The spin coated substrates were aligned to a stencil mask previously discussed in Chapter 5 and exposed to ultraviolet light for 6 minutes. Subsequently, the substrates were gently sprayed with deionised water to wash away the unexposed part. The results (Figure 6 - 2) show a good edge definition with the individual pattern well separated.

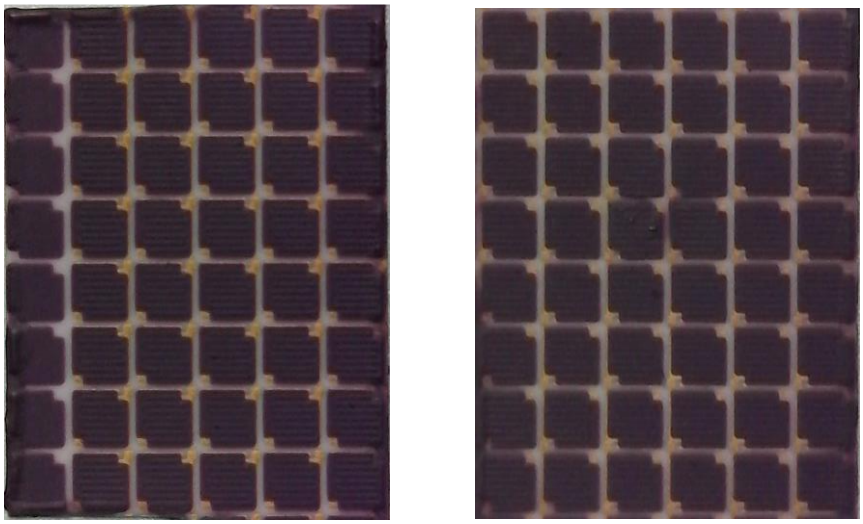

Figure 6 - 2 Spin coated indium oxide on patterned alumina substrates after 6 minutes UV exposure and developing.

6.2.5 Sintering Process

Thermogravimetric analysis, as used in the previous chapter, was also used here as the vehicle was the same. The first sintering point was ramped up at 450°C and dwelled for 2 hours to burn out the vehicle before increased to either 850°C or 900°C and left for 1.5 hours to solidify the material while leaving enough porosity on the body. The temperature inside the furnace (Lenton Furnace UAF 16-5, UK) was then cooled down to room temperature at 3°C/min. The sintering profile is illustrated in Figure 6 - 3.

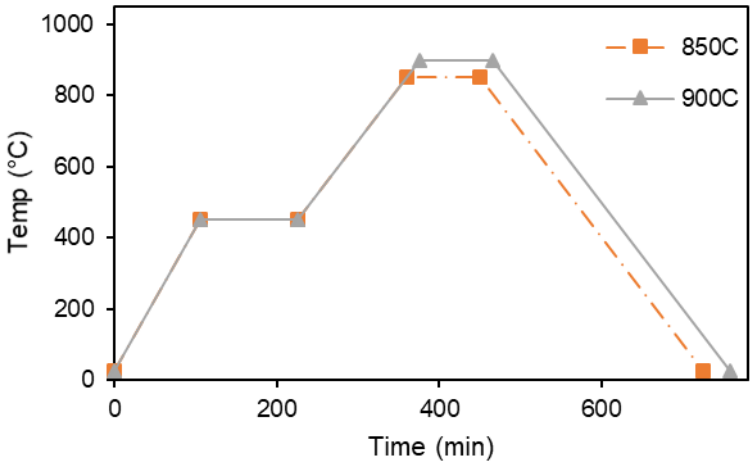

Figure 6 - 3 Sintering profile of spin coated In_2O_3.

Two annealing temperatures (850°C and 900°C) were used for each type of materials. The patterned tiles were snapped into individual pieces before sintering to avoid damage that may occur if snapping carried out afterwards. As illustrated in Figure 6 - 4, the results showed an intact structure. These individual tiles were then welded and packaged in to TO5 housing.

Figure 6 - 4 Spin coated In_2O_3 based samples sintered at 850°C.

6.3 Material Characterisation

The microstructure of the sensing material was examined by scanning electron microscopy (SEM) at 15 kV using Zeiss Supra 55 (Zeiss, Germany). The results are shown in Figure 6 - 5, Figure 6 - 6, and Figure 6 - 7 for In_2O_3, PdO-In_2O_3, and PtO_2-In_2O_3 respectively. Samples annealed at 850°C and 900° display porous structures

with particles size measured at average of 0.3 – 0.6 µm across all the surface. The thickness of the sensing material on alumina sensor substrate was measured using Contour GT 3D Optical Microscope (Bruker, USA) and found to be at 9 ± 1 µm (In_2O_3), 7.5 ± 2 µm (PdO-In_2O_3), and 8 ± 1 µm (PtO_2-In_2O_3).

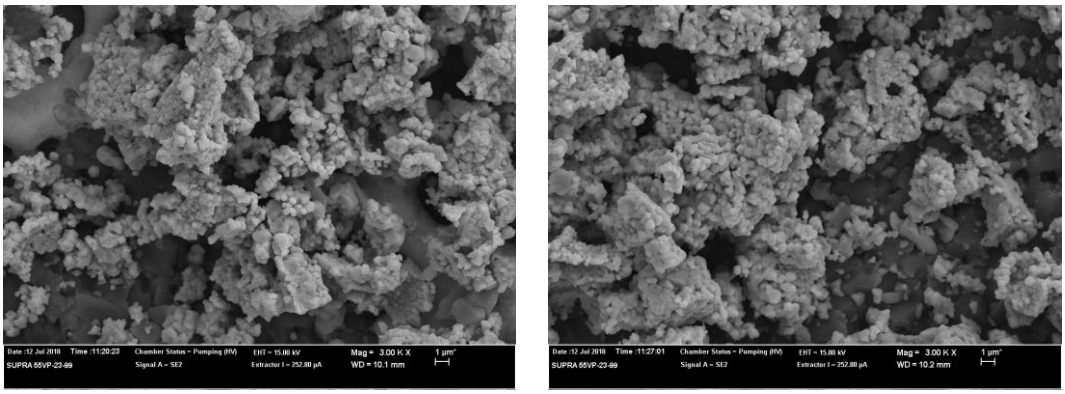

Figure 6 - 5 SEM images of pure In_2O_3 sensor annealed at 850°C (left) and 900°C (right).

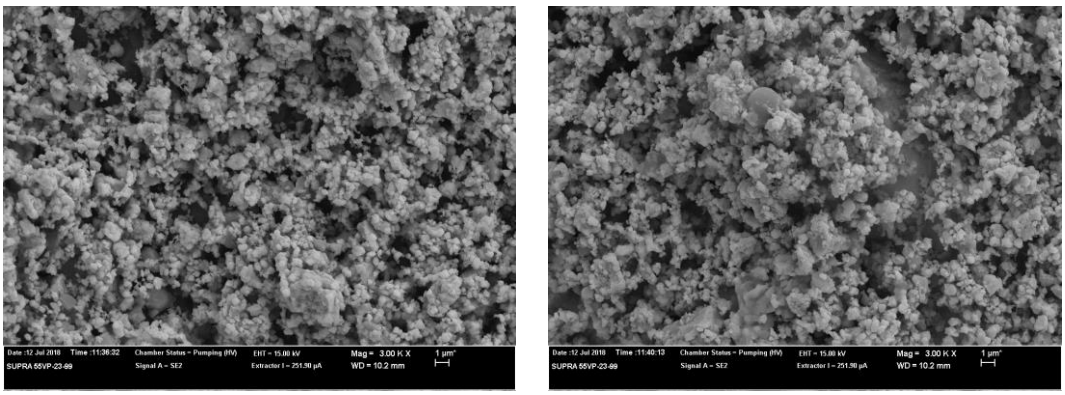

Figure 6 - 6 SEM images of PdO-In_2O_3 sensor annealed at 850°C (left) and 900°C (right).

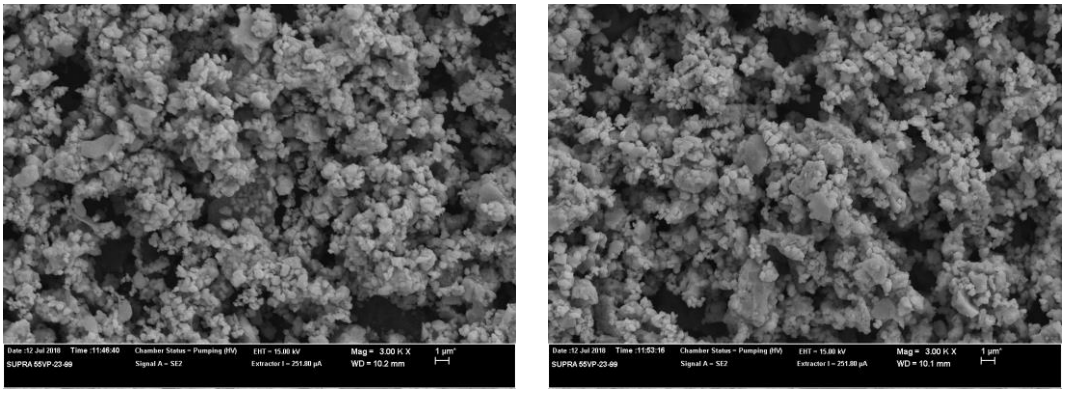

Figure 6 - 7 SEM images of PtO_2 - In_2O_3 sensor annealed at 850°C (left) and 900°C (right).

Comparison of the microstructure of the sensors at a higher magnification (Figure 6 - 8) show presence of nanoparticles (NPs) in PdO-In_2O_3 and PtO_2-In_2O_3 samples, which could be attributed to Pd and Pt NPs respectively. These NPs are not present in bare In_2O_3 samples.

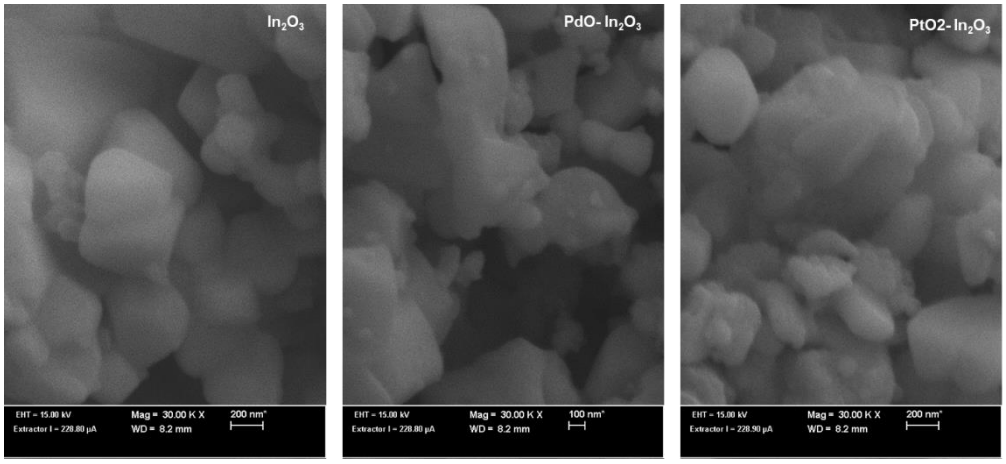

Figure 6 - 8 SEM images of In_2O_3 based sensor annealed at 850°C at a higher magnification.

Energy-dispersive X-ray spectroscopy (EDS or EDX) analysis also carried out using Oxford Instruments in conjunction with Zeiss Supra 55 (Zeiss, Germany). The analysis was intended to obtain the elemental composition for each type of the sensors and to confirm the presence of the decoration. The spectrum of the films, as seen in Figure 6 - 9, confirms the presence of indium and oxygen as expected. Other

elements such as aluminium (Al) and gold (Au) were detected as they were part of the substrate. Au was also used as the coating for the sensing material. Tungsten (W) was not expected but showed in the spectrum, which could be sign of contamination. The pot used to hold the sensor was used previously for tungsten, so it was possible some remained in the pot even after being cleaned. No peaks corresponding to platinum or palladium were detected in decorated films, likely due to small quantity of decorations used (≤1 wt%).

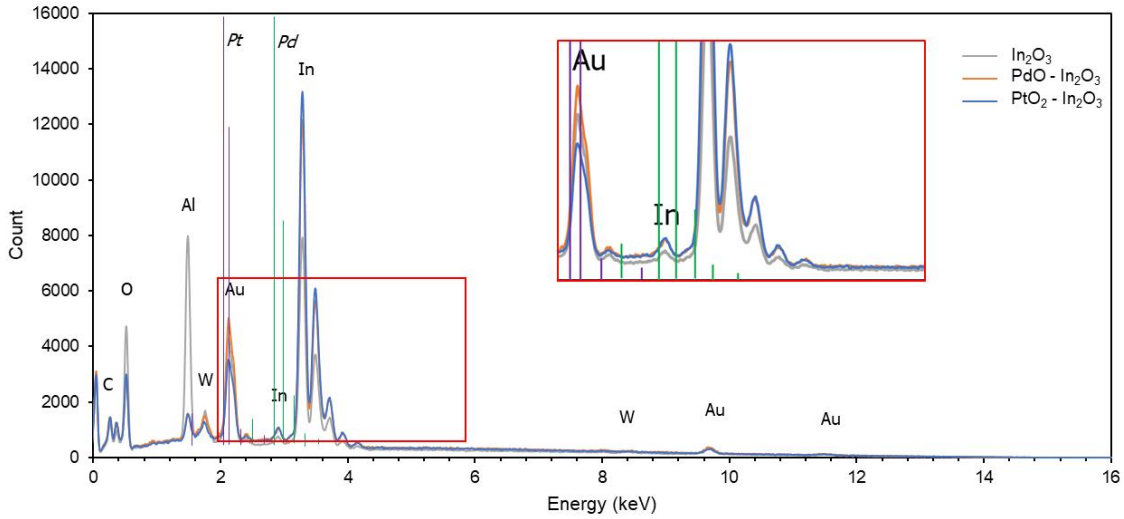

Figure 6 - 9 EDS spectrum of indium oxide-based sensors deposited by spin coating.

X-ray Powder Diffraction (XRD) analysis was conducted to provide supporting information on the material identification. The XRD data were collected with a PANalytical Aeris using Cu-Kα source (Malvern PANalytical, UK). Samples were prepared by removing the films from the substrates and grinding them into fine powders. The patterns (Figure 6 - 10) show diffraction peaks that are characteristics of the cube phase of In_2O_3 with the strongest peak centred at $2\theta = 30.5°$. The patterns of the decorated samples show mainly the strong reflection of indium oxide. No peaks of either platinum or palladium were observed.

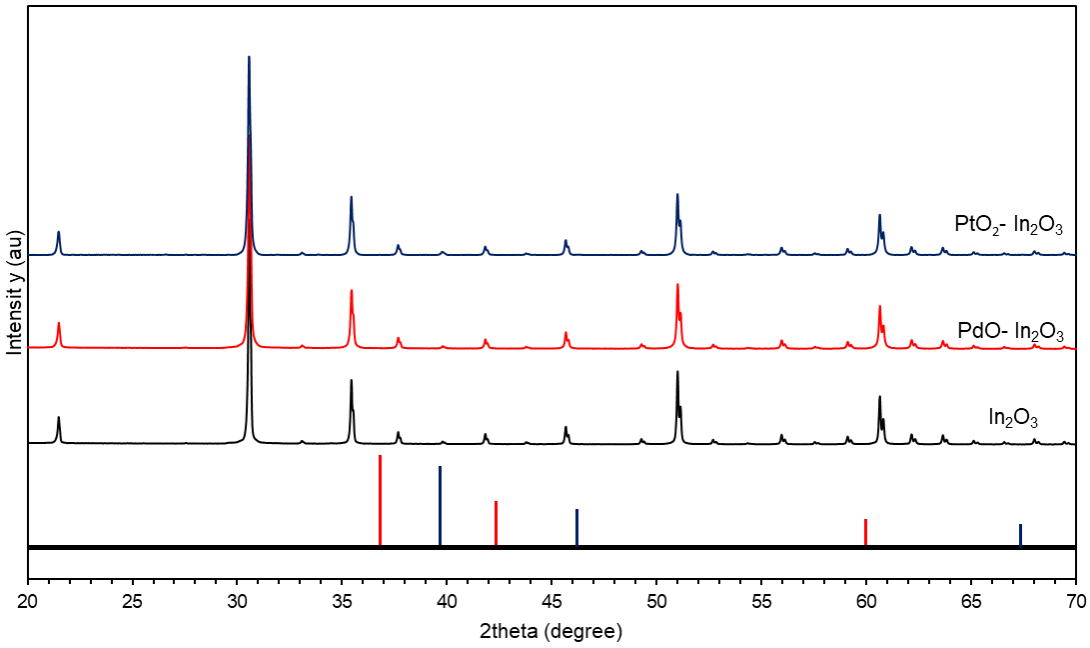

Figure 6 - 10 XRD patterns of indium oxide-based sensors deposited by spin coating.

In order to obtain a more detailed chemical composition of the samples, X-ray photoelectron spectroscopy (XPS) analysis was conducted and the spectra of the samples were compared. The complete spectra shown in Figure 6 - 11 (a) confirms the presence of In, O, and C atoms in decorated and pure In_2O_3 samples. Because the content of PdO/PtO_2 decoration is relatively small, the XPS peaks of the elements are not obvious in the survey. The details of In 3d XPS spectra of the samples in Figure 6 - 11 (b) display two intense peaks centred at 444.08 eV and 451.68 eV associated with the In $3d_{5/2}$ and In $3d_{3/2}$ respectively. These binding energies are consistent with the reference values found for In_2O_3 [19, 20]. XPS spectrum of palladium oxide decorated sensor (Figure 6 - 11 (c)) shows binding energies at 336.48 and 342.38 eV, associated with Pd $3d_{5/2}$ and $3d_{3/2}$ respectively. These values are consistent with the reference values found for PdO [21, 22]. As for platinum oxide decorated sensor, the spectrum displays binding energies at 74.68 and 79.38 eV,

associated with the Pt $4f_{7/2}$ and Pt $4f_{5/2}$ respectively. These peaks are attributed to PtO_2 as observed previously [23, 24].

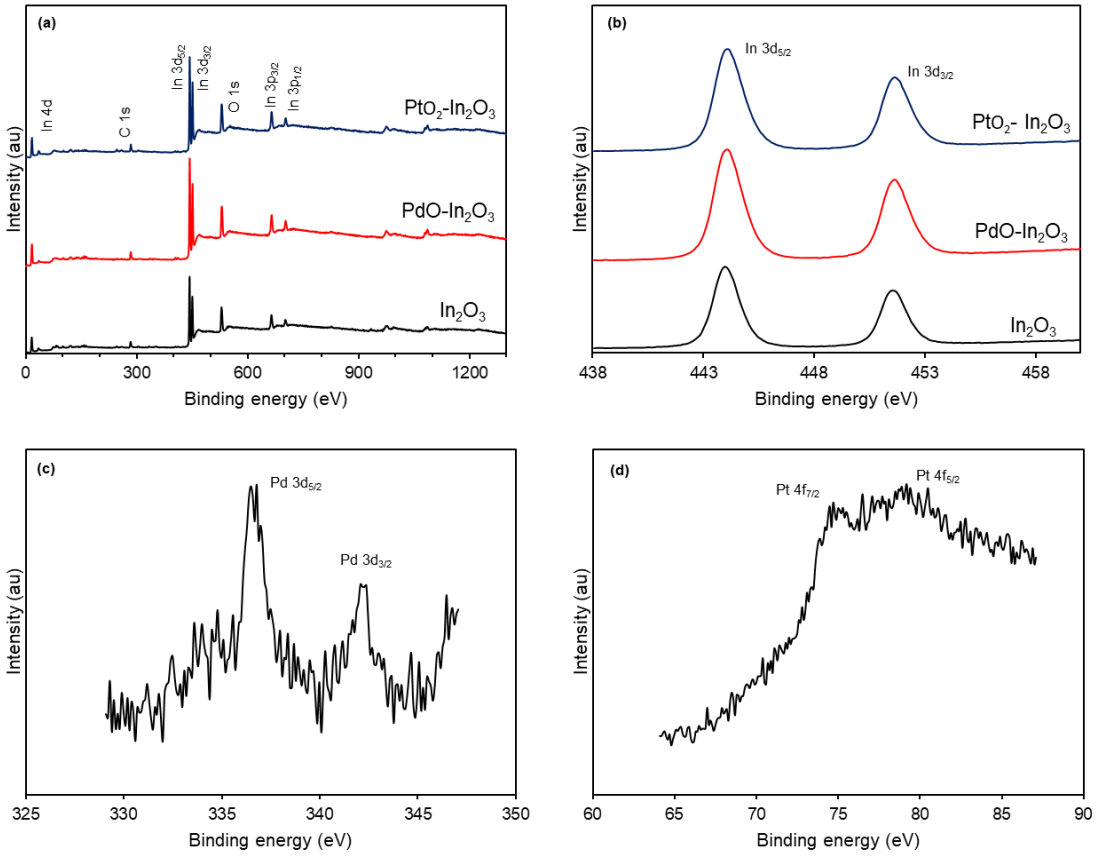

Figure 6 - 11 **(a)** Survey, **(b)** In 3d high resolution XPS spectra of In_2O_3, PdO-In_2O_3, and PtO_2-In_2O_3, **(c)** Pd 3d high resolution XPS spectrum of PdO-In_2O_3, **(d)** Pt 4f high resolution XPS spectrum of PtO=-In_2O_3.

6.4 Gas Testing

The fabricated indium oxide-based sensors were tested for oxygen at concentrations ranging between 0% and 20%. The test conditions were also varied to examine how it affected the sensor responses. This was achieved by carrying out the experiment in dry and wet/humid air and varying the working temperatures from 150° to 400°C.

6.4.1 Indium Oxide Films (In_2O_3)

Resistance differences were observed when In_2O_3 films were operated at different temperatures. At 200°C, sensor resistance from films annealed at 850°C was measured at 350 kOhm in dry ambient air. This increased to about 550 kOhm when the temperature was ramped up to 250°C. Further increase in temperature led to a decrease in resistance (150 kOhm at 300°C, 30 kOhm at 350°C, and 13 kOhm at 400°C). This is also the case for tests carried out in wet air (85% RH) where the resistance was found to be lower than in dry air. The sensor resistance when exposed to 20% humid O_2 was measured to be around 170 kOhm at 200°C. The resistance then increased to 300 kOhm at 250°C before decreasing to 80 kOhm at 300°C.

The fractional response (R_g/R_a) is illustrated in Figure 6 - 12, which shows that the best response was achieved at 300°C **(R_g/R_a = 5.5)** for sensors in dry air and at 250°C **(R_g/R_a = 7.3)** in humid air. The response and recovery times for sensors in dry air were calculated at 3 and 5 minutes. This is much faster than the response and recovery times calculated in humid air at around 14 and 11 minutes respectively.

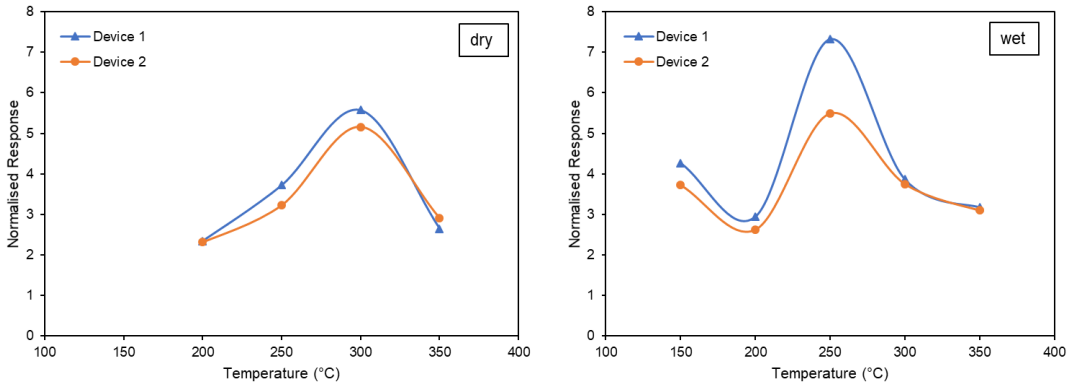

Figure 6 - 12 In_2O_3 (annealed at 850°C) responses to 20% O_2 in dry and humid environment.

Repeated measurements were undertaken using the same sensors and/or sensors fabricated by the same procedure, which showed reproducible responses as highlighted in Figure 6 - 13.

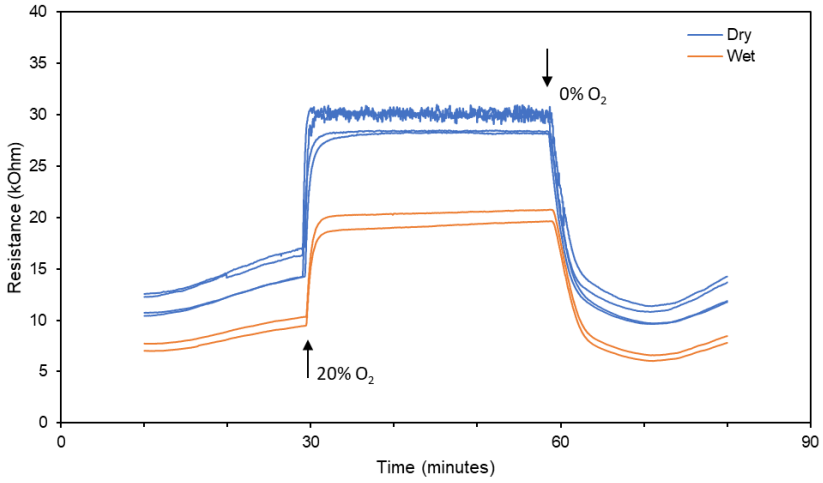

Figure 6 - 13 Resistance of In_2O_3 (annealed at 850°C) exposed to oxygen in dry and humid air at 350°C.

In_2O_3 films annealed at 900°C showed a lower resistance and a lower response than films annealed at 850°C. Sensor resistance at 150°C was around 26 kOhm, which reduced to 23 kOhm at 200°C and then increased to 25 kOhm at 250-300°C. At higher temperature (350°C), the resistance further increased to about 38 kOhm. The best response was observed at 300°C **(R_g/R_a = 3.1)**. Tests carried out in humid air generally showed higher resistance, especially at lower temperatures (76 kOhm at 150°C and 74 at 200°C). The best response was calculated higher **(R_g/R_a = 4.0)** also at 300°C. Sensor responses at different temperatures can be seen in Figure 6 - 14. The response time was calculated at 11 and 13 minutes for dry and humid air respectively. The recovery time was slightly faster at 10 minutes (dry air) and 9 minutes (humid air).

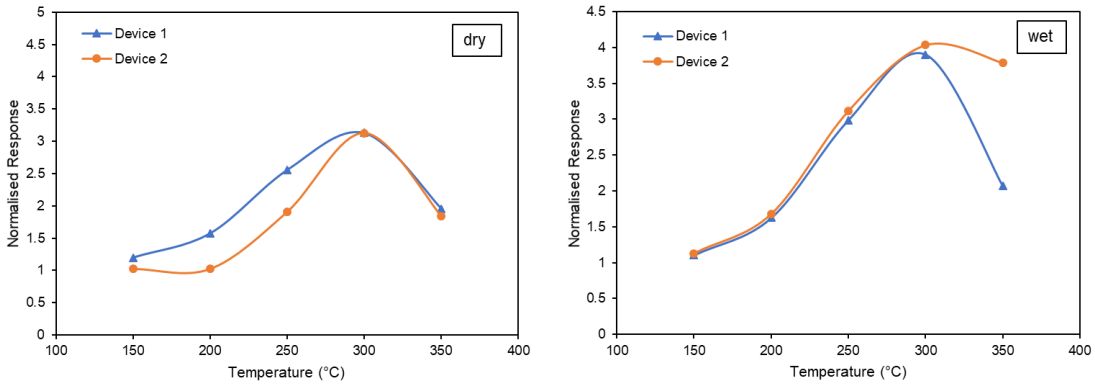

Figure 6 - 14 In_2O_3 (annealed at 900°C) responses to 20% O_2 in dry and humid environment.

6.4.2 Palladium Oxide Decorated Indium Oxide Film ($PdO\text{-}In_2O_3$)

Indium oxide films decorated with palladium showed lower resistance than pure indium oxide films. In ambient dry air at 200°C, the resistance of $PdO\text{-}In_2O_3$ films annealed at 850°C was found to be 250 kOhm, which decreased with increasing temperature (85 kOhm at 250°C, 10 kOhm at 300°C, and further reduced to about 3 kOhm at 350°C). In humid air, the resistance of Pd-decorated films at 200°C was around 25 kOhm, which reduced to 6 kOhm at 250°C, 4 kOhm at 300°C, and 1 kOhm at 350°C. The best response as seen in Figure 6 - 15, was calculated at 200°C **(R_g/R_a = 5.5)** for dry air and at 350°C **(R_g/R_a = 7.2)** for humid air.

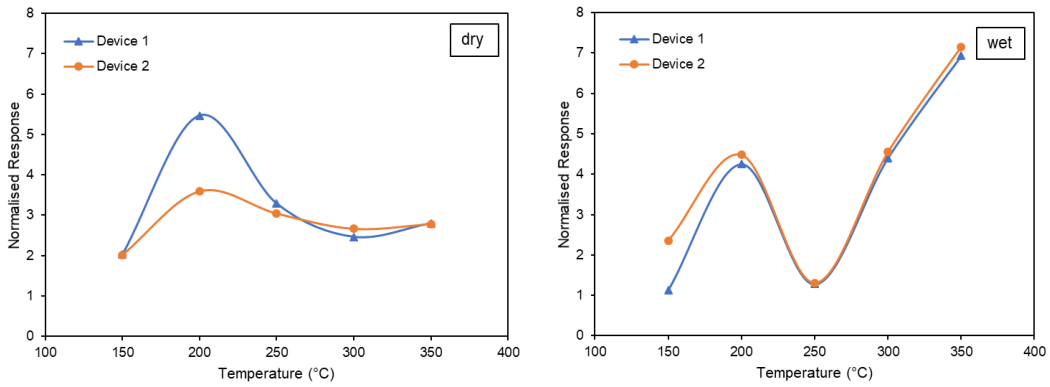

Figure 6 - 15 $PdO\text{-}In_2O_3$ (annealed at 850°C) responses to 20% O_2 in dry and humid environment.

In dry ambient air, PdO-In_2O_3 films annealed at 900°C exhibited lower resistance in lower temperature (220 kOhm at 200°C and 12 kOhm at 250°C) and higher resistance in higher temperature (19 - 20 kOhm at 300 and 350°C). The best response was found at 300-350°C **(R_g/R_a = 2.5-2.6)**. In humid air, the resistance was observed to be lower at 10 kOhm at 200°C. This reduced to 7.5 kOhm at 250°C and then increased back to around 10 kOhm at 300°C and 350°C. The best response was observed at **R_g/R_a = 6.0-6.3** (T = 300 - 350°C) as shown in Figure 6 - 16.

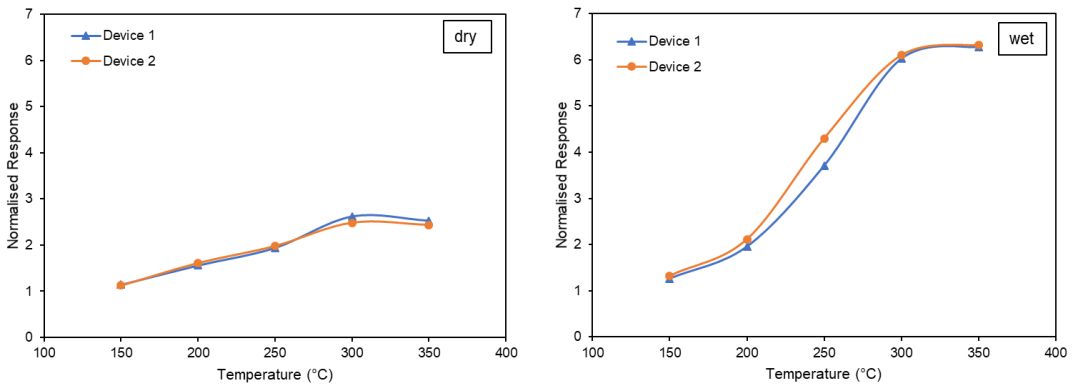

Figure 6 - 16 PdO-In_2O_3 (annealed at 900°C) responses to 20% O_2 in dry and humid environment.

The response and recovery time are summarised in Table 6 - 2. The response time and recovery time of the palladium oxide decorated sensors were found to be higher in wet air than dry air. The response and recovery time from sensors annealed at 850°C were particularly slow. As the tests were conducted in a controlled environment with the same settings for all the sensors, the slow response was most likely due to changes in sensor microstructure which may lead to reduced response and slower rate of response experimentally observed here. Annealing process involved in sensor fabrication could produce a mismatch of thermal expansion coefficient from sensor substrate and sensing layer is likely to occur, producing the variation in sensor morphology that would change the sensor characteristics. Here, faster response and recovery time were also observed from wet air. In humid

environment, water molecules are adsorbed on the on the surface of metal oxide, forming hydroxyl groups and blocking the water-absorbable sites. This reduces the actives sites for the adsorbed oxygen species. As the surface area decreases, the adsorption of oxygen species occurs at a faster rate as observed here. This is in agreement with a discussion on hydroxyl groups that may act as promotors or inhibitors of adsorption of the gas [25].

Table 6 - 2 Response and recovery time of PdO-In_2O_3 films.

Annealing Temp (°C)	Environment	Response time (min)	Recovery time (min)
850	dry	24	23
850	wet (85% RH)	6	5
900	dry	14	11
900	wet (85% RH)	4	6

6.4.3 Platinum Oxide Decorated Indium Oxide Film (PtO_2- In_2O_3)

Indium oxide films decorated with platinum showed generally a lower resistance compared to pure In_2O_3 and PdO-In_2O_3 films. In ambient dry air at 200°C, the resistance of PtO_2-In_2O_3 films annealed at 850°C was measured at 3.5 kOhm, which increased to up to 8 kOhm at 250°C. Further increase in temperature reduced the resistance to 4 kOhm at 300°C and 1 kOhm at 350°C. In these conditions, the best response was found to be at 350°C **(R_g/R_a = 5.4)** with response and recovery time calculated at 4 and 6 minutes respectively. The resistance reduced further in humid air at lower temperatures, but as the temperatures increased to ≥300°C, the resistance in dry and humid air were similar (Figure 6 - 17). The response, illustrated in Figure 6 - 18, was calculated almost 200% higher at **R_g/R_a = 9.6** (T = 350°C). The response and recovery time were found at 11 and 9 minutes respectively.

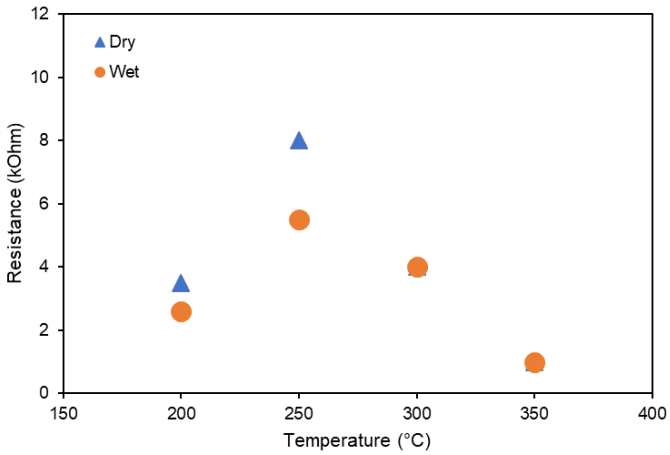

Figure 6 - 17 PtO_2- In_2O_3 (annealed at 850°C) resistance to 20% O_2 in dry and humid environment.

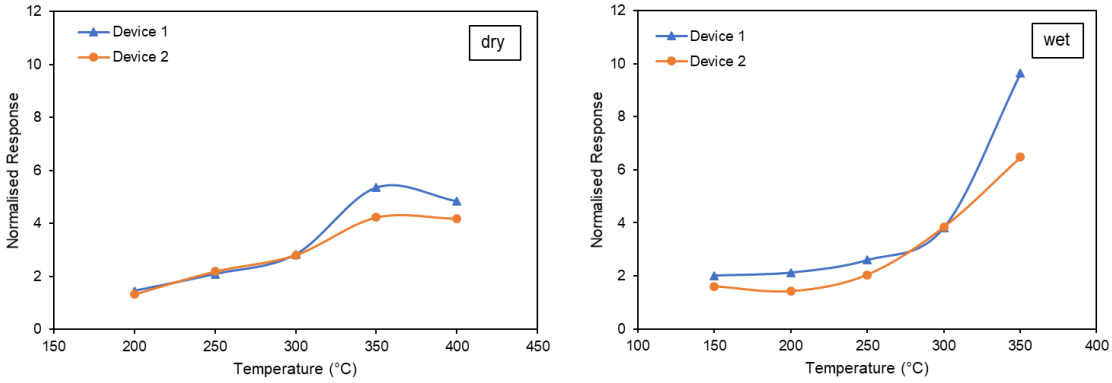

Figure 6 - 18 PtO_2-In_2O_3 (annealed at 850°C) responses to 20% O_2 in dry and humid environment.

The resistance of films annealed at 900°C was higher at lower temperature (≤200°C) in dry air. At 250°C and, the resistance was observed at 2 kOhm, which increased slightly to 2.3 kOhm at 300°C and further reduced to 0.5 kOhm at 350°C. At 200°C, the resistance was found to be much lower at 1.6 kOhm in humid air. As the temperatures ramped up to 250°C and higher, the resistance was found to be similar in both dry and humid air as shown in Figure 6 - 19. The best response was observed at 350°C for both conditions with higher response noted at $\mathbf{R_g/R_a = 15}$ in dry air compared to $\mathbf{R_g/R_a = 4.5}$ in wet air (Figure 6 - 20). The response and recovery time are summarised in Table 6 - 3.

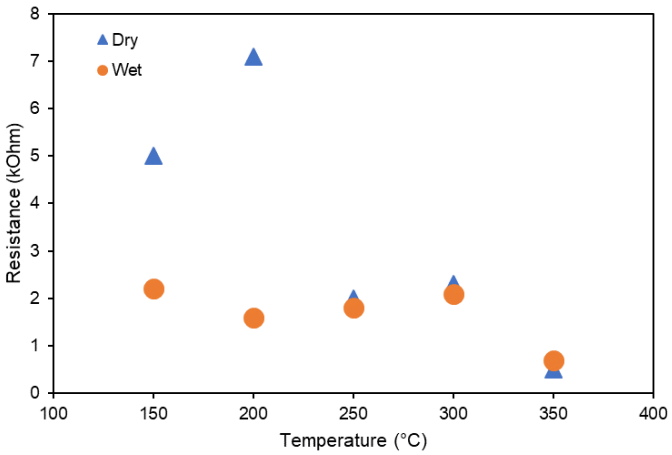

Figure 6 - 19 PtO_2- In_2O_3 film (annealed at 900°C) resistance to 20% O_2 in dry and humid environment.

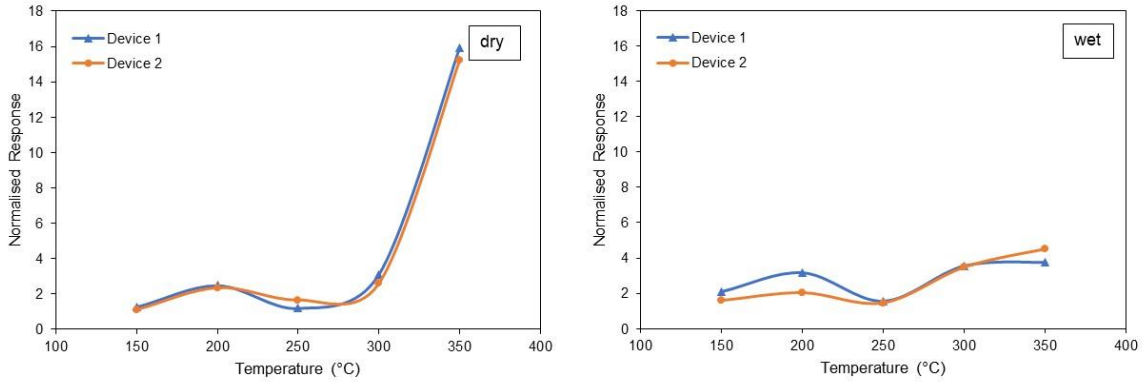

Figure 6 - 20 PtO_2-In_2O_3 film (annealed at 900°C) responses to 20% O_2 in dry and humid environment.

Table 6 - 3 Response and recovery time of PtO_2-In_2O_3 films.

Annealing Temp (°C)	Environment	Response time (min)	Recovery time (min)
850	Dry	4	6
850	Wet	11	9
900	Dry	15	3
900	wet	6	3

6.5 Analysis and Discussion

The gas sensing results presented here show that gas responses are influenced by the operating temperature, material microstructure, humidity, and decoration of noble metal. Each will be discussed in further details in the following.

6.5.1 Effect of Operating Temperature

Operating temperature has been known to affect sensor performance [11, 26-27]. At lower temperatures, dissociation of oxygen molecules is not favoured as not enough energy is present to overcome the activation energy needed. At a higher temperature range, oxygen molecules can dissociate and adsorbed on the surface of the metal oxide. In this range, the abstraction of electrons from the surface occurs at a high rate, leading to a higher response and faster response time than in a lower temperature range. A further increase in temperature will lead to sensor overcoming desorption barrier. At this point, the response of the sensor is usually decreased as desorption becomes predominant.

The discussion on the operating temperature effects is presented here based on the results discussed in the earlier section, taking example of the sensors annealed at 850°C and tested in dry air. Indium oxide sensors exhibited best response at 300°C **(R_g/R_a = 5.5)**. The resistance of the sensors was higher at lower temperatures and

lower at higher temperatures as illustrated in Figure 6 - 21. For the decorated sensors, PdO-In_2O_3 and PtO_2-In_2O_3 films showed best response at 200°C **(R_g/R_a = 5.5)** and 350°C **(R_g/R_a = 5.4)** respectively.

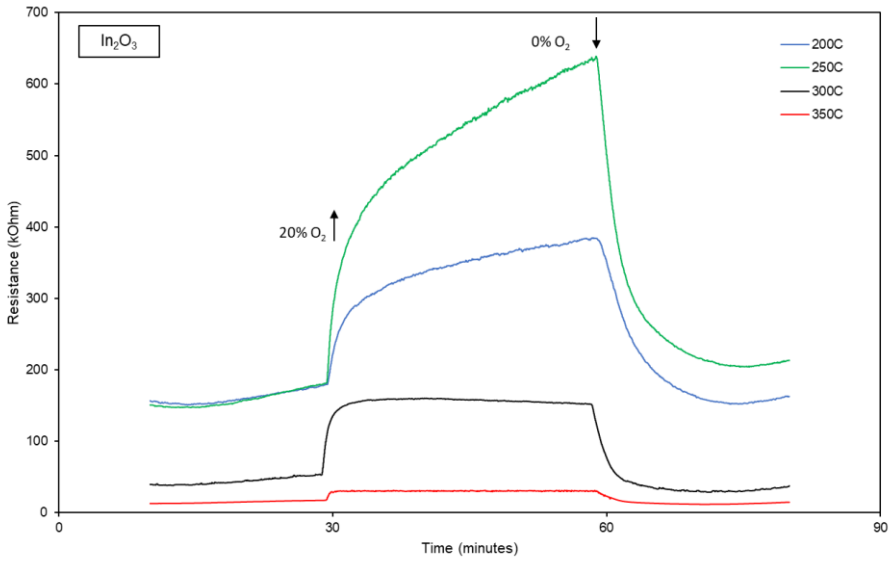

Figure 6 - 21 Example of In_2O_3 sensor responses to 20% dry O_2 at various operating temperatures.

Decorated sensors also presented a higher resistance at lower temperatures and lower resistance at higher temperatures (higher temperatures for platinum oxide decorated sensors were not tested due to low resistance ≤1 kOhm). Changing temperature is clearly shown to affect the sensor performance. Therefore, tests need to be carried out to find the optimum operating temperature for any fabricated sensors.

6.5.2 Effect of Sintering Temperature

The microstructure of sensors sintered at 850ºC are quite similar to those sintered at 900ºC. Both exhibit good porosity that will facilitate gas adsorption. Lower sintering temperatures, as previously mentioned in Chapter 5, results in more porosity, which in turn leads to better sensor response.

In this work, pure indium oxide sensors show better performance that those from films annealed at lower temperature. Response of pure indium oxide annealed at 850ºC **(R_g/R_a= 5.5)** is almost twice higher than sensors annealed at 900ºC **(R_g/R_a= 3.1)** in dry air. Similarly, films decorated with palladium oxide (annealed at 850ºC) showed the best response at **R_g/R_a= 5.5** compared to **R_g/R_a= 2.6** for film annealed at 900ºC. Sensors decorated with platinum oxide show a higher response from film annealed 900ºC **(R_g/R_a= 15 vs R_g/R_a= 5.4),** which contradicts the results from the other sensors. This singularity might be caused by the presence of the catalyst in the sensing film and will be discussed further in a later section.

Comparison of the test results with the literature showed similar outcomes. For example, Jørgensen et al. [28] found the microstructure of composite electrodes comprising lanthanum strontium manganate (LSM) and yttria stabilised zirconia (YSZ) was found to be less dense with smaller grains size as the sintering temperatures decreased. The performance of the LSM-YSZ composite cathode improved when the sintering temperature was lowered. Similarly, Naisbitt et al. [29] found the particles size of chromium titanate (CTO) sensors to be increasing with increasing sintering temperature. The transient response of CTO to carbon monoxide showed a higher response from sensors sintered at lower temperatures. Zhang and Liu [30] reported lower sintering temperature of SnO_2(CuO) sensors obtained a more porous microstructure and reduce particles size, which lead to improvement in sensor response.

6.5.3 Effect of Humidity

The results showed sensors overall responded better under humid environment. Pure indium oxide films (850ºC) for example, showed best response at **R_g/R_a= 5.5** (300ºC) in dry air whereas in wet the response increased up to **R_g/R_a= 7.3** (250ºC).

Decorated sensors also showed higher response under humid condition. PdO-In_2O_3 annealed at 900ºC had best response at **R_g/R_a= 2.6** (300ºC) in dry air, much lower compared to the response in wet air at **R_g/R_a= 6.3** (300-350ºC). For sensor with platinum oxide decoration (850ºC), the response at 350ºC in dry **(R_g/R_a= 5.4)** was lower than in humid environment **(R_g/R_a= 9.6).** PtO_2-In_2O_3 annealed at 900ºC also showed a lower response in dry air up to 300ºC. At 350ºC, sensor showed higher response in dry **air (R_g/R_a= 15 vs R_g/R_a= 4.5)**.

As previously discussed in Chapter 5, the presence of water molecules reduced the sensor resistance and so reduced the sensor response. This is supported by studies on the effect of humidity found in the literatures [31-34]. Here, lower resistance was also observed when introducing humidity to the sensors (Figure 6 - 22). As water molecules dissociate with oxygen molecules, hydroxyl ions are formed. This leads to less oxygen species adsorbed on the surface of the metal oxide and so decrease the sensor resistance. However, this resistance decrease was found to improve sensor performance (except for PtO_2 decorated sensor aforementioned), which contradicts the results obtained in Chapter 5 as well as literatures.

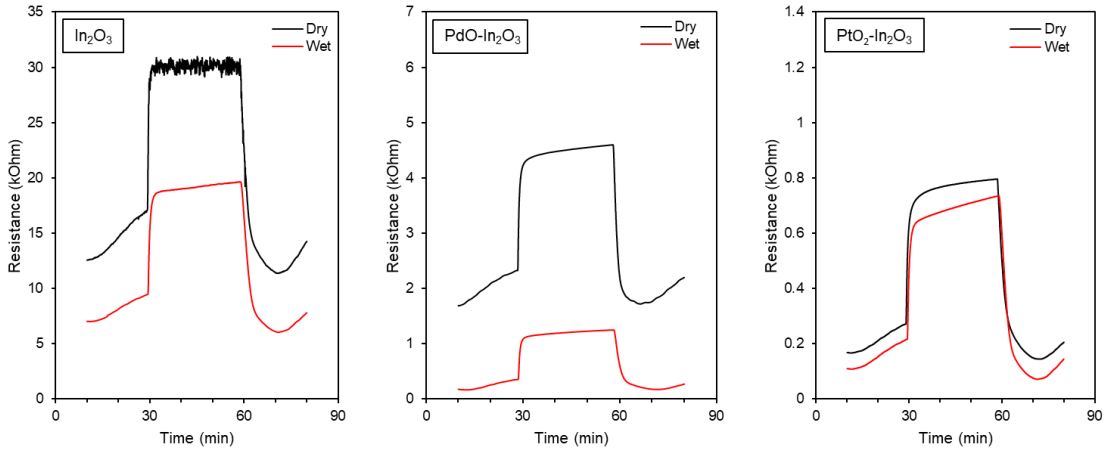

Figure 6 - 22 Resistance of indium oxide-based sensors in dry and humid environment at 350°C.

In chapter 5, the sensor baseline resistance was not affected by humidity as the values were similar in dry and humid air. Hence, lower resistance in humid air resulted in lower response, which is not the case for indium oxide-based sensors. Many studies in the literatures, as reported here, tested their sensors to reducing gases and under different humidity levels (dry/humid). This work was aimed to detect oxygen hence the measurement for lower oxygen concentration was carried out under nitrogen gas. The experiments here revealed that the baseline of the sensors was also affected by the humidity (reduced resistance) at a higher rate. Therefore, introducing humidity for indium oxide-based gas sensors lead to an increase in sensor response.

6.5.4 Effect of Catalyst

The addition of palladium oxide and platinum oxide to indium oxide lead to a decrease in sensor resistance as shown in Figure 6 - 23. For example, indium oxide (annealed at 850°C) exhibited resistance 550 kOhm at 300°C in dry air whilst under the same condition, the resistance of decorated sensors dropped to 8 kOhm for palladium and 4 kOhm for platinum.

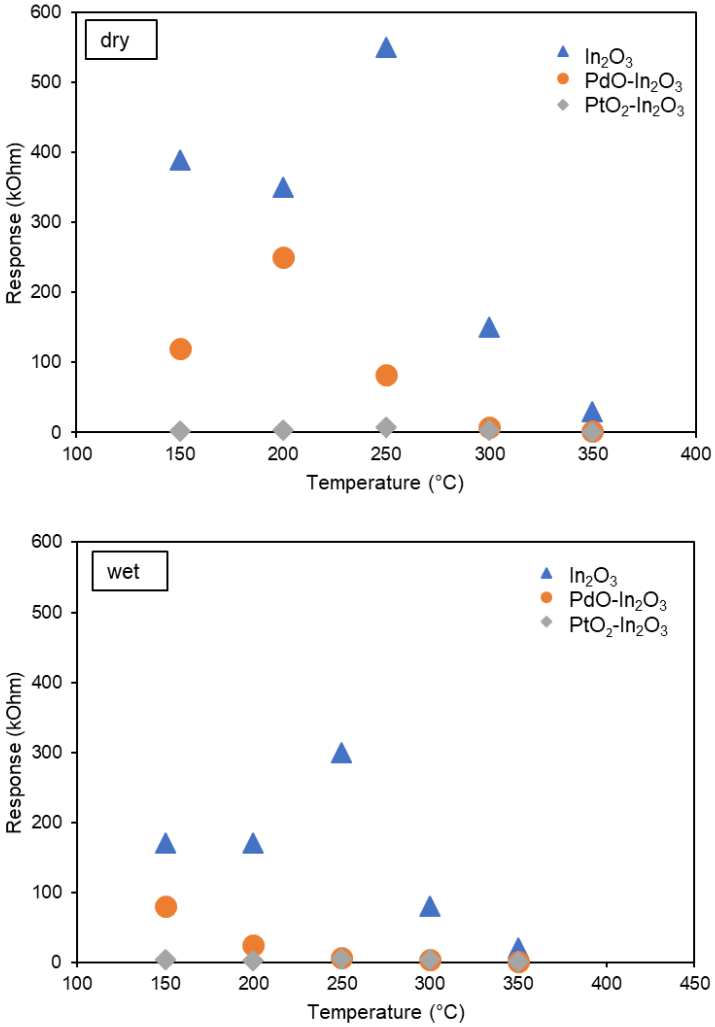

Figure 6 - 23 Resistance of the indium oxide-based sensors in dry (top) and humid environment (bottom).

The role of the catalyst in metal oxide gas sensors has been proposed by two sensitisation mechanisms, i.e. chemical and electronic sensitisation [35]. For palladium, electronic sensitisation is more likely to occur as it formed oxides in air and reduced to metal upon contact with inflammable gas. XPS analysis confirmed the presence of palladium oxide in the film. Upon contact the palladium oxide particles will exchange electrons with indium oxide, with the direction of exchange expected toward In_2O_3. Data found in the literature showed the conduction band of In_2O_3 at 3.55 – 3.85 eV [36] whereas PdO at about – 4.00 [37]. The potential difference provides a

considerable driving force from the electrons in PdO to populate the conduction band of In_2O_3. This would increase the carrier concentration and therefore reduce the resistance of the sensors which was observed experimentally. The response of the pure In_2O_3 and PdO decorated In_2O_3 sensors were quite similar in dry air as the electrons exchange would not enhance sensitivity of the sensors.

Electronic sensitisation is likely to occur for platinum decorated sensors as well. XPS analysis confirmed the presence of platinum oxide in the film although the intensity of the peaks was found to be rather weak. Upon exposure to oxygen, the potential difference of indium oxide and platinum oxide will drive electrons from PtO_2 to populate the conduction band of the indium oxide. The response from PtO_2-In_2O_3 sensors was similar with pure In_2O_3 except at 350°C. Here, enhanced response was observed (instead of reduced) at 350°C and more significantly for films annealed at 900°C. This enhanced sensitivity could be due to changes in oxygen partial pressure, which would change electron density at the PtO_2 particles and this was reflected by a measured change in In_2O_3 resistance, however there was no evidence to support this. On the other hand, spill-over mechanism cannot be ruled out either. Spill-over could take place whereby PtO_2 could act to spill-over oxygen, increasing the O_2 population on the surface of metal oxide. If the decoration enriched In_2O_3 with oxygen species, this could explain a higher response towards oxygen.

6.6 Conclusion

Deposition of indium oxide-based sensors were carried out by spin coating to create a thin film pure and decorated In_2O_3 with palladium oxide and platinum oxide. Sensors were tested for oxygen and the responses were varied depending on the annealing temperature, operating temperature, humidity level, and presence of

catalyst. Optimum operating temperature was found at 300°C (In_2O_3), 200°C (PdO-In_2O_3), and 350°C (PtO_2-In_2O_3). Higher annealing temperature lead to lower sensor responses. Humidity reduced resistance of the sensors but overall enhanced sensor sensitivity. Addition of palladium oxide and platinum oxide decorations to indium oxide decreased the resistance of the sensors but no significant changes in response were observed.

6.7 References

[1] X. Duan, Y. Huang, Y. Cui, J. Wang, and C. M. Lieber, "Indium phosphide nanowires as building blocks for nanoscale electronic and optoelectronic devices," *Nature,* vol. 409, p. 66, 01/04/online 2001.

[2] T. Margalith *et al.*, "Indium tin oxide contacts to gallium nitride optoelectronic devices," *Applied Physics Letters,* vol. 74, no. 26, pp. 3930-3932, 1999.

[3] M. H. Ahn, E.-S. Cho, and S. J. Kwon, "Effect of the duty ratio on the indium tin oxide (ITO) film deposited by in-line pulsed DC magnetron sputtering method for resistive touch panel," *Applied Surface Science,* vol. 258, no. 3, pp. 1242-1248, 2011/11/15/ 2011.

[4] C. D. Sheraw *et al.*, "Organic thin-film transistor-driven polymer-dispersed liquid crystal displays on flexible polymeric substrates," *Applied Physics Letters,* vol. 80, no. 6, pp. 1088-1090, 2002/02/11 2002.

[5] S. Masato, H. Masatoshi, K. Susumu, and S. Hiroyasu, "Characteristics of Indium-Tin-Oxide/Silver/Indium-Tin-Oxide Sandwich Films and Their Application to Simple-Matrix Liquid-Crystal Displays," *Japanese Journal of Applied Physics,* vol. 40, no. 5R, p. 3332, 2001.

[6] H. Imai, A. Tominaga, H. Hirashima, M. Toki, and M. Aizawa, "Ultraviolet-Laser-Induced Crystallization of Sol-Gel Derived Indium Oxide Films," *Journal of Sol-Gel Science and Technology,* vol. 13, no. 1, pp. 991-994, 1998/01/01 1998.

[7] J. S. Kim *et al.*, "Indium–tin oxide treatments for single- and double-layer polymeric light-emitting diodes: The relation between the anode physical, chemical, and morphological properties and the device performance," *Journal of Applied Physics,* vol. 84, no. 12, pp. 6859-6870, 1998/12/15 1998.

[8] H. Yamaura, T. Jinkawa, J. Tamaki, K. Moriya, N. Miura, and N. Yamazoe, "Indium oxide-based gas sensor for selective detection of CO," *Sensors and Actuators B: Chemical,* vol. 36, no. 1, pp. 325-332, 1996/10/01/ 1996.

[9] N. Du *et al.*, "Porous Indium Oxide Nanotubes: Layer-by-Layer Assembly on Carbon-Nanotube Templates and Application for Room-Temperature NH3 Gas Sensors," *Advanced Materials,* vol. 19, no. 12, pp. 1641-1645, 2007/06/18 2007.

[10] M. Suchea, N. Katsarakis, S. Christoulakis, S. Nikolopoulou, and G. Kiriakidis, "Low temperature indium oxide gas sensors," *Sensors and Actuators B: Chemical,* vol. 118, no. 1, pp. 135-141, 2006/10/25/ 2006.

[11] N. Barsan, D. Koziej, and U. Weimar, "Metal oxide-based gas sensor research: How to?," *Sensors and Actuators B: Chemical,* vol. 121, no. 1, pp. 18-35, 2007/01/30/ 2007.
[12] N. Barsan and U. Weimar, "Conduction Model of Metal Oxide Gas Sensors," *Journal of Electroceramics,* journal article vol. 7, no. 3, pp. 143-167, December 01 2001.
[13] E. Comini, A. Cristalli, G. Faglia, and G. Sberveglieri, "Light enhanced gas sensing properties of indium oxide and tin dioxide sensors," *Sensors and Actuators B: Chemical,* vol. 65, no. 1, pp. 260-263, 2000/06/30/ 2000.
[14] K. K. Makhija, A. Ray, R. M. Patel, U. B. Trivedi, and H. N. Kapse, "Indium oxide thin film based ammonia gas and ethanol vapour sensor," *Bulletin of Materials Science,* vol. 28, no. 1, pp. 9-17, 2005/02/01 2005.
[15] C. Xiangfeng, W. Caihong, J. Dongli, and Z. Chenmou, "Ethanol sensor based on indium oxide nanowires prepared by carbothermal reduction reaction," *Chemical Physics Letters,* vol. 399, no. 4, pp. 461-464, 2004/12/01/ 2004.
[16] V. S. Vaishanv, P. D. Patel, and N. G. Patel, "Indium Tin Oxide Thin-Film Sensor for Detection of Volatile Organic Compounds (VOCs)," *Materials and Manufacturing Processes,* vol. 21, no. 3, pp. 257-261, 2006/05/01 2006.
[17] N. G. Patel, P. D. Patel, and V. S. Vaishnav, "Indium tin oxide (ITO) thin film gas sensor for detection of methanol at room temperature," *Sensors and Actuators B: Chemical,* vol. 96, no. 1-2, pp. 180-189, 2003.
[18] J. Xu, Y. Chen, and J. Shen, "Ethanol sensor based on hexagonal indium oxide nanorods prepared by solvothermal methods," *Materials Letters,* vol. 62, no. 8, pp. 1363-1365, 2008/03/31/ 2008.
[19] X. C. Wu, J. M. Hong, Z. J. Han, and Y. R. Tao, "Fabrication and photoluminescence characteristics of single crystalline In2O3 nanowires," *Chemical Physics Letters,* vol. 373, no. 1, pp. 28-32, 2003/05/13/ 2003.
[20] Y. Wang *et al.*, "Room temperature H2S gas sensing properties of In2O3 micro/nanostructured porous thin film and hydrolyzation-induced enhanced sensing mechanism," *Sensors and Actuators B: Chemical,* vol. 228, pp. 74-84, 2016/06/02/ 2016.
[21] K. S. Kim, A. F. Gossmann, and N. Winograd, "X-ray photoelectron spectroscopic studies of palladium oxides and the palladium-oxygen electrode," *Analytical Chemistry,* vol. 46, no. 2, pp. 197-200, 1974/02/01 1974.
[22] M. Brun, A. Berthet, and J. C. Bertolini, "XPS, AES and Auger parameter of Pd and PdO," *Journal of Electron Spectroscopy and Related Phenomena,* vol. 104, no. 1, pp. 55-60, 1999/07/01/ 1999.
[23] V. A. Saveleva *et al.*, "Operando Near Ambient Pressure XPS (NAP-XPS) Study of the Pt Electrochemical Oxidation in H2O and H2O/O2 Ambients," *The Journal of Physical Chemistry C,* vol. 120, no. 29, pp. 15930-15940, 2016/07/28 2016.
[24] T. Dickinson, A. F. Povey, and P. M. A. Sherwood, "X-ray photoelectron spectroscopic studies of oxide films on platinum and gold electrodes," *Journal of the Chemical Society, Faraday Transactions 1: Physical Chemistry in Condensed Phases,* 10.1039/F19757100298 vol. 71, no. 0, pp. 298-311, 1975.
[25] O. Merdrignac-Conanec, Y. Bernicot, and J. Guyader, "Humidity effect on baseline conductance and H2S sensitivity of cadmium germanium oxynitride thick film gas sensors," Sensors and Actuators B: Chemical, vol. 63, no. 1, pp. 86-90, 2000/04/20/ 2000.

[26] K. Wetchakun *et al.*, "Semiconducting metal oxides as sensors for environmentally hazardous gases," *Sensors and Actuators B: Chemical,* vol. 160, no. 1, pp. 580-591, 12/15/ 2011.
[27] E. Comini, "Metal oxide nano-crystals for gas sensing," *Analytica Chimica Acta,* vol. 568, no. 1, pp. 28-40, 2006/05/24/ 2006.
[28] M. J. Jørgensen, S. Primdahl, C. Bagger, and M. Mogensen, "Effect of sintering temperature on microstructure and performance of LSM–YSZ composite cathodes," *Solid State Ionics,* vol. 139, no. 1, pp. 1-11, 2001/01/02/ 2001.
[29] S. C. Naisbitt, K. F. E. Pratt, D. E. Williams, and I. P. Parkin, "A microstructural model of semiconducting gas sensor response: The effects of sintering temperature on the response of chromium titanate (CTO) to carbon monoxide," *Sensors and Actuators B: Chemical,* vol. 114, no. 2, pp. 969-977, 2006/04/26/ 2006.
[30] G. Zhang and M. Liu, "Effect of particle size and dopant on properties of SnO2-based gas sensors," *Sensors and Actuators B: Chemical,* vol. 69, no. 1, pp. 144-152, 2000/09/10/ 2000.
[31] M. Egashira, M. Nakashima, S. Kawasumi, and T. Selyama, "Temperature programmed desorption study of water adsorbed on metal oxides. 2. Tin oxide surfaces," *The Journal of Physical Chemistry,* vol. 85, no. 26, pp. 4125-4130, 1981/12/01 1981.
[32] J. Gong, Q. Chen, M.-R. Lian, N.-C. Liu, R. G. Stevenson, and F. Adami, "Micromachined nanocrystalline silver doped SnO2 H2S sensor," *Sensors and Actuators B: Chemical,* vol. 114, no. 1, pp. 32-39, 2006.
[33] Q. Qi *et al.*, "Electrical response of Sm2O3-doped SnO2 to C2H2 and effect of humidity interference," *Sensors and Actuators B: Chemical,* vol. 134, no. 1, pp. 36-42, 2008/08/28/ 2008.
[34] N. Bârsan and U. Weimar, "Understanding the fundamental principles of metal oxide based gas sensors; the example of CO sensing with SnO 2 sensors in the presence of humidity," *Journal of Physics: Condensed Matter,* vol. 15, no. 20, p. R813, 2003.
[35] N. Yamazoe, "New approaches for improving semiconductor gas sensors," *Sensors and Actuators B: Chemical,* vol. 5, no. 1, pp. 7-19, 1991/08/01/ 1991.
[36] C. Miao, C. Chen, Q. Dai, L. Xu, and H. Song, "Dysprosium, Holmium and Erbium ions doped Indium Oxide nanotubes as photoanodes for dye sensitized solar cells and improved device performance," *Journal of Colloid and Interface Science,* vol. 440, pp. 162-167, 2015/02/15/ 2015.
[37] H. Zhang *et al.*, "PdO Doping Tunes Band-Gap Energy Levels as Well as Oxidative Stress Responses to a Co3O4 p-Type Semiconductor in Cells and the Lung," *Journal of the American Chemical Society,* vol. 136, no. 17, pp. 6406-6420, 2014/04/30 2014.

Chapter 7. Screen Printed Indium Oxide Based Thick Film Sensor

7.1 Introduction

Screen printing has been in use since its invention in China during the Song Dynasty. It then spread to other Asian countries, before later being introduced to Europe in the 18th century. Since then, it has been used in many applications, from printing logos on various garments to posters for marketing and advertisements. The development of screen-printing technology has also enabled deposition of materials over precisely defined areas. The technique can be used in advanced manufacturing for diverse applications, such as printed electronics, medical devices, touch panels, solar cells, RFID, and thick film technology.

In previous chapters, we have explored several deposition techniques to make thin-film metal oxide gas sensors. In this chapter, a thick-film based sensor is fabricated by a screen-printing method. The first part of this chapter describes the screen-printing technology for thick film deposition used here, followed by the other steps used to fabricate sensor. The subsequent section discusses the characterisation of the sensing materials. Next, the gas sensing results are presented followed by the analysis and discussion.

7.2 Screen Printing Technology for Thick-Film Deposition

Screen printing is the process of forcing ink through a mask to create patterns or structures on to a surface. The mask as shown in Figure 7 - 1, could be a stencil made from metal, with the desired pattern cut out of it, or a mesh made from a porous

fabric, which is stretched across a frame called screen. A rubber or plastic squeegee is used to push the ink across the mask area, which forces the ink through the open areas onto a substrate or surface.

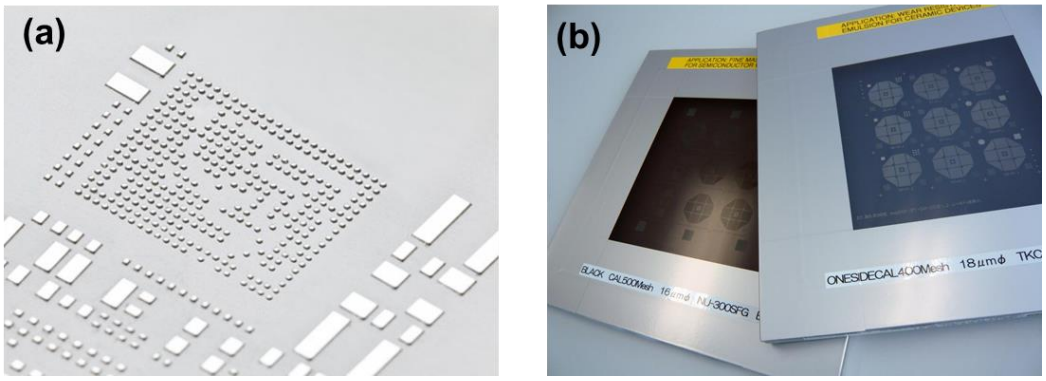

Figure 7 - 1 Screen printing masks made of: (a) stencil metal [1] and (b) mesh [2].

7.2.1 Screen Printing Components

The components of a screen-printer include a frame, screen, screen printing station, squeegee, printing medium/ink and oven/furnace. Each of these items are described below:

(1) Frame: the primary function of a frame is to serve as a support especially for the screen fabric/wire. The frame size should be selected based on the image size of the pattern.

(2) Screen: the choice of screen would depend on the intended application of the screen-printed products. The most important factors that influence the screen-printing quality are [3]:

- The ratio of pattern size to the frame size. For applications that require fine pattern printing, the frame pattern size is suggested to be maximum of 30% of the frame size.

- Type of screen mesh such as mesh count, mesh weave, mesh material, the diameter of the mesh wire. The fabric material influences screen life and durability whereas mesh count and diameter greatly affect the edge definition and print detail.
- Photosensitive emulsion such as the emulsion type, thickness, and exposure time.
- Frame type such as aluminium die casted or aluminium extrude.
- Mesh attaching system which could be direct mesh to frame or trampoline/combination mask.

(3) Screen printing station, squeegee, and ink distributor blade: the quality of the final print not only relies on the frame and screen characteristics, but also other factors including the screen-printing machine, squeegee, and ink distributor blade. These need to be set up to meet certain requirement to create a uniform and consistent printing at a fine detail.

(4) Printing medium/ink: the ink for screen printing needs to be formulated at the right viscosity using a vehicle (if required) such that it can go through the mask and stick to the substrate.

(5) Oven/furnace: an oven is used to dry the ink before another deposition process takes place or to burn out the unwanted vehicle from the material.

7.2.2 Screen Printing Setup

The section describes the screen-printing setup suitable for DEK 1202, which was the machine used here to fabricate thick-film sensors. However, the general setup would also work on similar printers.

The screen printing set up can be summarized in the following.

(1) Assembly and loading of screen: the printer comes with a chase to hold the screen in place. This assembly should be done by removing the chase from the screen printer and screwing the screen onto the chase. Once assembled, the screen is to be loaded into the printer.

(2) Fitting workholder to the system: workholders are customized to suit the size of the substrate and mounted on the worktable of the screen printer. They utilise a mechanical grip and vacuum action to hold the substrate in position

(3) Positioning screen image: the substrate needs to be placed onto the workholder and the screen can be aligned exactly over the substrate by turning the screen-positioning screw.

(4) Setting squeegee, ink distributor blade, and print stroke: the squeegee blade must be straight and flat, the ink distributor blade needs to be parallel to the screen and set such that it does not touch the screen during the print stroke. The length of the print stroke should be as long as possible, with the squeegee fully supported by the substrate fixture throughout the length of its stroke.

(5) Adjusting gap: the gap between the squeegee-to-screen should be 1 mm or smaller whereas the gap between the workholder-to-screen should be 1 mm for a polyester screen, 0.6 mm for a metal mask/stainless screen and 1.5 mm for nylon screens.

7.3 Sensor Fabrication

Sensors were fabricated as thick films using indium oxide decorated with palladium and platinum particles as the sensing materials. The thickness of the

sensing layer was targeted to be in the range of 60 – 70 µm. The fabrication process started by formulating the ink followed by film deposition on the same sensor array substrates used in the previous chapters.

7.3.1 Ink Formulation

The ink was prepared by incorporating the catalyst to the indium oxide powder by wet mixing. The indium oxide powders of 99.9% pure, -325 mesh grade were obtained from ABSCO Ltd, UK. The catalyst used were Pd-based salt of tetraamminepalladium(II) acetate ($Pd(NH_3)_4(CH_3CO_2)_2$) and Pt-based salt of tetraammineplatinum(II) hydroxide hydrate ($Pt(NH_3)_4(OH)_2 \cdot xH_2O$), both obtained from Sigma-Aldrich, UK. Table 7 - 1 shows the mixture to create palladium ($Pd\text{-}In_2O_3$) and platinum indium oxide ($Pt\text{-}In_2O_3$) powder. The components were placed in a ceramic ball and milled with a laboratory mill (Nannetti slr, Italy) for 6 minutes and then poured through 1 mm aperture sieve and left to dry overnight.

Table 7 - 1 Palladium and platinum dispersed in In_2O_3 powders recipe.

Components	**$Pd\text{-}In_2O_3$ powder**	**$Pt\text{-}In_2O_3$ powder**
Salt additive (g)	0.3075 – Pd salt	0.3087 – Pt salt
In_2O_3 powder (g)	20	20
5 mm media (g)	50	50
3 mm media (g)	100.2	100
Distilled water (g)	32	30

The dried powder was sieved through 75 µm sieve and weighed. Vehicle of 8% ethyl cellulose in butyl carbitol (sourced from McGowan Sensors Ltd, UK) was added to the powder with a 2:3 ratio with the powder and milled for 3 minutes.

Table 7 - 2 Pd-In_2O_3 and Pt-In_2O_3 ink recipe.

Components	Pd-In_2O_3 ink	Pt-In_2O_3 ink
Dry oxide (g)	16.57	17.44
Vehicle (g)	11.05	11.61
5-7 mm media (units)	30	30
Large media (g)	8	8

7.3.2 Deposition Process

The screen used for depositing sensing material was made for a DEK 1202 frame using a V-mesh V330-23 45° 34 – 45 µm (supplied by MCI Precision Screens Ltd, UK). V-mesh was produced by using filaments of Vecry and was chosen because of its ability to provide a very fine detail. The screen was assembled to the screen chase and then loaded into the printer.

Alumina substrate was mounted on to the workholder, which was supplied to fit a substrate size of 50 mm x 50 mm. The gap between workholder and screen was adjusted to be approximately 1 mm. Squeegee was mounted into the printer and set to be fully in contact with the surface and parallel with its holder. The main components used for the screen-printing process is shown in Figure 7 - 2.

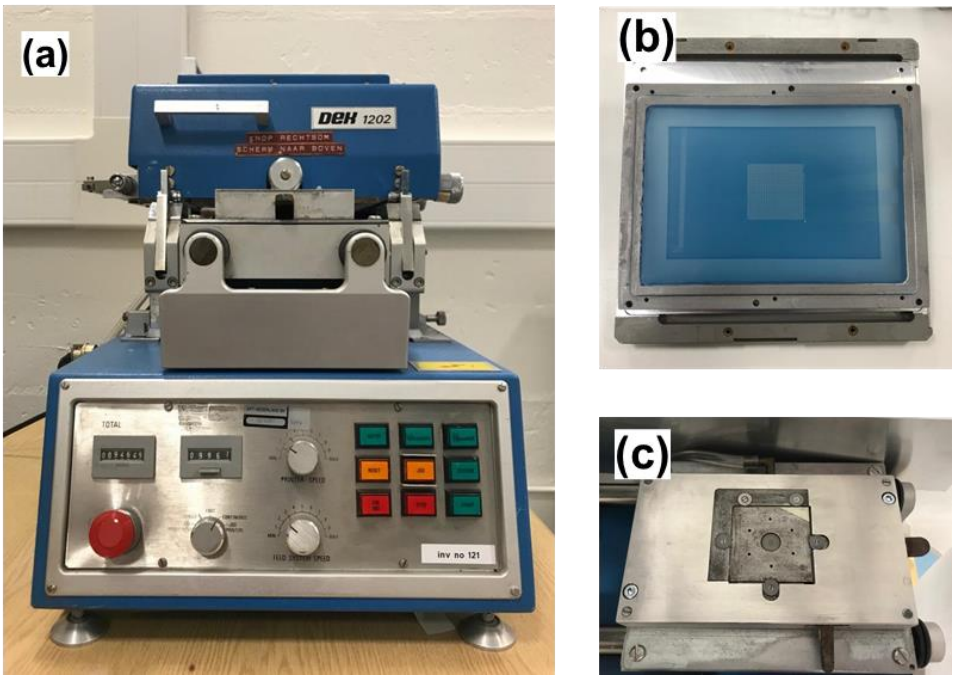

Figure 7 - 2 Basic of screen-printing instrument: (a) screen printer body, (b) mesh to print the pattern, and (c) the workholer to hold the substrate.

With the squeegee and ink distributor blade in place, ink paste was spread on to the screen. The squeegee was adjusted such that the gap from the screen was about 1 mm and the pressure was just slightly depressing the screen. High-tack adhesive polyethylene tape (3M) was applied on to alumina substrate for set up purpose. Once the screen and the substrate were aligned, the tape was removed and then the ink was pasted on to the screen.

After each printing cycle, the substrate was placed in an oven set at 100°C to dry the paste. Printing cycles were repeated such that the thickness of the substrate was around 70 – 80 µm. Sensors were subsequently annealed following a standard thick-film temperature profile with peak temperatures ranging between 500°C and 950ºC to burn out the vehicle. The sensors were individually snapped and then welded to a TO5 package.

7.4 Material Characterisation

The thickness of the sensors after annealing was measured using a white light interferometry, a Bruker GT-K (Bruker, Germany) and found to be 65 ± 2 µm for PdO-In_2O_3 and 70 ± 3 µm and for PtO_2-In_2O_3 sensors. The microstructure of the sensing material was examined by SEM Zeiss Supra 55 (Zeiss, Germany) at 15 kV. The results (Figure 7 - 3) show porous structures and presence of nanoparticles that could be attributed to the additives used.

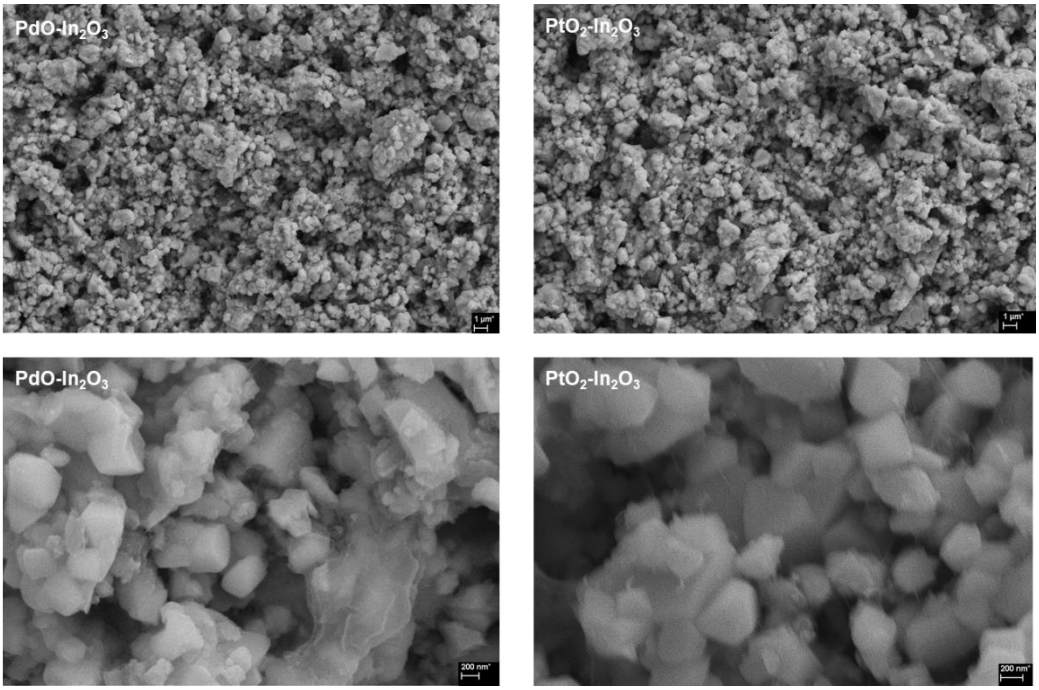

Figure 7 - 3 SEM images of PdO-In_2O_3 and PtO_2-In_2O_3 at lower magnification (top) and higher magnification (down).

EDS analysis using Oxford Instruments in conjunction with Zeiss Supra was carried out to confirm the presence of decoration in the indium oxide materials. The result, shown in Figure 7 - 4, reveals presence of the indium and oxygen as expected. Other elements including C, Al, and Au were present as they are part of the sensor substrate and the sensor was also gold-coated. No palladium or platinum were

detected in the samples, this is likely due to the small quantity of the decorations used (≤1 wt%).

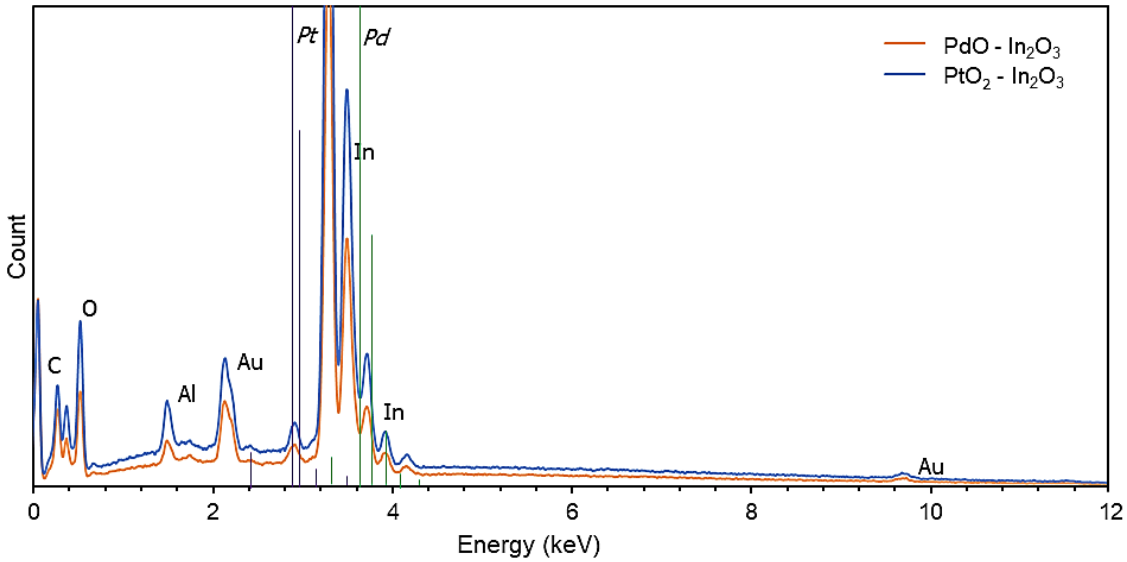

Figure 7 - 4 EDS spectra of indium based thick-film sensors deposited by screen printing.

Elemental analysis was also conducted using wavelength dispersive X-ray fluorescence (WDXRF) spectrometer, Rigaku ZSX Primus IV (Rigaku, Japan). The results are shown in Table 7 - 3. The analysis confirms the present of palladium and platinum additives in the samples and the spectrum of the samples are shown in Figure 7 - 5.

Table 7 - 3 XRF analysis of PdO and PtO_2 based In_2O_3 sensors.

Component	Elemental composition (%)	
	PdO sensor	PtO_2 sensor
In_2O_3	93.6986	94.1654
Al_2O_3	4.2976	4.5463
Au_2O	0.1819	0.6138
PdO	0.4171	
PtO_2		0.4947
Others	1.4048	0.1798

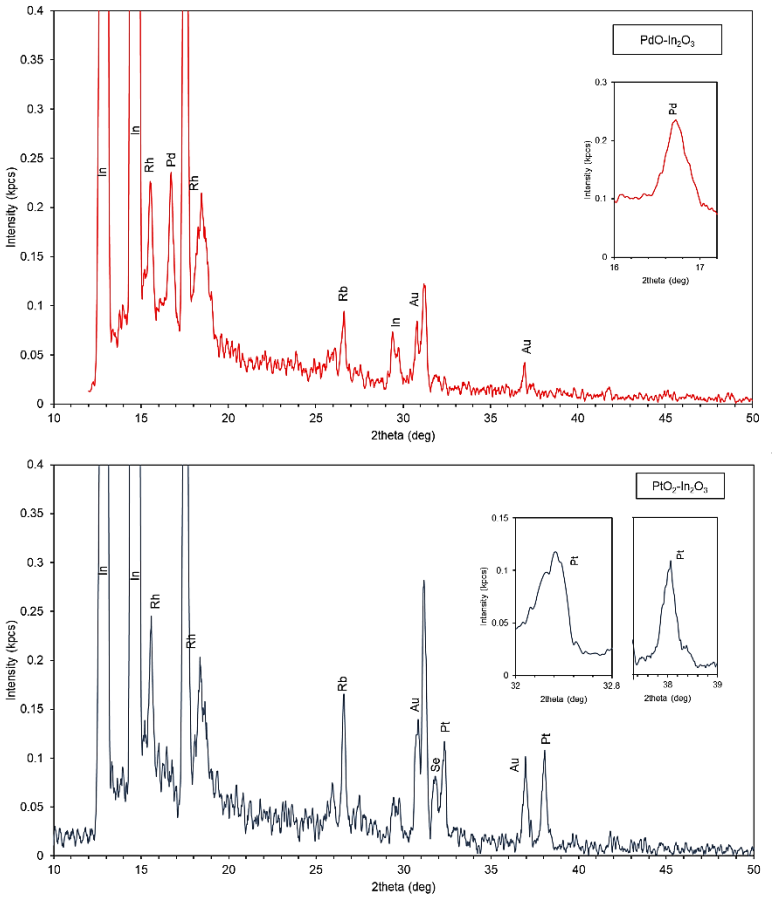

Figure 7 - 5 WDXRF spectra of PdO and PtO_2 decorated In_2O_3 thick-film sensors.

XPS analysis was carried out (Thermo Fisher Scientific, UK) using a monochromatic Al Kα X-ray source to measure the elemental composition and electronic states of the elements. The complete spectra shown in Figure 7 - 6 (a) confirms the presence of In, O and C atoms in the decorated thick-film In_2O_3 sensors. Higher resolution analysis shows details of In 3d XPS spectra of the samples (Figure 7 - 6 (b)) of two intense peaks centred at 444.08 and 451.68 eV for PdO based sensors and at 444.9 eV and 452.3 eV for PtO_2 based sensors, associated with the In $3d_{5/2}$ and In $3d_{3/2}$ respectively. These binding energies are consistent with the reference values found for In_2O_3 [4, 5]. The spectrum of palladium decorated sensor show binding energies at 335.6 eV and 340.9 eV, which are ascribed to Pd $3d_{5/2}$ and Pd $3d_{3/2}$ of PdO respectively [6, 7]. XPS spectrum of platinum decorated sensor shows

the binding energies centred at 75.3 eV and 78.8 eV, which are consistent with Pt $4f_{7/2}$ and Pt $4f_{5/2}$ attributed to PtO_2 [8, 9].

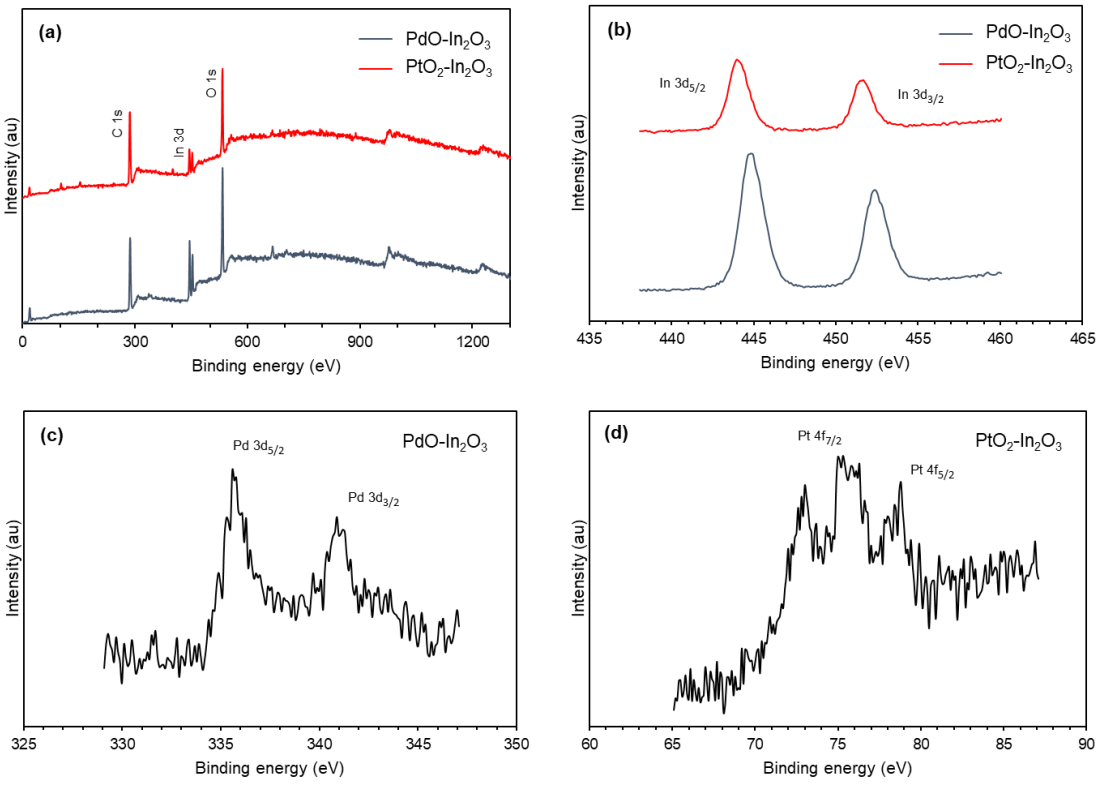

Figure 7 - 6 (a) Survey, (b) In 3d high resolution XPS spectra of In_2O_3, PdO-In_2O_3, and PtO_2-In_2O_3, (c) Pd 3d high resolution XPS spectrum of PdO-In_2O_3, (d) Pt 4f high resolution XPS spectrum of PtO_2-In_2O_3.

7.5 Gas Testing

The fabricated indium oxide thick film sensors were tested to oxygen concentrations ranging from 0% and 20% across 24 months period. The test conditions were varied to examine how they influenced sensor responses by undertaking experiments in dry and wet/humid air and varying the operating temperatures. The response of the sensors was measured by calculating the ratio of sensor response at 20% O_2 to sensor baseline resistance (99.999% N_2).

7.5.1 Palladium Oxide Decorated Indium Oxide Films ($PdO\text{-}In_2O_3$)

A total of 10 $PdO\text{-}In_2O_3$ sensors were tested to detect O_2 under humid conditions and at operating temperatures ranging between 150 – 400°C. Repeated measurements were taken for each sensor and the results were compiled and compared across sensors. For most sensors, the resistance at 20% O_2 was found to be in the range 10^3 – 10^4 Ohm and the resistance at 0% O_2 (99.999% N_2) was found at 10^2 – 10^3 Ohm. A few sensors however, showed resistance to 20% O_2 at a higher range up $7x10^4$ Ohm as shown in Figure 7 - 7.

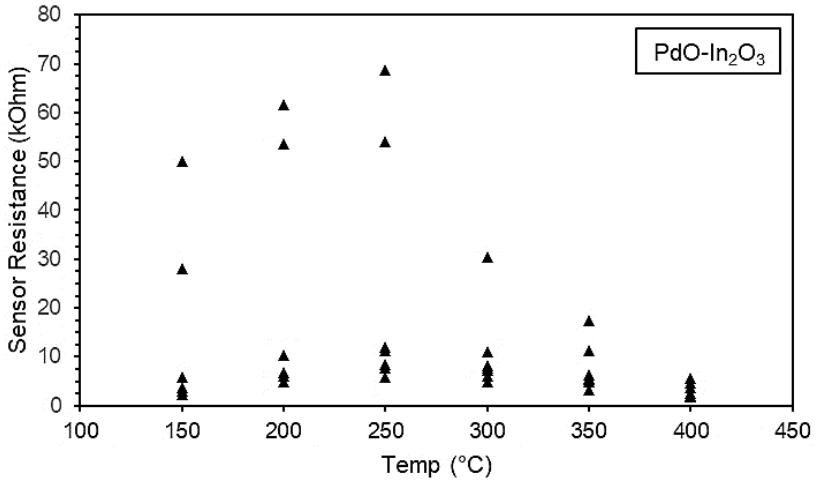

Figure 7 - 7 Resistance value across $PdO\text{-}In_2O_3$ thick films upon exposure to 20% O_2 (85% RH).

The sensors were also tested in dry air. The resistance of the sensors at 20% O_2 was found to be in the range 10^3 – 10^4 Ohm and the resistance at 0% O_2 was found at 10^2 – 10^3 Ohm. A few sensors showed higher resistance values to 20% O_2, just like the ones observed in humid air. The ranges of the sensor response were basically the same, but sensors tested in dry air showed lower resistance values compared to tests in humid air across all the operating temperatures tested as shown in Figure 7 - 8. More responses from some other sensors can be found in Appendix C.

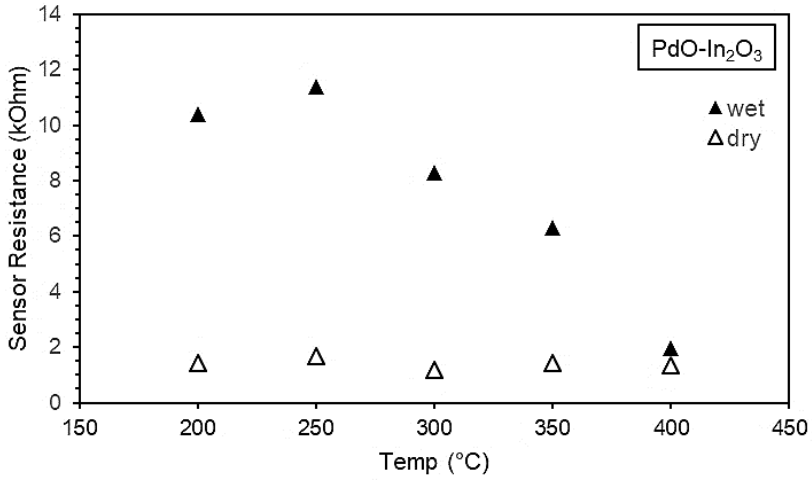

Figure 7 - 8 Example of $PdO\text{-}In_2O_3$ sensor responses to 20% O_2 in dry and humid (85% RH) air.

As the operating temperatures varied, the response of the thick-film sensors also changed accordingly. At lower temperatures, the resistance of the sensors generally went up with increasing temperature. Furthermore, the resistance of the sensors was found to reduce as the temperature increased. This point was found to be in range of 300 – 350°C for most sensors, although some sensors showed reduced resistance at lower operating temperatures between 200 – 250°C, just like the example in Figure 7 - 8.

$PdO\text{-}In_2O_3$ sensors tested in humid environment showed the best response at 200°C **(R_g/R_a = 7.8)** as observed in Figure 7 - 9. The sensors generally exhibited higher response in dry air, except at 250°C and 150°C where the responses were found to be higher in humid air. The best response in dry air was also observed at 200°C **(R_g/R_a = 12.9)**. Despite the lower response, sensors tested in humid air showed more stable responses and better repeatability and reproducibility across sensors, as indicated by the lower error rates. These characteristics will be discussed further in a later section.

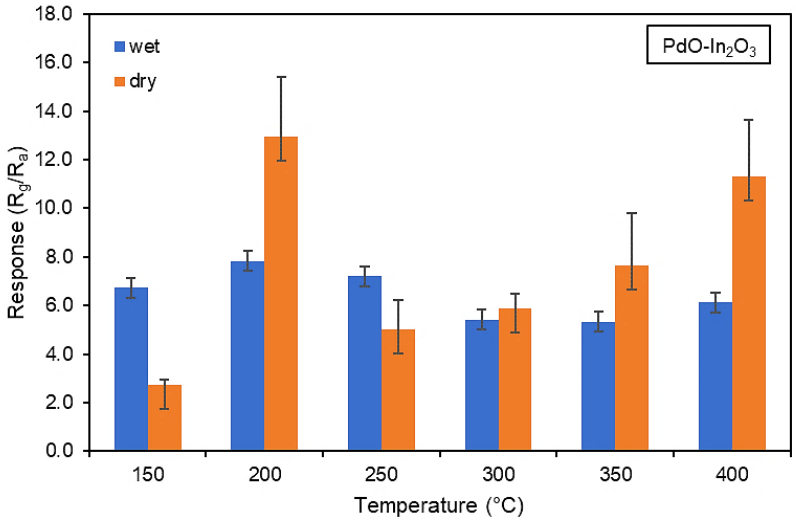

Figure 7 - 9 PdO-In_2O_3 thick film responses to 20% O_2 in dry and humid air (85% RH).

Figure 7 - 10 illustrates the change in resistance of PdO-decorated In_2O_3 thick-film sensors at their optimal operating temperature. The response (T_{res}) and recovery times (T_{rec}) correspond to a 90% change in resistance and were calculated for PdO decorated films at 20% O_2 in humid and dry air. The results indicate that sensors tested under humid air (T_{res} = 11.3 min) responded much slower than in dry air (T_{res} = 2.4 min). A complete recovery to the baseline resistance was observed within 10.9 min and 5.5 min for sensors tested in humid and dry air respectively.

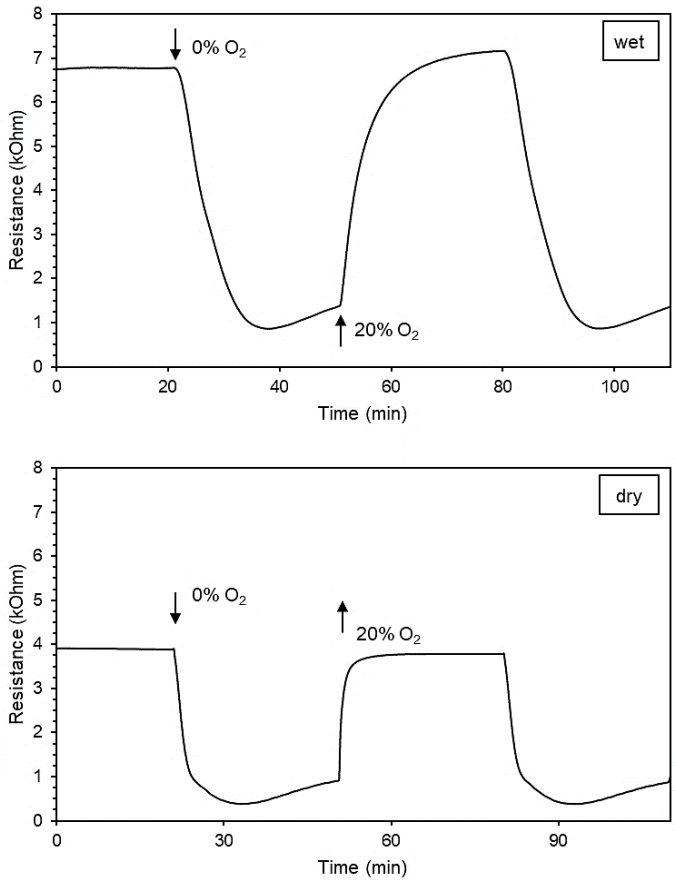

Figure 7 - 10 Film resistance changes of PdO-In_2O_3 toward 20% O_2 in humid air (top) and dry air (bottom).

The gas response relationship is expressed as a function of oxygen concentration at the optimum operating temperature. In humid air, the alpha value (α) was calculated at **0.5 ± 0.15** over concentration range 5 – 20% whereas in dry air, α was found to be **0.3 ± 0.02**. This indicates PdO decorated sensors show good oxygen in humid air, but rather poor in dry air. An example of a sensor response toward various O_2 concentration is shown in Figure 7 - 11 and Figure 7 - 12 for humid and dry air respectively.

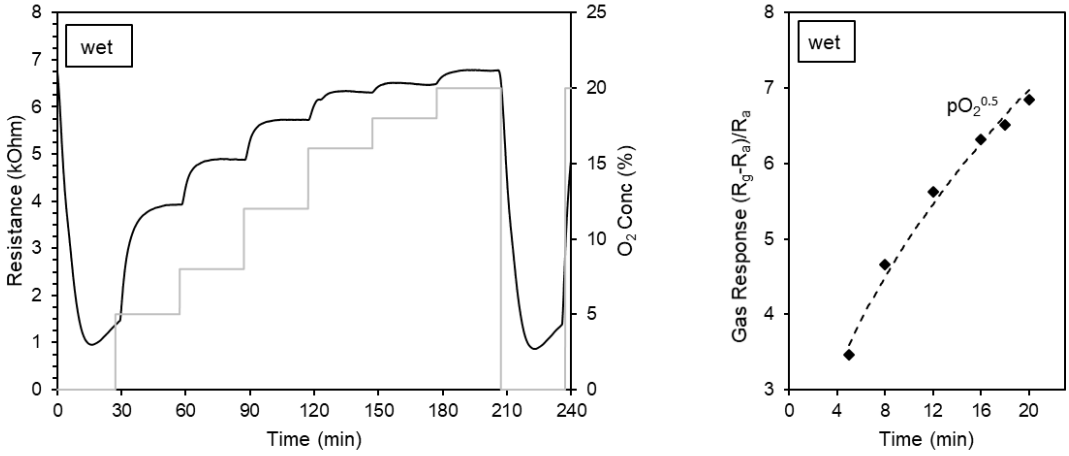

Figure 7 - 11 PdO-In_2O_3 sensor response in humid air (85% RH): resistance changes toward various O_2 concentration (left) and the gas response relationship as a function of O_2 concentration (right).

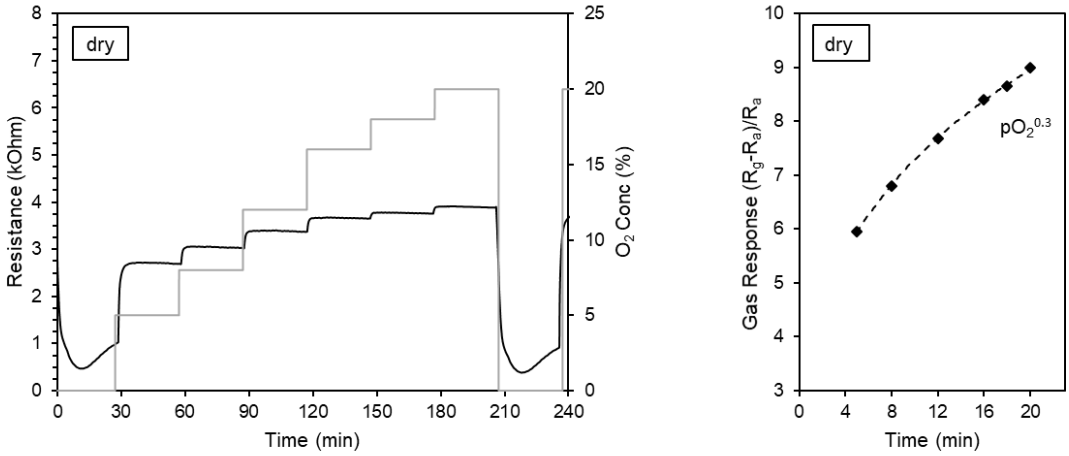

Figure 7 - 12 PdO-In_2O_3 sensor response in dry air: resistance changes toward various O_2 concentration (left) and the gas response relationship as a function of O_2 concentration (right).

7.5.2 Platinum Oxide Decorated Indium Oxide Films (PtO_2- In_2O_3)

PtO_2-In_2O_3 sensors were tested at 20% O_2 over 150 – 400°C under humid air. A total of 10 sensors were tested with repeated measurements taken for each sensor. The results were compiled and compared across different sensors. The resistance of the sensors at 20% O_2 was generally observed to be around 10^2 Ohm up to 10^3 Ohm

with the values mostly lower than the resistance of PdO based sensors. However, some measurements of the sensors showed higher resistance values of up to $5x10^4$ Ohm depending on the operating temperatures. The resistance of the sensors at 0% O_2 was also lower than PdO based sensors at 10^1 – 10^2 Ohm, although some measurements was observed at higher resistance up to 8. 10^3 Ohm. Comparison with PdO based sensors revealed the resistance of the PtO_2 based sensors varied more significantly across measurements as illustrated in Figure 7 - 13.

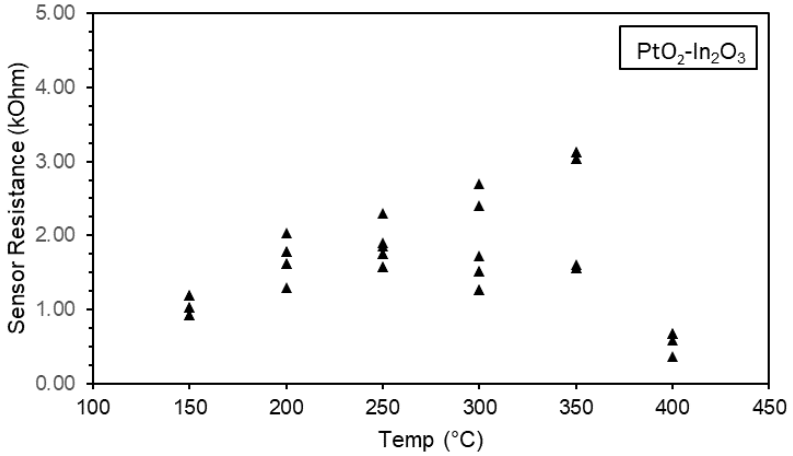

Figure 7 - 13 Resistance value across PtO_2-In_2O_3 thick films upon exposure to 20% O_2 (85% RH).

The sensors were also tested in dry air. The resistance of the sensors at 20% O_2 was found to be in the range 10^2 – 10^3 Ohm and the resistance at 0% O_2 was found at 10^1 – 10^2 Ohm. Some measurements showed higher resistance values at 20% O_2, similar with the ones observed in humid environment. The ranges of the sensor response were the same, but sensors tested in dry air generally showed lower resistance values compared to tests in humid air across all the operating temperatures tested (Figure 7 - 14).

The resistance of PtO_2-In_2O_3 sensors increased as the operating temperature ramped from 150°C to 350°C. The resistance then went down when the temperature

increased to 400°C. For a few measurements, a decreased resistance value was observed at 300°C and further increased with higher temperatures.

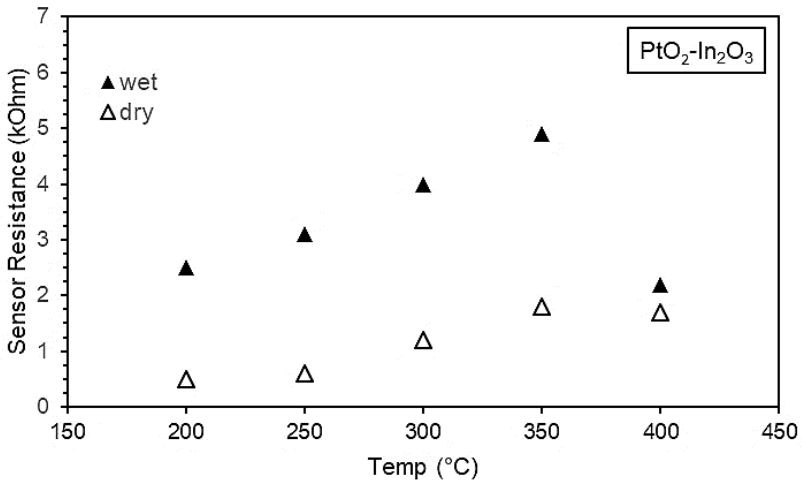

Figure 7 - 14 Example of PtO_2-In_2O_3 sensor responses to 20% O_2 in dry and humid (85% RH) air.

PtO_2-In_2O_3 sensors tested in humid environment showed the best response at 250°C **(R_g/R_a = 35.4)** as shown in Figure 7 - 15. The sensors exhibited higher response in wet air at temperature ranges between 150 and 250°C and higher response in dry air between 300°C and 400°C. The best response in dry air was observed at 350°C **(R_g/R_a = 32.4)**. Repeated measurements were taken for each and across the sensors and the variance of the response was calculated and displayed as the error bar. Unlike PdO decorated sensors, PtO_2 based In_2O_3 sensors showed smaller response variations in dry environment.

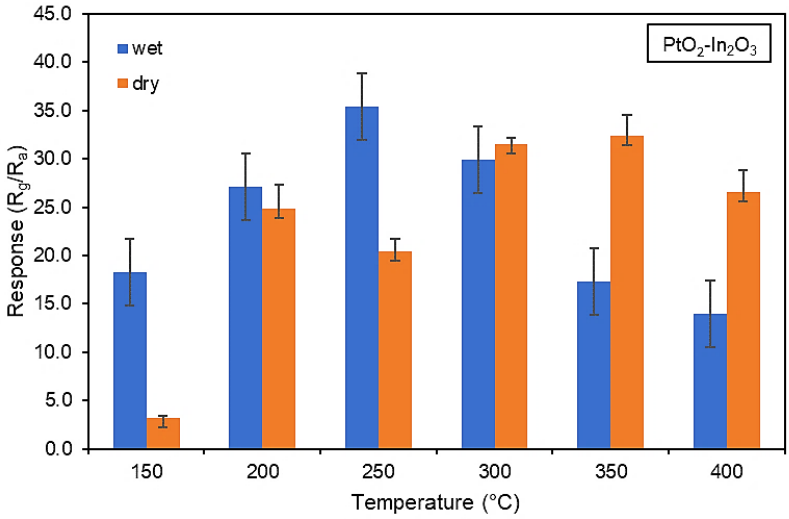

Figure 7 - 15 PtO_2-In_2O_3 thick film responses to 20% O_2 in dry and humid air (85% RH).

Figure 7 - 16 illustrates the change in resistance of PtO_2-In_2O_3 thick-film sensors in humid air at 250°C and at 350°C in dry air. At 20% O_2, the response and recovery times were calculated for PtO_2 decorated films and found around 6.1 min and 22 min for sensors tested under humid and dry air respectively. The recovery time (T_{rec}= 9 min) in humid air was noted at a similar rate as with the dry air (T_{rec}= 8 min). Comparison with PdO decorated sensors show PtO_2 based films responded faster in high humidity, but slower in dry environment.

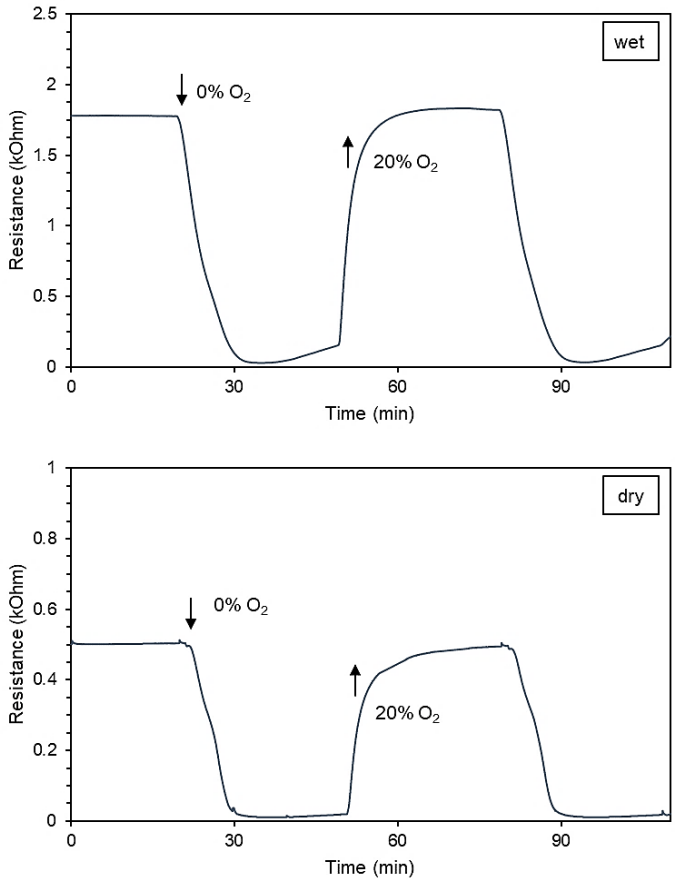

Figure 7 - 16 Film resistance changes of PtO_2-In_2O_3 toward 20% O2 in humid air (top) and dry air (bottom).

The gas response relationship is expressed as a function of oxygen concentration. At 250°C in humid air, the alpha value (α) was calculated at **0.7 ± 0.05** over concentration range 4 – 20% whereas at 350°C in dry air, α was noted at **0.6 ± 0.3**. This indicates PtO_2 decorated sensors demonstrate good oxygen differentiation, at said range, in both humid and dry air, although responses in dry air showed a higher variance. Overall, PtO_2 based films show better oxygen differentiation than PdO based films. The example of sensor response is shown in Figure 7 - 17 and Figure 7 - 18 for humid and dry air respectively.

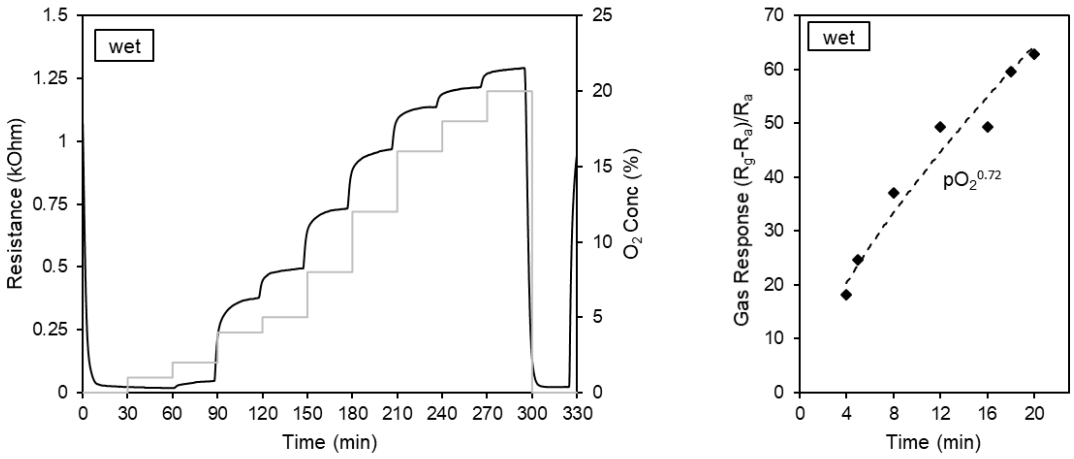

Figure 7 - 17 PtO_2-In_2O_3 sensor response in humid air (85% RH): resistance changes toward various O_2 concentration (left) and the gas response relationship as a function of O_2 concentration (right).

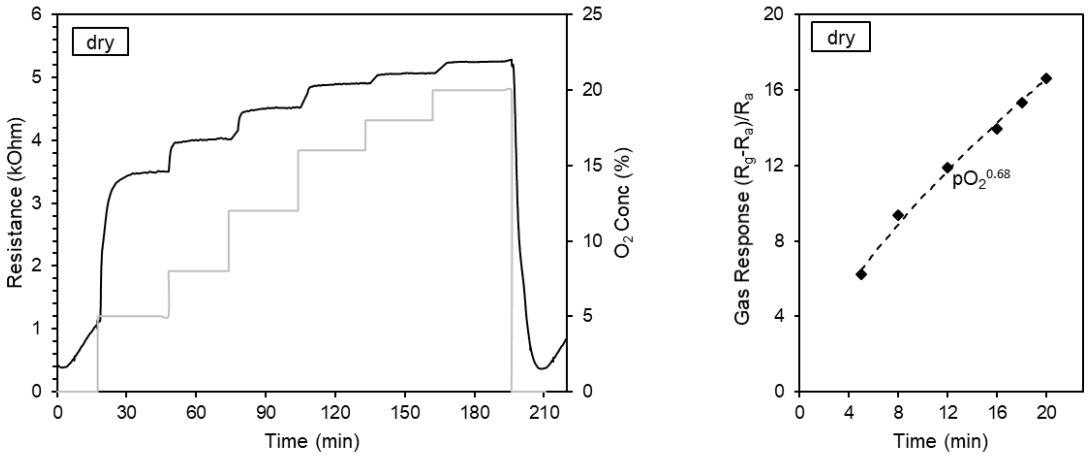

Figure 7 - 18 PtO_2-In_2O_3 sensor response in dry air: resistance changes toward various O_2 concentration (left) and the gas response relationship as a function of O_2 concentration (right).

7.6 Analysis and Discussion

Sensor responses presented in earlier section showed that changes in resistance were observed due to changes in operating temperature, humidity, and decoration of PdO and PtO_2 particles to the host material.

7.6.1 Influencing Factors on Sensor Performance

As previously observed in earlier chapters, operating temperatures affect sensor performance. It also influences sensor dynamic response as demonstrated in Figure 7 - 20. For PdO decorated sensors, the optimum temperature was observed at 200°C in humid air. Increasing the temperature resulted in faster response rate as noted when the temperature ramped up from 200°C to 400°C, the response time increased from 11.3 min to 3.4 min. Likewise, higher operating temperature for PtO_2 based sensors also reduced the response time. The highest response was observed at 250°C in humid air and ramping the temperature to 400°C increased the response time from 6.1 min at 250°C to 2.7 min at 400°C.

Higher operating temperature provides more energy for the oxygen species to undergo adsorption desorption process at a higher rate. This leads to a faster response time, but not necessarily higher response because at higher temperature, oxygen species not only adsorb at the surface of metal oxide but could also overcome the energy barrier to desorb off the surface of the material.

As previously discussed in Chapter 3, there is not energy present to facilitate adsorption/desorption process at low temperature. Therefore, the process occurs gradually at a slow rate, producing a transient response that is shape like a triangle. As indium oxide has higher conductivity than tungsten oxide materials, the activation energy required for this adsorption/desorption process is lower. Moreover, addition of

decorations to the sensing materials could further reduce the activation energy. Hence, the transient responses observed in Figure 7 - 19 are generally closer to a square shape than a triangle shape. When oxygen is introduced to the system, dissociation of oxygen species is favoured and the oxygen species are chemisorbed on the surface of metal oxide which attracts electrons from the conduction band. This produces a space charge layer thus increasing sensor resistance. When oxygen is purged out by of the system by introducing N_2 gas, oxygen species desorb off the surface of metal oxide and electrons are released back into the conduction band thus a decreased resistance is observed. At 200≤°C for both PdO and PtO_2 decorated sensors, the binding of oxygen species and electrons are not strong as adsorption occurs at a slower rate than the desorption process. At 250°C, this is still the case for PtO_2-In_2O_3 based sensors where desorption happens at a faster rate than adsorption. However, higher operating temperature leads to more oxygen species adsorbed on the surface of metal oxide therefore increasing the sensor response. Further increase to 300°C leads to higher adsorption/desorption rate but lower sensor response. This is because further increase in temperature enables the sensors to overcome desorption energy, causing a reduced response. This is consistent with the response observed at 400°C, where oxygen species started to desorb even before O_2 gas purged out of the system. For PdO-In_2O_3, increasing the temperature to 250°C leads to faster adsorption/desorption rate but lower response. This temperature is lower than the one for PtO_2-In_2O_3 (at 300°C) which indicates that the activation energy for palladium oxide decorations is lower than the one for platinum oxide decorations. Further increase in temperatures leads to lower response at 350°C which increased slightly at 400°C. This is likely due to the variation of the energy present to facilitate oxygen dissociation.

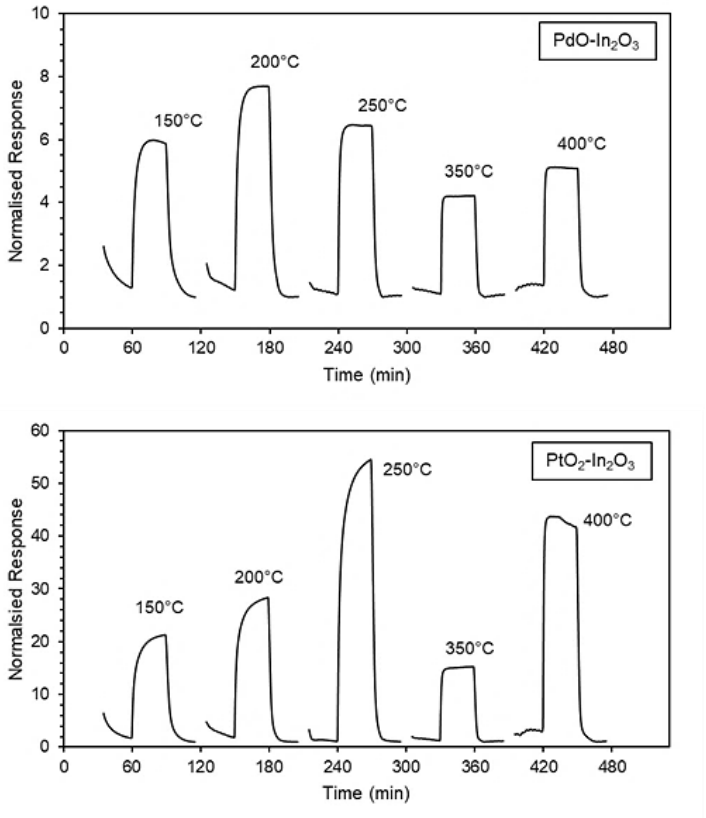

Figure 7 - 20 PdO and PtO_2 based In_2O_3 sensor responses toward 20% O_2 in humid environment at various operating temperatures.

Humidity effect can be reviewed by comparing the tests carried out in humid and dry air. The results showed that higher resistance values were observed for both PdO and PtO_2 decorated In_2O_3 sensors (Figure 7 - 21). It is quite intriguing as literatures suggested the opposite. Previous studies on humidity effects on MOX sensor performance reported lower resistance and thus lower response [10-12]. The results obtained in the previous chapters also demonstrated lower resistance in humid air. However, it must be noted that lower resistance does not necessarily mean lower response. Introducing humidity in the absence of oxygen (baseline resistance) could result in reduced resistance, which makes the normalised response (R_g/R_a) either higher or lower depending on how much the reduced resistance was measured at 20%

and 0% O_2. Here, higher resistance was observed under humid air. This suggested a different mechanism could take place during the interaction of water molecules and the metal oxide surface. It is possible a reaction occurs between the hydrogen atom and the lattice oxygen, creating oxygen vacancy that will produce additional electrons [12]. This results in higher grain boundaries and so higher resistance could be observed. However, there is no evidence to assert this and further investigations will be required to validate the proposed mechanism.

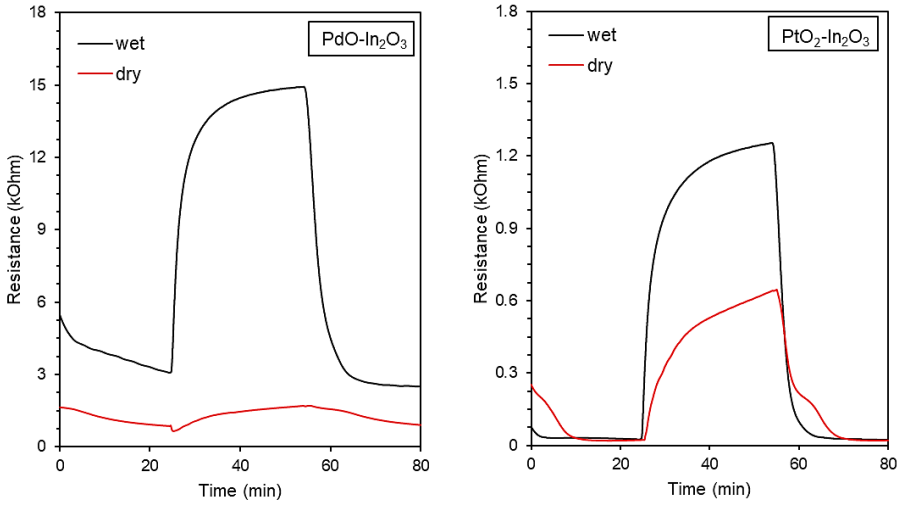

Figure 7 - 21 Resistance toward 20% O_2 at 200°C for PdO-In_2O_3 sensor (left) and 250°C for PtO_2-In_2O_3 (right).

The role of catalyst incorporated in the host materials and its sensitisation mechanism have been discussed in the previous chapters. Here, comparison of the two catalysts also show lower resistance observed form PtO_2 based sensors upon exposure to 20% O_2 at the same operating temperature. For instance, resistance of PdO-In_2O_3 was noted at 15 kOhm at 200°C whereas at this point, the resistance was noted at 2.5 kOhm for PtO_2 based sensor. The resistance changes of PdO and PtO_2 based sensors are shown in Figure 7 - 22.

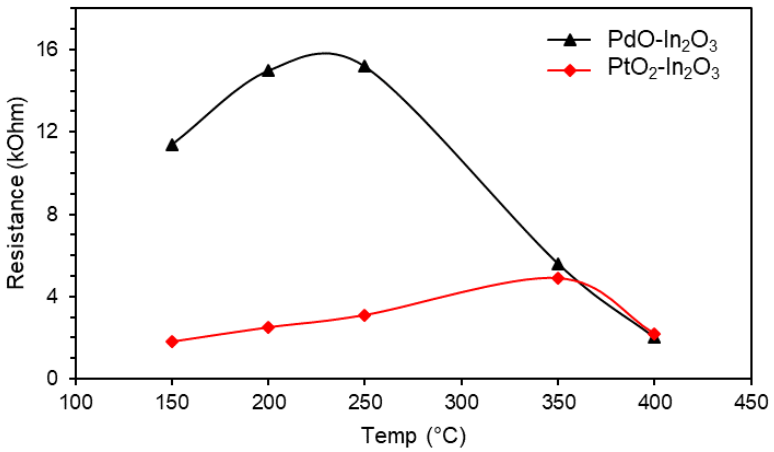

Figure 7 - 22 Example of resistance changes of PdO and PtO_2 decorated In_2O_3 toward 20% O_2 (85% RH) at various operating temperatures.

In chapter 6, decorations of PdO and PtO_2 particles in In_2O_3 host materials reduced the resistance of the films, but no significant changes in response were observed. Here, PtO_2 decorated sensors clearly showed higher response compared to PdO based sensors as observed in Figure 7 - 23.

Both catalysts are present in their oxide form and likely to be reduced to metal upon contact with an inflammable gas [13]. This mechanism is an electronic sensitisation, which contributed to the reduced resistance observed in the films but not responsible for the enhanced response. The higher response is likely to be attributed to chemical sensitisation. In this case, the decorations served to spill-over oxygen species, which increased the oxygen population on the surface of In_2O_3 material. Chemical sensitisation is favourable for Pt catalyst as reported in the literature [14]. Therefore, higher response was expected and observed from PtO_2 decorated sensors.

It is interesting to note that despite the same ratio of catalyst and host materials were used to fabricate the thin and thick film sensors, the responses were significantly

apart. Thick film based In_2O_3 sensors showed much higher response than thin film sensors, which indicate the thickness of sensors played a substantial role in enhancing sensor response.

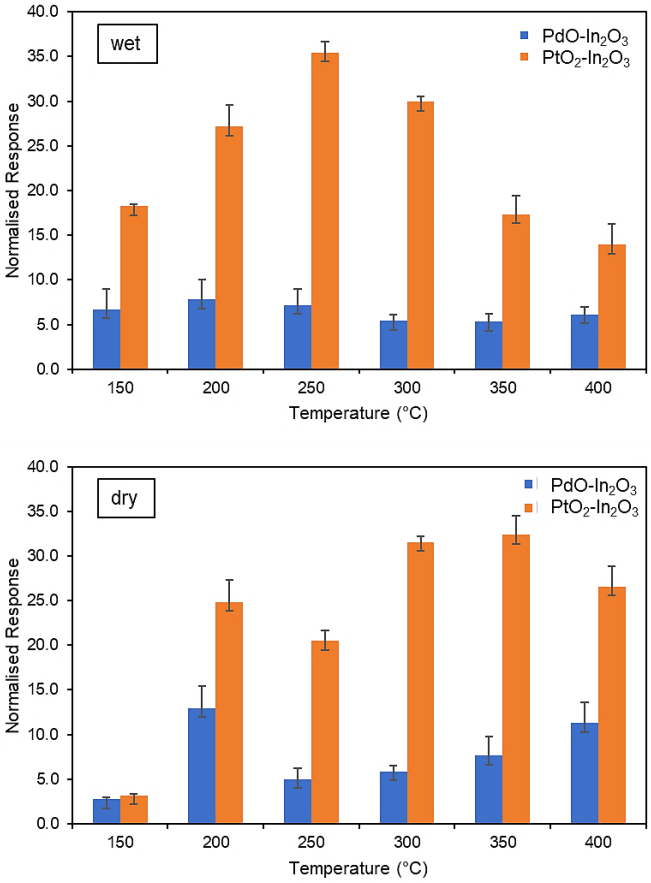

Figure 7 - 23 PdO and PtO_2 decorated In_2O_3 thick film responses to 20% O_2 in humid air (top) and dry air (bottom).

7.6.2 Sensor Repeatability and Reproducibility

Sensors not only needs to have good responses, but also good repeatability and reproducibility. This means when taking repeated measurements of a sensor, the response should be reversible and recovered to its initial condition. Sensor transient responses in earlier sections showed stable and reversible response from both type of sensors. Repeated measurements shown in Figure 7 - 24 for PdO-In_2O_3 and Figure

7 - 25 for PtO_2-In_2O_3 sensor demonstrated good repeatability with the latter showed almost identical responses.

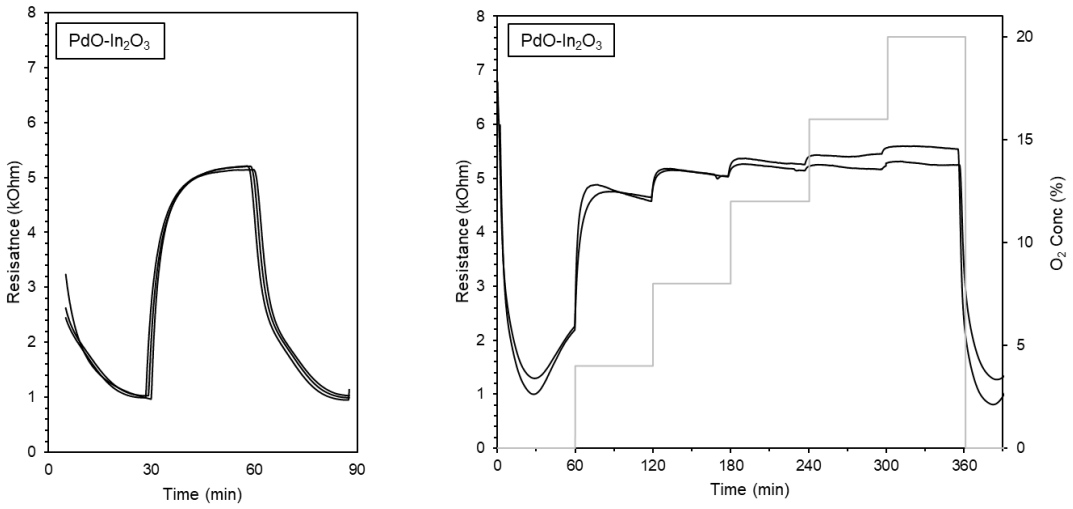

Figure 7 - 24 Repeated measurements of PdO-In_2O_3 sensor under humid air at 200°C toward: 20% O_2 (left) and various O_2 concentration (right).

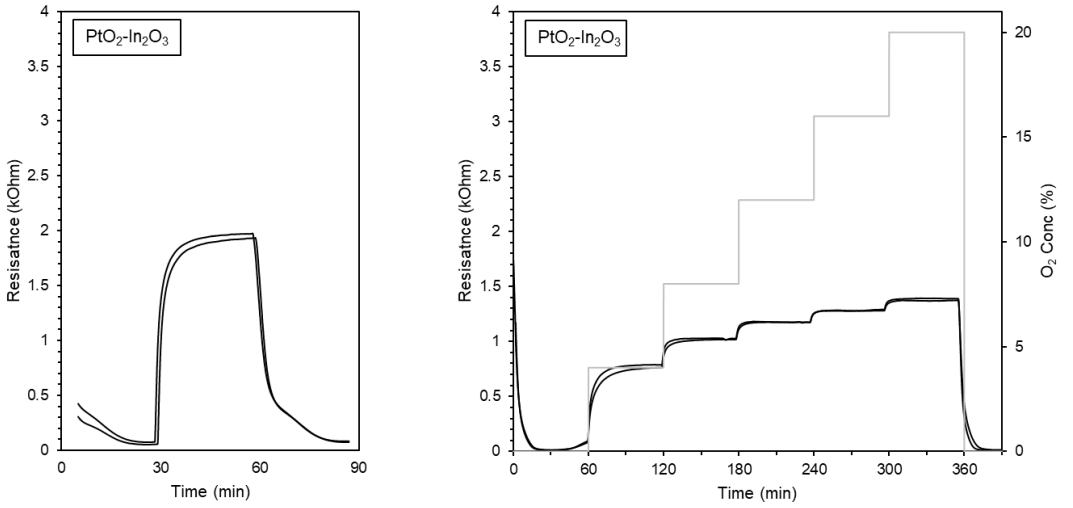

Figure 7 - 25 Repeated measurements of PtO_2-In_2O_3 sensor under humid air toward: 20% O_2 (left) and various O_2 concentration (right).

Measurements were also taken across PdO-In_2O_3 sensors to assess their reproducibility (Figure 7 - 26). Detection toward 20% appeared to produce better

results at 22 ± 2.5 kOhm with less variance compared to measurements toward O_2 with incremental concentration. A few sensors exhibited a significantly higher resistance, which could be due to different active sites available at the surface of metal oxide. Identical measurements were carried out for PtO_2 based sensors as illustrated in Figure 7 - 27. PtO decorated In_2O_3 sensors showed higher resistance variations toward 20% O_2. In detection toward various O_2 concentration, some sensors demonstrated good reproducibility while some others showed different responses at much lower or higher resistance values.

The reproducibility of the fabricated thick-film sensors could be seen as both good and poor. Simple resistance measurements for each sensor would enable sensors with poor responses to be excluded from the group, leaving only sensors with similar responses. However, if all sensors were taken into account then the overall reproducibility of the sensors became poor.

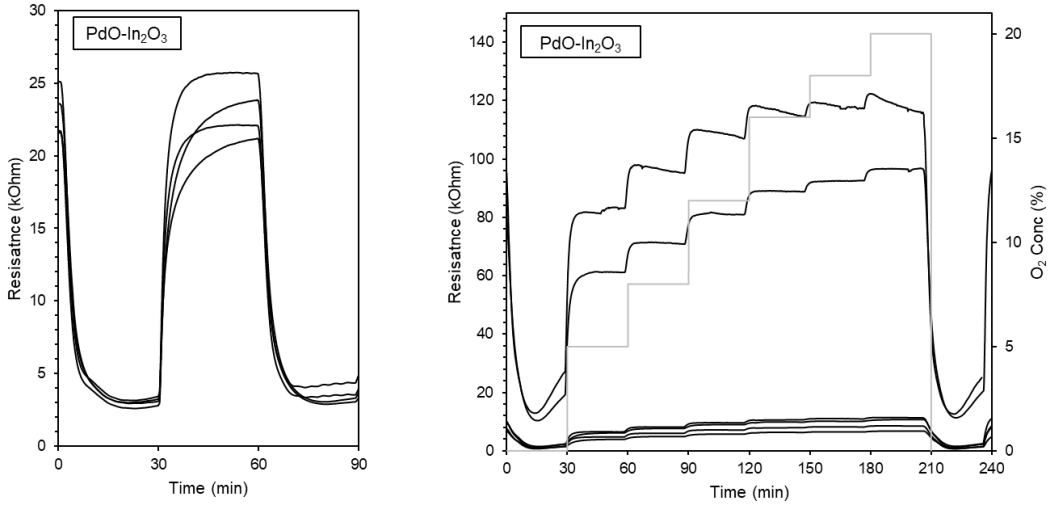

Figure 7 - 26 Repeated measurements across PdO-In_2O_3 sensors under humid air toward: 20% O_2 (left) and various O_2 concentration (right).

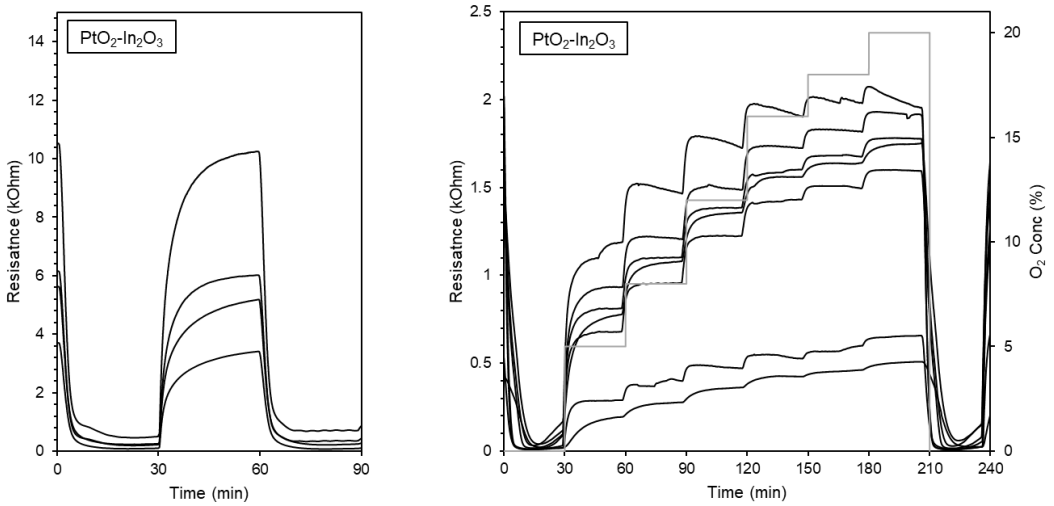

Figure 7 - 27 Repeated measurements across PtO_2-In_2O_3 sensors under humid air toward: 20% O_2 (left) and various O_2 concentration (right).

7.7 Conclusion

PdO and PtO_2 decorated indium oxide based thick-film sensors have been successfully deposited by screen printing technique and tested for oxygen detection in dry and humid environment at various operating temperatures. PdO-In_2O_3 showed the best response at 200°C in humid air (R_g/R_a =7.8) and dry air (R_g/R_a =12.9) whereas PtO_2- In_2O_3 showed the highest response at 250°C in humid air (R_g/R_a =35.4) and at 350°C in dry air (R_g/R_a =32.4). Humidity reduced sensor response for PdO based sensors whereas the opposite was true for PtO_2 based sensors where highest response was observed in humid air at lower operating temperature compared to tests in dry air. Both types of sensors follow power law relationship with PtO_2 decorated films showed better oxygen differentiation.

Repeated measurements revealed that both sensors have good repeatability and stable responses. However, the reproducibility across sensors still need to further improvement as responses for a few sensors varied significantly with the others.

7.8 References

[1] ALLPCB, "SMT Stencil," 2018.

[2] Kuroda, "Screen mask black vs standard," 2018.

[3] Kuroda, "Screen printing masks," http://www.kuroda-electric.eu/screen-mask, [December 11, 2018, 2018].

[4] X. C. Wu, J. M. Hong, Z. J. Han *et al.*, “Fabrication and photoluminescence characteristics of single crystalline In2O3 nanowires,” *Chemical Physics Letters,* vol. 373, no. 1, pp. 28-32, 2003/05/13/, 2003.

[5] Y. Wang, G. Duan, Y. Zhu *et al.*, “Room temperature H2S gas sensing properties of In2O3 micro/nanostructured porous thin film and hydrolyzation-induced enhanced sensing mechanism,” *Sensors and Actuators B: Chemical,* vol. 228, pp. 74-84, 2016/06/02/, 2016.

[6] K. S. Kim, A. F. Gossmann, and N. Winograd, “X-ray photoelectron spectroscopic studies of palladium oxides and the palladium-oxygen electrode,” *Analytical Chemistry,* vol. 46, no. 2, pp. 197-200, 1974/02/01, 1974.

[7] M. Brun, A. Berthet, and J. C. Bertolini, “XPS, AES and Auger parameter of Pd and PdO,” *Journal of Electron Spectroscopy and Related Phenomena,* vol. 104, no. 1, pp. 55-60, 1999/07/01/, 1999.

[8] V. A. Saveleva, V. Papaefthimiou, M. K. Daletou *et al.*, “Operando Near Ambient Pressure XPS (NAP-XPS) Study of the Pt Electrochemical Oxidation in H2O and H2O/O2 Ambients,” *The Journal of Physical Chemistry C,* vol. 120, no. 29, pp. 15930-15940, 2016/07/28, 2016.

[9] T. Dickinson, A. F. Povey, and P. M. A. Sherwood, “X-ray photoelectron spectroscopic studies of oxide films on platinum and gold electrodes,” *Journal of the Chemical Society, Faraday Transactions 1: Physical Chemistry in Condensed Phases,* vol. 71, no. 0, pp. 298-311, 1975.

[10] J. Gong, Q. Chen, M.-R. Lian *et al.*, “Micromachined nanocrystalline silver doped SnO2 H2S sensor,” *Sensors and Actuators B: Chemical,* vol. 114, no. 1, pp. 32-39, 2006.

[11] Q. Qi, T. Zhang, X. Zheng *et al.*, “Electrical response of Sm2O3-doped SnO2 to C2H2 and effect of humidity interference,” *Sensors and Actuators B: Chemical,* vol. 134, no. 1, pp. 36-42, 2008/08/28/, 2008.

[12] N. Bârsan, and U. Weimar, “Understanding the fundamental principles of metal oxide based gas sensors; the example of CO sensing with SnO 2 sensors in the presence of humidity,” *Journal of Physics: Condensed Matter,* vol. 15, no. 20, pp. R813, 2003.

[13] N. Yamazoe, “New approaches for improving semiconductor gas sensors,” *Sensors and Actuators B: Chemical,* vol. 5, no. 1, pp. 7-19, 1991/08/01/, 1991.

[14] H. Gao, D. Wei, P. Lin *et al.*, “The design of excellent xylene gas sensor using Sn-doped NiO hierarchical nanostructure,” *Sensors and Actuators B: Chemical,* vol. 253, pp. 1152-1162, 2017/12/01/, 2017.

Chapter 8. Development of Metal Oxide Based Sensor for Oxygen Detection

8.1 Introduction

Oxygen sensors are one of the most commonly used gas sensors on the market today. They made a significant contribution to the $812.3 million sales in 2016 [1]. This is likely to increase further due to the use of oxygen sensors in automobiles for maintaining cabin air quality and monitoring emission levels [2]. Oxygen sensors are also used in monitoring of respiration, hypoxic air for fire prevention system, monitoring fermentation process, food and beverage packaging, and medical and pharmaceutical applications.

Though oxygen can be detected using optical and electrochemical techniques (both solid-state and aqueous), the most common technology for measuring atmospheric oxygen levels is by using a galvanic cell, which relies on a lead anode [3]. These sensors work by reducing oxygen to hydroxyl ion upon contacts with the cathode, while a balancing reaction of lead oxidation occurs at the anode. When all the lead in the anode has oxidised, the sensors fails [4]. Galvanic based sensors are reliable and were first developed in the 19th century. Although these sensors have been highly successful, the use of lead is likely to be restricted in the near future, leading to the requirement for a lead-free replacement. Moreover, these sensors are quite bulky and have limited life span around 1 – 3 years. Lead-free zirconia based solid electrolyte sensors are available in the market. These sensors are mainly used in automotive and reside in the exhaust system to evaluate air to fuel ratio. However, they are expensive (even more expensive than the current Pb-based sensors) and

operate at temperature higher than 600°C, making them too high-power for alternative applications. This leads to the requirement of an alternative oxygen-based sensor that is lead free and able to operate in the middle temperature ranges for the aforementioned applications.

This chapter discusses development of metal oxide-based sensor for oxygen detection. The first part of the chapter compares the deposition techniques used to deposit the sensing material. Subsequently, further gas testing including selectivity and/or cross-sensitivity tests were carried out to assess the sensor potential as oxygen sensor followed by the analysis and discussion on the results obtained.

8.2 Metal Oxide Sensor for Oxygen Detection

Metal oxide semiconductor (MOX) sensors have been widely used in the field of gas sensors. Application of MOX sensors include monitoring and measuring pollution of gases such as carbon monoxide and nitrogen dioxide [5], gas fuel combustion monitoring [6], detection of hazardous gases [7], and air quality control in residential and industrial zones [8]. MOX sensors offer low manufacturing cost, wide detection range, high sensitivity, and a long life-span. Moreover, they come in a compact size and ease of integration with electronic devices, making them an attractive alternative for oxygen sensing applications.

It has been known that MOX materials respond to oxygen changes and several materials have been studied as potential oxygen sensors. Ga_2O_3 thin-films deposited by sputtering method showed high and reversible response to oxygen, but the operating temperature was high at 1000°C [9]. TiO_2 sensors showed significantly increased response and lower operating temperature from 800°C down to 400°C when the sensor decorated with Nb material [10]. However, no transient or reversible

response was demonstrated in the paper. The response of CeO_2 thin film [11] showed good differentiation to various O_2 concentration but the sensor was not recovered to the baseline condition hence it's difficult to judge its reversibility.

Other materials explored include $SrTiO_3$ [12] and ZnO [13], both operated at low temperature at 40°C and room temperature respectively. Both sensors responded to oxygen, but the latter suffered from drifts. In_2O_3 based sensors exhibited reversible response and showed increased sensitivity with platinum decoration as previously observed [14, 15]. The sensors also operated in the middle temperature range between 200 – 270°C which make them ideal for oxygen detection at lower temperatures.

The studies mentioned mainly reported MOX sensors tested under dry air atmosphere which does not represent real condition where the relative humidity in the air can be quite high (RH >50%). The effect of humidity for oxygen sensing using MOX sensors has not been investigated either, despite the well-known fact they suffer from humidity interference. Furthermore, no assessment on the sensor selectivity has been discussed and this leaves a big hole in evaluating the potential of MOX sensor as oxygen sensors.

8.3 Sensor Fabrication Technique

Several fabrication techniques have been employed to produce metal oxide-based sensors for oxygen detection. Thin film sensors were fabricated by AACVD and spin coating techniques whereas thick film sensors were deposited by screen printing method. Furthermore, comparison of different materials based on tungsten oxide and indium oxide were also presented.

AACVD grown Ag/Ag_2O-WO_3 based sensor tested under humid environment showed the best response obtained at 350°C. The addition of silver decoration to the host material not only improved the response by more than 400% (from R_g/R_a=5 to R_g/R_a=23) but also lowered the operating temperature (from 400°C to 350°). On the other hand, spin-coated WO_3 film tested under the same settings revealed the highest response obtained at 350°C (R_g/R_a= 11.3). Comparison of pure WO_3 sensors deposited by both techniques showed spin coating method was much better at producing higher response. This can be attributed to the higher porosity observed in the spin coated materials.

Spin coating method was employed to deposit indium oxide-based material. Tests under humid air revealed the best response at R_g/R_a = 7.3 for plain In_2O_3. Decoration of palladium oxide to the host material showed the similar response at R_g/R_a = 7.2 whereas decoration of platinum oxide improved sensor response to R_g/R_a = 9.6. These results demonstrate that indium oxide-based sensors are preferable material than WO_3 for oxygen detection.

Decorated indium oxide-based sensors were fabricated as thick-film sensors by screen printing method. The highest response was noted at R_g/R_a = 7.8 for material decorated with palladium oxide. Sensors decorated with platinum oxide showed the best response at R_g/R_a = 35.4 which demonstrates that platinum oxide decoration served as a better catalyst to enhance sensor performance for oxygen detection.

Amongst the deposition techniques presented in this thesis, indium oxide-based sensor deposited as thick films by screen printing method demonstrated the best performance. Therefore, thick-film In_2O_3 sensor decorated with PdO and PtO_2 were chosen for further study on sensor selectivity and cross-sensitivity test.

8.4 Gas Testing

MOX sensors have been known as broad sensors as they cannot selectively detect a particular compound of interest. As commercial products, MOX based sensors are widely used for air quality monitoring to detect general VOCs. Other compounds that can be detected include H_2S, CO_2, CO, and NH_3. For MOX based sensors to be reliable oxygen sensors, their cross-sensitivity and selectivity to other gases need to be assessed.

8.4.1 Experimental Set-up

Humidity effects on sensor performance have been discussed in previous chapters by comparing sensor responses in dry and humid air. Here, an additional test was carried out using the humidity generator in the gas mixture. Screen printed PdO and PtO_2 based sensors were tested for 20% oxygen at varied humidity level to examine how changes in humidity influences sensor response.

The selectivity of the fabricated films toward oxygen was studied by measuring sensor response to different gases such as isobutylene and ethylene. The concentration was chosen at 1 ppm for both as these are higher than those expected to be found in ambient air [16-18].

Both isobutylene and ethylene were sourced from BOC (UK), supplied at 50 pm and 100 ppm respectively. The desired concentration of isobutylene and ethylene was achieved by diluting the gas in air. As the baseline resistance for the detection of oxygen was done in N_2 gas, the baseline resistance for the selectivity tests with isobutylene and ethylene were also carried out using nitrogen. The response was measured by calculating the sensor response ratio of nitrogen to the interference gas.

Selectivity test is useful to determine which gas the sensor is more sensitive to. However, it only measures the sensor response toward interfering gases independently, meaning it doesn't examine the sensor response when the interfering gas is present alongside the targeted gas which is likely to be the case in reality. Here, interference test was carried out to investigate sensor response toward oxygen when other interfering gases (i.e. isobutylene and ethylene) were present. It was done by introducing the interference gas to the sensors for a few minutes during the oxygen measurement.

As the relative humidity in ambient air can be quite high (>50% RH), both selectivity and interference tests were carried out under humid air (85% RH). The sensors were operated at their optimum working temperature which was at 200°C for PdO-In_2O_3 and 250°C for PtO_2- In_2O_3.

8.4.2 Humidity Test

The humidity tests where both PdO and PtO_2 based In_2O_3 sensors exposed to oxygen in humid and dry air were carried in Chapter 7. Here, the result as seen in Figure 8 - 1 show that higher resistance observed in humid air. This result contradicted studies on humidity effects on metal oxide sensors as found in the literatures [19-21]. The results obtained from the spin coated tungsten oxide and indium oxide-based sensors also showed lower resistance in humid air. As discussed in Chapter 7, a different mechanism might occur during these tests which resulted in higher response observed from humid environment. Additionally, the tests in humid and dry air were conducted separately and so other parameter such as oxygen pressure might influence sensor responses.

PdO and PtO2-Ini2O3 were tested to detect 20% oxygen at varied relative humidity level as shown in Figure 8 - 2. Here, both types of sensors exhibit higher response at 20% RH. The resistance decreased as the relative humidity increased to 40% and further reduced at 60% RH. Increasing the relative humidity to 80% showed no change in the response. This response supports the ones found in the literature but contradicts the humidity effects previously obtained. Further investigation is necessary to assess the possible reasons as to why the sensors respond or behave in such as way. Nonetheless, the results obtained indicate that humidity indeed affects sensor responses and this could hinder its performance as oxygen sensors.

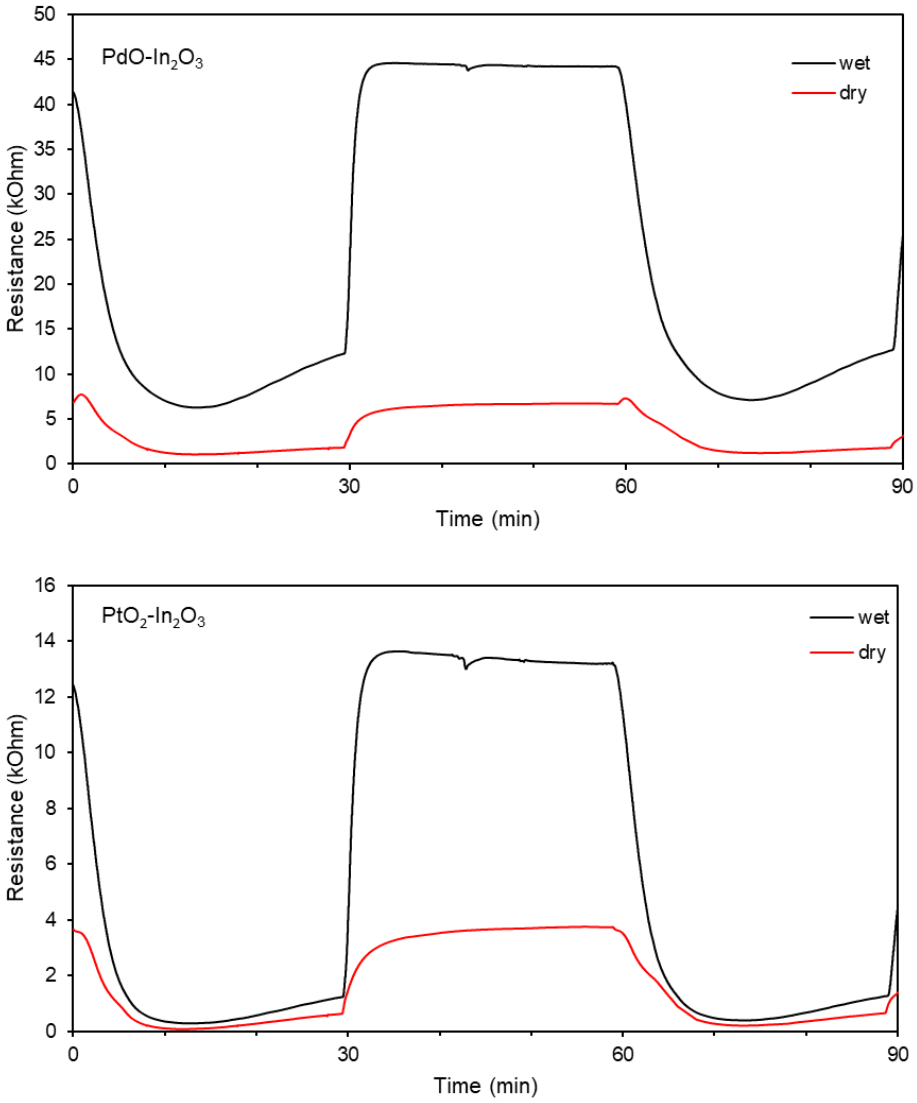

Figure 8 - 1 Example of sensor responses toward 20% O_2 at 300°C for PdO-In_2O_3 sensor (top) and 250°C for PtO - In_2O_3 (bottom).

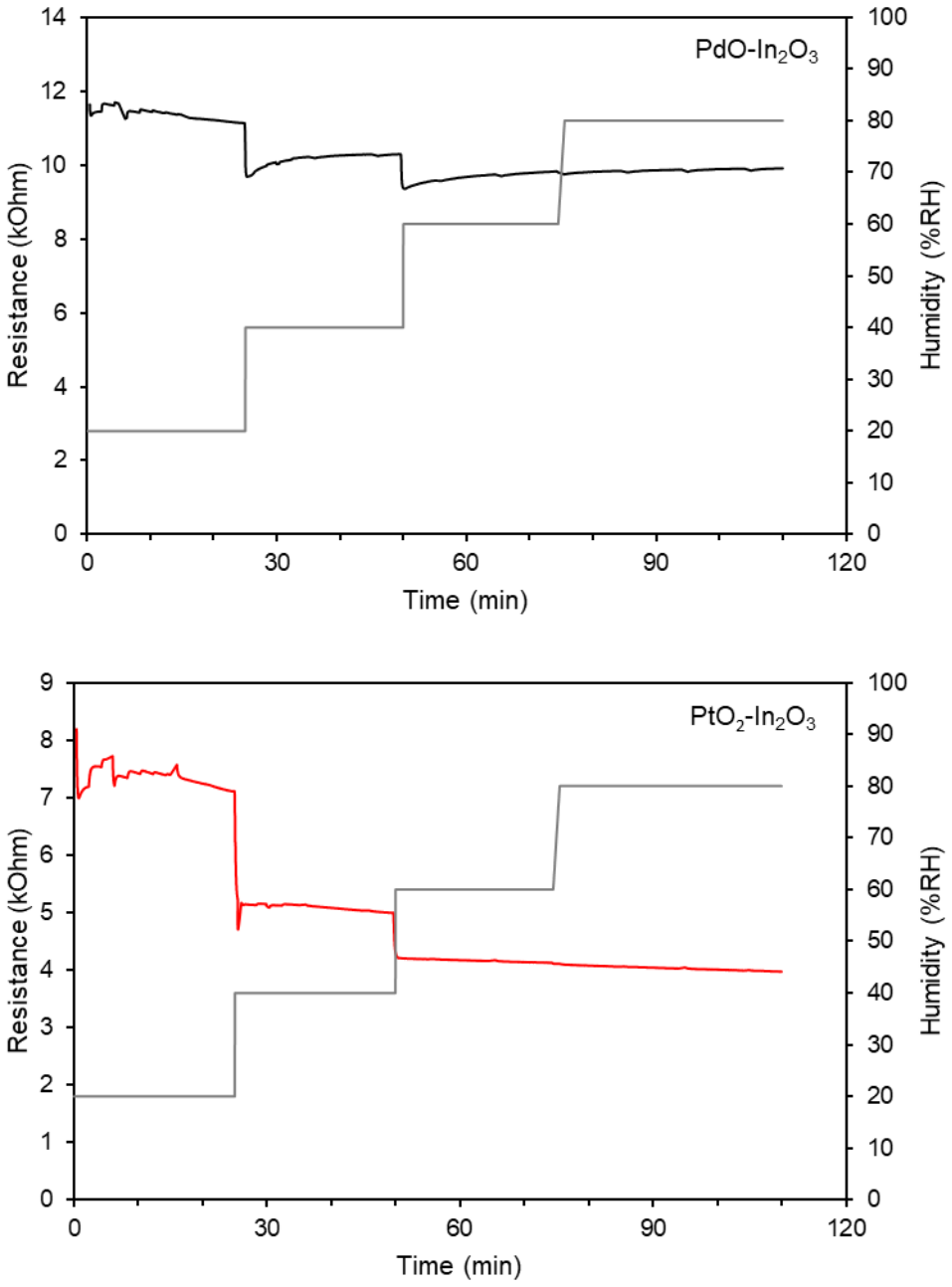

Figure 8 - 2 Example of sensor responses at various relative humidity level toward 20% O2 at 300°C for $PdO\text{-}In_2O_3$ sensor (top) and 250°C for $PtO\text{-}In_2O_3$ (bottom).

8.4.3 Selectivity Test

$PdO\text{-}In_2O_3$ and $PtO_2\text{-}In_2O_3$ sensors were tested for isobutylene and ethylene. As shown in Figure 8 - 3, it is clear that the decorated In_2O_3 thick film sensors were more

sensitive to oxygen than to the interfering gases. The response of PdO-In_2O_3 toO_2 was 2x higher than that to isobutylene and almost 7x higher than that to ethylene gas. The response of PtO_2-In_2O_3 sensor to oxygen, on the other hand, was almost 13x and 8x higher than those of isobutylene and ethylene respectively. These results indicate that the screen-printed indium oxide-based sensors are suitable for oxygen detection.

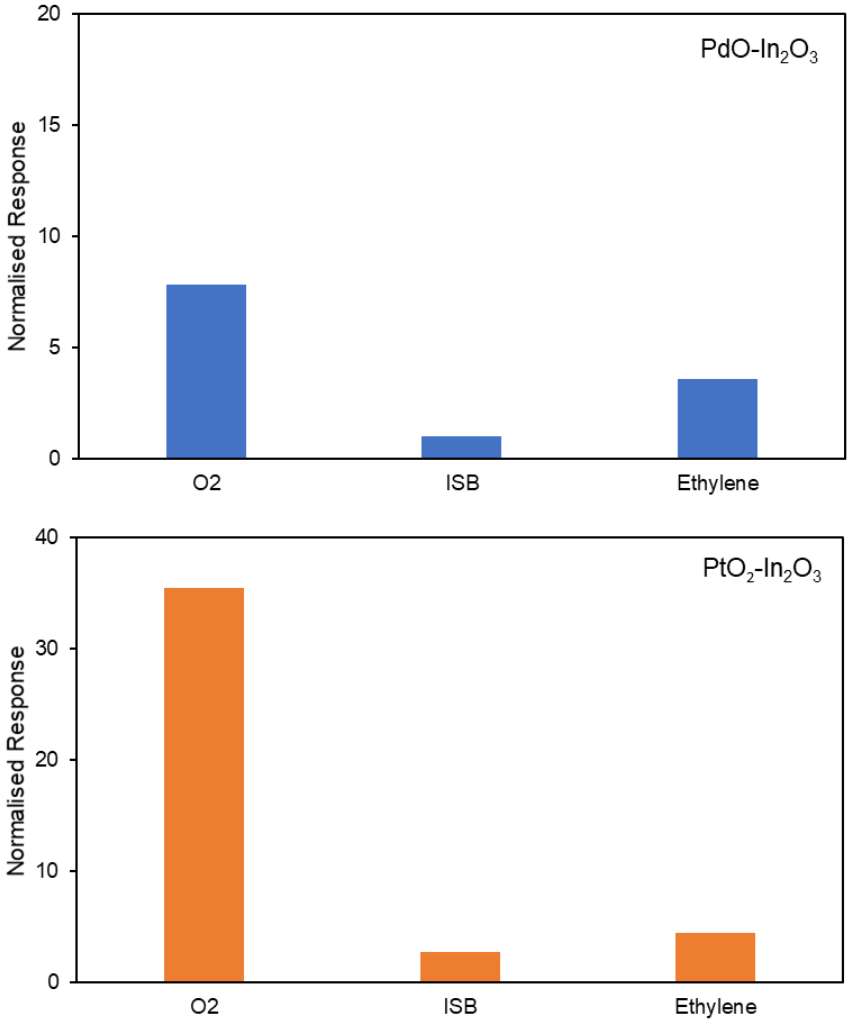

Figure 8 - 3 Selectivity toward different gases tested under humid air (85% RH) of PdO-In_2O_3 at 200°C (top) and PtO_2-In_2O_3 at 250°C (bottom).

8.4.4 Interference Test

PdO-In_2O_3 and PtO_2-In_2O_3 sensors were tested for oxygen detection, during which the sensors were introduced to the interfering gas. Figure 8 - 4 demonstrates sensor responses when introduced to 1 ppm isobutylene during measurement of 20% oxygen. Despite showing the highest selectivity toward oxygen amongst other gases, the sensor was indeed influenced by the present of isobutylene as indicated by the reduced response. The PdO-In_2O_3 sensor was less affected by the isobutylene than that of PtO_2-In_2O_3 sensor.

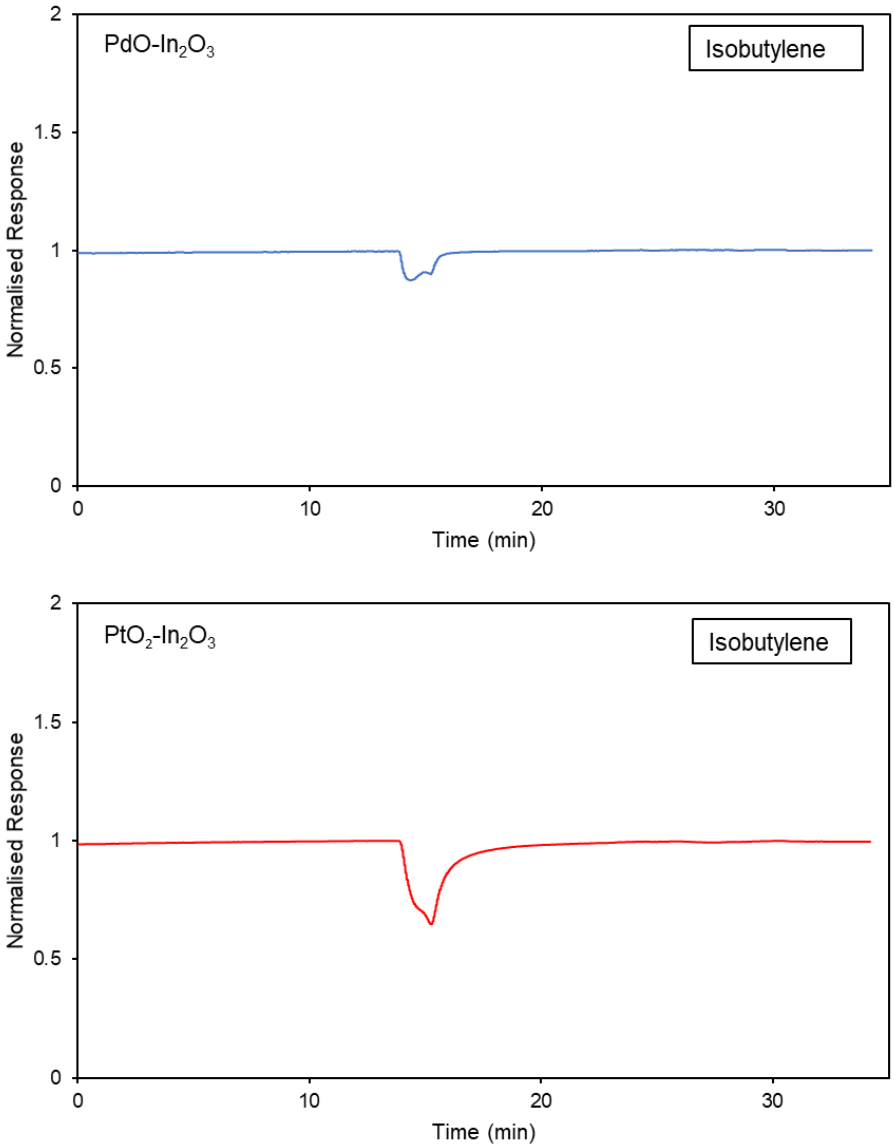

Figure 8 - 4 Responses of $PdO\text{-}In_2O_3$ (top) and $PtO_2\text{-}In_2O_3$ (bottom) toward 1 ppm isobutylene as interference gas during oxygen measurement (20%).

Similarly, the sensors were introduced to 1 ppm ethylene during 20% oxygen measurement. The results (Figure 8 - 5) also show that sensors responses were affected by the presence of the ethylene. Here, $PtO_2\text{-}In_2O_3$ sensor was less responsive toward ethylene than the $PdO\text{-}In_2O_3$ sensor.

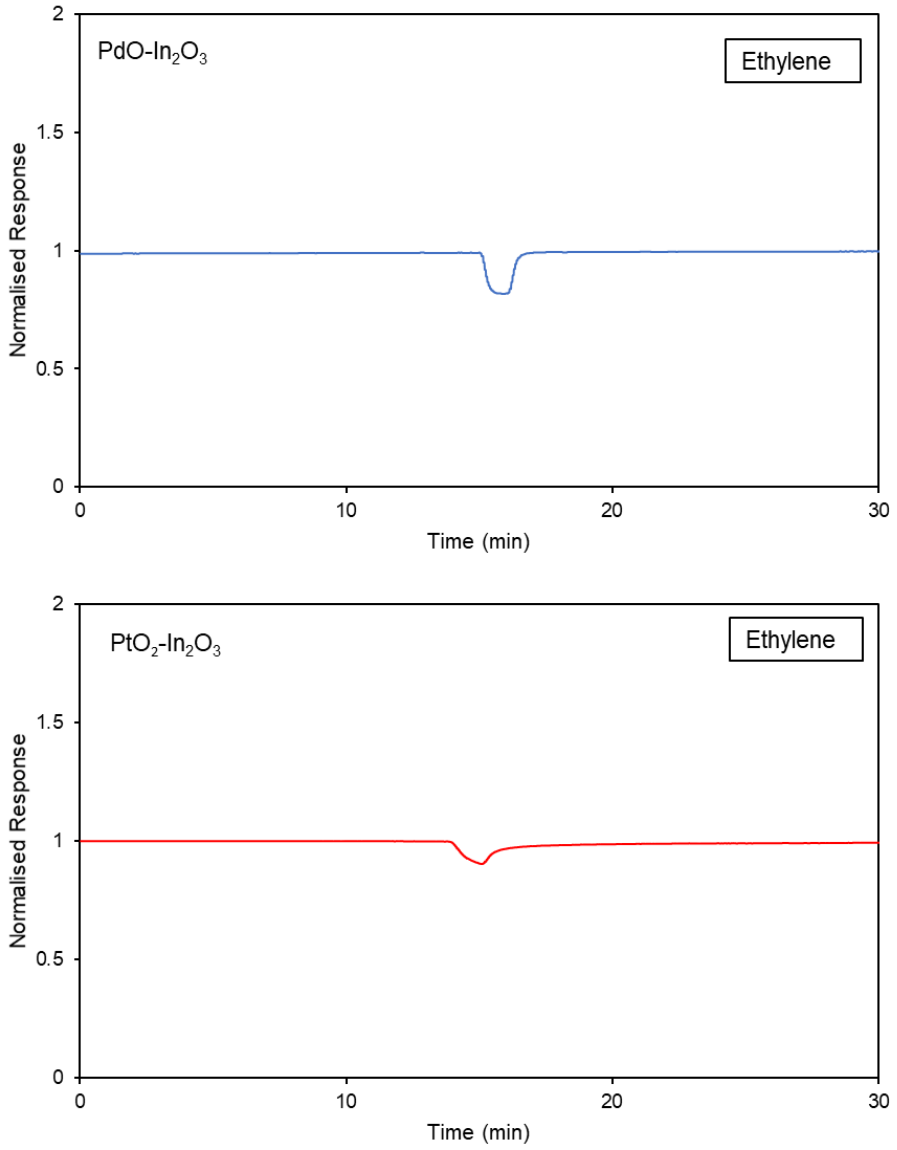

Figure 8 - 5 Responses of $PdO\text{-}In_2O_3$ (top) and $PtO_2\text{-}In_2O_3$ (bottom) toward 1 ppm ethylene as interference gas during oxygen measurement (20%).

8.5 Analysis and Discussion

Indium oxide-based sensors as well as tungsten oxide-based sensors fabricated by several deposition techniques have been tested under humid and dry air. All results consistently showed that humidity cross-reference is inevitable for metal oxide-based sensors. This means in the application of MOX materials for oxygen

detection, the combination of two sensors, namely PtO_2- or PdO- decorated indium oxide and a humidity sensor would be required to enable suppression of humidity interference.

Sensor interference toward other gases is another issue commonly encountered in metal oxide sensors. This could be minimised by using a passive filter integrated into the sensor system or an active layer which serves to absorb the interference gas. In this work, the former method was applied by integrating active carbon cloth (ACC) FM 100 (Chemviron, Belgium) to the system. ACC was chosen due its rapid adsorption kinetics, large surface area of 1000-2000 m^2/g [22] and the capability to adsorb to a higher level of purity. Additionally, using passive layer means the filter can be replaced if required.

ACC layer was cut into small piece of 80 x 5 mm and placed inside a quarter tube fittings as seen in Figure 8 - 6 (a). Mesh was cut following the diameter of the neck of the connector and placed inside (Figure 8 - 6 (b)). This is done to block dust from flowing through and entering the chamber. Finally, the connectors are then connected to 1/8 fittings as the inlet of the chamber requires 1/8 fittings. Once the connectors assembled, it is connected to the inlet of the sensor chamber so that any gas flowing through will pass the ACC filter before entering the sensors.

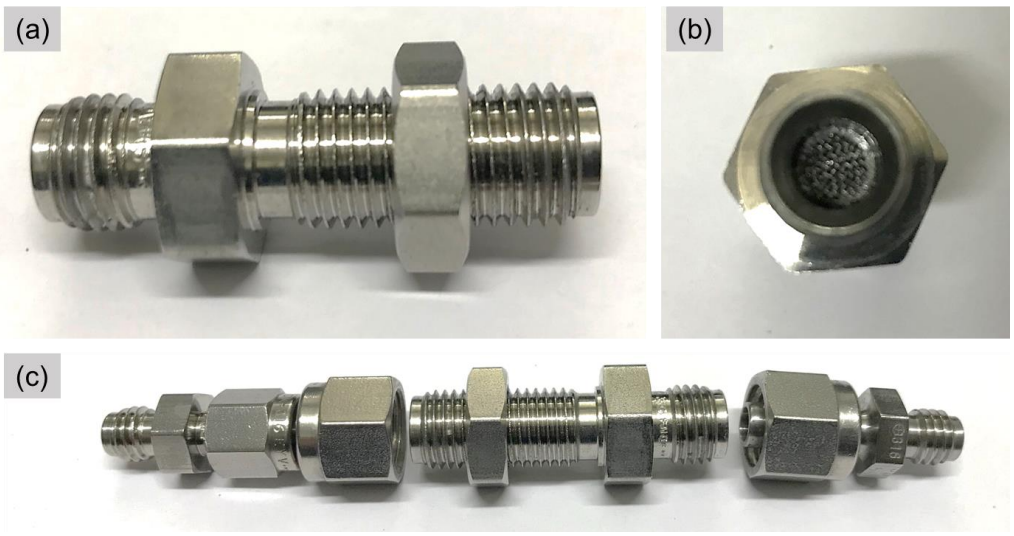

Figure 8 - 6 ACC tube connector set-up: (a) side view of the tube containing ACC filter, (b) front view of the tube connector, (c) 1/4 tube connectors adapted to 1/8 fittings.

The interference tests were repeated with ACC in place. Firstly, isobutylene gas was introduced during oxygen measurement and the result is highlighted in Figure 8 - 7. When in use, the ACC was able to filter out the isobutylene gas from the response. PdO-In_2O_3 sensor showed a more stable response than the PtO_2-In_2O_3 sensor, which had a slightly reduced response after isobutylene was introduced. Nonetheless, the use of ACC during the sensor measurements eliminated the peak of isobutylene that would be otherwise present.

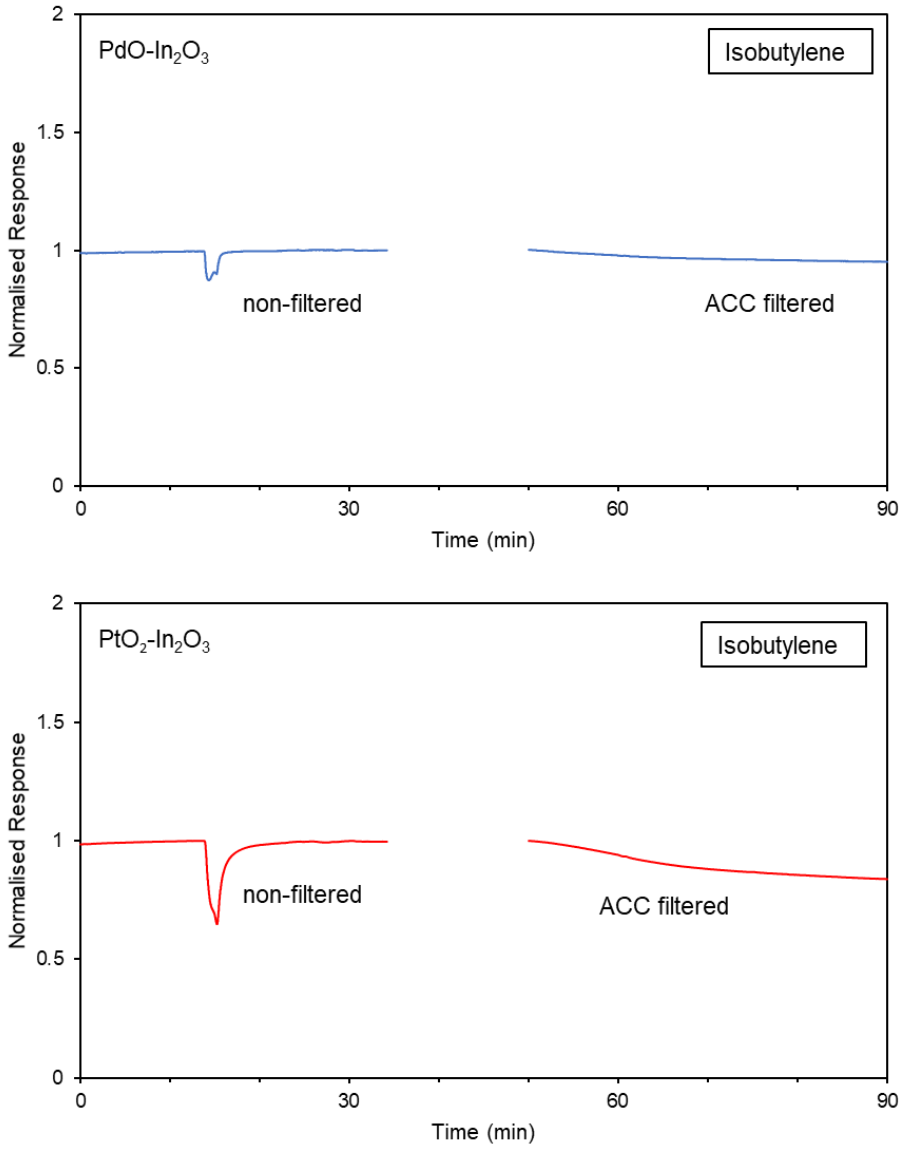

Figure 8 - 7 Responses of $PdO\text{-}In_2O_3$ (top) and $PtO_2\text{-}In_2O_3$ (bottom) toward 1 ppm isobutylene as interference gas during oxygen measurement (20%) with and without ACC filter.

Figure 8 - 8 shows the sensor response when ethylene 1 ppm was introduced during oxygen measurement. ACC filter was able to filter out the ethylene from the sensor response. Here, $PdO\text{-}In_2O_3$ sensor also showed a more stable response than the $PtO_2\text{-}In_2O_3$ sensor which had a slightly reduced response after ethylene was introduced. Nevertheless, no peak of the ethylene was observed when the ACC filter was integrated to the sensor system.

Other test with higher concentration of ethylene was also carried out. The results as seen in Figure 8 - 9 show ACC filter was able to filter 2.5 ppm ethylene. When a higher concentration of 10 ppm ethylene was introduced, the ACC filter was less effective. A peak of ethylene was still observed in the response in both PdO-In_2O_3 and PtO_2-In_2O_3 sensor, although the peak was less pronounced compared to when the ACC was not in use.

Just like any other metal oxide-based sensors, the fabricated metal oxide-based sensors in this thesis were not extricated from poisoning. Presence of contaminants alongside the targeted gas could reduce sensor performance or even poison the sensor, rendering it useless. However, the results obtained in this chapter demonstrate that ACC is an effective way to eliminate or at the very least, reduced sensor cross-sensitivity to other interference gas.

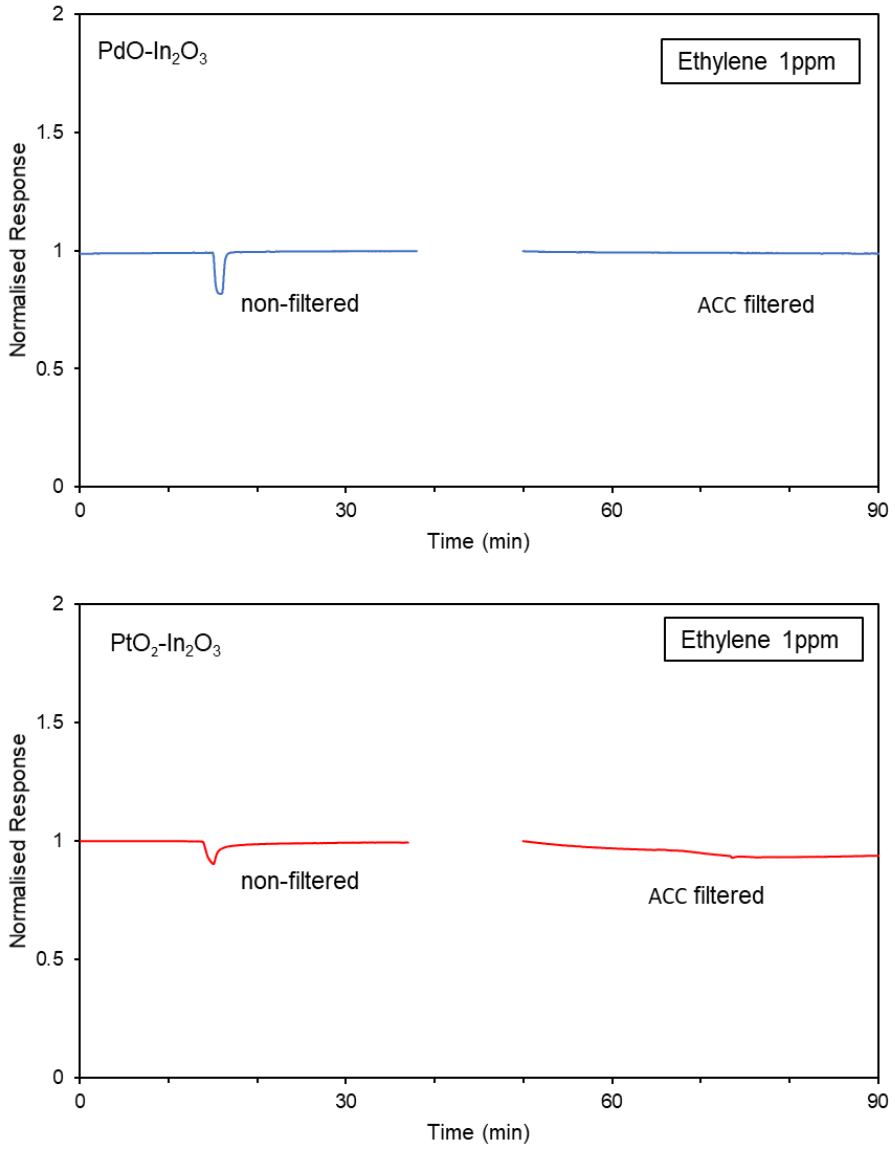

Figure 8 - 8 Responses of $PdO\text{-}In_2O_3$ (top) and $PtO_2\text{-}In_2O_3$ (bottom) toward 1 ppm ethylene as interference gas during oxygen measurement (20%) with and without ACC filter.

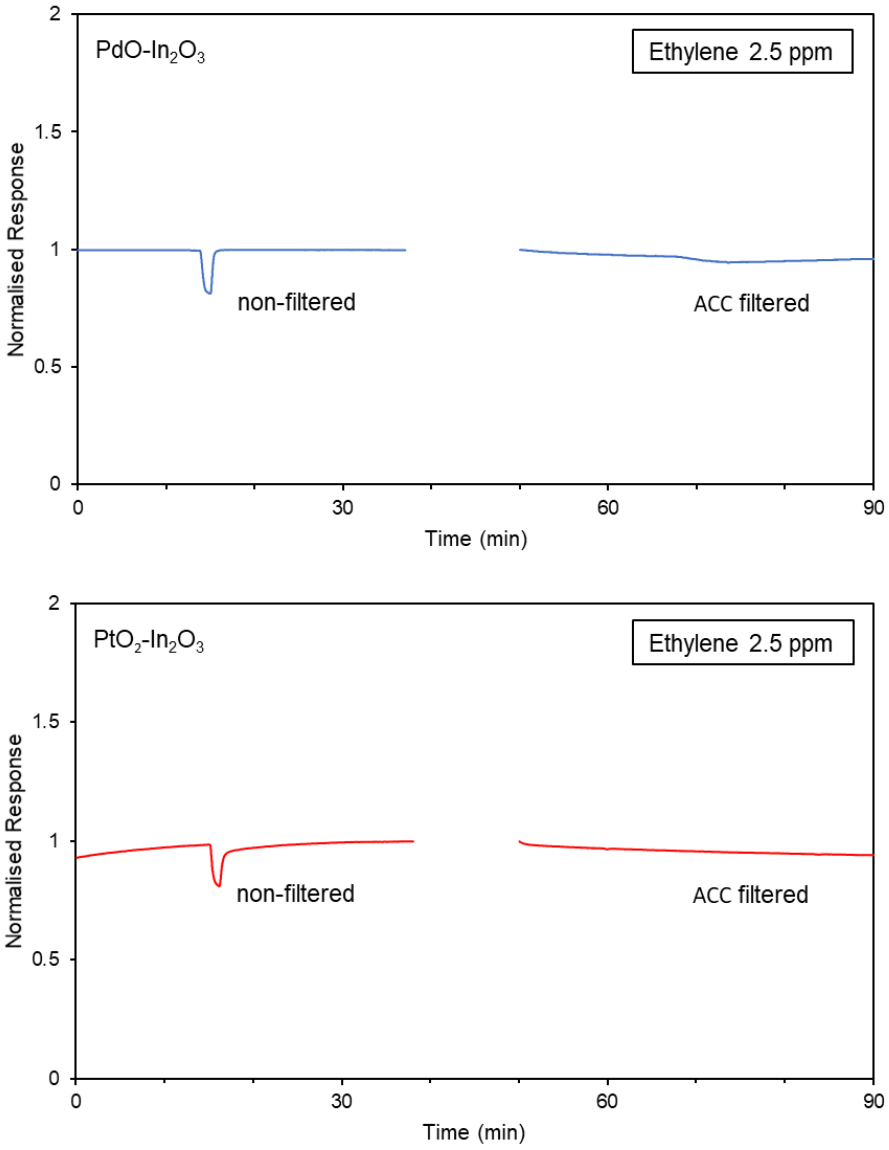

Figure 8 - 9 Responses of $PdO\text{-}In_2O_3$ (top) and $PtO_2\text{-}In_2O_3$ (bottom) toward 2.5 ppm ethylene as interference gas during oxygen measurement (20%) with and without ACC filter.

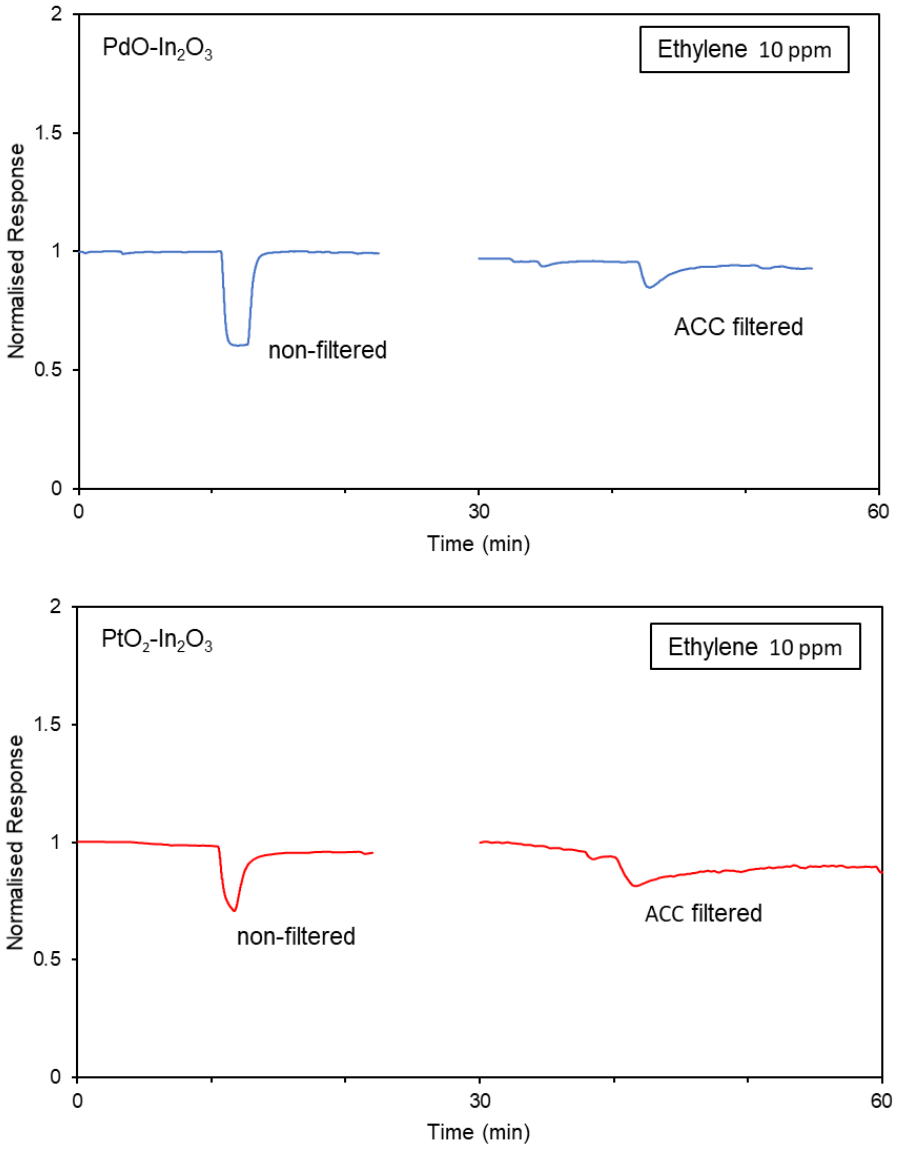

Figure 8 - 10 Responses of $PdO\text{-}In_2O_3$ (top) and $PtO_2\text{-}In_2O_3$ (bottom) toward 10 ppm ethylene as interference gas during oxygen measurement (20%) with and without ACC filter.

8.6 Conclusion

Screen printed $PdO\text{-}In_2O_3$ and $PtO_2\text{-}In_2O_3$ thick film sensors obtained the best response amongst other fabricated sensors. These sensors were further tested for their selectivity and interference to other gases.

Both type of sensors suffers from humidity interference as their responses varied when tested in humid and dry environment. This issue could be addressed by combining a humidity sensor so suppress the humidity cross-reference.

The sensors were measured against interference gases, namely isobutylene (1 ppm) and ethylene (1 ppm). Comparing the sensor responses, it was revealed that the fabricated sensors were most sensitive toward oxygen, making it justifiably fit as oxygen sensors. Further tests included introducing the interference gases to the sensors during oxygen measurement showed that sensor responses were affected by these interference gases. However, the use of activated carbon cloth (ACC) integrated to the sensor system could eliminate/reduce the interference effects.

8.7 Reference

[1] M. a. Markets. (2017, 14 Jan). *Gas Sensors Market by Gas Type (Oxygen, Carbon Monoxide, Carbon Dioxide, Ammonia, Chlorine, Hydrogen Sulfide, Nitrogen Oxide, Volatile organic Compounds, Hydrocarbons), Technology, End-Use Application, Geography - Global Forecast 2023*. Available: https://www.marketsandmarkets.com/Market-Reports/gas-sensor-market-245141093.html

[2] G. M. Insights, "Gas Sensors Market Size Worth USD 2.89 Billion by 2022: Global Market Insights Inc.," ed. Abnewswire.com, 2016.

[3] Alphasense. (13 November). *FAQs*. Available: http://www.alphasense.com/index.php/air/faqs/

[4] Alphasense. (13 November). *aan 009 how oxygen sensors work - Alphasense*. Available: www.alphasense.com/WEB1213/wp-content/uploads/2013/07/AAN_009.pdf

[5] G. F. Fine, L. M. Cavanagh, A. Afonja, and R. Binions, "Metal Oxide Semi-Conductor Gas Sensors in Environmental Monitoring," *Sensors (Basel, Switzerland),* vol. 10, no. 6, pp. 5469-5502, 2010.

[6] S. Capone, M. Zuppa, D. S. Presicce, L. Francioso, F. Casino, and P. Siciliano, "Metal oxide gas sensor array for the detection of diesel fuel in engine oil," *Sensors and Actuators B: Chemical,* vol. 131, no. 1, pp. 125-133, 4/14/ 2008.

[7] K. Wetchakun *et al.*, "Semiconducting metal oxides as sensors for environmentally hazardous gases," *Sensors and Actuators B: Chemical,* vol. 160, no. 1, pp. 580-591, 12/15/ 2011.

[8] L. A. Obvintseva, "Metal oxide semiconductor sensors for determination of reactive gas impurities in air," *Russian Journal of General Chemistry,* vol. 78, no. 12, pp. 2545-2555, 2008// 2008.

[9] C. Baban, Y. Toyoda, and M. Ogita, "Oxygen sensing at high temperatures using Ga2O3 films," *Thin Solid Films,* vol. 484, no. 1–2, pp. 369-373, 7/22/ 2005.
[10] R. K. Sharma, M. C. Bhatnagar, and A. L. Sharma, "Mechanism in Nb doped titania oxygen gas sensor," *Sensors and Actuators B: Chemical,* vol. 4, pp. 194-201, 1998.
[11] P. Jasinski, T. Suzuki, and H. U. Anderson, "Nanocrystalline undoped ceria oxygen sensor," *Sensors and Actuators B: Chemical,* vol. 95, no. 1–3, pp. 73-77, 10/15/ 2003.
[12] Y. Hu, O. K. Tan, W. Cao, and W. Zhu, "A low temperature nano-structured SrTiO3 thick film oxygen gas sensor," *Ceramics International,* vol. 30, no. 7, pp. 1819-1822, // 2004.
[13] F. Chaabouni, M. Abaab, and B. Rezig, "Metrological characteristics of ZNO oxygen sensor at room temperature," *Sensors and Actuators B: Chemical,* vol. 100, no. 1-2, pp. 200-204, 2004.
[14] G. Neri, A. Bonavita, G. Micali, G. Rizzo, N. Pinna, and M. Niederberger, "In2O3 and Pt-In2O3 nanopowders for low temperature oxygen sensors," *Sensors and Actuators B: Chemical,* vol. 127, no. 2, pp. 455-462, 2007.
[15] D. Selvakumar, N. Dharmaraj, N. S. Kumar, and V. C. Padaki, "Oxygen Sensing Properties of Platinum Doped Indium Oxide Nanoparticles Prepared by Hydrothermal Method," *Synthesis and Reactivity in Inorganic, Metal-Organic, and Nano-Metal Chemistry,* vol. 45, no. 5, pp. 753-758, 2014.
[16] H. E. Heggestad, "Ethylene: An Urban Air Pollutant AU - Abeles, Fred B," *Journal of the Air Pollution Control Association,* vol. 23, no. 6, pp. 517-521, 1973/06/01 1973.
[17] K. Na, Y. P. Kim, K.-C. Moon, I. Moon, and K. Fung, "Concentrations of volatile organic compounds in an industrial area of Korea," *Atmospheric Environment,* vol. 35, no. 15, pp. 2747-2756, 2001/05/01/ 2001.
[18] J. Retamales and R. Campos, "EXTREMELY LOW ETHYLENE LEVELS IN AMBIENT AIR ARE STILL CRITICAL FOR KIWIFRUIT STORAGE," 1997, pp. 573-578: International Society for Horticultural Science (ISHS), Leuven, Belgium.
[19] M. Egashira, M. Nakashima, S. Kawasumi, and T. Selyama, "Temperature programmed desorption study of water adsorbed on metal oxides. 2. Tin oxide surfaces," *The Journal of Physical Chemistry,* vol. 85, no. 26, pp. 4125-4130, 1981/12/01 1981.
[20] J. Gong, Q. Chen, M.-R. Lian, N.-C. Liu, R. G. Stevenson, and F. Adami, "Micromachined nanocrystalline silver doped SnO2 H2S sensor," *Sensors and Actuators B: Chemical,* vol. 114, no. 1, pp. 32-39, 2006.
[21] Q. Qi *et al.*, "Electrical response of Sm2O3-doped SnO2 to C2H2 and effect of humidity interference," *Sensors and Actuators B: Chemical,* vol. 134, no. 1, pp. 36-42, 2008/08/28/ 2008.
[22] Zorex acc, October 2018.

Chapter 9. Conclusions and Further Work

As one of the most commonly used technology with large market share in the global sensor market, metal oxide (MOX) based sensors have been extensively studied with growing interest to improve sensor performance and further explore the applications. Here, the key application was found in oxygen detection. Oxygen sensor has a wide range of applications including in cabin air quality, respiration, fermentation, process controls, and many others. Currently, the market is dominated by electrochemical sensor which works based on the oxidation of lead. In the near future, the use of lead is likely to be restricted following the bans on lead in almost all electronic devices. Furthermore, electrochemical sensors are quite bulky and have limited life span. Lead-free zirconia based oxygen sensors are available in the market, mainly used in exhaust system in automotive to monitor the fuel combustion ratio. They are usually operated in temperature >600°C, hence not suitable for applications in middle/lower temperature range. MOX based sensors can be an attractive alternative. They offer simple measurement, high sensitivity, and low manufacturing cost. The sensors come in compact size with long life span and the ability to operate in harsh or high temperature environment. Furthermore, the technology enables easy integration with smart electronic devices associated with the internet of things (IoT).

The aim for the thesis was to investigate various manufacturing techniques through the integration of inorganic materials into a range of binder system for metal oxide-based films for gas sensing application. To meet the aim, the following objectives were set:

- To determine if sensor responses are improved with a particular manufacturing technique
- To determine if sensor responses are improved when applying different materials and combination of materials as the sensing layer
- To investigate the influencing factors in metal oxide sensors and optimise them to give the best responses
- To understand any interactions between the sensor and compound of interest
- To investigate the interference of humidity and other gases in sensor responses
- Finally, to understand the effects of overall factors including microstructures, material composition and thickness, porosity, and temperature on the behaviour of the fabricated sensors.

9.1 Conclusions

In order to address the aim of the study, several deposition techniques were employed to fabricate sensor devices based on tungsten oxide and indium oxide materials. These were three-dimensional printing (3DP) fused deposition modelling (FDM), aerosol assisted chemical vapour deposition (AACVD), spin coating, and screen-printing techniques. The summary of the conclusions as described in the following shows how the aims and objectives were fulfilled through various experimental investigations in this thesis.

FDM deposition technique was used to fabricate tungsten oxide-based thick film sensors. These sensors were tested for volatile organic compounds which included isobutylene, ethanol, and acetone. They could detect these compounds and showed

better selectivity toward ethanol (down to 5 ppb). Here, a novel deposition technique using FDM was presented. This method has not been reported for gas sensing application before and showed (as a proof of principle) the feasibility to 3D print gas sensing materials.

Thin films tungsten oxide-based sensors were fabricated by AACVD and spin coating methods. These sensors were tested for oxygen under humid air and the results showed that spin coated sensors had higher response by more than x4 compared to the AACVD grown sensors (from R_g/R_a=5 to R_g/R_a=22.7). This demonstrates that sensor response could be improved with a certain manufacturing technique.

The same deposition technique was employed to fabricate sensors with different materials and/or combination of materials. AACVD grown sensors showed higher response when silver decoration was added to tungsten oxide material. The response of decorated sensors was noted higher by more than 200% (from R_g/R_a=5 to R_g/R_a=11.3). Similarly, spin coated indium oxide-based sensors showed that a higher response is obtained from sensors decorated with platinum oxide (from R_g/R_a=7.3 to R_g/R_a=9.6).

Influencing factors in metal oxide were considered and optimised to obtain better responses. In fabrication process, the deposition method itself has shown to influence sensor morphology as demonstrated by tungsten oxide based AACVD and spin coated sensors. Furthermore, layer thickness revealed to have significant effect on sensor response. Here, thick film indium oxide-based sensors showed higher response than the thin film ones. Other influencing factor was sintering temperature, which showed lower temperature could increase sensor responses. However, it must be noted that the temperature should be within the range such that the sensing

materials were porous yet structurally rigid. For the 3DP sensors, spin coated, and screen-printed sensors, the best sintering temperature was found around 850 – 900°C. Operating temperature also affected sensor response. For each deposition method, temperature sweep was required to obtain the optimum working temperature as it could be different for each type of sensors. AACVD grown tungsten oxide sensors (tested in humid air) obtained the best response at 400°C, which reduced to 350°C when silver was incorporated to the sensing materials. For tungsten oxide sensor deposited by a spin coating method, the optimum temperature was found at 350°C. Whereas spin coated indium oxide sensors showed the best response obtained at 300°C (dry air) and 250°C (wet air). Changes in humidity influenced sensor responses as well. Tests carried out in this work have demonstrated that, aligned with those found in the literatures, an increase in humidity generally reduced the sensor resistance. Although literatures reported lower resistance produced lower sensor response, this was not necessarily the case observed in this work. It was found that sensors, such as spin coated indium oxide sensors and screen printed PtO_2-In_2O_3 thick-film sensors, showed a higher response in humid than dry air. However, this was inked to the sensors baseline (99.999% N_2) was also being affected by the change in humidity.

In order to optimise sensor response, it is imperative to understand the interaction that occurs between the sensor and the compound of interest, which here was mainly oxygen. In atmospheric air, oxygen molecules are adsorbed on the metal oxide surface, drawing electrons from the conduction band that results in the formation of electron depleted layer (EDL) at the surface of the metal oxide. When the oxygen concentration decreases in the air, less molecules are adsorbed, decreasing the number of electrons drawn to the surface. This reduces the potential barrier in the metal oxide and lowers the resistance observed in the sensor.

The addition of metal/metal oxide to the base sensor material can improve sensor performance in detecting oxygen. There are two proposed sensitisation mechanisms for additives, which are electronic and chemical sensitisation. In electronic sensitisation, the additives promote changes in sensor electrical properties through a change in the oxidation state. Whereas in chemical sensitisation, the additives can facilitate chemical reactions and increase chemical rate between oxygen molecules and the surface of metal oxide material via a spill-over mechanism. With regard to oxygen detection, electronic sensitisation would change the resistance of the sensors (due to the potential difference in the conduction band of the additives and the host material) but would not improve sensor response toward O_2. An enhanced response is likely due to a spill-over mechanism, which enriches the oxygen population on the surface of metal oxide.

9.1.1 Sensor Comparison and Evaluation

Various deposition techniques were employed to fabricate thin and thick film. The comparison and evaluation are carried out for sensors fabricated for oxygen detection. The desired thickness for thin film range here was 6 – 9 µm, whereas thick film was targeted between 60 and 70 µm. Sensors fabricated by spin coating were measured at 9 ± 1.5 µm for tungsten oxide and 9 ± 1 µm for indium oxide. The measurements were varied for decorated sensors but still within the desired range (7.5 ± 2 µm for PdO-In_2O_3 and 8 ± 1 µm for PtO_2-In_2O_3). Thick film sensors produced by screen printing technique were measured at 65 ± 2 µm for PdO-In_2O_3 and 70 ± 3 µm for PtO_2-In_2O_3 sensors.

Table 9 - 1 summarises sensor response for each material fabricated and tested. AACVD grown WO_3 based sensors, spin coated WO_3 and In_2O_3, as well as screen printed decorated In_2O_3 sensors showed a reversible and stable responses having

similar resistance value before and after oxygen exposure. Amongst the deposition techniques presented, thick film indium oxide sensors demonstrated higher response than the thin film ones. Therefore, the thick film sensors were selected for further tests. In humid air, PdO-In_2O_3 showed highest response at 200°C (R_g/R_a=7.8) whereas best response of PtO_2-In_2O_3 was noted at 250°C (R_g/R_a=35.4). Repeated measurements were taken for each and across sensors within 24 months period. The results showed that sensor responses were stable, reversible, and overall reproducible. A few sensor responses were noted at a much higher resistance but simple resistance measurements at the start of a test could exclude these sensors.

Table 9 - 1 Response comparison of sensors fabricated by different deposition methods.

Deposition method	Material	Best response (Rg/Ra)			
		Humid	Temp (°C)	Dry	Temp (°C)
AACVD	WO_3	~6	400		
AACVD	Ag/Ag_2O-WO_3 A	8	400		
AACVD	Ag/Ag_2O-WO_3 B	23	350		
Spin coating	WO_3 (st= 850°C) *	11.3	350	26	350
Spin coating	WO_3 (st= 900°C)	12	350	19	350
Spin coating	In_2O_3 (st= 850°C)	7.3	250	5.5	300
Spin coating	In_2O_3 (st= 900°C)	4.0	300	3.1	300
Spin coating	PdO-In_2O_3 (st= 850°C)	7.2	350	5.5	200
Spin coating	PdO-In_2O_3 (st =900°C)	6.3	350	2.6	350
Spin coating	Pt_2O-In_2O_3 (st= 850°C)	9.6	350	5.4	350
Spin coating	Pt_2O-In_2O_3 (st= 900°C)	4.5	350	15	350
Screen printing	PdO-In_2O_3	7.8	200	12.9	200
Screen printing	Pt_2O-In_2O_3	35.4	250	32.4	350

*st refers to the sintering temperature of the films

Thick film sensors were tested under humid and dry air. A humidity test was also carried out to examine the effect of humidity changes in metal oxide sensors. The results showed that humidity indeed influenced sensor responses, generally by reducing the resistance observed the in sensors. This means for MOX materials to be used as oxygen sensors, the use of humidity sensor in conjunction with the MOX

sensor is necessary to suppress humidity interference. Selectivity test revealed that the sensors responded highest to oxygen than to the interfering gases, demonstrating sensors' suitability for oxygen detection. However, when interference gases were introduced alongside oxygen, it was revealed that sensor responses were affected by the interference gases. Here, the use of activated carbon cloth (ACC) integrated to the sensor system was shown to be able to eliminate/reduce the effect of this interference gases.

9.1.2 Source of Error and Limitations

Thick film 3D printed sensors showed stable and repeatable responses. However, responses between sensors varied quite significantly, which was likely attributed to the accuracy of the FDM instrument itself. The 3D printer cannot produce identical sensing material in term of shape and thickness. Hence, some sensors may perform better than the others.

In the fabrication process by spin coating, 2-layer deposition was required for the tungsten oxide whereas indium oxide could do with 1-layer deposition. As the masking for the sensing material was done manually by visual observation, inaccuracy of the alignment could produce variations in the sensing material. Furthermore, 2-layer deposition could potentially double the error. Ideally, instead of going for 2-layer deposition, one layer should be deposited using more viscous ink (higher WO_3 loading). However, as the UV was not able to cure thicker layer, this option could not be considered.

9.2 Further Work

Development of the research in this thesis can be extended in many directions, given the diverse nature of the investigation. An assessment of various experimental work carried out in this research has highlighted some key future investigations which are classified into 3 sections:

9.2.1 Fabrication

The work carried out in this thesis has demonstrated that thickness of sensing material played an important role in enhancing sensor response. Decorated indium oxide thin film sensors had thickness of <10 µm whereas the thickness for the decorated indium oxide thick film sensors was measured up to 70 µm. This shows that thick film sensors were better for oxygen detection. It would be interesting to investigate if further increase in sensing layer thickness contribute to even higher response.

Incorporation of additives into the host materials has shown to improve sensor performance as observed experimentally in this thesis. One ratio was used to fabricate the decorated materials across various deposition techniques. The next step would be to find the optimum ratio of the additives to obtain the highest response. Additionally, more additives could be incorporated into tungsten oxide material. The spin coated tungsten oxide (no decoration) showed a high response and this could be potentially improved further by adding decorating materials such as silver, palladium, and platinum.

Addition of the decoration was mostly carried out by wet mixing the additives with the host material. Alternative method is to deposit the additive material on top of the host material instead. This was done in AACVD method (Chapter 4) and could be

explored for spin coating and screen printing as well. The effects of these two methods can be investigated to optimise sensor response.

Further investigation on sensor active and passive filter is required to improve sensor selectivity and interference to other gases.

9.2.2 Tests and Evaluation

Further tests would be required to assess the feasibility of MOX materials for oxygen detection. This include testing with wider range of interference gas that might come in contact with the sensor, such as CO, CO_2, NO_x.

One of the most important aspects of metal oxide sensors is long-term stability of the sensors. Further tests need to be carried out to investigate sensor performance in long term bases. This should be done by operating the sensors continuously for several months up to a few years in order to explore the stability of the sensors and measure the sensor lifetime.

The effect on sensor response when interference gas is present should be further investigated. As demonstrated in Chapter 8, activated carbon cloth can filter 1 ppm isobutylene and up to 2.5 ppm ethylene. When introducing 10 ppm ethylene to the system, the sensor could not completely filter the interference gas which resulted in reduced response (though this is a high concentration). The sensors should be exposed to wider concentration range of interference gases to find the effective limit of ACC. Furthermore, the effects of poisoning on the sensors upon exposure to higher gas concentration can be explored. For example, to find out if the effects of poisoning would be permanent or reversible.

Another important test to be undertaken is to benchmark the fabricated sensors to existing commercial oxygen sensors. These tests are useful for MOX sensor evaluation whilst exploring its benefits and drawback against the commercial products.

9.2.3 Design and Packaging

Oxygen sensors based on MOX material will suffer from humidity interference as demonstrated in this thesis. If the sensor is to be used in controlled environment where humidity level is fixed, then MOX sensor could perform well. However, if the humidity is likely to changed, MOX oxygen sensor needs be incorporated with humidity sensor to suppress the humidity effect. The next step is to use the combination of these two sensors and investigate whether they can effectively differentiate changes in response due to change in humidity or oxygen level.

More compact design can be achieved by using a single sided sensor where the electrodes also serve as the heater. This would require more complex electronics as the heating and sensor reading will not be continuous/simultaneous. Instead, the system will alternate the two functions, so they can serve both as heater and electrodes. This would potentially reduce the manufacturing cost even lower and enable sensor miniaturisation.

Another step would be integration to MEMS devices. Other deposition techniques should be explored in order to deposit the sensing material onto MEMS such as drop-coating and photolithography. This approach will not only significantly shrink the size of the sensor but can also reduce the power consumption

Appendices

Appendix A

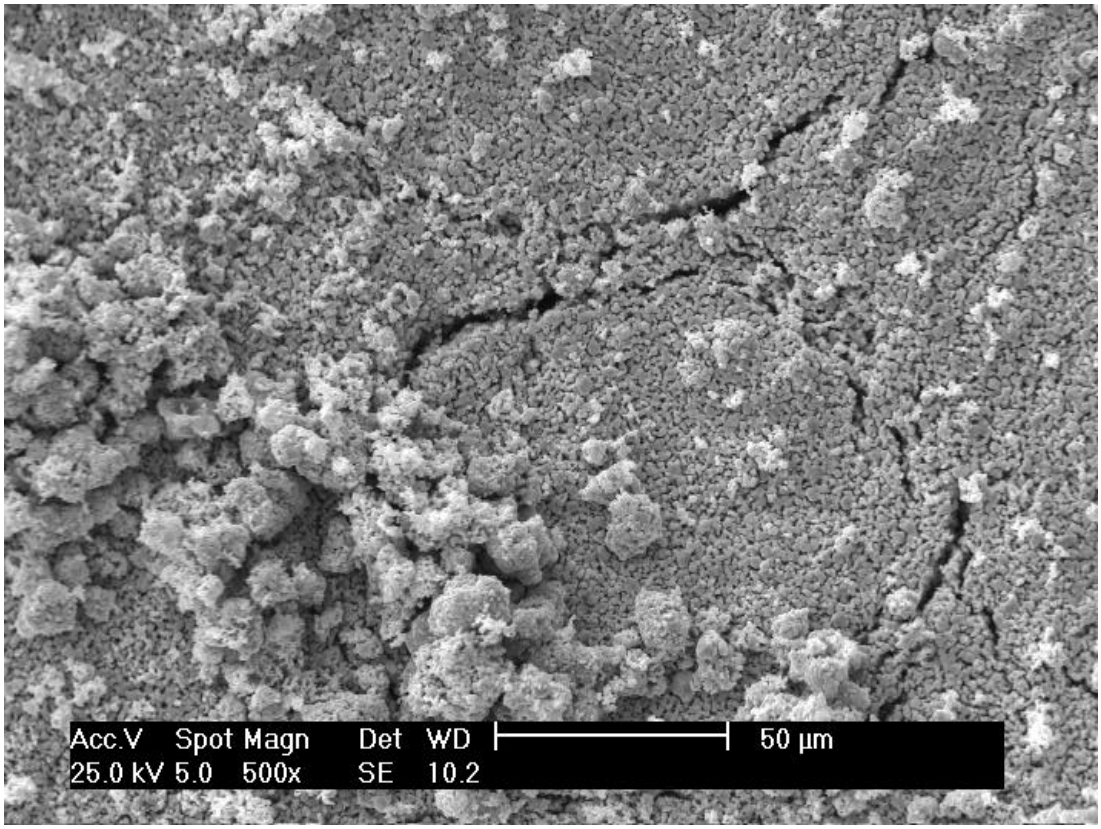

Figure A - 1 Cracks on 3D-printed WO_3 sensor.

Appendix B

Material characterisation of AACVD grown WO_3 and Ag/Ag_2O-WO_3 deposited on glass substrates

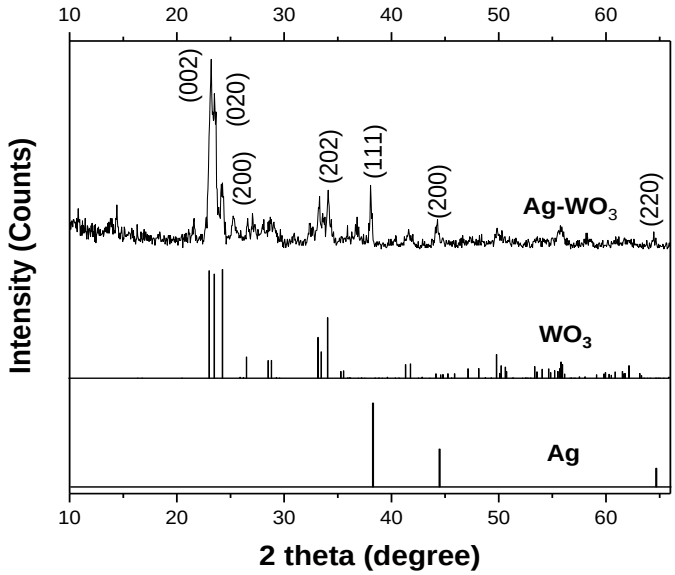

Figure A - 2 XRD patterns of Ag decorated WO_3 film on glass substrate as compared to standard data of monoclinic WO_3 (JCPDS, 72-0677) and metal Ag (JCPDS, 87-0718).

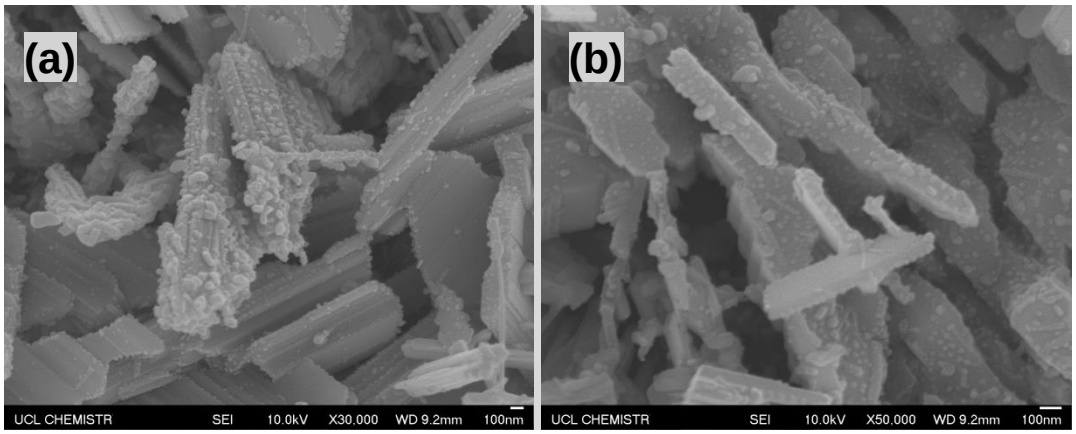

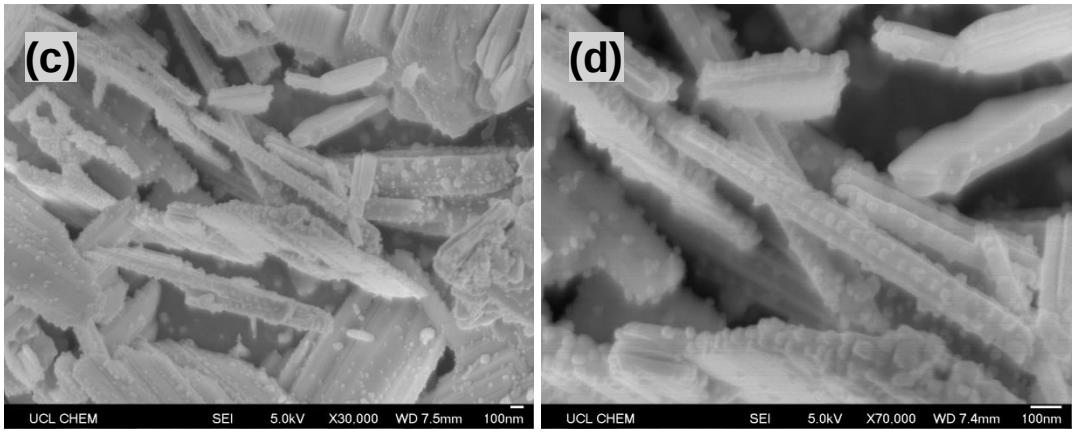

Figure A - 3 SEM images of Ag-WO_3 on glass substrate at 200 °C (a and b) 0.06g $AgNO_3$ precursor used under different magnifications and (c and d) 0.09g $AgNO_3$ precursor used under different magnifications.

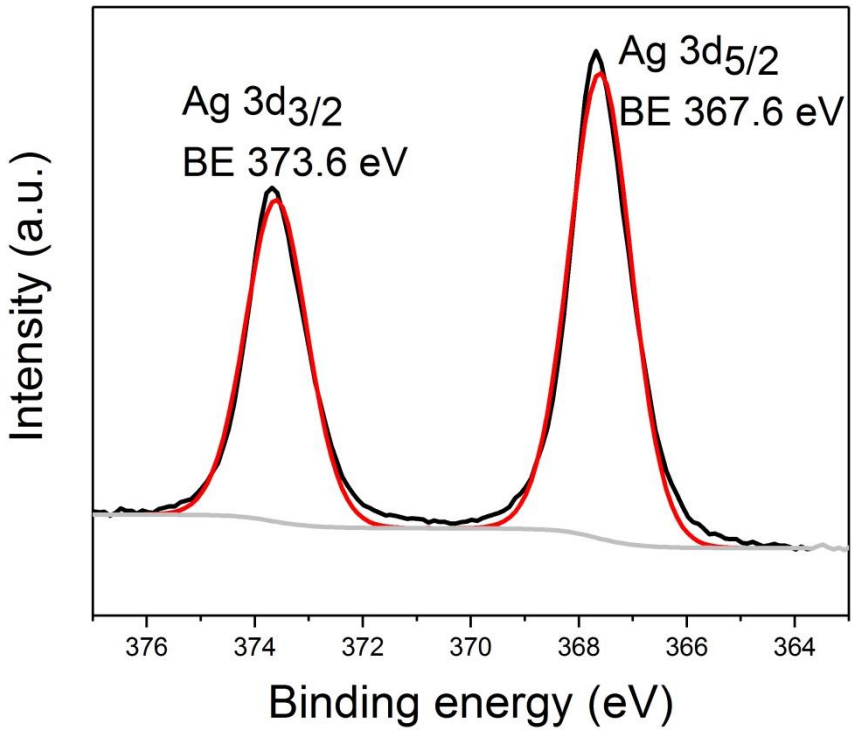

Figure A - 4 High resolution scans XPS of Ag 3d core-level spectra of Ag on glass substrate by using AgNO3 in a 2:1 mixed solvent of acetone and methanol, at 250 °C and a flow of nitrogen.

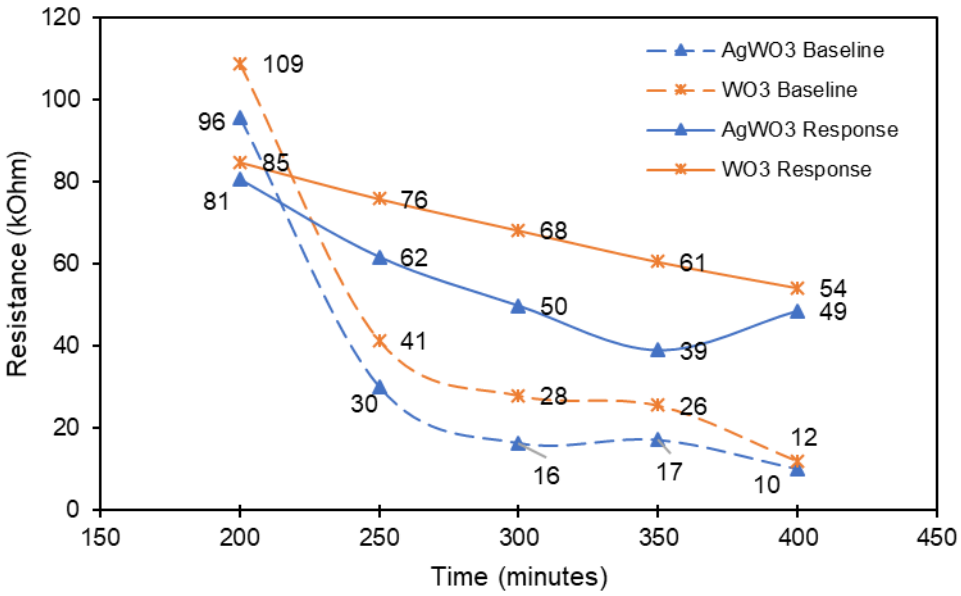

Figure A - 5 Baseline resistance and response comparison between WO_3 and Ag/Ag_2OWO_3 sensor with data label.

Appendix C

Responses of Screen Printed $PdO\text{-}In_2O_3$ and $PtO_2\text{-}In_2O_3$ Sensors

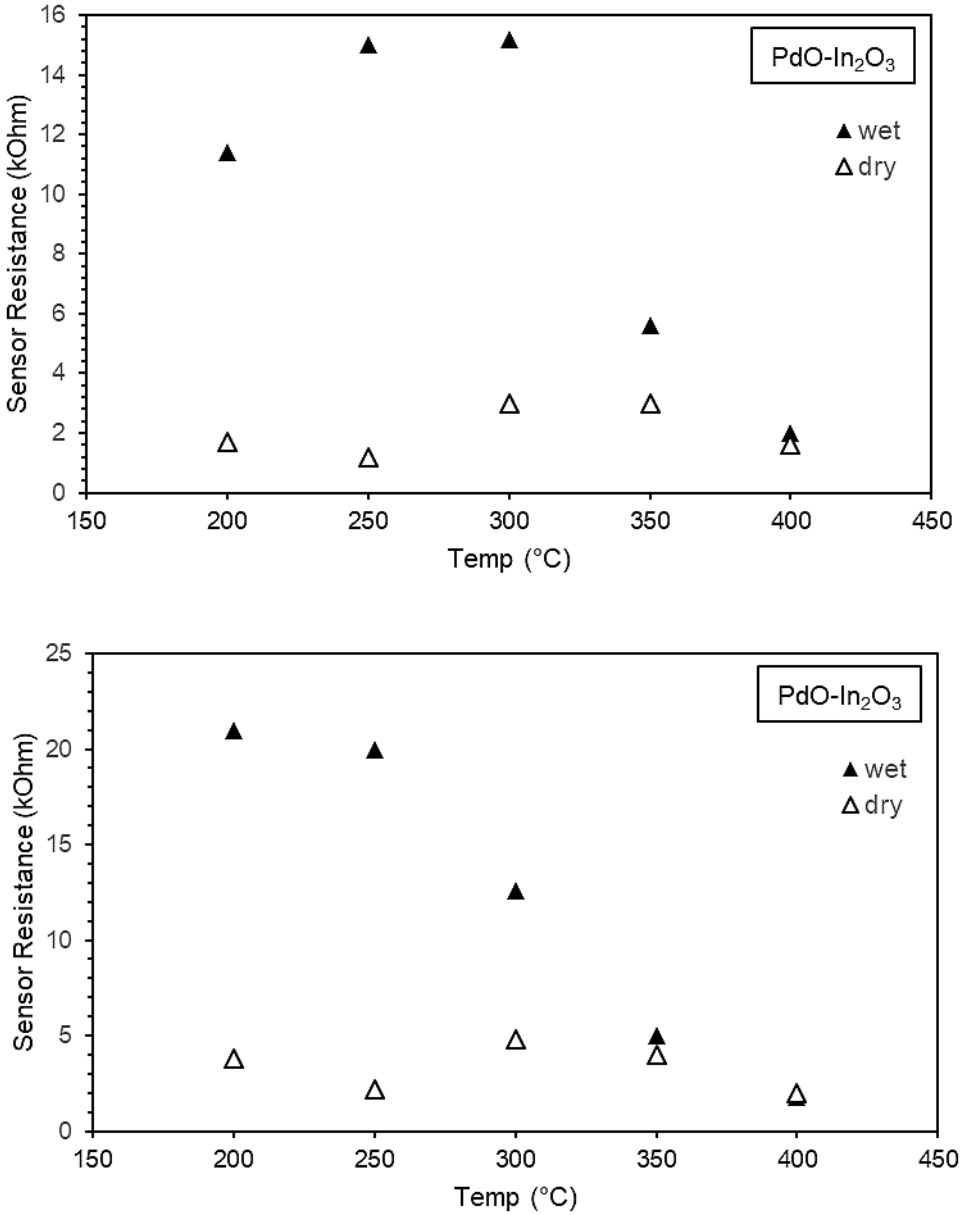

Figure A - 6 More example responses of $PdO\text{-}In_2O_3$ sensor to 20% O_2 in dry and humid (85% RH) air. Here, both sensors showed higher resistance observed in humid air than in dry air.

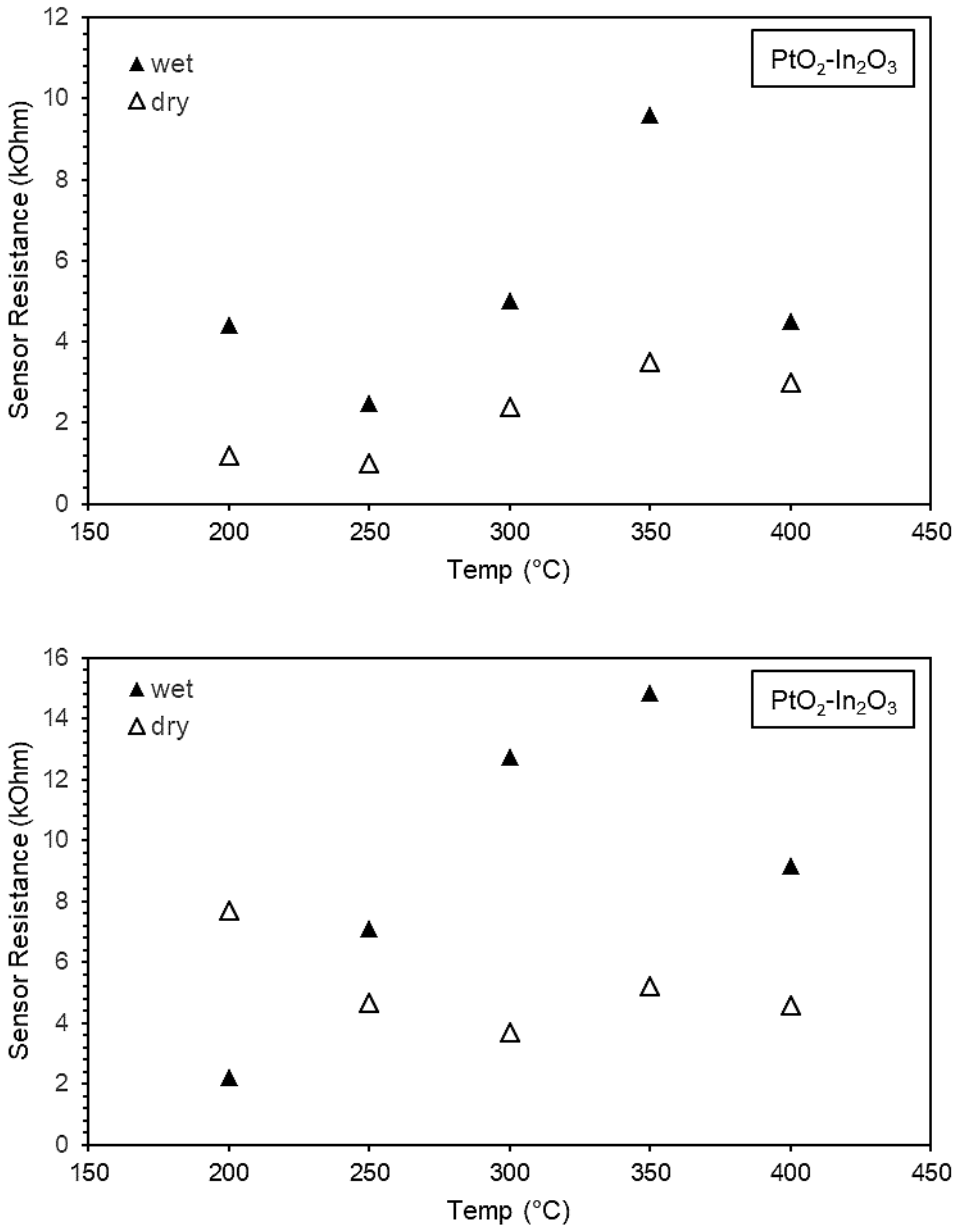

Figure A - 7 More example responses of PtO_2-In_2O_3 sensor to 20% O_2 in dry and humid (85% RH) air. Here, both sensors showed overall higher resistance observed in humid air than in dry air.